HYPERPOLARISED NOBLE GAS NUCLEAR MAGNETIC RESONANCE AND MAGNETIC RESONANCE IMAGING STUDIES OF COMPLEX POROUS MEDIA

Fraser Hill-Casey, MSci

Thesis submitted to The University of Nottingham
for the degree of Doctor of Philosophy

August 2018



It is not the mountain we conquer, but ourselves.
- Sir Edmund Hillary

Abstract

The ability to non-invasively probe void spaces is an extremely valuable tool for applications ranging from chemical engineering to biomedical, pulmonary imaging studies. Nuclear Magnetic Resonance (NMR) and Magnetic Resonance Imaging (MRI) provide such a methodology. To achieve suitable signal intensity from the magnetic resonance experiment, a probe molecule such as H_2O is introduced to the void space to generate enough detectable signal for an MR system. The use of liquids, however, restricts the time scales accessible and confines characterisation of diffusion to that of the molecular regime. In recent years, gas phase measurements have been made with probe molecules such as sulphur hexafluoride SF_6 but such measurements typically require high pressures to achieve suitable sensitivity and as such are subject to the same limitations as liquid measurements. However, via use of hyperpolarisation (hp) techniques such as Spin Exchange Optical Pumping (SEOP) it is possible to perform measurements of noble gases at atmospheric pressure and room temperature. As such, it is possible to utilise these hp gasses to investigate low-density, gas-phase mass-transport, such that the diffusion may be studied in the Knudsen regime. Understanding of diffusion processes are particularly valuable to the design of hierarchical porous media such as catalysed diesel particulate filters (DPF) and other industrial catalytic processes. The characterisation of the structure-transport

relationships of porous solids is extremely valuable for the design of new advanced catalysed materials for a range of applications.

The work within this document has applied a variety of MR techniques to the investigation of structure-transport relationships in complex porous media. Further new production methodologies have allowed for new, novel gas probes to be produced, further increasing applicability of hp noble gas MR techniques to probing void spaces within porous media.

Hp ^{129}Xe has been shown to be a valuable probe of flow within complex porous media via MRI phase-shift velocimetry. Measurements were performed in channels with porous walls and velocity profiles were shown to provide good correlated with theoretical models.

Structure-transport relationships within the hierarchical pore structure of the DPF was probed via a multi-modal, multi nuclei-study. NMR relaxometry and MRI of gas phase ^{129}Xe were used as to interrogate the contributions of each level of the structural hierarchy of the sample to the dispersive mass transport.

A novel methodology of SEOP for the production of highly polarised ^{129}Xe and ^{83}Kr spin states via use of hydrogen-noble gas mixtures is presented. Catalytic separation techniques were employed for purification of the polarised spin system from its buffer gas of H_2. These developments enhance the applicability of ^{129}Xe and ^{83}Kr to material science applications, as well as vastly increasing viability of clinical applications.

Finally, SEOP of ^{21}Ne was performed and for the first time produced a highly polarised sample, suitable for NMR spectroscopy and relaxometry studies. The quadrupolar relaxation of ^{21}Ne was characterised in a range of void spaces and surface chemistries. ^{21}Ne is shown to be a promising probe for investigations of porous media.

Publications resulting from This Thesis

Peer Reviewed Journal Publications

1. Hill-Casey F., Hitchcock I., Meersmann T, Hotchkiss T, Hardstone K.A., Pavlovskaya G.E., Rigby S.P., Hyperpolarised Xenon MRI Studies of Structure-Transport Relationships in Hierarchical Porous Media, *Manuscript in preparation*

2. Rogers N.J., Hill-Casey F., Stupic K. K., Six J.S., Lesbats C,. Rigby S.P., Fraissard J., Pavlovskaya G.E., Meersmann T. "Molecular hydrogen and catalytic combustion in the production of hyperpolarized Krypton-83 and Xenon-129 MRI contrast agents." Proceedings of the National Academy of Sciences 2016; 113(12).

Oral Presentations at International Conferences

1. Hill-Casey F., Rigby S.P., Pavlovskaya G.E., Meersmann T., "Development of continuous flow hyperpolarized (hp) ^{129}Xe for gas phase NMR velocimetry studies in porous media", Magnetic Resonance In Porous Media (MRPM) 13, 4th-8th September 2016 Bologna, Italy

2. Hill-Casey F., Rogers N J, Stupic K F,. Six J S, Lesbats C,. Rigby S.P, Fraissard J,. Pavlovskaya G.E, Meersmann T., "'Explosive' production of hyperpolarized ^{83}Kr and ^{129}Xe MRI contrast agents", EUROMAR, 3rd-7th June 2016, Aarhus, Denmark

Acknowledgements

I would like to acknowledge and express gratitude towards a great deal of people who have helped and supported me throughout my PhD. Whilst it is difficult to thank everyone appropriately, i shall at least, try here.

Firstly I must, of course, thank my supervisors: Sean Rigby, Thomas Meersmann and Galina Pavloskaya for giving me the opportunity to work with them, and the extensive advice they provided during the past three and a half years. I must also express my thanks to Johnson Matthey and its employees: Iain Hitchcock, Katherine Hardstone and Thomas Hotchkiss without whom this work could not have been performed. I would also like to thank Paul Glover and Mick Mantle for agreeing to conduct my *viva voce*.

Next I would like to thank the team I worked with during my time in Nottingham. Particularly to Clémentine Lesbats without whose (variable) patience and friendship I would never have learnt a great deal of experimental skills necessary for me to produce the work herein. I also wish to thank Zahra Rahemtulla who in her times at Nottingham has proved to be a great friend. The travelling postdoc Josh Bray, who whilst on his occasional lab visits would show up at my flat with beer asking to sleep on my sofa. And Wasif Zia who provided mentorship and challenged me in during my final year at Nottingham. It has been a true pleasure to work with you all.

A massive thanks must go to my friends at Nottingham Trent University, specifically Rob Morris and Theodore Hughes-Riley who set me down the path of MR research.

I must thank Adam Gaunt who has been a partner in crime through this whole endeavour. I thoroughly enjoyed our lively debates and shared (semi-successful/semi-calamitous) engineering projects. It has been nice to suffer together.

I next must thank Elena Kleban, whose cheerful and optimistic nature provided an excellent foil to my grumpy cynicism in the office while writing our respective thesis. It may have even begun to rub off on me in the end.

I would be remiss, if I did not express my deep thanks to Alan Dorkes and his phenomenal skills in fixing broken equipment and his ability to interpret and vastly improve any and all of my (attempts) of technical drawings and designs.

Additionally i would like to give my thanks to everyone else in the SPMIC: George, Simon, Ben McGeorge-Henderson, Ed Breeds, Glynn, Lesley, Liz, Antonio, Andrea, Chris Mirfin, Chris Bradley, Fed, Subhradip, Tom Deo and anyone else who I am forgetting here!

I must thank my friends Lewis, Tom and Ryan from outside the SPMIC who know nothing of MR but helped keep me sane throughout my PhD with climbing, skiing and assorted adventurous endeavours.

Finally, I would like to thank my all my family and my wonderful partner Imogen. All of whom have put up with and supported me in the ups and downs over the past three and a half years. Without you all, none of this would have been possible.

Contents

Abstract ii

Publications resulting from This Thesis iv

Acknowledgements v

1 Introduction 1
1.1 Aims of this Work 3

Reference 5

2 NMR Theory 7
2.1 Introduction 7
2.2 Nuclear Spin 8
2.2.1 Magnetic Moment 9
2.2.2 Resonance 10
2.3 Zeeman Effect 11
2.3.1 Nuclear Zeeman Splitting 11
2.4 Polarisation at Thermal Equilibrium 12
2.5 The NMR Signal 16
2.5.1 Radio Frequency Excitation 16
2.5.2 The Free Induction Decay 17
2.5.3 Fourier Transform 18
2.5.4 The Spin Echo 19
2.6 Relaxation Mechanisms 20
2.6.1 Spin-Lattice Relaxation: T_1 21
2.6.2 Spin-Spin Relaxation: T_2 24
2.6.3 Spectral Density and correlation times 27
2.7 Magnetic Resonance Imaging 33
2.7.1 Slice Selection 34
2.7.2 Frequency Encoding 35
2.7.3 Phase Encoding 36
2.7.4 Gradient Echo Imaging 36
2.7.5 Spin Echo Imaging 37
2.8 Summary 38

Reference 39

3 Hyperpolarisation of Noble Gasses **41**
3.1 Introduction . . . 41
3.2 Hyperpolarisation methods . . . 43
3.2.1 Dynamic Nuclear Polarisation . . . 43
3.2.2 Brute-Force Polarisation . . . 46
3.2.3 Metastable Exchange Optical Pumping . . . 48
3.2.4 Spin Exchange Optical Pumping . . . 49
3.3 SEOP Mechanisms . . . 51
3.3.1 Polarisation of the Alkali Metal vapour . . . 51
3.3.2 Alkali Metal-Noble Gas interactions . . . 54
3.3.3 Spin Exchange Rates and Noble Gas Polarisation 56
3.4 Summary . . . 59

Reference **60**

4 MRI Velocimetry measurements in channels with porous walls **65**
4.1 Introduction . . . 66
4.1.1 MRI: Principles of MR Velocimetry . . . 68
4.1.2 Diffusion mechanisms . . . 70
4.1.3 Mercury Porosimetry . . . 74
4.2 Experimental . . . 76
4.2.1 Flow System . . . 76
4.2.2 X-Ray Computed Tomography . . . 78
4.2.3 Continuous flow Spin Exchange Optical Pumping 78
4.2.4 MRI Parameters . . . 79
4.3 Results and Discussion . . . 81
4.3.1 Mercury Porosimetry . . . 81
4.3.2 X-Ray CT . . . 82
4.3.3 Flow in an empty cell . . . 84
4.3.4 Flow in Steam Reformer pellets . . . 89
4.4 Conclusions . . . 93

Reference **95**

5 Hyperpolarised Xenon MRI Studies of Structure - Transport Relationships in Hierarchical Porous Media **100**
5.1 Motivation . . . 101
5.2 Introductions . . . 102
5.3 Experimental . . . 106
5.3.1 Computerised X-ray Tomography . . . 106
5.3.2 Mercury Porosimetry . . . 107
5.3.3 Relaxometry . . . 107
5.3.4 NMR and MRI studies of drying. . . . 109
5.3.5 Hyperpolarised ^{129}Xe gas production and delivery. 113
5.3.6 NMR and MRI experiments . . . 114
5.3.7 MRI: Principles of MR velocimetry . . . 116

5.3.8 MRI studies of mass transport . . . 117
5.4 Results . . . 119
5.4.1 Computerised X-ray Tomography . . . 119
5.4.2 Mercury porosimetry . . . 120
5.4.3 NMR relaxometry studies of drying . . . 121
5.4.4 ^{2}H MRI studies of drying of monolith . . . 124
5.4.5 ^{129}Xe NMR relaxometry studies of drying of monolith 126
5.4.6 MRI velocity imaging studies of flow in monoliths 133
5.5 Discussion . . . 137
5.6 Conclusions . . . 138

Reference 140

6 Explosive production of Hyperpolarised ^{129}Xe and ^{83}Kr MRI contrast agents 144
6.1 Introduction . . . 145
6.1.1 Apparent polarisation . . . 146
6.1.2 Cryogenic separation of hp gas . . . 147
6.2 Spin Exchange Optical Pumping of ^{83}Kr and ^{129}Xe . . . 151
6.2.1 Stopped Flow Spin Exchange Optical Pumping . 151
6.2.2 On Resonance Rubidium Hydride Formation. . . 152
6.2.3 Molecular hydrogen as a radiation quenching agent 153
6.3 Catalytic separation of H_2 hyperpolarisation mixes . . . 156
6.4 Conclusions . . . 163

Reference 166

7 Neon-21 As A New Probe Of Porous Media 173
7.1 Introduction . . . 173
7.2 Materials and Methods . . . 177
7.2.1 NMR parameters . . . 177
7.2.2 Hyperpolarised ^{21}Ne Production by batch mode Spin Exchange Optical Pumping . . . 178
7.2.3 Polarization build-up of hyperpolarised ^{21}Ne in batch mode . . . 180
7.2.4 Measurements of D_2 Fluorescence . . . 183
7.2.5 Longitudinal Relaxation measurements in hyperpolarised systems . . . 185
7.2.6 Sample Preparation . . . 186
7.3 Results and Discussion . . . 187
7.4 Conclusions . . . 191

Reference 194

8 Conclusions and Outlook 199

Reference 205

A Flow propagators **207**

B Monolith Channels Velocity Line Profiles **208**

List of Figures

2.1 Ensemble of spins in a Magnetic field 10
2.2 precession of a spins in an externally applied Magnetic field 11
2.3 Zeemann sub level diagram of ^{1}H and ^{83}Kr 13
2.4 RF excitation of a ensemble of Spin 1/2 nuclei 17
2.5 Free Induction Decay of an excited nuclei 18
2.6 Examples of Fourier transform 19
2.7 Spin Echo Formation 20
2.8 Time course of the longitudinal magnetisation 22
2.9 Evolution of Longitudinal magnetization 23
2.10 Time course of the Transverse magnetisation 24
2.11 Evolution of Transverse magnetization after the application of a 90° pulse 26
2.12 Spectral Density Function 30
2.13 Longitudinal relaxation time of ^{129}Xe as a function of correlation time 33
2.14 Spatial Encoding with magnetic field gradients 34
2.15 Slice Selective Gradient Echo Imaging Sequence 37
2.16 Slice Selective Spin Echo Imaging Sequence 38

3.1 Thermal Vs. Hyperpolarised ^{129}Xe 43
3.2 Boltzmann spin polarisation as a function of temperature at a field strength of 3.35 T 44
3.3 Diagram of a Spin Exchange Optical Pumping Cell and Optics 51
3.4 Optical Pumping of the Rubidium valence electron . . . 53
3.5 Spin Exchange Mechanisms. 54

4.1 Slice Selective, Gradient Echo Velocimetry Imaging Sequence 71
4.2 Schematic of knudsen & molecular diffusion 73
4.3 Pellets Flow System 77
4.4 Continuous flow Spin Exchange Optical Pumping experimental apparatus 80
4.5 Mercury Intrusion Curve For Steam Reformer Pellets . . 82
4.6 X-Ray CT Of 4 Channel Pellets, Prior To and Post Intrusion of Mercury 83

4.7 Pore Size Distribution Of 4 Channel Pellets 84
4.8 V_z, V_y and V_y Velocity Images Of Hyperpolarised ^{129}Xe In An Empty Cell 86
4.9 Velocity Profiles Of Superficial Flow Within an Empty Cell 88
4.10 Magnitude and Flow offset Within An Empty Cell 89
4.11 Flow in Four channel pellets 91
4.12 Radial profiles 92

5.1 Schematic of the combined selective catalytic reduction monolith. 110
5.2 Experimental apparatus 115
5.3 Timing diagram of a MRI velocimetry experiment 116
5.4 X-ray CT of a Combined Selective Catalytic Reduction-Filtration Monolith 120
5.5 Mercury intrusion curve for a copper free Combined Selective Catalytic Reduction-Filtration Monolith 121
5.6 Spin-lattice relaxation of ^{1}H and ^{2}H as a function of filled pore volume 123
5.7 Raw Spin-lattice relaxation profile of ^{1}H and ^{2}H in monolith at 25 % saturation and dry. 124
5.8 MR spin density images of D_2O drying out of a Combined Selective Catalytic Reduction-Filtration Monolith . . . 125
5.9 T_2 map and associated histogram of D_2O in a Combined Selective Catalytic Reduction-Filtration Monolith . . . 127
5.10 Schematic of the sample used in the relaxation experiments and example ^{129}Xe spectra 128
5.11 T_1 of hyperpolarisation ^{129}Xe vs free pore volume 129
5.12 Schematic of gas flow in the Combined Selective Catalytic Reduction-Filtration Monolith used in this series of experiments 130
5.13 Gas Dispersion in Combined Selective Catalytic Reduction-Filtration Monolith 132
5.14 Axial Velocimetry maps in Combined Selective Catalytic Reduction-Filtration Monolith 135
5.15 3D Velocimetry in Combined Selective Catalytic Reduction-Filtration Monolith 136

6.1 Apparent and Full Spin Polarisation as a function of SEOP cell pressures for ^{83}Kr 148
6.2 Longitudinal relaxation T_1 of solid ^{83}Kr 150
6.3 Experimental apparatus used for stopped flow SEOP . . 152
6.4 ^{83}Kr and ^{129}Xe polarisation as a function of pressure for a range of gas mixes 154
6.5 D_2 fluorescence of a range of hyperpolarisation gas mixes 157
6.6 Combustion apparatus 158
6.7 Photos of the combustion process 159
6.8 NMR of the combustion of a ^{129}Xe - H_2 gas mixture . . . 161

6.9 NMR of the combustion of a ^{83}Kr - H_2 gas mixture . . . 163

7.1 Spin Exchange Optical Pumping set-up for ^{21}Ne production 178
7.2 Thermally and hyperpolarized ^{21}Ne 181
7.3 Neon SEOP build up curves 182
7.4 D_2 fluorescence of a range of hyperpolarisation gas mixes 184
7.5 Neon T_1 Decay 186
7.6 Relaxation Rate (R_1) verse the inverse bead radii 189
7.7 Longitudinal relaxation of hp ^{21}Ne as a function of pressure in 2.5 mm diameter beads pack 190

A.1 Flow propagator from within the SCR monolith channels 207

B.1 Theoretical Orthogonal and Diagonal line Profiles of Laminar Flow in a Rectangular Channel 208

List of Tables

2.1 Properties of nuclear isotopes 11

4.1 Constants A and B for analysis of mercury porosimetry data 76

5.1 Relevant properties of the combined SCR filtration monolith channels 110

7.1 ^{21}Ne relaxation times in void spaces of glass beads. . . . 189

Chapter 1

Introduction

Nuclear Magnetic Resonance (NMR) spectroscopy and Magnetic Resonance Imaging (MRI) are extremely informative methods for determining structure, interconnectivity and functionality of micro- and meso-porous materials [1–7]

NMR and MRI exploits the effect that magnetic fields have on subatomic particles and the energy-state population differences that arise from the subtle change in the energy levels of the quantum spin states. The achievable signal in any NMR/MRI experiment is proportional to the difference in population of these states. The population difference in each state is governed by the Boltzmann statistics [8]. Traditionally to increase the population difference in the energy states, and as such the NMR signal, scientists and engineers have pushed to higher magnetic field strengths or, where possible, lower temperatures.

However other methods may be employed to enhance sensitivity of the NMR exiperment. One such method is that of *batch* [9, 10] and *continuous flow* [11] Spin Exchange Optical Pumping (SEOP) which allows for significant signal enhancement of noble gasses to be produced at even low

concentrations [12, 13]. Xenon-129 for instance is a particularly attractive probe nuclei due to its (relatively) large gyromagnetic ratio (and thus receptivity) and large chemical shift when imbibed in a pore structure [14]. Further as a chemically inert probe noble gas NMR and MRI is an extremely attractive method for interrogation of porous structures.

One such area of significant interest is that of the Combined Selective Catalytic Reduction - Filtration catalyst. Heterogeneous catalysis is a extremely lucrative technology with a wide range of applications to chemical manufacturing and automotive exhaust gas filtration. Heterogeneous catalysts such as the C-SCR monolith are typically supported on microporous and mesoporous solids, such as alumina or silica. This is due in part to the extremely high surface area present in such materials, allowing a large area for the active catalyst to bind to. In such materials it is the transport of the reactant and products from the outer surface of this micro- /meso-porous material to the contained catalytic surfaces which determines the catalytic activity and deactivation behaviour. As such it is critical to characterise the pore structure to understand the effects it will play in the performance of chemical reactions.

Further significant challenges exist with industrial utilisation of such catalysts, with stringent performance criteria being required. Such as high catalytic selectivity and catalytic activity as to further adhere to both specific regulatory standards and to achieve sufficient revenue of the product in question.

The ability to accurately and effectively characterise complex porous media substrates allows of the development of new and advanced efficient catalysts. Hyperpolarised noble gas NMR and MRI is shown herein to provide a unique method of non-invasively probing the pore structure-

transport relationships of complex porous materials as to aid in characterisation.

1.1 Aims of this Work

The research presented within this document can be considered as being split into two major themes; firstly there is the development of techniques for the application of hyperpolarised Xenon-129 to porous media samples. Secondly is the optimisation of Spin Exchange Optical Pumping and production methodologies of hyperpolarised ^{129}Xe, ^{83}Kr and ^{21}Ne. A summary of each chapter is now given.

In **Chapter 2** an appropriate theoretical background of Nuclear Magnetic Resonance (NMR) and Magnetic Resonance Imaging (MRI) is discussed. Attention is placed upon specific aspects of relevance to porous media studies.

Chapter 3 provides an overview of hyperpolarisation techniques for producing a highly polarised spin state of noble gasses. Background is provided on Dynamic nuclear polarisation, *Brute Force* and Metastable Exchange Optical Pumping. A in-depth discussion of Spin Exchange Optical pumping will be presented with a focus on experimental minutia.

Chapter 4 describes the development of hp ^{129}Xe production in the continuous flow mode, and lead into the the use of hp ^{129}Xe MRI velocity imaging of gas flow in channels with porous walls.

Chapter 5 details the bulk of the porous media work performed within this theses. A combination of hyperpolarised Xenon-129 along with, Deuterium and Proton NMR and MRI is used to investigate the complex pore

structure of a Combined, Selective-Catalytic Reduction Monolith, commonly utilised for diesel filtration catalysts. ^{129}Xe is shown to be an effective probe of the pore structure and is sensitive to the hierarchically organised pore structure.

Chapter 6 describe the thorough investigation of a new production methodology for ^{129}Xe and ^{83}Kr. The details of apparent polarisation, SEOP with molecular hydrogen and combustive separation of the hp gas mixture and its buffer gas.

Chapter 7 describes the novel optical pumping of ^{21}Ne is investigated for the first time externally from the optical pumping cell. Studies were performed for the first time into the optical pumping parameters at ultra high field and comparisons to literature was made. Further the longitudinal relaxation of ^{21}Ne was probed as a function of pore volume for the first time, with a view to carrying out relaxometry investigations to micro porous structures.

Chapter 8 provides a conclusion to the work presented within the thesis and proposes future work.

Bibliography

[1] B. Blümich, "NMR Imaging of Materials," *Measurement Science and Technology*, vol. 14, no. 9, p. 1739, 2003.

[2] I. V. Koptyug, R. Z. Sagdeev, L. Y. Khitrina, and V. N. Parmon, "A nuclear magnetic resonance microscopy study of mass transport in porous materials," *Appl. Magn. Reson.*, vol. 18, pp. 13–28, 2000.

[3] L. F. Gladden, M. H. Lim, M. D. Mantle, A. J. Sederman, and E. H. Stitt, "MRI visualisation of two-phase flow in structured supports and trickle-bed reactors," *Catalysis Today*, vol. 79-80, pp. 203–210, 2003.

[4] A.J. Sederman, M. Johns, a.S. Bramley, P. Alexander, and L. Gladden, "Magnetic resonance imaging of liquid flow and pore structure within packed beds," *Chemical Engineering Science*, vol. 52, no. 14, pp. 2239–2250, 1997.

[5] N. Robinson, L. F. Gladden, and C. D'Agostino, "Exploring catalyst passivation with NMR relaxation," *Faraday Discuss.*, vol. 204, pp. 439–452, 2017.

[6] I. V. Koptyug, S. A. Altobelli, E. Fukushima, A. V. Matveev, and R. Z. Sagdeev, "Thermally Polarized 1H NMR Microimaging Studies of Liquid and Gas Flow in Monolithic Catalysts," *Journal of Magnetic Resonance*, vol. 147, pp. 36–42, nov 2000.

[7] L. F. Gladden and P. Alexander, "Applications of nuclear magnetic resonance imaging in process engineering," *Measurement Science and Technology*, vol. 7, pp. 423–435, 1999.

[8] P. T. Callaghan, *Principles of Nuclear Magnetic Resonance Microscopy*. Oxford science publications, Clarendon Press, 1993.

[9] T. Hughes-Riley, J. S. Six, D. M. L. Lilburn, K. F. Stupic, A. C. Dorkes, D. E. Shaw, G. E. Pavlovskaya, and T. Meersmann, "Cryogenics free production of hyperpolarized 129Xe and 83Kr for biomedical MRI applications," *Journal of Magnetic Resonance*, vol. 237, pp. 23–33, 2013.

[10] J. S. Six, T. Hughes-Riley, K. F. Stupic, G. E. Pavlovskaya, and T. Meersmann, "Pathway to Cryogen Free Production of Hyperpolarized Krypton-83 and Xenon-129," *PLoS ONE*, vol. 7, no. 11, 2012.

[11] E. Brunner, "Applications of laser-polarized129Xe under continuous flow," *Magnetic Resonance in Chemistry*, vol. 37, pp. S14–S22, dec 1999.

[12] D. A. Barskiy, A. M. Coffey, P. Nikolaou, D. M. Mikhaylov, B. M. Goodson, R. T. Branca, G. J. Lu, M. G. Shapiro, V. V. Telkki, V. V. Zhivonitko, I. V. Koptyug, O. G. Salnikov, K. V. Kovtunov, V. I. Bukhtiyarov, M. S. Rosen, M. J. Barlow, S. Safavi, I. P. Hall, L. Schröder, and E. Y. Chekmenev, "NMR Hyperpolarization Techniques of Gases," *Chemistry - A European Journal*, vol. 23, no. 4, pp. 725–751, 2017.

[13] B. M. Goodson, "Nuclear Magnetic Resonance of Laser-Polarized Noble Gases in Molecules, Materials, and Organisms," *Journal of Magnetic Resonance*, vol. 155, no. 2, pp. 157–216, 2002.

[14] T. Meersmann and E. Brunner, *Hyperpolarized Xenon-129 Magnetic Resonance: Concepts, Production, Techniques and Applications*. New developments in NMR, Royal Society of Chemistry, 2015.

Chapter 2

NMR Theory

2.1 Introduction

The purpose of this chapter is to present the basic concepts behind nuclear magnetic resonance (NMR) in order that the reader may understand the research presented later in this thesis. For a more in-depth overview the reader is directed to the following texts by Levitt [1], Callaghan [2, 3], Abragam [4] and Haacke [5].

This chapter will introduce the concept of angular momentum and "phenomenological" description of the nuclear spin. The nuclear gyromagnetic ratio, Zeemann splitting and further the importance of the Boltzmann distribution in spin population will be explained.

Secondly, the reader will be introduced to the Relaxation of the NMR signal from its high energy state, to it's thermal equilibrium, via Spin-Lattice T_1, and Spin-Spin T_2 relaxation. The BPP Relaxation Theory as proposed by Bloembergen, Purcell and Pound [6] will be discussed and the underling mechanisms will be examined.

Thirdly, the application of the NMR signal to produce an image will be discussed. These processes include spatial encoding by slice selection, fre-

quency encoding, phase encoding and the concept of k-space. The reader will finally be briefly introduced to the two primary imaging concepts of Spin-Echo and Gradient-Echo imaging.

2.2 Nuclear Spin

NMR and MRI relies on the fact that the atomic nucleus is composed of the nucleons: protons and neutrons. These nucleons possess a discreet intrinsic property known as the nuclear spin; The fundamental quantity being the angular momentum quantum number I, and magnetic moment μ. This quantity I also known as *Spin* may be a fixed integer or half-integer quantity. Spin arises from the fundamental symmetry of the nucleus in question with all fermions including proton.

Perhaps the first example of the inherent spin is that of the Stern-Gerlach experiment [7] in which a beam of silver atoms ($I = -1/2$) were passed through an inhomogeneous magnetic field. The beam of atoms is observed to separate into two well defined positions on a target screen. This demonstrated that atoms with nuclear spin have quantized energy levels in the presence of a external magnetic field, such as in the case of the silver atoms used in the Stern-Gerlach experiment, $I = -1/2$ or $I = +1/2$. This splitting of the energy levels are know as the Zeeman splitting and it is the manipulation of the spin population difference of these states that allows NMR to be be performed.

The single most commonly utilised nuclear spin species within NMR and magnetic resonance imaging (MRI) is that of Hydrogen (^{1}H) which with its single proton has a spin quantum number of $I = 1/2$. This is predominantly due to its extremely high natural abundance within

water making it extremely useful for studies examining biological tissue and other organic molecules.

Within this work nuclei with spin 1/2 and spin $> 1/2$ are heavily utilised. Nuclei with a nuclear spin of $I > 1/2$ such as ^{21}Ne, ^{83}Kr and ^{131}Xe have a further component known as the electric quadrupole moment, which results from the non-spherical nature of the nucleus. This effect destructively contributes to the nuclei's magnetisation due to the additional factors experienced by the nuclei in the presence of a electric field gradient.

2.2.1 Magnetic Moment

In much the same fashion as charge, particles have an electric field, and spinning charged particles create a magnetic moment. Thus spinning nuclei will also generate a magnetic field, which can be modelled as a magnetic dipole. As such Spin and magnetism are proportional to each other;

$$\mu = \gamma \boldsymbol{I}. \tag{2.1}$$

Where the proportionality constant γ is called the gyromagnetic ratio which may have either sign. For values of $\gamma > 0$ the magnetic moment is parallel to the angular momentum and for $\gamma < 0$ the magnetic moment is opposite in direction to the angular momentum as depicted in Figure 2.1.

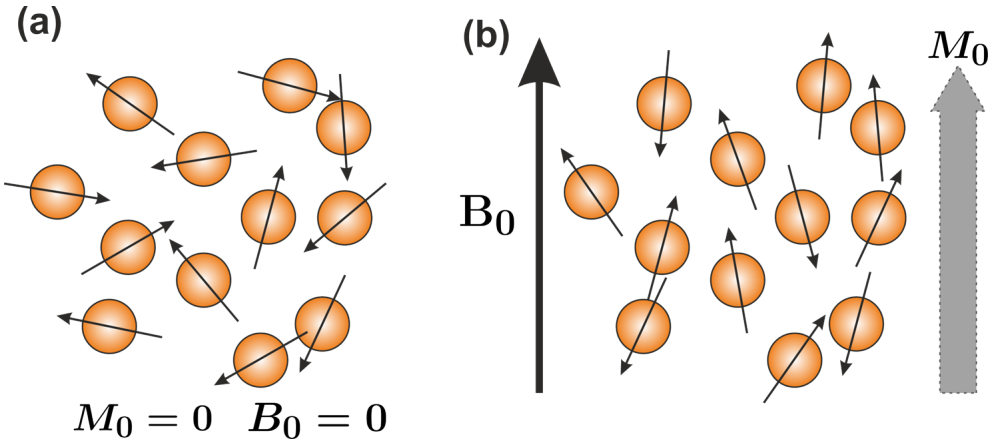


Figure 2.1: (a) A Random distribution of the magnetic moments of an ensemble of spins in the absence of magnetic field. (b) Anisotropic distribution of the magnetic moments in the presence of a static magnetic field B_0 yielding a net magnetization M_0.

2.2.2 Resonance

At thermal equilibrium the magnetic moment of the nuclei in question will have a randomly determined orientation, with an ensemble of spins thus having no net traverse magnetic field Figure 2.1. However when brought into an external magnetic field (B_0) the spins will tend to align parallel or anti parallel to the field.

This alignment of the nuclear magnetic moment to the external field B_0 exerts a *torque* on the nucleus and causes a gyroscopic precession to occur about the z axis B_0 field Figure 2.2. The frequency of the precession, is called the Larmor frequency ω_0 and is directly proportional to the gyromagnetic ratio of the nuclei in question and the magnetic field B_0 experienced by the nuclei, as given by;

$$\omega_0 = -\gamma B_0, \tag{2.2}$$

where ω_0 has units of rads s^{-1}. The direction of the precession depends

Table 2.1: Properties of nuclear isotopes relevant to this work.
Table values reproduced from reference [8].
* by definition

Nuclei	Spin	γ $10^7 rad$ $s^{-1}T^{-1}$	Frequency Ratio Vs ^{1}H	Frequency	Natural Abundance
^{1}H	1/2	26.75	1	400.18	100.00*
^{2}H	1	4.11	0.154	61.4	0.015
^{21}Ne	3/2	−2.11	0.079	31.59	0.27
^{83}Kr	9/2	−1.03	0.039	15.4	11.5
^{129}Xe	1/2	−7.44	0.278	110.69	26.4
^{131}Xe	3/2	2.21	0.083	32.81	21.23

upon the sign of the gyromagnetic ratio. Table 2.1 indicates the properties of a number of nuclei used in this work (reproduced from [8]).

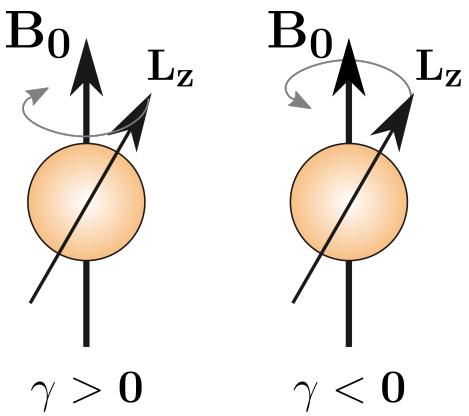


Figure 2.2: Precession of the nuclear spin magnetic moment around the external magnetic field with (a) a positive gyromagnetic ratio and (b) a negative. Figure adaptated from [1]

2.3 Zeeman Effect

2.3.1 Nuclear Zeeman Splitting

Nuclear spin species with an odd number of protons or neutrons will have multiple degenerate states. In the presence of an external magnetic field B_0 acting in the Z direction (as is convention) results in these states

splitting into discreet energy levels. Figure 2.3 depicts the Zeemann splitting and energy levels of a ^{1}H ($I = 1/2$) nucleus and a ^{83}Kr $I = 9/2$ nucleus. For the ^{1}H nuclei there are two energy levels with the separation between them being dependent on the external magnetic field B_0 and is described by,

$$\Delta E \; = \; \hbar \, \gamma B_0, \tag{2.3}$$

where $\hbar = \dfrac{h}{2\pi}$ and h is Plank's constant. The population distribution across the energy levels is described in terms of Boltzmann statistics.

2.4 Polarisation at Thermal Equilibrium

Consider an ensemble of ^{1}H nuclear spins, in an external magnetic field B_0, Zeeman splitting induces a residency within either the $m = +1/2$ or $m = -1/2$ states. The population difference between this *high energy* (N_{High}) and *low energy* (N_{Low}) states may be quantified with the aid of statistical mechanics, namely the Boltzmann distribution:

$$\frac{N_{High}}{N_{Low}} = exp\left(\frac{-\gamma\hbar B_0}{k_B T}\right), \tag{2.4}$$

where k_B is the Boltzmann constant and T is the temperature of the ensemble. The bulk polarisation may be calculated by,

$$P = \frac{N_{Low} - N_{High}}{N_{Low} + N_{High}}, \tag{2.5}$$

Equation 2.4 may then be substituted into Equation 2.5 in the case of a

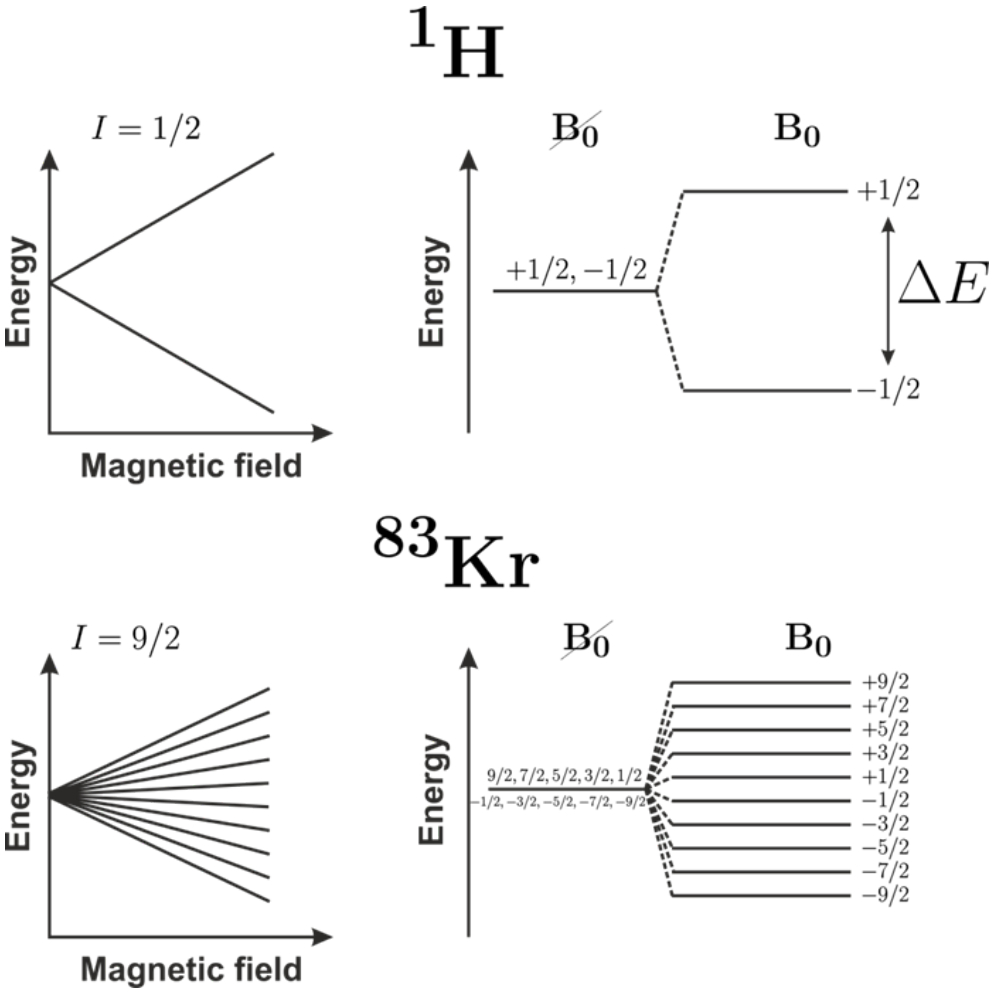


Figure 2.3: (a) B_0 dependence of the energy levels of (*i*) ^{1}H and (*ii*) ^{83}Kr on the magnetic field strength (b) Zeemann Effect: energy level diagram of the different states of (*i*) ^{1}H and (*ii*) ^{83}Kr with and without an external magnetic field.

spin $I = 1/2$ to become,

$$P = \frac{exp\left(\frac{-\gamma\hbar B_0}{2k_BT}\right) - exp\left(\frac{\gamma\hbar B_0}{2k_BT}\right)}{exp\left(\frac{-\gamma\hbar B_0}{2k_BT}\right) + exp\left(\frac{\gamma\hbar B_0}{2k_BT}\right)}. \tag{2.6}$$

Being as the thermal energy is substantially larger than the population difference between the Zeeman levels, the thermal equilibrium population difference is extremely small. As the high temperature limit is met ($(\gamma\hbar B_0/k_BT) << 1$) Equation 2.6 can then be simplified to:

$$P \approx \frac{|\gamma|\hbar B_0}{2k_BT}. \tag{2.7}$$

Equation 2.7 shows the direct dependence on both the magnetic field B_0 and the gyromagnetic ratio γ. Equation 2.7 illustrates one of the predominate challenges of NMR of nuclei with low γ, such as ^{131}Xe, ^{21}Ne and ^{83}Kr, as low γ results in less magnetization than a nuclei with a large γ such as ^{1}H.

Consider a ^{1}H nuclei sample having a $\gamma = 2.67 \times 10^8$ rad/sT at room temperature (293 K) and experiencing a reasonable polarising field strength of ($B_0 = 1.5$), there will be a spin polarisation of 3.28×10^{-5}. The NMR signal itself arises from the tiny population difference between the Zeemann levels which is determined by the difference in energy as described by Equation 2.3. In the case described only around 33 spins in every one million will contribute to the observed signal. Additionally this energy difference is minuscule in comparison to that of vibrational modes and electronic transitions.

It is useful to consider a classical analogy in the case of polarisation.

Using classical angular momentum and magnetic moment, in the presence of a magnetic field the Zeeman splitting causes nuclei in the N_{High} energy level to become aligned parallel to the magnetic field and the nuclei in the N_{low} level to become aligned anti-parallel to the field. This ratio is again determined by Equation 2.4 and means at thermal equilibrium there will be more nuclei aligned parallel to B_0 than anti-parallel, thus creating a net magnetization vector $\mathbf{M}$. At equilibrium $\mathbf{M}$ has a magnitude M_0 and is expressed by:

$$M_0 = \frac{N\gamma\hbar P}{2}, \tag{2.8}$$

where N is the total number of nuclear spins in the ensemble. The high temperature approximation of polarisation may be substituted into Equation 2.8 to produce:

$$M_0 = \frac{N\gamma^2\hbar^2 B_0}{4k_B T}, \tag{2.9}$$

which described the magnetisation at thermal equilibrium. The importance of Equation 2.9 is highlighted when considering the case of NMR spectroscopy of organic molecules. The ^{1}H signal is extremely strong and suitable data can be acquired with a limited number of scans, whereas, in the case of ^{13}C the signal is weak and requires a large number of scans to obtain adequate signal. This difference in available signal goes beyond the difference in polarisation Equation 2.7 as it also strongly depends on the amount of nuclei present in the sample. Again in terms of organic molecules, ^{1}H has a natural abundance of 100 % by definition whereas ^{13}C has only a 1.07 % natural abundance which makes signal acquisition a more time consuming process.

The majority of the work presented in the later chapters of this thesis deals with the use of magnetic resonance active noble gases, which bring with them additional challenges. Namely that of the inherently low density of gases as compared to that of liquids or solids. One must consider that the gyromagnetic ratios of the noble gas nuclei are significantly less than that of proton in all cases aside from ^{129}Xe and ^{3}He. Further exacerbating the already low NMR signal intensity the natural abundance of a number of the gases used in this work, namely ^{21}Ne is minuscule at 0.27 % thus making acquisition of thermally polarised signal impossible on a useful time-scale. To overcome the low signal intensities at thermal polarisation requires large number of signal averages. However, alternative methods can be used to artificially increase the spin polarisation beyond thermal equilibrium and will be discussed further in Chapter 3.

2.5 The NMR Signal

2.5.1 Radio Frequency Excitation

In the formative years of NMR the excitation field (B_1) was applied as a continuous wave so as to excite all transitions within the sample. In such experiments either the B_1 excitation field frequency or static B_0 field is swept across the expected chemical shift bandwidth. The sweep in such experiments is often very slow so to suitably excite all resonances within the sample.

Advancements in electronics however, led to the almost ubiquitous use of pulse field NMR [4]. By using short, high power pulses it is possible to excite all resonances within the sample in a single pulse.

The purpose of application of such a pulse to an ensemble of spins is to rotate the magnetisation vector from its equilibrium position (along B_0) to the transverse plane. The angle of rotation, θ is known as the flip angle and is defined by; 2.4,

$$\theta = \gamma B_1 P_1. \tag{2.10}$$

Where P_1 is length of the r.f. pulse, and B_1 is the strength of the r.f. pulse applied orthogonally to the static B_0 field depicted within Figure 2.4.

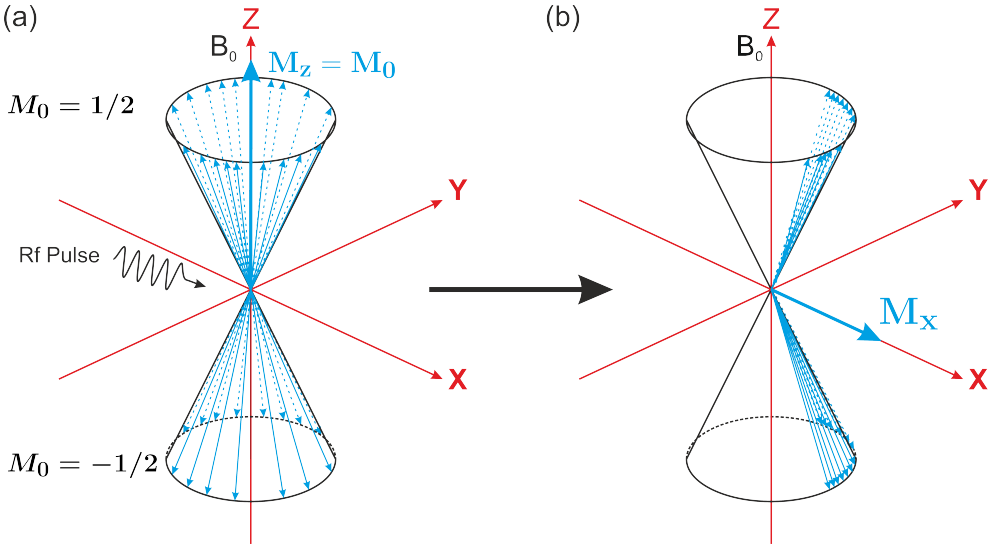


Figure 2.4: Excitation of a ensemble of Spin 1/2 nuclei (a) An ensemble of spins placed has an external magnetic field B_0 applied along the Z axis causing a net magnetisation along the same axis as B_0. (b) The time period immediately after application of a 90^o pulse; a phase coherence is induced, leading to a net magnetisation to form in the $x-y$ plane, in this case the magnetization if formed solely along the $x-axis$.

2.5.2 The Free Induction Decay

Forming the bedrock of the NMR experiment, the Free Induction Decay (FID) as shown in Figure 2.5. This is the experimentally observed result of the net magnetisation decaying, from the high energy state within the

transverse plane back to the thermal equilibrium along the axis of B_0. This decay is described in more detail in Section 2.6. The observation of this signal is possible due to the precession of the net magnetisation vector, inducing an electro motive force upon the r.f. coil which may be recorded by an attached spectrometer.

The detected signal contains complex information that represents both the real, and imaginary components of the FID. This allows for deconvolution of both the x and the y component of the magnetisation and further the *phase* of the spins.

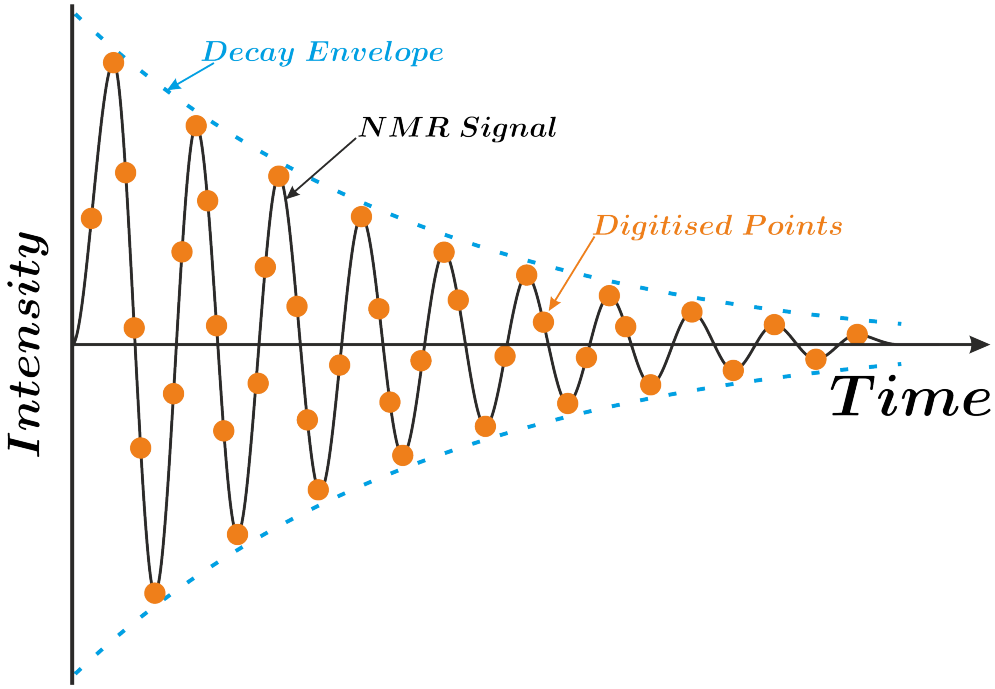


Figure 2.5: an idealised Free-Induction Decay (FID) NMR signal acquired after the application of a 90^o Rf pulse. The envelope is determined by the T_2^* decay.

2.5.3 Fourier Transform

To characterize the detected oscillating signal intensity detected after excitation, the Fourier Transform $\mathcal{F}$ is utilised to transform the detected time domain (f_x) signal into frequency domain (F_x) spectra (or image)

[9]. For a one dimensional transform Equation 2.11 may be used,

$$F(k) = \mathcal{F}\{f(x)\} = \int_{-\infty}^{\infty} f(x)e^{-ikx}dx, \tag{2.11}$$

as such, it follows that the inverse Fourier transform $\mathcal{F}^{-1}$ is given by,

$$f(x) = \mathcal{F}^{-1}\{F(k)\} = \frac{1}{2\pi}\int_{-\infty}^{\infty} F(k)e^{ikx}dk. \tag{2.12}$$

These equations may be applied to both time and spatially varying functions as shown in Figure 2.6.

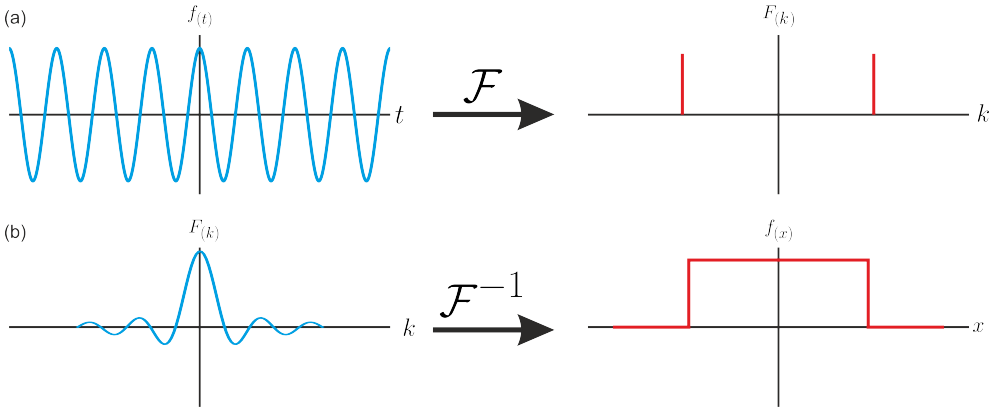


Figure 2.6: Examples of Fourier transform; (a) A cosine wave transform to a pair of Dirac delta functions at the given frequency of the signal, (b) A sinc function and its Fourier transformed rectangular pulse in the frequency domain

2.5.4 The Spin Echo

After excitation of the spin-ensemble to the transverse plane the spin-ensemble is fully coherent. Over time this coherence is lost due dephasing of the coherent spins, a relaxation process known as transverse or T_2 relaxation. It is possible however to recover a portion of this coherence lost to systematic T_2 effects. This is achieved by the application of a 180° pulse at time $\tau = TE/2$ as indicated in Figure 2.7.

This recovery is possible, as by time $TE/2$, the spin ensemble will have accrued a phase of Φ. Via application of the 180° pulse the ensemble phase will then be $-\Phi$. Allowing the phase to evolve over a second time increment of $TE/2$ means the ensemble phase will then be Zero. Crucially this process is only true of systematic contributions to T_2 such as local magnetic field inhomogeneity and r.f. pulse inhomogeneity and stochastic contributions to T_2 are not recovered.

The resulting signal is known in NMR parlance as an Echo, first studied by Hahn in [10, 11]. The time TE is known as the echo time. Further echoes provide the basis to MRI sequences and will be discussed in detail in Section 2.7.

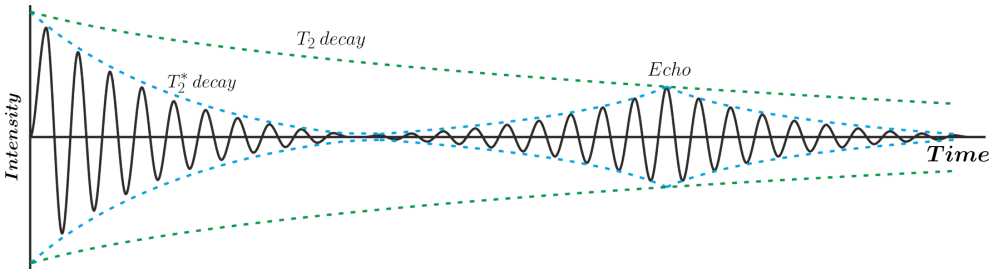


Figure 2.7: Formation of an Echo from the NMR signal at $t = TE$. Both the systematic T_2^* decay (blue dotted line) and the stochastic T_2 decay (green dotted line) are displayed

2.6 Relaxation Mechanisms

The excited state of the NMR signal does not last indefinitely; As alluded to above these mechanisms are driven by relaxation to thermal equilibrium. The two mechanisms which drive this relaxation are the Spin-Lattice (also known as the longitudinal) T_1 and Spin-Spin (also known as the transverse) T_2 relaxation as described by Bloch [12].

2.6.1 Spin-Lattice Relaxation: T_1

Spin-lattice or T_1 relaxation, refers to the process of the bulk magnetisation reorientating to thermal equilibrium. After rotation of the magnetisation vector from its thermal equilibrium, aligned with B_0, into the transverse plane the system is in a high energy state.

This relaxation or reorientation of the magnetisation vector arises from the interaction of the individual nuclear spin's microscopic magnetic field with that of the macroscopic magnetic fields of the spins in the lattice. This interaction leads to fluctuation within the magnitude and direction components of the magnetisation as the nuclei exchange energy. Finally resulting in the magnetisation reaching thermal equilibrium as described by Equation 2.13,

$$\frac{dM_z}{dt} = \frac{(M_z - M_0)}{T_1}, \tag{2.13}$$

where M_0 is the magnetization as described by the Equation 2.4, M_z is the magnetization in the z direction. When $M_z = M_0$ the rate of change is zero indicating that equilibrium has been reached. This recovery of the magnetisation is depicted 2.8.

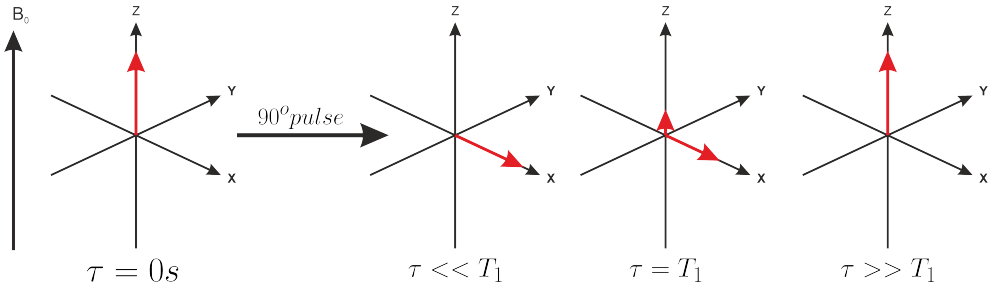


Figure 2.8: Time course of the longitudinal magnetisation: At thermal equilibrium the net magnetization aligned with the magnetic field B_0, a 90^o pulse is used to tip the magnetisation into the x-y plane, at τ << T_1 the magnetization is entirely in the x-y plane, as relaxation taxes effect the magnetization begins to return to thermal equilibrium at τ =T_1 approximately 63 % of the magnetization has returned to the direction; at τ >> T_1 the magnetization has totally returned to the thermal equilibrium

Measurement of this phenomenon is an extremely important aspect of NMR and is typically achieved either by a Saturation Recovery or Inversion Recovery sequence, which will be explored below.

Saturation Recovery

In a saturation recovery sequence, the net magnetization M is aligned with the magnetic field B_0 thus $M = M_z$. After the application of a 90° pulse the magnetisation is tipped into the $x - y$ plane meaning that $M = M_{xy}$. The subsequent recovery of the magnetization is probed by altering the evolution time τ and thus allows the measured signal to be fit to the following equation,

$$M_\tau = M_{\tau=0}\left(1 - \exp\left(-\frac{\tau}{\mathrm{T}_1}\right)\right), \tag{2.14}$$

where τ is the evolution, or inter-pulse delay time.

Inversion Recovery

An inversion recovery sequence the initial equilibrium net magnetisation vector is rotated by 180° by a r.f. pulse. A evolution time is then allowed τ and a second, 90° pulse is then applied. Again, by altering the evolution time τ the collected signal may be fit to,

$$M_\tau \;=\; M_{\tau=0}\left(1-2\exp\left(-\frac{\tau}{\mathrm{T}_1}\right)\right). \tag{2.15}$$

Where the factor of 2 difference between Equation 2.15 and Equation 2.14 arises because of the full inversion of the spin system to $M = -M$ at the start of pulse sequence. Figure 2.9 displays the recovery of the magnetisation during a saturation recovery and an inversion recovery experiment.

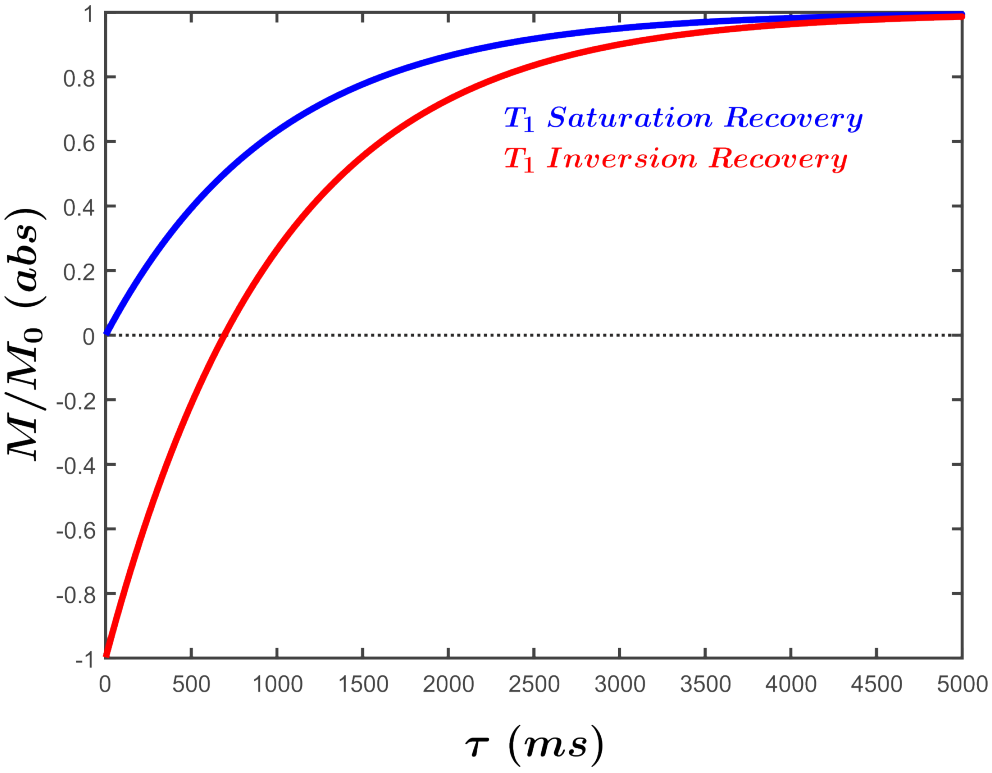


Figure 2.9: Evolution of longitudinal M_z component of magnetization in a Inversion recovery (red trace) and Saturation Recovery (blue trace) experiment.

2.6.2 Spin-Spin Relaxation: T_2

At thermal equilibrium, the magnetization is aligned with the externally applied magnetic field. When a 90^o excitation pulse is applied, a coherence is induced into the spin ensemble (Figure 2.10). The spins, now in the $x-y$ plane will continue to precess together around the direction of the magnetic field at the Larmor frequency. However molecular motion, interactions with neighbouring spins and lattice vibrations mean that the local magnetic field experienced by the spins is fluctuating. Due to the field dependence of the larmor frequency, any change in the local magnetic field leads to a local variance in Larmor frequency in the spin ensemble.

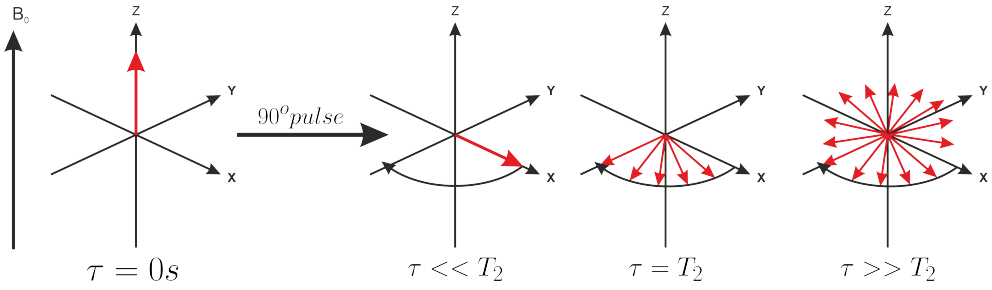


Figure 2.10: Time course of the Transverse magnetisation: At thermal equilibrium the net magnetization aligned with the magnetic field B_0, a imperfect 90^o pulse is used to tip the magnetisation into the x-y plane after which the spins will precess around the axis of the magnetic field, however due to the minute difference in individual Larmor frequencies the ensemble of spins will begin to lose coherence. At times much longer than T_2 the spins will have lost all coherence.

This effect, leads to a loss of coherence of the individual isochromats within the spin ensemble. This decay in coherence may be described by;

$$\frac{dM_{xy}}{dt} = -\frac{M_{xy}}{\mathrm{T}_2}, \tag{2.16}$$

which may be resolved for the individual components as;

$$M_x = -M_0 sin(\omega_o t) e^{-\frac{\tau}{T_2}}, \tag{2.17}$$

$$M_y = -M_0 cos(\omega_o t) e^{-\frac{\tau}{T_2}}. \tag{2.18}$$

Equation 2.16 can be further reduced as no magnetization exists in the transverse plane at equilibrium (M_{x-y} $(\tau = \infty) = 0$) the time course of the T_2 decay is given by;

$$M_{xy}(\tau) = M_{xy}(0) e^{(-\frac{\tau}{T_2})}. \tag{2.19}$$

This loss of coherence or, dephasing, (depicted in Figure 2.11) may be partially corrected for by the application of a 180° pulse, a short time after the initial 90°. The effect of this is that the total magnetisation vector within the transverse plane is inverted, allowing the local magnetic field perturbations to work in reverse and realign the individual magnetisation vectors. This rephrasing forms a Spin Echo [10].

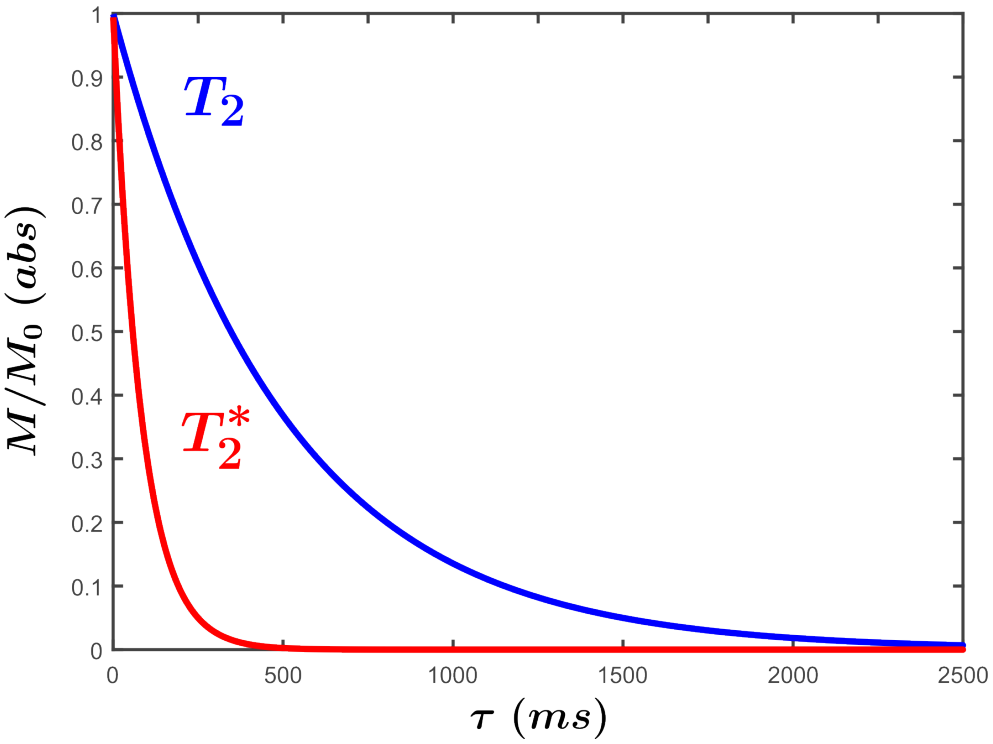


Figure 2.11: Evolution of Transverse M_{xy} component of magnetization. The Red trace indicates the $T_2^\star$ decay. The Blue trace indicates the *pure* T_2 decay which may be recovered from a CPMG exiperment [13, 14].

T_2^* Relaxation

The decay of the magnetisation coherence involves factors beyond the inter- and intra-nuclear effects [15]. Other parameters such as the spatial in-homogeneity of the static magnetic B_0 field and the applied, r.f. excitation pulse (B_1). Notably a further factor is that of local field in-homogeneity (δB_0) arising from differing magnetic susceptibility within the sample being examined. These factors play a significant role in the dephasing of the spin ensemble. As such it is useful to define the transverse relaxation as a combination of the nuclear and external effects, as denoted by T_2^*;

$$\frac{1}{T_2^*} = \frac{1}{T_2} + \frac{1}{T_{2'}}. \tag{2.20}$$

Where $T_2' = \gamma \cdot \delta B_0 \cdot T_2^*$ is always faster than T_2 (see Figure 2.11) and is the cause of the envelope of the FID as shown in Figure 2.7. A further method beyond a simple Spin-Echo (described above) may be used to rephase the magnetisation. First proposed by Carr and Purcell [11] and later expanded by Meiboom and Gill [13] The CPMG sequence is an alteration to the simple spin echo. The CPMG replaces the single 180° and echo by adding a train of 180° that are spaced at $\tau = TE$ to refocus the magnetisation.

When dealing with the CPMG experiment on liquids and gasses one must take care as diffusions of the spins will be continually occurring. If this diffusion is taking place across a magnetic field gradient the amplitude of the decaying echo train will be further given by [11, 13, 14],

$$S(t) = S_0 \cdot \exp\left[(-t/T_2) + \left(-1/3\, D\gamma^2\, G^2\tau^2 t\right)\right]. \qquad (2.21)$$

Where D is the diffusion coefficient, G is the magnetic field gradient, τ is the time between the 90° and the 180° pulses defined as $0.5 \cdot TE$. An important application of the CPMG experiments is the ability to probe the diffusion in porous media amoungst other enviroments [16, 17].

2.6.3 Spectral Density and correlation times

The quantum mechanical interpration of relaxation was provided by Bloembergen, Purcell and Pound in 1948 [6] and describes nuclear spin relaxation as induced by fluctuations in the local magnetic environment. These fluctuations are extremely subtle with even the change in field induced by local molecular tumbling being, significant enough to induce transition between energy levels and, thus relaxation [1, 6, 18].

Such induced local fluctuations for NMR experiments with liquids and gases may be considered rapid and random. As such we may consider that the average value for such relaxation to be zero; this is stated mathematically by $\langle B_x(t)\rangle = 0$. As we require a method of defining the magnitude of the fluctuating fields the average value does not suffice, instead the *mean square fluctuating field* is used and defined by $\langle B_x^2(t)\rangle \neq 0$.

To properly describe how rapidly the field fluctuates we must introduce an autocorrelation function, which is defined as,

$$G_\tau = \langle B_x(t) B_x(t+\tau)\rangle, \tag{2.22}$$

where, τ is a time interval. By definition at $\tau = 0$ the autocorrelation function is equal to the mean squared field, $G(\tau) = \langle B_x^2(t)\rangle$.

It follows that that the autocorrelation function will tend to be large for small value of τ, and small for large τ values. As convention, if we assume a simple exponential form for the autocorrelation function we may restate Equation 2.22 in the form of,

$$G(\tau) \;=\; \langle B_x^2\rangle \, e^{-\tau/\tau_c}, \tag{2.23}$$

Where τ_c is the correlation time of fluctuations. For an example of timescales, rotating molecules within a liquid experience a correlation time in the range of picoseconds to nanoseconds.

A further important factor within relaxation theory is that of the spectral density function J_w, which is defined as twice the Fourier transform of G_τ as stated by Equation 2.24,

$$J_w = 2\int_{-\infty}^{\infty} G(\tau)e^{-i\omega\tau}d\tau \;=\; 2\langle B_x^2\rangle \frac{\tau_c}{1+\omega^2+\tau_c^2}, \tag{2.24}$$

Further it is common to use the normalised spectral density function as stated by 2.25,

$$J(\omega) \;=\; \frac{\tau_c}{1+\omega^2\tau_c^2}. \tag{2.25}$$

Figure 2.12, displays the plot of J_ω as a function of $\log(\omega)$ for three correlation times. For τ_c values which are much less than $1/\omega_0$ a region of almost no decay is noted. This is due to Equation 2.25 reducing to $J(\omega) \approx \tau_c$ in the extreme narrowing condition. As $\log(\omega)$ increases the affomrentioned condition is violated at $\tau \;\approx\; 1/\omega_0$, where J_ω is fully dependent upon the full form of equation 2.25. It further displays a clear dependence of the magnetic field strength on the point at which the narrowing condition and as such indicates that nuclei with short correlation times may not have the same field dependence of J_ω even at high and ultra high fields.

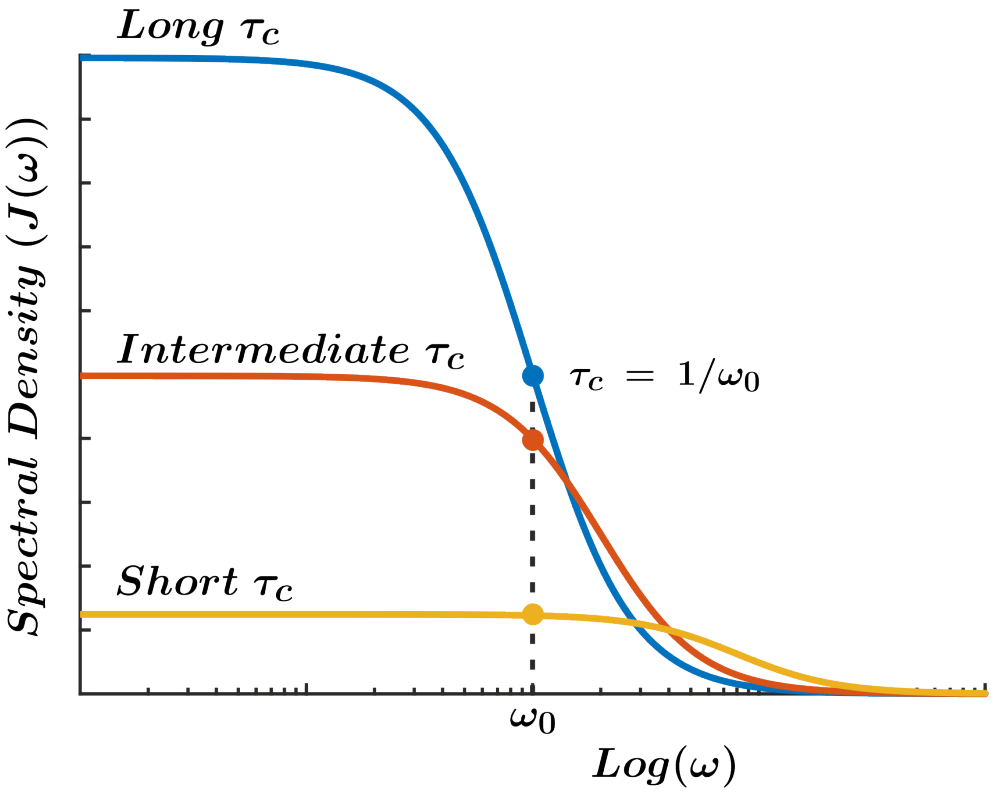


Figure 2.12: Spectral Density, $J(\omega)$ as a function of the log of frequency plotted from Equation 2.25. The three traces three different τ_c values as to demonstrate the effect of the correlation time upon the spectral density function. For each curve the frequency ω_0 has been indicated as reference. The indicated *Long* τ_c, where, τ_c is equal to the inverse of the Larmor frequency of the spin system. As such any change in the frequency ($log(\omega)$ leads to a change in the spectral density function. For *short* τ_c values the trace shows no significant change in $J(\omega)$ at the point ω_0. This is the extreme narrowing condition where $\tau_c << 1/\omega_0$ and indicates the field independent nature of the spectral density function.

Further, the nature of the relaxation itself plays a significant role on the functional dependence of $J(\omega)$. The three relaxation mechanisms are as follows and are stated in their relative importance to relaxation of a spin $I = 1/2$ system;

Dipole-Dipole > Chemical Shift Anisotropy (CSA) > Spin-Rotation

Whereas for spin systems of $I > 1/2$ the order of importances is in contrast;

Quadrupole >> Dipole-Dipole > CSA > Spin-Rotation

In most cases where $I > 1/2$ the electric quadrupole relaxation mecha-

nism dominates relaxation. In most experiments in a single mechanism dominates relaxation but there may be contributions from other mechanisms. When several mechanisms are present cross-correlation effects may be present, given the scope of this thesis these effects will not be covered, however this is covered extensively in the literature.

To elucidate the individual mechanisms they will be examined briefly here. However for a more comprehensive view the reader is directed to Levitt [1].

(1) Dipole-Dipole relaxation; typically the most influential mechanism for spin $I = 1/2$ nuclei is that of *through-space* dipole coupling between the spins. For a homonuclear sample, relaxation via dipole-dipole interaction of the magnetic moments is described by,

$$\frac{1}{\mathrm{T}_1^{DD_L}} = \frac{2}{5}\gamma^4\hbar^2 I(I+1)\sum_i r_i^{-6}\left(\frac{1}{1+\omega_0^2\tau_c^2} + \frac{1}{1+4\omega_0^2\tau_c^2}\tau\right). \quad (2.26)$$

(2) Chemical Shift Anisotropy (CSA); A further influence to the fast field perturbation is that of of CSA. Typically it provides large contribution to relaxation within molecular structures, via the orientation to the magnetic field. Further it is the CSA which gives rise to powder patterns within solid state NMR.

$$\frac{1}{\mathrm{T}_1^{CSA}} = \frac{2}{15}\gamma^2 B_0^2\left(\sigma_\parallel - \sigma_\perp\right)\frac{\tau_c}{1+\omega_0^2\tau_c^2}, \quad (2.27)$$

in which, $\left(\sigma_\parallel - \sigma_\perp\right)$ described the shielding anisotropy.

(3) Quadrupolar Interactions; In Spin $I > 1/2$ the charge distribution of the atom may no longer be considered to be spherical. It will instead

be either a oblate or prolate spheroid. As such there is a great dependence on variation in the Electric Field Gradients (EFG) coupled to the quadrupole moment of the spins;

$$\frac{1}{\mathrm{T}_1^{QR}} = \frac{3}{40}\frac{2I+3}{I^2(2I-1)}\left(1+\frac{\eta^2}{3}\right)\left(\frac{e^2Qq}{\hbar}\right)^2 \tau_c, \tag{2.28}$$

where, $eqQ/\hbar$ is the quadrupole coupling constant and e is the electron charge, q is the electric field gradient, Q electric quadrupole moment. η is the asymmetry parameter of the quadrupolar nucleus as defined by;

$$\eta = \frac{(q_{yy}-q_{xx})}{q_{zz}}, \tag{2.29}$$

where axes have been defined as $|q_{zz}| \geq |q_{xx}| \geq |q_{yy}|$ such that η is between zero and one.

In all presented modes of relaxation there is a large dependence upon the correlation time. To further elucidate this point Figure 2.13 indicates a plot of the behaviour of of T_1 as a function of τ_c for a range of field strengths.

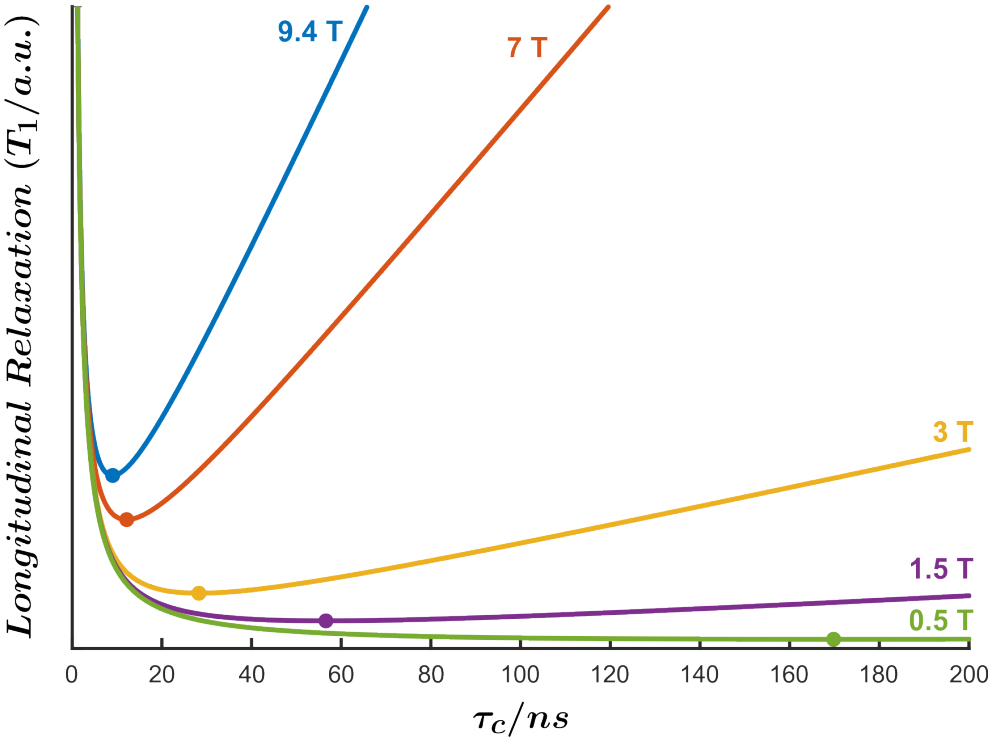


Figure 2.13: Longitudinal relaxation time (T_1) of ^{129}Xe as a function of correlation time at a range of field strengths. The curves are calculated independent of any specific relaxation mechanism, as such the T_1 values are arbitrary units. The relaxation was assumed to occur within a homogeneous magnetic field. Each curve decays to the minimum value, $\tau_c = 1/\omega_0$ (displayed upon each curve as a point) where it begins to increase.

2.7 Magnetic Resonance Imaging

Magnetic Resonance Imaging (MRI) is an extremely powerful tool which may be used to non-invasively probe the internal structure of a sample, via observing spin-active nuclei. MRI was pioneered by Sir Peter Mansfield and Paul Lauterbur whom recived the Nobel Prize in Medicine for their work in 2003 [19]. Only a general outline of the processes of MRI will be presented here in this work, for a full treatment the reader is directed to the authoritative work by Callaghan [2].

While in NMR spectroscopy, typically one is aiming to create a highly homogeneous field across the sample, so as to obtain narrow spectral

linewidths, in such a case the Larmor frequency as described above in the Larmor frequency is $\omega_0 = \gamma B_0$. However, in order to acquire data within the second dimension to form an imaging the magnetic field homogeneity may be intentionally disrupted with a magnetic field gradient. A gradient G_x, G_y, G_z may be applied so as to make the Larmor frequency a function of the position within the aforementioned field gradient as given by;

$$\omega_{(\mathbf{r})} + = \gamma \left(B_0 + \mathbf{G} \cdot \mathbf{r} \right), \tag{2.30}$$

where r is the a vector describing the spatial position of the nuclear spins. Figure 2.14 displays a schematic figure indicating how the application of a field gradient may encode a spatial location to a discreet frequency.

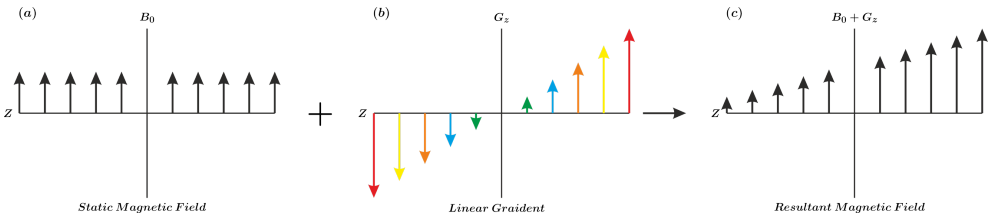


Figure 2.14: Magnetic field representation z-axis. The linear gradient field is added to the static B_0 field generating a resultant magnetic field which is spatially dependent along the gradient axis. In turn this provides a frequency offset to the ensemble of spins contained within the field

2.7.1 Slice Selection

In MRI it is often favourable to only excite a small region or *slice* of the sample. Such techniques may be used to collect multiple slices across the sample, as to produce a image stack.

Typically the *slice* direction is considered to be along the z-direction. This is achieved by applying a linear field gradient in the G_z direction, such that the magnetic field of the sample may be displayed as shown

in Figure 2.14. The Larmor frequency of the spins within the sample will thus be dependent upon it's location within the sample. With this a sample volume may be defined by careful selection of gradient field strength and the bandwidth of a given r.f. pulse. The Field Of View (FOV) within the z (or *slice*) direction is given by [16]:

$$FOV_{slice} = \frac{BW}{\gamma \cdot G_z}. \tag{2.31}$$

Where BW is the bandwidth of the applied r.f. pulse and γ is the gyromagnetic ratio.

2.7.2 Frequency Encoding

Beyond the selection of the slice position in the z direction, it is further necessary to encode the spin position x and y planes to produce an image. For convenience the x or *frequency encoding* direction will be discussed first. As the name implies the encoding is performed in a similar fashion to that of slice selection. The key difference however is that the spin system is allowed to evolve in the presence of a gradient in order to allow an enforced dephasing of the magnetisation in the x direction. The FOV in the frequency direction is described by Equation 2.32.

$$FOV_{frequency} = \frac{1}{\gamma G_z DW}, \tag{2.32}$$

where DW is the dwell time or sampling interval of the FID in seconds.

2.7.3 Phase Encoding

To achieve spatial encoding within the y direction a tertiary set of gradients must be applied. In the case of phase encoding a G_y gradient is applied to the sample prior to frequency encoding. Similar to frequency encoding, Phase encoding utilises a short lived pulse of field gradient G_y which enforces a distribution of the phase of the spins across the gradient. As such the FOV in the y direction may be described by Equation 2.33,

$$FOV_{phase} = \frac{1}{\gamma \Delta G_y \delta}, \tag{2.33}$$

where δ is the duration of the phase encoding gradient and ΔG_y is the strength of the phase encoding gradient step.

2.7.4 Gradient Echo Imaging

Many imaging sequences rely on the formation of an echo. Figure 2.15 displays an example of a typical Gradient echo sequence.

In a Gradient echo imaging sequence, the spins are first tipped into the $x - y$ plane via use of a 90°, slice selective r.f. pulse. The resulting FID is then dephased via the application of a field gradient, and subsequently rephased using a gradient of an equal and opposite magnitude. Thus the weighting of such images is inherently weighted by T_2^* and made sensitive to effects such as magnetic susceptibility.

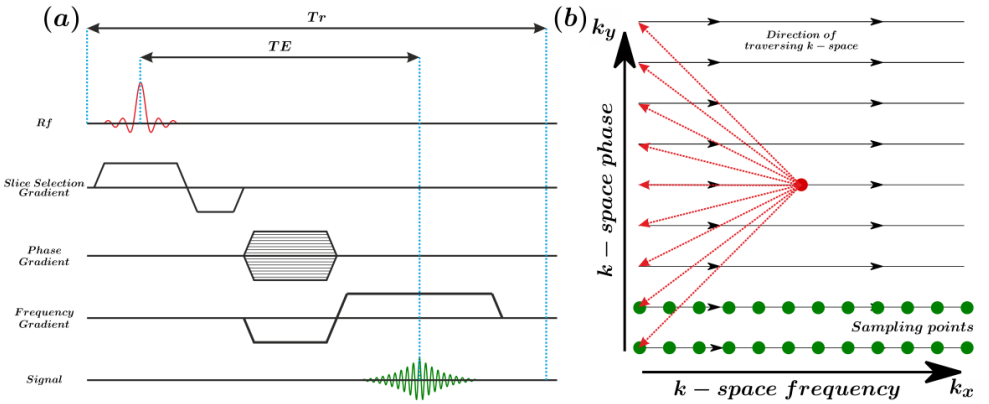


Figure 2.15: (a) Timing diagram of a Slice Selective Gradient Echo Imaging Sequence; a sinc RF pulse is applied in conjunction with a slice section gradient. The FID produced after the 90° sinc pulse is rapidly dephased by use of the frequency gradient, the echo is then formed by use of the alternate gradient pulse of twice the length of the dephasing gradient producing the *direct dimension of the image*. The indirect dimension is collected by linearly stepping the phase gradient N times. The echo time TE is the time between the initial pulse and the echo forming. Tr is the repetition time between each of the the phase-encoded loop. (b) The k-space trajectory of the sequence. The signal is acquired left-to-right along the black lines in the K_x dimension as indicated by the green dots. The shift in the phase or *indirect* dimension K_y is depicted by the red arrows.

2.7.5 Spin Echo Imaging

For spin echo imaging, the echo is created via application of an r.f. pulse. Figure 2.16 displays a timing diagram of a typical spin echo sequence. Much like Gradient Echo the magnetisation is tipped to the $x-y$ transverse plane via a 90° r.f. pulse, a secondary r.f. pulse is then applied at $t = TE/2$ that rotates the magnetisation through 180° as such to rephase the spins and form an echo in much the same fashion as the Hahn Echo as discussed in Section 2.5.4. As such the typical benefit of such a sequence is the rephasing of the T_2^* effects allowing for images to be T_2 weighted.

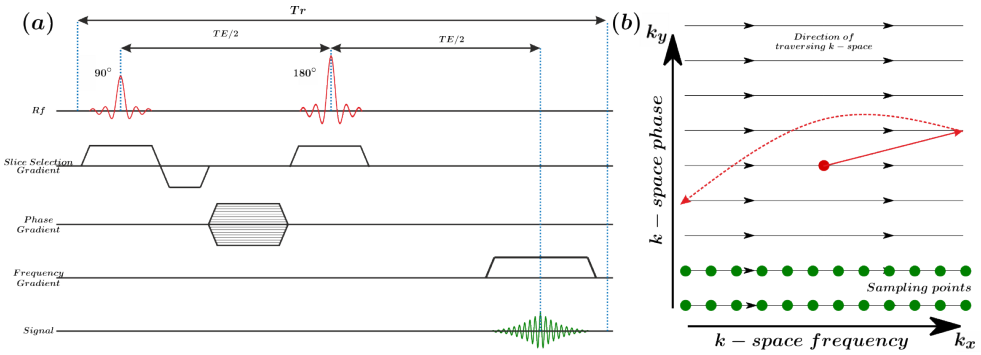


Figure 2.16: (a) Timing diagram of a Slice Selective Spin Echo Imaging Sequence; a sinc RF pulse is applied in conjunction with a slice section gradient. The FID produced after the 90° sinc pulse is rapidly dephased by use of the frequency gradient, the echo is then formed by use of the alternate gradient pulse of twice the length of the dephasing gradient producing the *direct dimension of the image*. The indirect dimension is collected by linearly stepping the phase gradient N times. The echo time TE is the time between the initial pulse and the echo forming. Tr is the repetition time between each of the the phase-encoded loop. (b) The k-space trajectory of the sequence. The signal is acquired left-to-right along the black lines in the K_x dimension as indicated by the green dots. The shift in the phase or *indirect* dimension K_y via the phase gradient is indicated by the solid red line. The effect of the 180° pulse is indicated via the dashed red line.

2.8 Summary

Within this chapter the concepts of Nuclear Magnetic Resonance were introduced. Factors essential for understanding the spin polarisation were discussed. The steps behind the excitation and detection of the NMR signal pertinent for understanding experimental work presented later in this work are introduced. The theory of relaxation of a spin ensemble was examined in terms of thermally polarised systems.

The basis for Magnetic Resonance Imaging was presented. The use of gradients for spatial localisation was discussed. Finally, gradient echo imaging and spin echo imaging sequences and their relevant k-space trajectory's were presented.

Bibliography

[1] M. H. Levitt, *Spin Dynamics*. John Wiley & Sons, 2nd ed., 2001.

[2] P. T. Callaghan, *Principles of Nuclear Magnetic Resonance Microscopy*. Oxford science publications, Clarendon Press, 1993.

[3] P. T. Callaghan, *Translational Dynamics and Magnetic Resonance: Principles of Pulsed Gradient Spin Echo NMR*. OUP Oxford, 2011.

[4] A. Abragam, *The Principles of Nuclear Magnetism*. International series of monographs on physics, Clarendon Press, 1961.

[5] R. W. Brown, E. M. Haacke, Y. C. N. Cheng, M. R. Thompson, and R. Venkatesan, *Magnetic Resonance Imaging: Physical Principles and Sequence Design*. Wiley, 2014.

[6] N. Bloembergen, E. M. Purcell, and R. V. Pound, "Relaxation effects in nuclear magnetic resonance absorption," *Physical Review*, vol. 73, no. 7, pp. 679–712, 1948.

[7] W. Gerlach and O. Stern, "Der experimentelle Nachweis der Richtungsquantelung im Magnetfeld," *Zeitschrift fur Physik*, vol. 9, pp. 349–352, dec 1922.

[8] R. K. Harris, E. D. Becker, S. M. Cabral de Menezes, R. Goodfellow, and P. Granger, "NMR nomenclature: nuclear spin properties and conventions for chemical shifts.," *Magnetic Resonance in Chemistry*, vol. 40, no. 7, pp. 489–505, 2002.

[9] D. Shaw, *Fourier transform N.M.R. spectroscopy*. Elsevier, 1984.

[10] E. L. Hahn and D. E. Maxwell, "Spin Echo Measurements of Nuclear Spin Coupling in Molecules," *Physical Review*, vol. 88, pp. 1070–1084, dec 1952.

[11] H. Y. Carr and E. M. Purcell, "Effects of diffusion on free precession in nuclear magnetic resonance experiments," *Physical Review*, vol. 94, no. 3, pp. 630–638, 1954.

[12] F. Bloch, "Nuclear induction," *Physical Review*, vol. 70, no. 7-8, pp. 460–474, 1946.

[13] S. Meiboom and D. Gill, "Modified spin-echo method for measuring nuclear relaxation times," *Review of Scientific Instruments*, vol. 29, no. 8, pp. 688–691, 1958.

[14] E. Fukushima and S. B. W. Roeder, *Experimental pulse NMR: a nuts and bolts approach*. The Advanced Book Program, Addison-Wesley Pub. Co., Advanced Book Program, 1981.

[15] G. B. Chavhan, P. S. Babyn, B. Thomas, M. M. Shroff, and E. M. Haacke, "Principles, Techniques, and Applications of T2*-based MR Imaging and Its Special Applications," *RadioGraphics*, vol. 29, no. 5, pp. 1433–1449, 2009.

[16] B. Blümich, "NMR Imaging of Materials," *Measurement Science and Technology*, vol. 14, no. 9, p. 1739, 2003.

[17] S. Stapf and S. I. Han, *NMR Imaging in Chemical Engineering*. Wiley, 2006.

[18] A. G. Redfield, "On the Theory of Relaxation Processes," *IBM Journal of Research and Development*, vol. 1, pp. 19–31, jan 1957.

[19] Nobelprize.org, "The Nobel Prize in Physiology or Medicine 2003," 2003.

Chapter 3

Hyperpolarisation of Noble Gasses

3.1 Introduction

The purpose of this chapter is to introduce the reader to the main methodologies required to produce an Nuclear Magnetic Resonance (NMR) signal enhancement via hyperpolarisation (hp). As the majority of this work utilises Spin Exchange Optical Pumping (SEOP) this chapter will hold the same focus. To provide the reader with an overview of the area other major hyperpolarisation techniques will also be discussed with their, relative applications and merits. Knowledge of these concepts will prove crucial for understanding the experimental design and constraints in future, chapters.

To begin it is helpful to return to the concepts of thermal or, Boltzmann polarisation as stated by,

$$P = \tanh\left(\frac{\gamma\hbar B_0}{2k_B T}\right). \tag{3.1}$$

Where γ is the gyromagnetic ratio, k_B is the Boltzmann constant and

T the temperature. The temperature dependence described in Equation 3.1 details the population distribution and crucially indicates that only a small difference in energy level populations is present at thermal equilibrium. This provides the motivation for the need to seek out polarisation enhancement methods. For example considering a liquid state sample of water at room temperature ($\sim 293\ K$), within a high magnetic field ($3.34\ T$) the ^1H spin polarisation is $1.18 \cdot 10^{-15}$. The practical effect of this concept means that only ~ 12 nuclear spins in a million actually contributes to the detected NMR signal.

The effect of hyperpolarisation in its most basic form is to induce a significant population difference between the energy energy levels to increase the attainable signal. Such techniques are particularly useful when considering lower γ nuclei such as ^{129}Xe the effects are much more pronounced, notably so being as majority of the studies performed within this work are focused upon NMR and MRI of gasses. A significant challenge due to the low density and the low gyromagnetic ratio. An example of the spin polarisation and signal intensity of gas phase, thermally polarised ^{129}Xe is shown in Figure 3.1 (a). With Figure 3.1 (b) indicating the possible enhancement possible with SEOP.

Hyperpolarisation techniques are not limited to simply noble gasses, but are used for a wide range of applications [1, 2]. The following sections aims to provide the reader with a general overview of a range of hp techniques and their application to noble gasses.

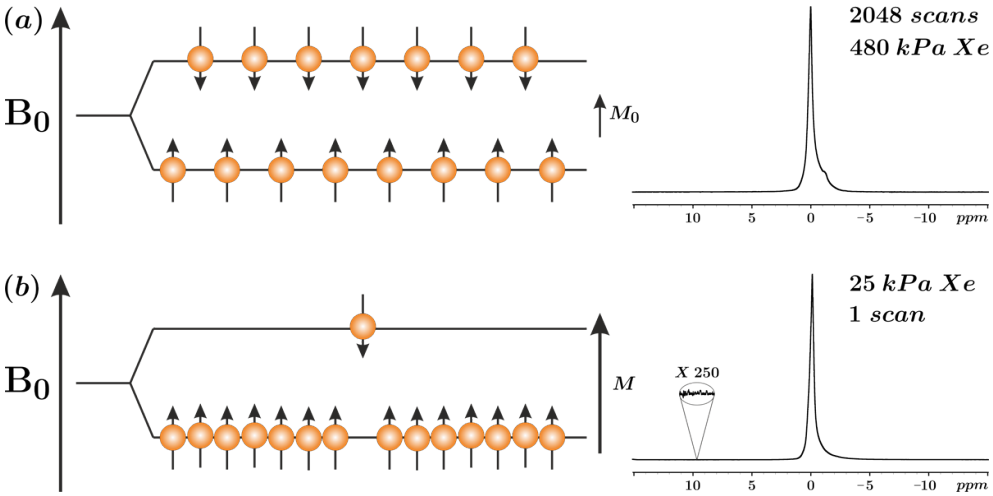


Figure 3.1: Thermally polarised spectra as compared to hyperpolarised ^{129}Xe ; (a) a diagram representing the energy level distribution at thermal equilibrium ($\sim$ 295 K) with ^{129}Xe signal displayed from a high density (480 kPa) sample acquired from 2048 averaged scans at 9.4 T. (b) diagram representing the extreme population difference between the energy levels in a system which has been subjected to Spin Exchange Optical Pumping. The associated spectra indicates a single scan of hyperpolarised ^{129}Xe taken at ($\sim$ 295 at low pressures $\sim$ 25 kPa). Note that the resonance frequency is dependent upon the gas pressure, in both (a) and (b) the radio frequency pulse was set to the resonance frequency in each case.

3.2 Hyperpolarisation methods

3.2.1 Dynamic Nuclear Polarisation

Dynamic Nuclear polarisation (DNP) is a method for enhancing the population difference in the nuclear spin state of a target nuclei via transfer of polarisation from the electrons to the proton, or other lower gyromagnetic ratio nuclei such as ^{129}Xe or ^{13}C. This technique is possible due to the extremely high gyromagnetic ratio of the electron which is, 658 times larger than that of proton. The maximum attainable polarisation transfer between an electron and a nuclear spin is given by the ratio of gyromagnetic ratios as given by Equation 3.2;

$$\varepsilon = \frac{\gamma_e}{\gamma_n}. \tag{3.2}$$

For lower γ nuclei such as ^{13}C (with its gyromagnetic ratio being just over a quarter of that of proton) additional enhancement is possible and produces $\varepsilon \approx 2640$. The polarisation and possible maximum enhancement at 3.35 T in the solid state are displayed in Figure 3.2.

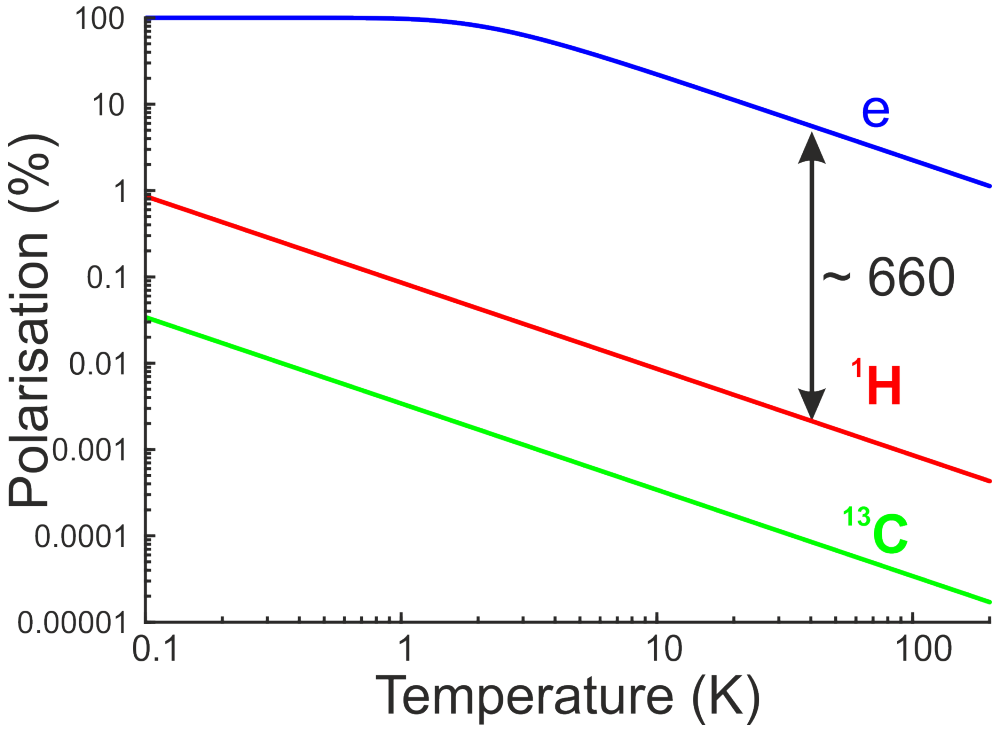


Figure 3.2: A log, log plot of polarisation of NMR species as a function of temperature at a magnetic field strength of 3.35 T. The potential enhancement factor between the electron spin polarisation and the proton is displayed.

Figure 3.2 indicates that at extremely low temperatures and high magnetic fields the electron spin possesses unity polarisation. Therefore having the effect of allowing greater polarisation to transfer.

There are, however, significant challenges with using such techniques to produce a hp spin state, most notably that when performing polarisation transfer the sample is a solid. As discussed briefly within the previous chapter, NMR within the solid state produces very broad lines in NMR

spectra due to a lack of motional averaging. As such it is necessary to return from solid state back to liquid state as to faciliate the acquistion of high resoulation, liquid state NMR spectra. A key requirement of this however, is that the temperature jump must be rapid in comparison to the T_1 relaxation of the sample. To achieve this A number of methods have been proposed [3, 4], however for this introduction only that which has been directly applied to ^{129}Xe will be discussed.

Dissolution DNP

A commonly used method for converting the solid state sample to the liquid is that of dissolution DNP [3].

To achieve the temperature jump a hot solvent is pushed into contact with the solid state sample, turning it to a liquid. A key benefit of this method is that the dissolution itself is extremely rapid. Typically the experimental set-up for such a system will utilise an external, polarising magnet in which the DNP is performed before being dissolved and *pushed* into a higher field system for spectroscopy or imaging by the hot solvent typically taking on the order of $\sim\ 10 - 15$ seconds. Other systems however, such as that designed by Köckenberger and co-workers [5] uses a novel dual iso-center magnet system which can perform the dissolution and sample shuttling within $\sim$ 300 ms, thus allowing samples with very short T_1 to be probed.

However a significant drawback to using a dissolution system is that each given experiment is a single shot process. This is due to dissolution of the sample in effect destroying it by placing it within solution.

Despite the non recoverable nature of the sample, dissolution-DNP is the method which is currently receiving the majority of interest in terms of

commercialisation with the SPINlab (General Electric healthcare, Illinois, USA) using this method as the resulting solution may be injected to patients to study metabolism of tumours [6, 7].

^{129}Xe has been hyperpolarised via d-DNP, initially shown by Ardenkjaer-Larsen et al in 2003 [8] and more recently by Comment et al [9]. This approach requires the ^{129}Xe to be mixed in a glassing agent and doped with molecules with unpaired election spins (e.g. the radical). The glassing agent causes the sample to form an amorphous solid at cryogenic temperatures. However typical ^{129}Xe spin polarisations achieved via these techniques is fairly low, on the order of $10 - 30$ % in comparison to Spin Exchange Optical Pumping which may achieve near unity polarisation [10–12] on much shorter time scales. This is due to a number of issues relating to the spin-diffusion *bottleneck* between the electron and the ^{129}Xe spins. However a benefit to the use of such a method is an increasing number of the aforementioned commercial DNP polarisers within clinical settings [8, 13].

While it is possible to perfom hyperpolarisation of higher spin order nuclei via techniques such as DNP and Brute Force (which will be discussed in the following section) significant drawbacks exist. Quadrupole ($I > 1/2$) nuclei such as ^{21}Ne, ^{83}Kr and ^{131}Xe as discussed in Chapter 7 will have a rapid T_1 in the solid phase, which will be significantly increased during any phase transitions [14, 15] thus meaning in most cases the dissolution process will be significantly slower than the T_1.

3.2.2 Brute-Force Polarisation

Brute Force polarisation [16–19] is a concept similar to dissolution DNP, in which the sample in question is placed in a high magnetic field, and

cooled to very low temperatures.

A brief overview of an experimental protocol to produce a highly polarised spin state via Brute force polarisation is presented here: The sample is initially placed within a very high magnetic field ($\sim$ 14 T) and cooled below 50 mK. At this temperature there is a high spin polarisation simply due to the Boltzmann distribution of the energy level populations. After a given polarisation time at this low temperature the sample is returned to liquid state via a method similar to that of D-DNP. The dissolution must be many times faster than the T_1 relaxation time of the sample. This method is currently capable of of achieving polarisation enhancements (within the liquid state) of $\sim$ 1500. Further a particular benefit of this technique is that it allows multiple samples to be polarised at once and, unlike DNP, it requires no radical. However the sample being polarised may include include a relaxation agent (often a paramagnetic compound such as gadolinium) as to reduce the total polarisation time.

Brute Force polarisation has been utilised to produce both ^{129}Xe and ^{3}He with a spin polarisation of 41 % and 37 % respectivly [20]. Notably this process lends itself to high volume production of gasses for clinical purposes as large amounts of gasses may polarised at a time (it is claimed that from $\sim 100 - 1000$ litres is possible).

Disadvantages of such a system do exist, most notably that the high magnetic field and low temperatures lead to extremely long T_1. This leads to the polarisation build up time on the order of days meaning it is more time efficient to perform cross polarisation from proton to the target nuclei within the solid state. This is due to the proton T_1 being often much quicker than other low γ species [18, 20]. Again it must be stated

that this process is not applicable to quadrupole nuclei used in this work due to the extremely rapid T_1 time during the phase transitions.

3.2.3 Metastable Exchange Optical Pumping

Metastable Exchange Optical Pumping (MEOP) is a method of polarisation of ^{3}He first observed in 1963 by Colegrove et al [21]. ^{3}He atoms in the ground state are polarized by collisions with optically pumped ^{3}He atoms in the metastable state [22]. The process is performed at room temperature and at very low pressures of < 200 mbar [23] and as such must be compressed after production. Production volumes for such systems are typically on the order of $100 - 1000$ ml of gas.

MEOP process requires a weak, homogeneous magnetic field in which circularly polarised laser light is applied to a low pressure sample of pure ^{3}He. This laser light is tuned to optical transition ($\lambda = 1083$ nm) between the ^{3}He 2^3S_1 state, to the metastable 2^3P state. After excitation, a spontaneous remission to both sub-levels of the 2^3S_1 state occurs. This results in an equal re-population of both sub-levels, however, due to the continued excitation of the one of 2^3S_0 sub-level results in a higher net population of the 2^3S_1 state. This resultant population in equivalent to the net polarization of the total angular momentum of the metastable atoms.

The nuclear polarization of the metastable state is transferred to the ground state ^{3}He via metastability exchange collisions. During which polarised metastable and ground state atoms exchange electronic states with the nuclear polarisation remaining unaffected. As a result there is an atom in the ground state with the polarized nucleus, and a new metastable atom that can be further optically pumped by the laser.

A continuous application of r.f and laser irradiation leads to the formation of equilibrium polarization, the magnitude of which depends on several parameters such as metastable atom density, polarization build-up time, and the relaxation rate of polarized atoms. The latter depends on laser power, pumping transition, gas pressure and intensity of discharge.

Being as this process requires a very low ^{3}He density, for it to be delivered to a sample it subsequently has to be compressed via a pump to a sufficient density for use. MEOP is highly effective for ^{3}He production on the clinical scale with high polarisation being achieved (> 60 %). However it is significantly less effective for heavier noble gas isotopes due to stronger relaxation mechanisms present [24–27]. In recent years however, MEOP and ^{3}He have been receiving less interest. This is in part due ^{3}He only occurring naturally in trace quantities: only 0.000138 % of total natural helium. Further, the primary source of ^{3}He manufacture is through Tritium decay in nuclear fusion thus limiting the supply. Furthermore, ^{3}He has additional uses beyond hyperpolarised gas NMR and MRI, as such ^{3}He is exceedingly expensive and difficult source [28].

3.2.4 Spin Exchange Optical Pumping

Spin exchange Optical Pumping (SEOP), is the most commonly employed method for generating hp noble gases. The basis of this technique is credited to Kastler [29, 30], who demonstrated that electron spin order may be created in alkali metal vapours using circularly polarised laser light.

Varnum and co-workers [26], demonstrated the ability to perform polarisation transfer via spin exchange collisions, to ^{3}He as to produce a highly polarised spin state. This was later extended to ^{129}Xe by Grover in [31].

More recently, both the understanding of the physical SEOP processes and the advancement in laser technology have allowed for the production of large quantity's of highly polarised ^{129}Xe and ^{3}He. Beyond spin $I = 1/2$ additional interest is that of the quadrupole species ^{21}Ne, ^{83}Kr and ^{131}Xe which despite, often rapid relaxation, may be used as probes of surface chemistry [32, 33].

The underlying phenomenon and processes of SEOP will be briefly discussed. For a full treatment the reader is directed to the reviews by Barskiy, Walker, Appelt and Happer [34–38]. SEOP is a multi stage process in which a high electronic spin polarisation is induced within an alkali metal vapour via irradiation by circularly polarised light in a similar fashion to MEOP. Gas phase collisions transfer polarization from the alkali electrons to the spins of the noble gas nuclei via Fermi-contact interactions.

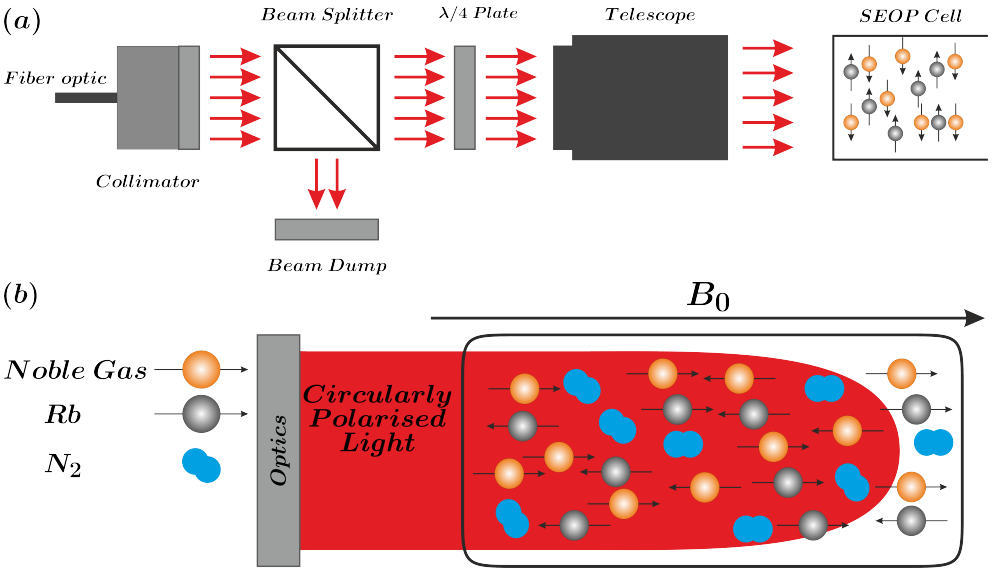


Figure 3.3: Diagram of a Spin Exchange Optical Pumping cell and optics arrangement. (a) schematics of the optical components used for the process of SEOP. The Laser light is collimated and passed through a beam splitter so as to linearly polarise the light. The light is then circularly polarised (σ^+) by the quarter wave plate. The beam is expanded with a telescope to create a parallel beam the size of the target SEOP cell. After the SEOP cell the Laser light is absorbed by a beam splitter. (b) Diagram of the SEOP cell. The aforementioned laser light irradiates the SEOP cell and specifically the Rb atoms. The polarised light creates a non-equilibrium polarisation in the alkali metal valence electron and orients the spin in the direction of the externally applied magnetic field ($B_0 \sim 15$ mT) subsequent interactions with noble gas atoms transfer polarisation. The diatomic N_2 is present to non-radiatively quench the excited state of the Rb as to prevent radiation trapping. Experimental practicality dictates that there will be areas of low or non irradiated regions in poorly aligned cells resulting in regions of 'dark rubidium' in which the alkali metal vapour is unpolarised. Interactions between the hyperpolarisation noble gas atoms and the 'dark rubidium' can produce substantial depolarisation of the noble gas in these areas. Gas from these areas is referred to 'Dark gas'.

3.3 SEOP Mechanisms

3.3.1 Polarisation of the Alkali Metal vapour

The process of creation of the a high nuclear spin polarisation of a noble gas, first requires the creation of a high electron polarisation in the alkali metal vapour.

The SEOP process takes place within a glass cell containing the alkali

metal with a gas mixture containing both the noble gas to be polarised, and a *buffer* or *quenching* gas (typically molecular nitrogen). The glass cell is heated between 373-473 K (dependent on noble gas being polarised) as to create a vapour of alkali metal atoms (with the vapour pressure dependent upon noble gas in question). The heated cell is is contained within a magnetic field of $\sim\ 50 - 100$ G. This arrangement (as shown in Figure 3.3) is further aligned to the path of a Laser tuned to the D_1 transition of the alkali metal valence electron. The Hamiltonian for an akali metal atom in the ground state given by Walker et al [35] is,

$$\hat{H}_a = A_a \hat{\mathbf{I}}_a \cdot \hat{\mathbf{S}} \ + \ g_s \mu_b \hat{S}_z B_0 \ - \frac{\mu_a}{I_a} \hat{I}_{az} B_0, \tag{3.3}$$

where the term $A_a \hat{\mathbf{I}}_a \cdot \hat{\mathbf{S}}$ describes the hyperfine interactions, A_a is the magnetic dipole coupling coefficient, I_a is the alkali metal nuclear spin operator, and S is the valence electron spin operator. The second term $g_s \mu_b S_z B_0 \ - \frac{\mu_a}{I_a} I_{az} B_0$ describes the Zeeman interaction of the electronic and nuclear spins with the externally applied magnetic field B_0.

Application of circularly polarised light (σ^+ or σ^-) with a wavelength tuned to the D_1 transition of the alkali metal ($\lambda = 794.7\ nm$) may allow for selective *pumping* of the electron. This is due to the conservation of angular momentum, via a selection rule of $\Delta z = 1$ (for right hand or σ^+) or $\Delta z = -1$ (for left hand or σ^-). Therefore as shown in Figure 3.4, the valence electron of the alkali metal may be selectively pumped from the $^2S_{1/2}$ ground state to the $^2P_{1/2}$ excited state.

At typical pressures within the SEOP cell, gas phase collisions will allow for rapid mixing of the $^2P_{1/2}$ sublevel populations, leading to equalisation of the spin polarisation produced by the adsorption of the laser light.

Subsequently the excited states will relax back to the ground state, via either a radiative or radiately quenched process and leads to a equal re-population of the ground states; however electrons relaxing back into the $m_i = -1/2$ sublevel will be re-excited into the $^2P_{1/2}$ state via the continual application of the laser light. This process leads to a depletion of spins within the pumped sublevel and a build-up of spin population in the non-pumped state. In ideal experimental conditions it is possible to achieve *near-unity* polarisation of the alkali metal [39].

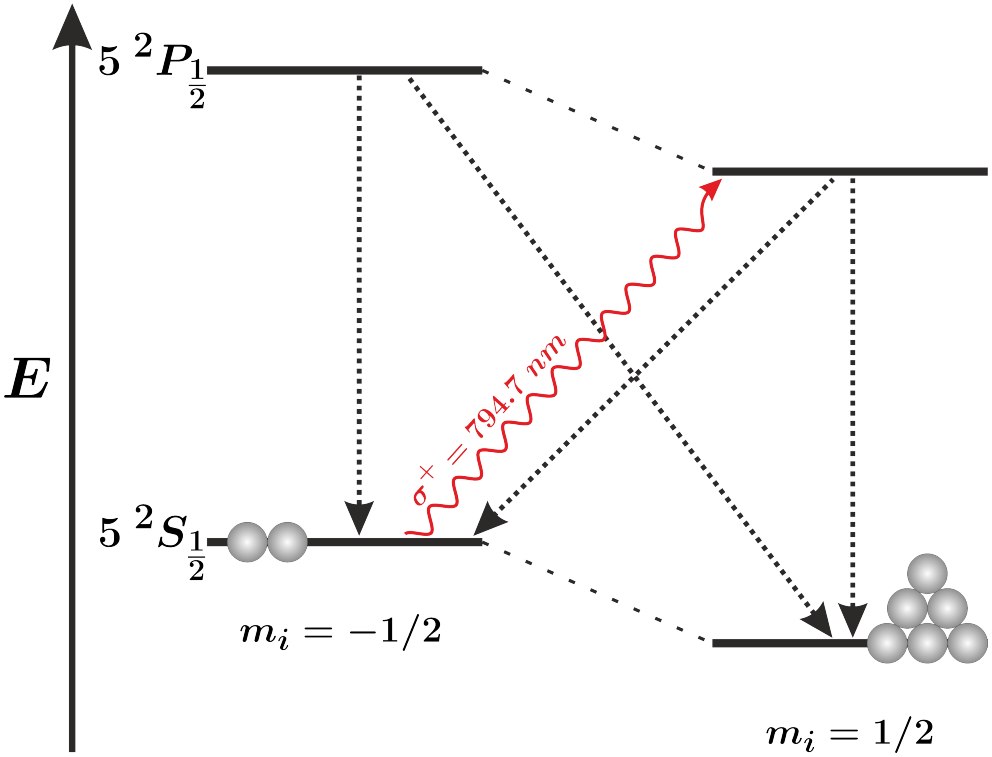


Figure 3.4: Schematic of the optical pumping of the valence electron of rubidium metal vapour. In the case of this diagram hyperfine splitting has been excluded for simplicity. Circular polarised laser light (σ^+) is used to excite the alkali metal valence electron from the sublevel of the $^2S_{1/2}$ ground state ($m_i = -1/2$) to the spin up $^2P_{1/2}$ excited state ($m_i = +1/2$) via the D_1 transition. Following, collisional mixing rapidly equalises the population of the $^2P_{1/2}$ sublevels, and subsequently *radiative* or *non-radiative* transitions repopulate both ground states with equal probability. Radiative transitions may be quenched with the addition of molecular nitrogen to the SEOP fuel mix. Due to the continual pumping on the D_1 transition depleting the $^2S_{-1/2}$ ground state ($m_i = -1/2$) and populating the ($m_i = 1/2$) sublevel a high non-equilibrium population may be reached in the alkali metal.

3.3.2 Alkali Metal-Noble Gas interactions

High electron polarisation of the alkali metal vapour is reached via optical pumping. The second stage is the polarisation transfer, from the valence electron of the alkali metal vapour to the nucleus of noble gas. This spin exchange is achieved via two primary methods, either binary collisions or van der waals complexes, as depicted in Figure 3.5.

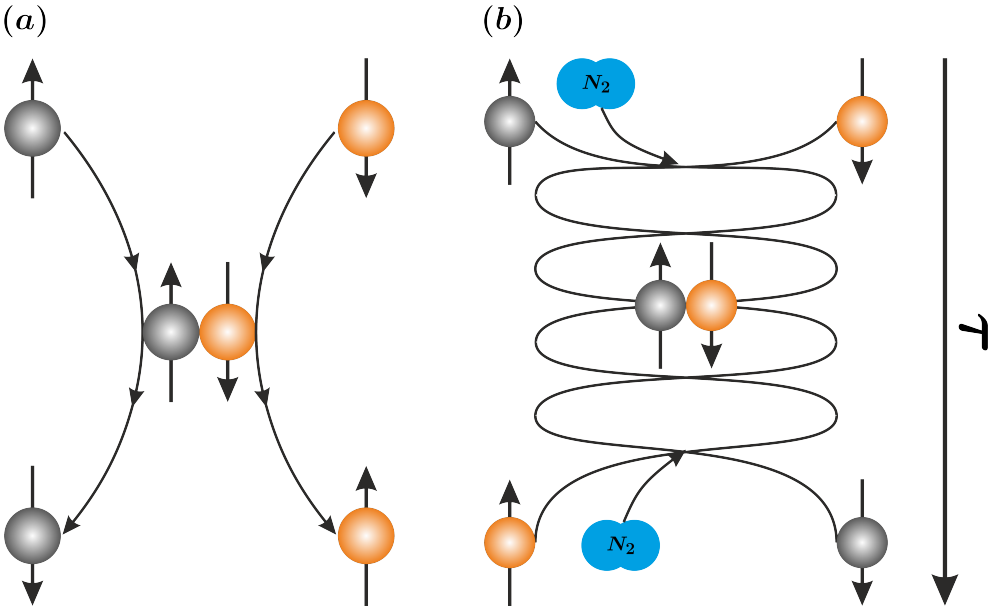


Figure 3.5: Spin exchange mechanisms. (a) Binary collisions; In this case interactions between the alkali metal and the noble gas are extremely short in respect to the nuclear polarisation of the alkali metal. Thus hyperfine coupling between the nuclei is negligible, and the interaction is dominated by the Fermi contact between the the alkali metal valence electron and the Nobel gas nuclei. Finally the Fermi contact induces a spin flip transition between the nuclei, de-polarising the alkali metal nucleus and polarising the noble gas nucleus (b) Spin Exchange, by Van der Waals complexes; Three body collisions between an alkali metal, a noble gas and a third body. The third body, typically nitrogen in the work contained within this thesis, transfers energy away from the Alkali-Noble gas pair producing a *sticking* collision. The complex remains bound for some lifetime τ, during which time polarisation may be transferred from the alkali metal atom and the noble gas nuclei by the Fermi contact until the complex is again broken by a subsequent collisions.

Binary collisions are the dominant method of polarisation transfer of low atomic number atoms such as ^{3}He. In contrast, Noble gasses with larger atomic numbers such as ^{129}Xe have polarisation transfer dominated via van der waals complexes. The pertinent Hamiltonian which describes the

spin transfer and relaxation in the alkali metal vapour and noble gas mix is given by [40];

$$\mathbf{H} \;=\; A\hat{\mathbf{I}}\cdot\hat{\mathbf{S}} + \gamma\hat{\mathbf{N}}\cdot\hat{\mathbf{S}} \;+\; \alpha\hat{\mathbf{K}}\cdot\hat{\mathbf{S}} + ... \tag{3.4}$$

Where $A\hat{\mathbf{I}}\cdot\hat{\mathbf{S}}$ is the hyperfine interaction between the alkali metal valence electron spin, $\hat{\mathbf{S}}$ and the alkali metal nuclear spin, $\hat{\mathbf{I}}$. The $\gamma\hat{\mathbf{N}}\cdot\hat{\mathbf{S}}$ term describes the spin-rotation interaction between the rotational angular moment, $\hat{\mathbf{N}}$ of the alkali metal-noble gas pair and the term $\hat{\mathbf{S}}$. $\alpha\hat{\mathbf{K}}\cdot\hat{\mathbf{S}}$ describes the Fermi contact between $\hat{\mathbf{S}}$ and the nuclear spin of the noble gas, $\hat{\mathbf{K}}$. The $\gamma\hat{\mathbf{N}}\cdot\hat{\mathbf{S}}$ term is the process responsible for the spin-relaxation in the alkali metal vapour [41], the primary point of interest is the Fermi contact which dominates the creation of the non-equilibrium nuclear spin polarisation.

The Fermi contact term itself is comprised of two components, α and $\hat{\mathbf{K}}\cdot\hat{\mathbf{S}}$. Where α is the magnetic dipole contact interaction as derived by [42]. The aspect of α pertinent to the description of polarisation transfer is the Dirac delta function, $\delta(R)$. This is a three dimensional function which details the location of the alkali metal valence electron compared to the nucleus of the noble gas atom. Where at the nucleus $\delta(R) = 1$ and everywhere else $\delta(R) = 0$. The Fermi contact term may further be written using the ladder operator formalism, to provide;

$$\mathbf{K}\cdot\mathbf{S} \;=\; \hat{K}_z\hat{S}_z + \frac{1}{2}\left(\hat{K}^{+}\hat{S}^{-} + \hat{K}^{-}\hat{S}^{+}\right). \tag{3.5}$$

Where the *flip flop* operators $\hat{K}^{+}\hat{S}^{-}$ and $\hat{K}^{-}\hat{S}^{+}$ that transfer the angular moment of the valence electron of the alkali metal and the nucleus of the noble gas. However, rather than the angular momentum transfer it is the

spin-rotation ($\gamma\hat{\mathbf{N}}\cdot\hat{\mathbf{S}}$) term that dominates the relaxation of the polarized alkali metal vapour. Further, it has been shown by Happer and coworkers [40, 43] that for each unit angular momentum lost the by alkali metal-Nobel gas collision only $\sim$ 10 % of these interactions will actually result in momentum transfer.

3.3.3 Spin Exchange Rates and Noble Gas Polarisation

When considering hyperpolarisation by SEOP, the process is described by the intermeditry steps in order to properly account for the polarisation transfer from the valence electron of the alkali metal to the noble gas atom, we must first consider the build-up of polarisation within the alkali metal. It must be noted that various alkali metal such as caesium, potassium and rubidium have been used throughout literature in the SEOP process with their own advantages and disadvantages, primarily due to the exchange cross sections. However in this work we have solely used rubidium as our alkali metal of choice, as such all calculations presented herein will refer solely to rubidium. Returning to the consideration of the practical SEOP experiment as presented in Figure 3.3, it is clear that as the laser light passes through the cell practical effects of adsorption will lead to a polarisation gradient across the cell. As such we may treat the rubidium polarisation as a function of its position along the $Z-axis$ of the SEOP cell, given by $P_{Rb}(z)$ [37];

$$P_{Rb}(z) \;=\; \frac{\gamma_{op}(z)}{\gamma_{op}(z) \;+\; \gamma_{sd}}, \tag{3.6}$$

where $\gamma_{op}(z)$ is the optical pumping rate per Rb atom at position z. As

alluded to above, we must account for the fact that the Laser power used to induce the electronic polarisation in the alkali metal vapour will weaken as it passes through the cell. As such we must consider that the value of γ_{op} will vary along the Z-axis of illumination. γ_{sd} is the Rb spin destruction rate as given by,

$$\gamma_{sd} = \sum_i \kappa^i_{sd}[M_i], \tag{3.7}$$

where κ^i_{sd} is the spin destruction rate coefficient for a given gas composition where $[M_i]$ is the number density. Nuclear polarisation in the noble gas atoms P_{NG} can be defined as a function of time t_p as described by [44],

$$P_{Ng}(\tau_p) \;=\; \frac{\gamma_{se}}{\gamma_{se} + |\Gamma|} \cdot \frac{\gamma_{op}(z)}{\gamma_{op}(z) + \sum_i \kappa^i_{sd}[M_i]} \left(1 - \exp\left(-(\gamma_{se} + \Gamma)t_p\right)\right). \tag{3.8}$$

Where γ_{se} is the Spin Exchange Rate and Γ is the Noble gas rate of self destruction arising from collisions with SEOP, cell walls or NG-NG collisions. Within the optical pumping process to create a polarisation state in the noble gas atoms there is a requirement for γ_{se} to be positive (i.e. generating polarisation) and Γ (i.e. spin destruction is negligible). Thus meaning that the polarisation of the noble gas atoms is increasing faster than the relaxation can destroy it. The spin exchange rate γ_{se} is the factor which governs the the polarisation transfer between Rb and the noble gas nucleus is defined by [40, 45],

$$\gamma_{se} \;=\; [Rb]\left(\frac{\gamma_{RbNg}\xi_{Rb}}{[N_g] \;+\; \sum_i b_i\,[M_i]} \;+\; \langle\sigma v\rangle\right), \tag{3.9}$$

where $[Rb]$ is the number density of rubidium (as experimentally deter-

mined by [46]). γ_{RbNg} is the rate contribution from van der waals complex to spin exchange via Fermi contact. ξ_{Rb} is the isotropic composition of Rb [45], $[Ng]$ is the number density of the noble gas, and $\langle \sigma v \rangle$ is the velocity averaged binary spin exchange cross-section.

In this thesis all hp gas, NMR and MRI measurements are performed at high-field after extraction from the SEOP cell. As such the factor $\gamma_{op}(z)$ is not possible to be interrogated directly, however others such as [10] have probed the $\gamma_{op}(z)$ as a function of position via very-low field NMR detection within the SEOP cell. For the hp by SEOP used in this work we may simplify the factor to γ_{op}. An additional factor for simplification may be considered. As the spin destruction coefficient for Xenon is approximately three orders of magnitude greater than that against N_2, thus for the current treatment of ^{129}Xe SEOP spin destruction from other components such as the buffer gas [39, 44] may be ommited. A final simplification comes for nuclei ^3He and ^{129}Xe, where, $\Gamma << \gamma_{se}$ for these nuclei, therefor the Γ term may be disregarded [39]. In the case of SEOP of ^{129}Xe Equation 3.8, may be simplified to;

$$P_{^{129}Xe}(\tau_p) \; = \; \frac{\gamma_{op}}{\gamma_{op} \; + \; \kappa_{sd}^{Xe}\,[Xe]} \left(1 - \exp\left(-\gamma_{se}\tau_p\right)\right). \tag{3.10}$$

Where only the spin destruction coefficient κ_{sd} for ^{129}Xe is considered. For quadrupole nuclei ($I \; > 1/2$) such as ^{21}Ne , ^{83}Kr and ^{131}Xe the relaxation coefficient Γ may not be ignored due to substantially increased relaxation arising from NG-NG interactions and NG-wall interactions. Further, when considering quadrupole nuclei, at high number densities, the relaxation rate will further increase indicating that the above treatment is dependent upon the noble gas density. Indicating that the noble gas polarisation will be highly dependent on noble gas density as, at

high density the noble gas polarisation will decrease due to higher spin destruction.

3.4 Summary

This chapter has presented a comprehensive overview of the methods to produce a hyperpolarised spin state. A particular focus is made to methods directly applicable to noble gasses. Spin Exchange Optical Pumping is examined in depth as to provide the reader a basis to understand the work presented within this thesis.

Bibliography

[1] J. Kurhanewicz, D. B. Vigneron, K. Brindle, E. Y. Chekmenev, A. Comment, C. H. Cunningham, R. J. DeBerardinis, G. G. Green, M. O. Leach, S. S. Rajan, R. R. Rizi, B. D. Ross, W. S. Warren, and C. R. Malloy, "Analysis of Cancer Metabolism by Imaging Hyperpolarized Nuclei: Prospects for Translation to Clinical Research," *Neoplasia*, vol. 13, no. 2, pp. 81–97, 2011.

[2] M. L. Hirsch, N. Kalechofsky, A. Belzer, M. Rosay, and J. G. Kempf, "Brute-Force Hyperpolarization for NMR and MRI," *Journal of the American Chemical Society*, vol. 137, no. 26, pp. 8428–8434, 2015.

[3] J. H. Ardenkjaer-Larsen, "On the present and future of dissolution-DNP," *Journal of Magnetic Resonance*, vol. 264, pp. 3–12, 2016.

[4] J. H. Lee, Y. Okuno, and S. Cavagnero, "Sensitivity enhancement in solution NMR: Emerging ideas and new frontiers," *Journal of Magnetic Resonance*, vol. 241, pp. 18–31, apr 2014.

[5] J. Leggett, R. Hunter, J. Granwehr, R. Panek, A. J. Perez-Linde, A. J. Horsewill, J. McMaster, G. Smith, and W. Köckenberger, "A dedicated spectrometer for dissolution DNP NMR spectroscopy," *Physical Chemistry Chemical Physics*, vol. 12, no. 22, p. 5883, 2010.

[6] S. E. Day, M. I. Kettunen, F. A. Gallagher, D.-E. Hu, M. Lerche, J. Wolber, K. Golman, J. H. Ardenkjaer-Larsen, and K. M. Brindle, "Detecting tumor response to treatment using hyperpolarized ^{13}C magnetic resonance imaging and spectroscopy," *Nature Medicine*, vol. 13, no. 11, pp. 1382–1387, 2007.

[7] S. J. Nelson, D. Vigneron, J. Kurhanewicz, A. Chen, R. Bok, and R. Hurd, "DNP-Hyperpolarized ^{13}C Magnetic Resonance Metabolic Imaging for Cancer Applications," *Applied Magnetic Resonance*, vol. 34, pp. 533–544, aug 2008.

[8] J. H. Ardenkjaer-Larsen, B. Fridlund, A. Gram, G. Hansson, L. Hansson, M. H. Lerche, R. Servin, M. Thaning, and K. Golman, "Increase in signal-to-noise ratio of $>$ 10,000 times in liquid-state NMR," *Proceedings of the National Academy of Sciences*, vol. 100, no. 18, pp. 10158–10163, 2003.

[9] A. Comment, S. Jannin, J.-N. Hyacinthe, P. Miéville, R. Sarkar, P. Ahuja, P. R. Vasos, X. Montet, F. Lazeyras, J.-P. Vallée, P. Hautle, J. A. Konter, B. van den Brandt, J.-P. Ansermet, R. Gruetter, and G. Bodenhausen, "Hyperpolarizing Gases via Dynamic Nuclear Polarization and Sublimation," *Physical Review Letters*, vol. 105, p. 018104, jul 2010.

[10] P. Nikolaou, A. M. Coffey, L. L. Walkup, B. M. Gust, N. Whiting, H. Newton, S. Barcus, I. Muradyan, M. Dabaghyan, G. D. Moroz, M. S. Rosen, S. Patz, M. J. Barlow, E. Y. Chekmenev, and B. M. Goodson, "Near-unity nuclear polarization with an open-source ^{129}Xe hyperpolarizer for NMR and MRI," *Proceedings of the National Academy of Sciences*, vol. 110, no. 35, pp. 14150–14155, 2013.

[11] J. S. Six, T. Hughes-Riley, K. F. Stupic, G. E. Pavlovskaya, and T. Meersmann, "Pathway to Cryogen Free Production of Hyperpolarized Krypton-83 and Xenon-129," *PLoS ONE*, vol. 7, no. 11, 2012.

[12] T. Hughes-Riley, J. S. Six, D. M. Lilburn, K. F. Stupic, A. C. Dorkes, D. E. Shaw, G. E. Pavlovskaya, and T. Meersmann, "Cryogenics free production of hyperpolarized ^{129}Xe and ^{83}Kr for biomedical MRI applications," *Journal of Magnetic Resonance*, vol. 237, pp. 23–33, dec 2013.

[13] J. H. Ardenkjaer-Larsen, A. M. Leach, N. Clarke, J. Urbahn, D. Anderson, and T. W. Skloss, "Dynamic nuclear polarization polarizer for sterile use intent," *NMR in Biomedicine*, vol. 24, no. 8, pp. 927–932, 2011.

[14] D. F. Cowgill and R. E. Norberg, "Spin-lattice Relaxation and Chemical Shift of ^{83}Kr in Solid and Lifiuid Krypton," *Physical Review B*, vol. 8, pp. 4966–4974, dec 1973.

[15] R. Henry and R. E. Norberg, "Pulsed Nuclear Magnetic Resonance of ^{21}Ne in Solid and Liquid Neon," *Physical Review B*, vol. 6, pp. 1645–1653, sep 1972.

[16] J. R. Owers-Bradley, A. J. Horsewill, D. T. Peat, K. S. K. Goh, and D. G. Gadian, "High polarization of nuclear spins mediated by nanoparticles at millikelvin temperatures," *Physical Chemistry Chemical Physics*, vol. 15, no. 25, p. 10413, 2013.

[17] M. Tanaka, T. Kunimatsu, M. Fujiwara, H. Kohri, T. Ohta, M. Utsuro, M. Yosoi, S. Ono, K. Fukuda, K. Takamatsu, K. Ueda, J. P. Didelez, G. Prossati, and A. De Waard, "Nuclear spin imaging with hyperpolarized nuclei created by brute force method," *Journal of Physics: Conference Series*, vol. 295, no. 1, 2011.

[18] G. Frossati, "Polarization of ^{3}He, D_2 and (eventually) ^{129}Xe Using Low Temperatures and High Magnetic Fields," *Journal of Low Temperature Physics*, vol. 111, pp. 521–532, 1998.

[19] J. D. O'Neill, E. V. Krjukov, J. R. Owers-Bradley, and Y. Xia, "NMR Spectroscopy of Adsorbed ^{129}Xe at Low Temperatures

and High Magnetic Fields," *Journal of Low Temperature Physics*, vol. 146, no. 5-6, pp. 563–579, 2007.

[20] E. V. Krjukov, J. D. O'Neill, and J. R. Owers-Bradley, "Brute Force Polarization of ^{129}Xe," *Journal of Low Temperature Physics*, vol. 140, no. 5-6, pp. 397–408, 2005.

[21] F. D. Colegrove, L. D. Schearer, and G. K. Walters, "Polarization of ^{3}He Gas by Optical Pumping," *Physical Review*, vol. 132, no. 6, pp. 2561–2572, 1963.

[22] M. Batz, P. J. Nacher, and G. Tastevin, "Fundamentals of metastability exchange optical pumping in helium," *Journal of Physics: Conference Series*, vol. 294, p. 012002, jun 2011.

[23] K. Suchanek, K. Cieslar, Z. Olejniczak, T. Palasz, N. Suchanek, and T. Dohnalik, "Hyperpolarized ^{3}He gas production by metastability exchange optical pumping," *Optica Applicata*, vol. 35, no. 2, pp. 263–276, 2005.

[24] L. D. Schearer, "Optical pumping of neon $^{3}P_2$ metastable atoms," *Physical Review*, vol. 180, no. 1, pp. 83–90, 1969.

[25] R. Fitzgerald, K. Sauer, and W. Happer, "Cross-relaxation in laser-polarized liquid xenon," *Chemical Physics Letters*, vol. 284, no. 1-2, pp. 87–92, 1998.

[26] G. Navon, Y.-Q. Song, T. Room, S. Appelt, R. E. Taylor, and a. Pines, "Enhancement of Solution NMR and MRI with Laser-Polarized Xenon," *Science*, vol. 271, no. 5257, pp. 1848–1851, 1996.

[27] L. D. Schearer, "Depolarization Cross Sections for the Metastable Noble Gases by Optical Pumping," *Physical Review*, vol. 188, pp. 505–506, dec 1969.

[28] D. A. Shea and D. Morgan, "The Helium-3 Shortage: Supply, Demand, and Options for Congress," *Congressional Research Service*, no. R41419, p. 27, 2010.

[29] A. Kastler, "Quelques suggestions concernant la production optique et la d ´ etection optique d ' une in ´ egalit ´ e de population des niveaux de quantifigation spatiale des atomes . Application ' a l ' exp ´ erience de Stern et Gerlach et ' a la r ´ esonance magn ´," *J Phys Radium*, vol. 11, no. 6, pp. 255–265, 1950.

[30] A. Kastler, "Les Méthodes Optiques d ' Orientation Atomique et leurs Applications," *Proceedings of the Physical Society*, vol. 67, no. Section A, pp. 853–863, 1954.

[31] B. C. Grover, "Noble-Gas NMR Detection through Noble-Gas-Rubidium Hyperfine Contact Interaction," *Physical Review Letters*, vol. 40, pp. 391–392, feb 1978.

[32] J. S. Six, T. Hughes-Riley, D. M. Lilburn, A. C. Dorkes, K. F. Stupic, D. E. Shaw, P. G. Morris, I. P. Hall, G. E. Pavlovskaya, and T. Meersmann, "Pulmonary MRI contrast using Surface Quadrupolar Relaxation (SQUARE) of hyperpolarized ^{83}Kr," *Magnetic Resonance Imaging*, vol. 32, pp. 48–53, jan 2014.

[33] K. F. Stupic, Z. I. Cleveland, G. E. Pavlovskaya, and T. Meersmann, "Hyperpolarized ^{131}Xe NMR spectroscopy," *Journal of Magnetic Resonance*, vol. 208, no. 1, pp. 58–69, 2011.

[34] D. A. Barskiy, A. M. Coffey, P. Nikolaou, D. M. Mikhaylov, B. M. Goodson, R. T. Branca, G. J. Lu, M. G. Shapiro, V. V. Telkki, V. V. Zhivonitko, I. V. Koptyug, O. G. Salnikov, K. V. Kovtunov, V. I. Bukhtiyarov, M. S. Rosen, M. J. Barlow, S. Safavi, I. P. Hall, L. Schröder, and E. Y. Chekmenev, "NMR Hyperpolarization Techniques of Gases," *Chemistry - A European Journal*, vol. 23, no. 4, pp. 725–751, 2017.

[35] T. G. Walker and W. Happer, "Spin-exchange optical pumping of noble-gas nuclei," *Reviews of Modern Physics*, vol. 69, pp. 629–642, apr 1997.

[36] S. Appelt, A. Baranga, C. Erickson, M. Romalis, A. Young, and W. Happer, "Theory of spin-exchange optical pumping of ^{3}He and ^{129}Xe," *Physical Review A*, vol. 58, no. 2, pp. 1412–1439, 1998.

[37] W. Happer and W. A. Van Wijngaarden, "An optical pumping primer," *Hyperfine Interactions*, vol. 38, pp. 435–470, dec 1987.

[38] W. Happer, "Optical Pumping," *Reviews of Modern Physics*, vol. 44, pp. 169–249, apr 1972.

[39] M. E. Wagshul and T. E. Chupp, "Laser optical pumping of high-density Rb in polarized He3 targets," *Physical Review A*, vol. 49, no. 5, pp. 3854–3869, 1994.

[40] W. Happer, E. Miron, S. Schaefer, D. Schreiber, W. A. van Wijngaarden, and X. Zeng, "Polarization of the nuclear spins of noble-gas atoms by spin exchange with optically pumped alkali-metal atoms," *Physical Review A*, vol. 29, pp. 3092–3110, jun 1984.

[41] R. M. Herman, "Theory of Spin Exchange between Optically Pumped Rubidium and Foreign Gas Nuclei," *Physical Review*, vol. 137, pp. A1062–A1065, feb 1965.

[42] M. A. Bouchiat, J. Brossel, and L. C. Pottier, "Evidence for Rb-Rare-Gas Molecules from the Relaxation of Polarized Rb Atoms in a Rare Gas. Experimental Results," *The Journal of Chemical Physics*, vol. 56, pp. 3703–3714, apr 1972.

[43] X. Zeng, Z. Wu, T. Call, E. Miron, D. Schreiber, and W. Happer, "Experimental determination of the rate constants for spin exchange between optically pumped K, Rb, and Cs atoms and ^{129}Xe nuclei in alkali-metal–noble-gas van der Waals molecules," *Physical Review A*, vol. 31, no. 1, pp. 260–278, 1985.

[44] B. Driehuys, G. D. Cates, E. Miron, K. Sauer, D. K. Walter, and W. Happer, "High-volume production of laser-polarized ^{129}Xe," *Applied Physics Letters*, vol. 69, pp. 1668–1670, sep 1996.

[45] G. D. Cates, R. J. Fitzgerald, A. S. Barton, P. Bogorad, M. Gatzke, N. R. Newbury, and B. Saam, "Rb-^{129}Xe spin-exchange rates due to binary and three-body collisions at high Xe pressures," *Physical Review A*, vol. 45, pp. 4631–4639, apr 1992.

[46] T. J. Killian, "Thermionic Phenomena Caused by Vapors of Rubidium and Potassium," *Physical Review*, vol. 27, pp. 578–587, may 1926.

Chapter 4

MRI Velocimetry measurements in channels with porous walls

This chapter will detail the optimisation of hyperpolarised ^{129}Xe continuous flow Spin Exchange Optical Pumping and its application to velocimetry studies within the channels of steam reformer pellets with porous walls. This work resulted in an oral presentation at the 13^{th} International Bologna Conference on Magnetic Resonance in Porous Media (MRPM 13) in 2016. This work is currently unpublished and is intended an technical note and introduction to the work presented in Chapter 5.

Mr Fraser Hill-Casey performed the optimisation of continuous flow Spin Exchange Optical Pumping, Velocimetry measurements within the samples, processed and interpreted all data contained herein. Dr Galina Pavloskaya assisted with the pulse programming of the velocimetry sequences and interpretation. Professor Sean Rigby and Professor Thomas Meersmann provided assistance with interpretation of results. Professor Rigby supplied the Steam Reformer pellets used in this study and provided the Hg Porosimetry data.

4.1 Introduction

Flow measurements by Nuclear Magnetic Resonance (NMR) are well established and have found uses including rheology [1–3], process engineering [4, 5], catalysis [6–10], diffusion in porous media [11–13] and food science [14–16]. However, typically these measurements are confined to liquid measurements. This is primarily due to the fundamental insensitivity of NMR where even proton measurements at ultra-high magnetic fields provide minuscule sample magnetisation (0.01 % at 298 K and 9.4 T). In the gas phase, measurements are further hampered by the inherent low density of the sample at even high pressures and the inherently lower gyromagnetic ratios of the probes nuclei (i.e. ^{19}F and ^{129}Xe) in the gas phase.

Despite this, gas phase spectroscopy, relaxometry and imaging are becoming increasingly commonplace [9, 10] and provide an extremely versatile method of probing various factors of mass transport. Further gas phase measurements allow for a number of factors to be probed which are typically unavailable to liquid based measurements perhaps most notable alteration of pressure which influences a wide range of aspects such as spin density, T_1 and T_2 relaxation times increasing proportionally with pressure and molecular self-diffusion coefficients reducing.

Nevertheless, gas phase flow monitoring provides a particular challenge for NMR due to the both the aforementioned inherently lower density; hence, lower signal density with dry air density being only 1.197 kg/m^3 compared to 998.2 kg/m^3 for that of water at STP.

Common gas phase probes include sulphur hexafluoride (SF_6) [17, 18] and alkenes, however such molecular probes suffer from short T_1 and T_2

relaxation times making imaging problematic and impacting the accessible time-scales. Further, these common thermally polarised samples often require extremely high pressure within the measurement system to achieve a suitable sensitivity. The impact of this however means that diffusion within systems is typically confined to the *molecular regime*.

Such restrictions may be overcome by utilising hyperpolarisation techniques such as continuous flow Spin Exchange Optical Pumping (SEOP) [19–22] for production of hp ^{129}Xe. Through this technique it is possible to circumvent a number of the challenges associated with thermally polarised gas probes. Crucially with continuous flow hp ^{129}Xe it is possible to perform measurements at room temperature and atmospheric pressure thus leading to a larger mean free path. Hence allowing for diffusion within the Knudsen regime to be probed in a wider range of pore structures than possible with other gas phase probes. Further, with the versatility of the SEOP process it is possible to tune pressures to also probe the molecular regime [23].

In this Chapter, Magnetic Resonance Imaging (MRI) techniques are employed to investigate the flow patterns within a highly porous sample. Imaging techniques are of particular interest to probing porous media due to the ability of MRI to provide an abundance of information into a variety of media such as catalysts [18, 24–26], pharmaceuticals [27–29], building materials [9, 30] and environmental considerations [31–34] in a non-invasive fashion. A further benefit regarding the use of MR is its ability to interrogate opaque samples. As such, in this work we present a methodology to produce a stream of highly polarised ^{129}Xe with a consistent, stable polarisation for interrogation of flow within porous media.

4.1.1 MRI: Principles of MR Velocimetry

Beyond simple spin density measurements (described in Chapter 2) MRI may also be made sensitive to motional effects in samples and may be used to probe such characteristics as dispersion, diffusion and, of specific interest to this work, velocity. This section provides a simplified introduction to magnetic resonance velocity imaging.

Consider an MRI active nuclei such as ^{129}Xe in an external applied magnetic field it will precess about the applied field at the Larmor frequency. This precession frequency may be encoded spatially by the application of enforced field variation or gradients.

Collection of signal in a traditional MR experiment is achieved by use of a radio frequency coil in which the precessing nuclei induce a voltage and the complex NMR signal S_t is detected in the time domain, as given by;

$$S_t = \int \rho_r \, exp(i\phi_{r,t}) dr, \tag{4.1}$$

where ρ_r is the spin density function and $\phi_{r,t}$ is the phase of the signal collected of time t.

This time domain signal may then be Fourier transformed into the frequency domain. Which will provide the absolute value of the ρ_r, in turn giving a spatially resolved image of the distribution of spins with the signal intensity being proportional to the number of spins in a given volume.

The displacement of spins over a given time (Δ) can be measured by use of MR velocimetry. The basic premise of this measurement is that

the spatial position (in a given axis) of the spins can be encoded into the phase of the spin during its precession. This is performed by the rapid application of a further magnetic field gradient ($\mathbf{g}$). The effect this gradient has on the spins at $\Delta = 0$ can be stated as shown in Equation (4.2),

$$\phi_{\Delta=0} = \gamma\delta\mathbf{g} \cdot \mathbf{r}, \tag{4.2}$$

where δ is the ramping time of the gradient.

Considering the case where after a given time $\Delta = \Delta^{'}$ the spins have remained motionless $\mathbf{r} = \mathbf{r}$. The application of an equal but opposite polarity will cause the phase to perfectly refocus thus no phase shift. In the case where after time $\Delta = \Delta^{'}$ where the spins have moved to position $\mathbf{r} = \mathbf{r}^{'}$ then the net phase shift can be stated as,

$$\phi_{res} = \phi_{\Delta=0} - \phi_{\Delta=\Delta'} = \gamma\delta\mathbf{g} \cdot (\mathbf{r} - \mathbf{r}^{'}), \tag{4.3}$$

which clearly shows that the net phase shift is proportional to the displacement of the spins. Hence,

$$\phi_{res} \propto (\mathbf{r} - \mathbf{r}^{'}). \tag{4.4}$$

Considering that in a traditional MR velocimetry experiment the flow gradient will only be applied in a single direction g_i, so as to probe the velocities in the given direction V_i. Further, given the basic knowledge that velocity is the displacement divided by the time of observation our above equations can be arranged to a more familiar form,

$$V_i = \frac{d_i}{t}, \tag{4.5}$$

where,

$$d_i = \frac{\phi_{\Delta=0} - \phi_{\Delta=\Delta'}}{\gamma g_i}, \tag{4.6}$$

and,

$$t = \delta\Delta. \tag{4.7}$$

This allows for the entire equation to be explicitly stated as,

$$V_i = \frac{\phi_{\Delta=0} - \phi_{\Delta=\Delta'}}{\gamma g_i \delta\Delta}. \tag{4.8}$$

Thus in the MR velocimetry the tunable parameters are the gradient strength, direction g_i, pulse duration (typically an order of magnitude smaller than the total application time) δ and the observation period Δ.

Due to the simple nature of this measurement it is possible to easily combine the measure of phase shift with traditional imaging methodologies such as, in the case of this work a gradient echo sequence 4.1.

4.1.2 Diffusion mechanisms

Mass transport in porous media is typically dominated by either molecular or knudsen diffusion. In cases where both effects are present transitional diffusion also occurs. The dominant mechanism is typically de-

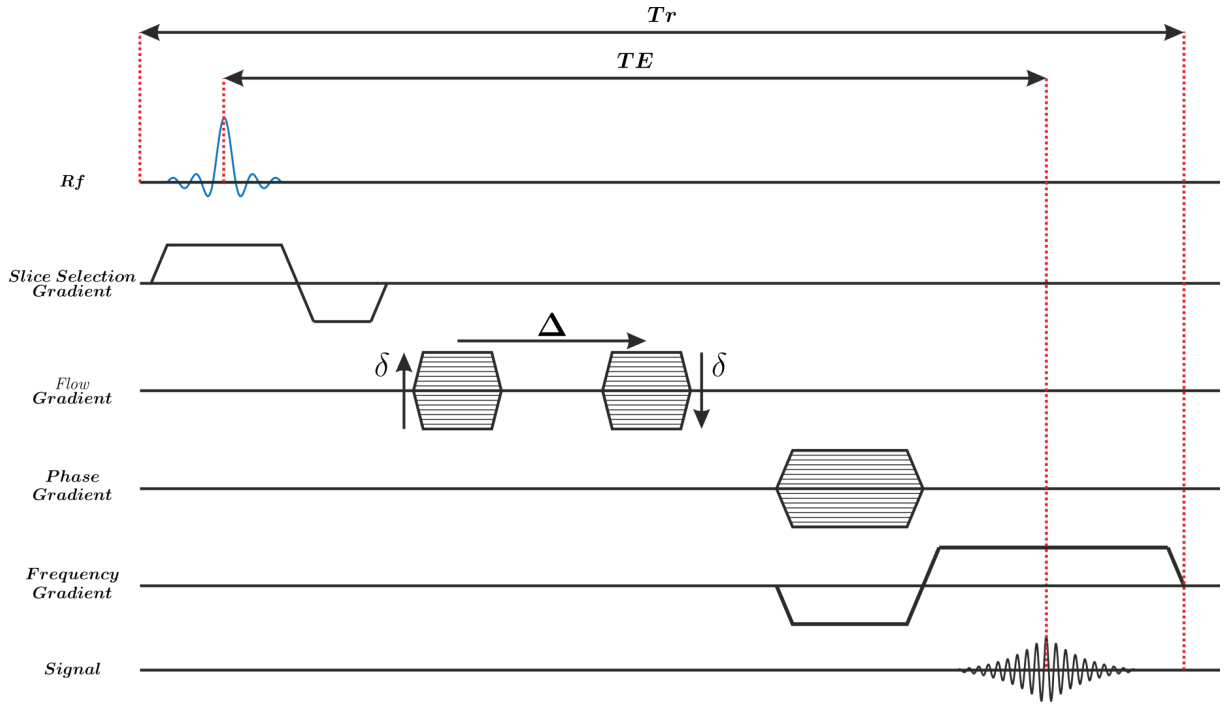


Figure 4.1: Timing diagram of a slice selective, gradient echo imaging sequence with the addition of a velocity encoding module; The first flow encoding gradient pulse of duration δ serves to encode the initial position of the spins. Molecular displacement during the delay Δ serves to both attenuate the amplitude of the collected signal (via stochastic motion) and imparts a net phase shift on the spins (via coherent motion). A second, equal and opposite flow encoding gradient is applied to refocus the magnetization. Being as the magnetization is stored in the direction of flow during time Δ the primary dephasing effect is due to longitudinal relaxation. With the T_1 of Hp ^{129}Xe being sufficiently long within the system of interest the measurement of velocities is only limited by spins flowing out of the detection region.

termined by the environment of which the diffusion is present, e.g. the size of the pore it is passing though along with the driving force of the fluid passing through. First however the mean free path (λ) may be defined. The distance travelled by a molecule before collision with a second body, be that another molecule (molecular diffusion) or a boundary wall (knudsen diffusion) may be mathematically stated in Equation 4.9:

$$\lambda = \frac{1}{\sqrt{2}\pi\sigma^2 N_v}, \tag{4.9}$$

where, σ is the collisional cross section of the molecule and N_v is the number of atoms per unit volume. In the case of an ideal gas where pressure is defined by Equation 4.10,

$$P = N_v k_b T, \tag{4.10}$$

where, P is the pressure, T is the temperature and k_B is Boltzmann's constant. Meaning that the mean free path of an ideal gas is defined by,

$$\lambda = \frac{k_B T}{\sqrt{2}\pi\sigma^2 P}. \tag{4.11}$$

When the mean free path of the diffusing molecule is much smaller than the pore diameter (Figure 4.2 (a)) molecular diffusion is dominant. Thus meaning that intermolecular collisions are much more prevalent than collisions with pore walls and may be described by,

$$D_F = \frac{\lambda v}{3}, \tag{4.12}$$

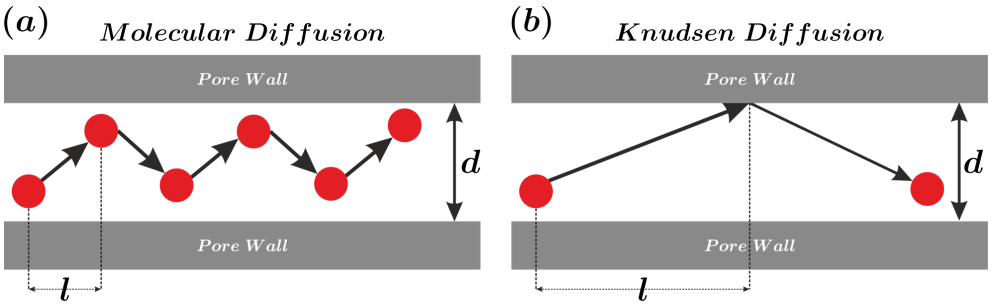


Figure 4.2: Schematic of knudsen & molecular diffusion.(a) an example pathway of a system undergoing molecular diffusion in a cylindrical pore, the mean free path in this case is greater than the length of the system. (b) A schematic of a molecule in a cylindrical pore of diameter d, where the mean free path l is less than length of the system indicating that diffusion is in the Knudsen regime.

where D_F is the molecular diffusivity, λ is the mean free path of the molecule and v is the molecular velocity.

Thus Knudsen diffusion (4.2) (b)) is dominant in systems where the mean free path of the diffusing molecules is greater than that of the pore diameter, meaning that the diffusing molecules will collide with the pore walls much more frequently. As such the Knudsen diffusivity is only relevant at low pressures and small pore diameters and may be defined by equation,

$$D_k = \frac{dv}{3}, \tag{4.13}$$

where D_k is the Knudsen diffusivity, d is the pore diameter.

However real systems tend to possess a mixture of both molecular and Knudsen characteristics, as such this regime is known as transitional diffusion and is usually encountered in networks with hierarchical pore structure. Transitional diffusion may be be described by Equation 4.14:

$$D_T = \left(\frac{1}{D_F} + \frac{1}{D_K} \right)^{-1}, \tag{4.14}$$

where D_T is the transitional diffusion.

To easily determine the dominant effect we may make use of the dimensionless *Knudsen number* K_n in Equation 4.15,

$$\mathrm{K}_n = \frac{\lambda}{d}, \tag{4.15}$$

where the symbols retain their previously defined meanings. In cases where $\mathrm{K}_n > 10$ the diffusion is predominately within the Knudsen regime. When $0.1 < \mathrm{K}_n < 10$ then diffusion is in the transitional regime and when $\mathrm{K}_n < 0.1$ the diffusions is within the molecular regime.

While flow experiments have been previously performed in Combined SCR monoliths using both water [35] and ^{19}F [18] these techniques both suffer from the operating solely within the molecular regime due to the short λ of liquid water at STP and due to high pressures required as to detect sufficient SNR of thermally polarised ^{19}F. Hyperpolarised ^{129}Xe however does not require such high pressures due to its high SNR measurements may be routinely made at atmospheric pressure with no compromise to SNR.

4.1.3 Mercury Porosimetry

Mercury porosimetry is a well-developed technique used for probing the pore size distribution, of complex porous materials, radii ranging from 2 nm to $\sim$ 3 μm [36, 37]. Being as mercury is non-wetting it must be forced into a pore structure with pressure. The pressure applied may be used to characterise the pore size of the material being as the smaller the pore size the greater the external pressure required to cause mercury to enter. Further, when the external pressure is lowered the mercury may

then leave the sample. The relationship between the pore radii and the applied pressures was characterised by Washburn et al (1921) [38] and may be stated as:

$$P_{Hg} = -\frac{2\gamma_{ls}\cos(\theta)}{r}, \tag{4.16}$$

where r is the pore radius, θ is the contact angle between the mercury liquid and the porous material, γ_{ls} is the surface tension between the liquid mercury and porous material, and P_{Hg} is the externally applied pressure.

Mercury porosimitry experiments experience hysteresis between the intrusion and extrusion pressures. Such effects arise typically due to either changes of the contact angle between the mercury liquid and pore material or structural effects.

Predominantly, mercury porosimetry is analysed using the Washburn equation [38] and thus includes both aspects structural and hysteresis. However Rigby et al (2002) [37, 39] proposed an alternative method of analysis as to remove the contact angle hysteresis via use of a semi-empirical equations. Having removed the contact angle hysteresis any remaining hysteresis of the intrusion/extrusion cycle may be attributed solely to structural effects. This semi-empirical equation is given by Equation 4.17:

$$r \;=\; \frac{-A + \sqrt{A^2 - 2B\,P_{hg}}}{P_{hg}}, \tag{4.17}$$

where A and B are both constants determined by the material and whether the meniscus is advancing or retreating (see Table 4.1). As

Equation 4.17 is empirical in origin and so of limited scope and only applicable in a limited range of applications however it has been previously applied to both silica and alumina samples [37, 39–41].

Table 4.1: Parameters for insertion into Equation 4.17 for analysis of mercury porosimetry data in alumina and silica materials. Values taken from [40].

Material	Advancing meniscus		Retreating meniscus	
	A	B	A	B
Silica	-302.533	-0.739	-68.366	-235.561
Alumina	-302.533	-0.739	-40	-240

Further the evaluated of Equation 4.17 has been independently calibrated via use of electron microscopy [42, 43]. Further, as this method has been derived empirically it contains experimental error of approximately 4-5 % [43].

4.2 Experimental

4.2.1 Flow System

To determine optimal flow conditions, and to begin the development of the flow imaging used within this study, for the continuous flow SEOP, initial experiments were performed in an empty perspex cylinder (12.8 mm i.d., 15.0 mm o.d., 70.0 mm length) with a 1/4" Swagelok (Solon, Ohio, U.S.) fitting as to allow for connection to the main gas system.

The main sample used within this study is that of steam reformer pellets. These were chosen due to their porous structure and interesting geometry. Figure 4.3 (a) displays the schematic of the steam reformer pellets

with dimensions of 10.7 mm o.d. and 4 channels of 2.6 mm i.d. The sample were degassed for 12 hours at 150 ^{o}C as to ensure the pore structure is entirely open. The samples are then placed in the acrylic sample container in an inert gas environment. The pellets were stacked four high, wrapped in parafilm and placed within the aforementioned sample container shown in Figure 4.3 (b), a delrin spacer was used as to ensure that the pellets sat within the confines of the RF coil. Figure 4.3 (c) displays the schematic of the sample within the acrylic container and indicates the flow path that the ^{129}Xe takes during the flow experiment.

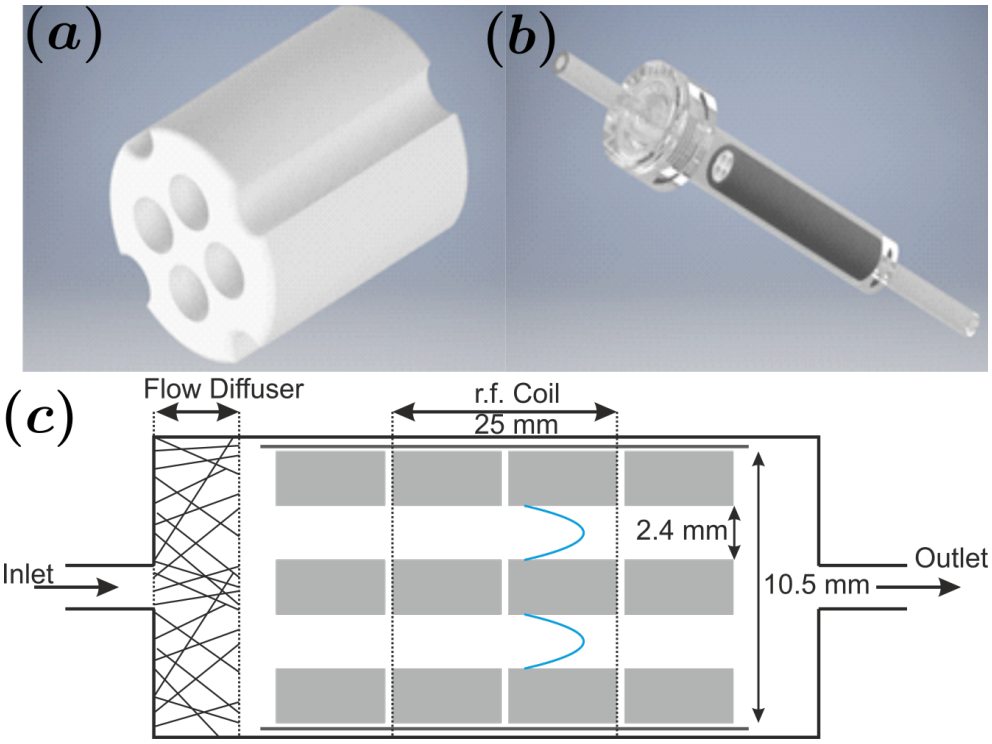


Figure 4.3: The flow system used for this series of experiments; (a) 4 channel pellets are aligned within the sample container so as to have one continuous flow path, the pellets are then wrapped in parafilm as to ensure orientation is consistent throughout experiments, and at the '*inlet*' of the container a flow diffuser is used to ensure even distribution of the flow field. (b) The representation of the 4 channel pellets used in this work. (c) Schematic representation of the flow system; 4 steam reformer pellets are stacked end to end, and the channels aligned so to ensure a continuous flow path through the system. The pellet stack was wrapped in parafilm to ensure both structural stability and to ensure the stack resides within the correct area of the sample container. The blue parabolic profiles indicate flow paths within the pellet channels.

4.2.2 X-Ray Computed Tomography

X-ray tomography images were obtained of a section of the 4 channel pellets. A single pellet was used to acquire the images. The sample was placed in an XRADIA Versa XRM - 500 X-Ray CT apparatus and images were acquired with a resolution of 15.6 um/pixel. After application of mercury porosimitry the X-Ray CT is repeated to localise the spatial distribution of the mercury within the pore structure.

4.2.3 Continuous flow Spin Exchange Optical Pumping

Figure 4.4 displays the experimental apparatus used in this series of experiments. Within this study, a 5 % Xenon (natural abundance) 95 % N_2 gas mixture was hyperpolarised in a borosilicate glass cell (length = 120 mm, inner diameter = 28 mm) containing $\sim$ 1 g of rubidium metal (99.75 %; Alfa Aesar, Heysham, England, UK). The SEOP cell was housed in an aluminium oven with quartz windows and temperature controlled by use of heated air gun (Steinel, Peterborough, England, UK). A pair of double Helmholtz coils were used to produce a homogeneous magnetic field of $B_0 \sim 10$ mT across the SEOP cell. A line narrowed laser system (30 W incident power, 0.15 nm linewidth, Spectra Physics, Santa Clara, CA, USA) tuned to the D_1 transition of rubidium (794.7 nm) was used to irradiate the SEOP Cell with a collimated, circularly polarised light (see Figure 4.4 (b)). The laser power at the SEOP cell was measured to be 23.3 W.

In batch mode SEOP, steady state nuclear polarisation for ^{129}Xe is reached in 6 minutes as verified at both high and low pressure SEOP by the ex-

tensive studies by Six et al (2012) [44], Hughes-Riley et al (2013) [45] and Barskiy (2017) [19]. However in the case of the presented experiments, an alteration is made to the batch mode delivery.

In continuous flow mode, both valves on the SEOP cell remain open allowing the gas mixture to flow through the cell. The flow rate to the sample is controlled by the use of a pressure regulator on the high pressure gas cylinder with needle valves, both prior to and after the sample allowing fine control of the flow rate. The gas is then transferred by 1.5 mm (inner diameter) PFA tubing into the acrylic continuous flow cell (13 mm i.d., 15 mm o.d.). The detection cell is located within a 9.4 T superconducting magnet (Bruker, Germany) with a custom-built probe (15.5 mm i.d.) tuned to the resonance frequency of ^{129}Xe (110.5 MHz) used for detection.

4.2.4 MRI Parameters

Images are acquired at 9.4 T with a custom built ^{129}Xe probe. Gas mixtures used in these experiment were pre mixed to a 25 % research grade Xe (99.995 % purity, natural abundance, 26.4 % ^{129}Xe ; Airgas, Rednor, PA, USA), and research grade N_2 (99.999 % pure, Air Liquide, Coleshill, UK). For the SEOP setup described in Section 4.2.3, a flow rate of 150 mm/s was found to produce a spin polarisation of 2.4 % from a cell residency time of $\sim$ 5 seconds and when a steady state flow is allowed to form.

Gas velocity profiles were collected as detailed in Section 4.1.1 and a single horizontal non-slice selective image was acquired with a FOV = 17 cm $\times$ 23 cm, imaging matrix of 64 x 32 (pixel resolution of 0.359 mm $\times$ 0.533 mm), Tr = 1000 ms. The repetition time of the experiment

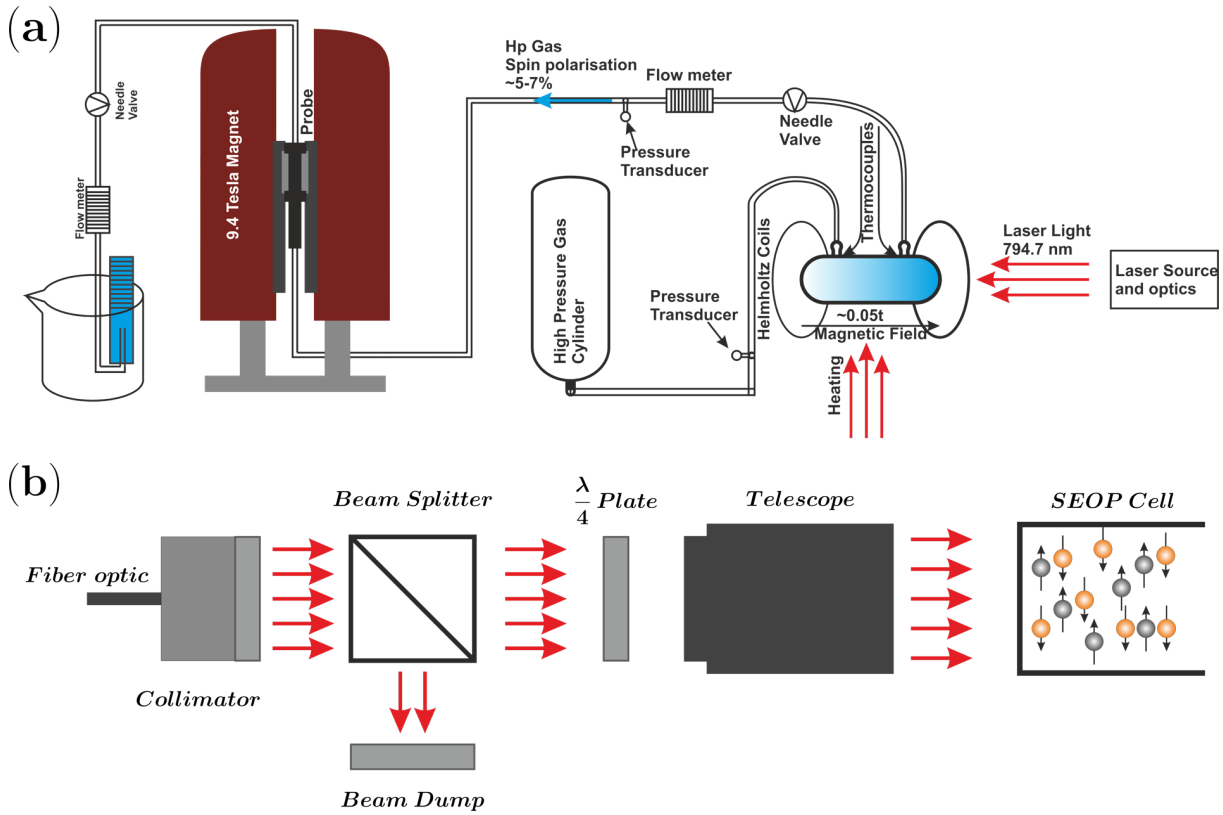


Figure 4.4: The experimental apparatus used for continuous flow Spin Exchange Optical Pumping ; (a) the delivery path of the hp gas to the high field magnet and major components of the experimental apparatus are outlined. The hyperpolarized gas mixture is delivered to the sample by simultaneously opening the inlet and outlet of the SEOP cell, allowing the gas to flow though the sample volume. The pressure of the SEOP cell is controlled by use of a pressure regulator at the high pressure gas cylinder, the needle valves allow for fine adjustment of the flow rate. (b) Outline of the optical elements used in Figure 4.4 (a).

was optimised so as to allow for a fresh gas load to be delivered to the sample after the magnetization has been destroyed by the preceding step and is thence not dependent upon the T_1 relaxation of the hp ^{129}Xe. Velocities were acquired in the Z direction and encoding parameters are $\Delta = 5$ ms, $\delta = 0.5$ ms and $G = 0.154$ T/m. The image was acquired with 16 flow encoding increments and a single scan was found to produce sufficient SNR. Image acquisition time was 8 minutes and 32 seconds.

4.3 Results and Discussion

4.3.1 Mercury Porosimetry

Figure 4.5 shows the mercury intrusion curve for the steam reformer pellets used in this study following analysis with the Kloubek (1981) correlations [43]. The data indicates a single intrusion mode at 1.06 μm. The slope of the porosimetry curve may be explained as a single intrusion into *large* macro-pores throughout the monolith. The conditions of temperature and pressure of the following hp ^{129}Xe experiments are such that the mean free path as calculated from kinetic theory (Equation 4.11) is $\sim$ 50 nm. Notably this is smaller than the single mode of macropores measured via hg porosimitry hence diffusion is within the molecular regime for this pellet.

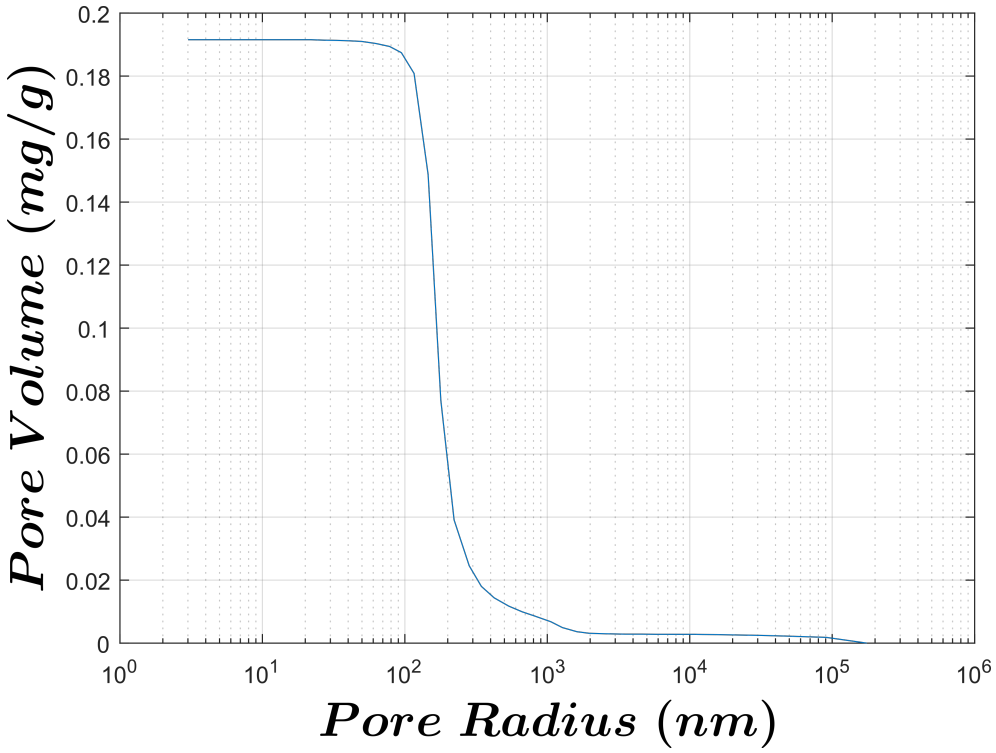


Figure 4.5: Mercury intrusion curve for Steam reformer pellets analysed using Kloubek (1981)[43] correlations displaying the single intrusion mode.

4.3.2 X-Ray CT

Figure 4.6 displays a reconstructed cross-section in the plane perpendicular to the axis of the circular channels for a typical section of the pellets used within this study obtained via an XRADIA Versa XRM-500 X-Ray CT with an in-plane resolution of 15.6 μ/pixel. Within the image, the mid grey pixels correspond to the walls of the alumina pore structure, while the bright white pixels contained within the grey regions in Figure 4.6 (b) are mercury located within the pores structure, obtained after mercury intrusion.

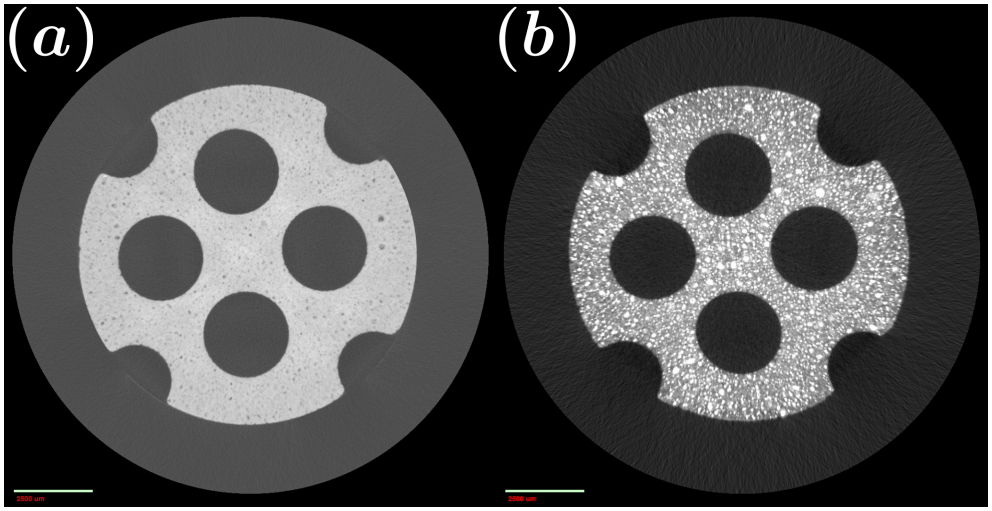


Figure 4.6: Reconstructed cross-section of 4 channel pellets (a) prior to and (b) post mercury intrusion, obtained from X-Ray CT. The bright white pixels indicated in figure (b) is mercury that is residing within the pore structure of the 4 channel pellets. Mid-grey pixels in (a) and (b) indicate the alumina substrate. The scale bar corresponds to 2500 μm. Resolution is 15.625 μm/pixel with a 1004 x 1024 acquisition matrix.

The image of the sample used in this study indicates that the mercury uniformly penetrates the pellet pore structure. Figure 4.7 (a), displays the result of particle size analysis (ImageJ, USA) with the bright white pixels indicating the intruded mercury within the pore structure. Figure 4.7 (b), displays a histogram result of the output of the particle size analysis displayed within (a).

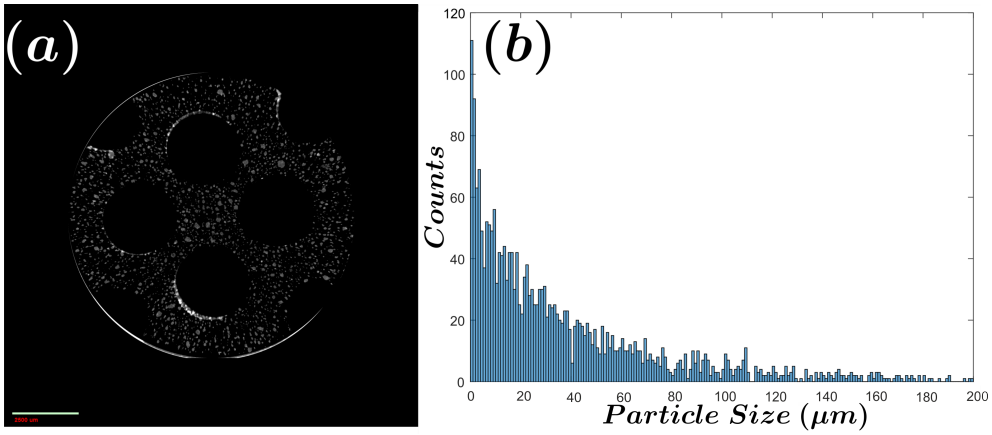


Figure 4.7: Reconstructed pore structure of 4 channel pellets: (a) displays the aligned and subtracted from Figure 4.6. The scale bar corresponds to 2500 μm. Resolution is 15.625 μm/pixel with a 1004 x 1024 acquisition matrix. The filled pores are detected via use of the image maths, and particle size analysis modules(ImageJ, USA). (b) displays a histogram of the pore size distribution taken from the image in (a). Bin size is 10 μm with 1000 bins.

4.3.3 Flow in an empty cell

To validate and characterise the phase shift velocimetry methodology used within this chapter, measurements were initially made within an empty sample container (i.d: 13 mm, o.d: 15.0 mm length: 60 mm).

Figure 4.8 displays maps of velocity acquired in three orthogonal directions within the empty cell. The colour scale displays the magnitude of the flow in each of the indicated directions V_z (4.8 (a)) V_y (4.8 (b)) and V_x (4.8 (c)). These images were acquired with a 64 x 64 acquisition matrix with 16 flow encoding steps and zero filed to 128 x 128. The acquisition time for each of these images is primarily determined by the rate at which the hp gases flow through the sample and as such each velocity component is acquired in 6 mins and 32 seconds. Therefore the maps do not show instantaneous velocity, but rather time averages showing only the coherent component of velocity. The hp ^{129}Xe flowed at a single feed rate with a Reynolds number of 52 as defined by Equation 4.18;

$$Re \;=\; \frac{\rho V_{av} D}{\mu}, \tag{4.18}$$

where ρ is the fluid density, V_{av} is the velocity in the direction of the superficial flow, μ is the fluid dynamic viscosity and D is the characteristic length scale; in this case it is the diameter of the channels within either an empty cell or the channels steam reformer pellets.

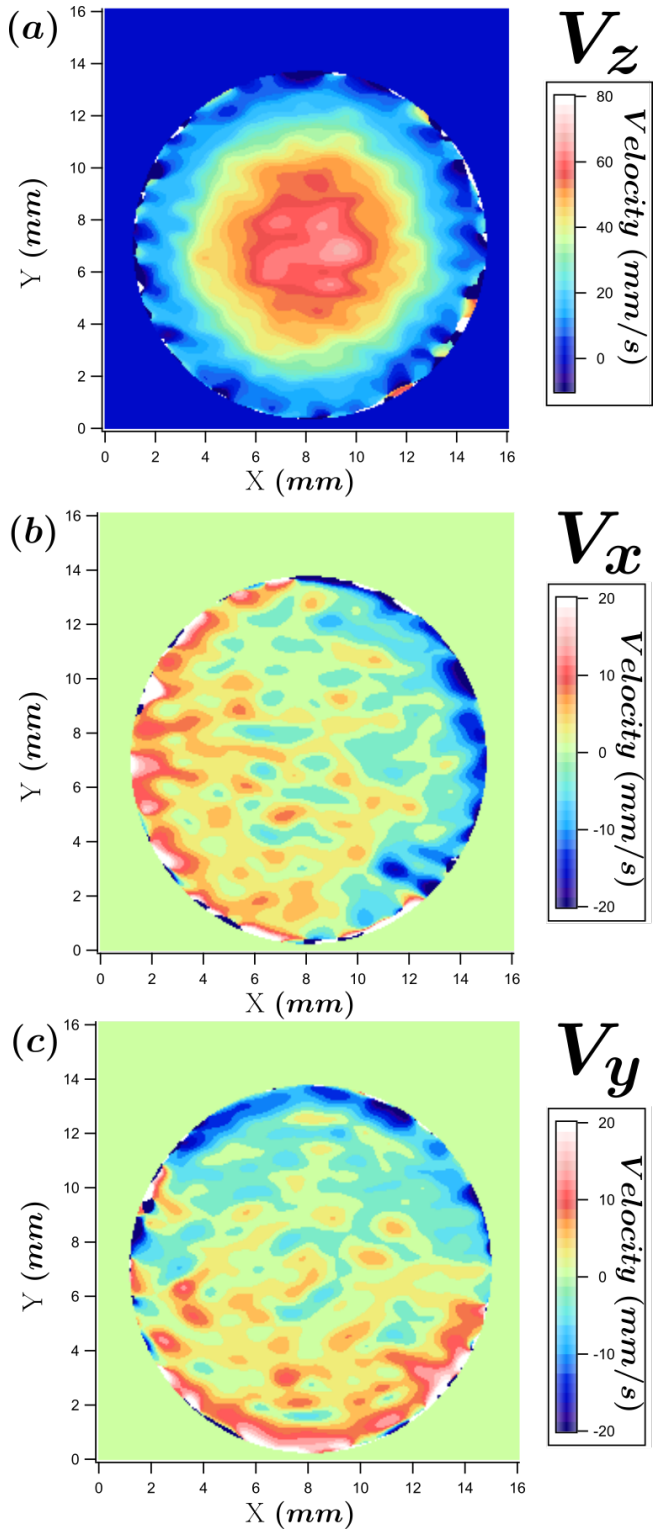


Figure 4.8: Three orthogonal component velocity images acquired at Re=56 with (a) indicating the superficial flow or V_z, (b) the transverse flow in x and (c) the transverse flow in y. The colour scale identifies the magnitude of the velocity in each direction, and ranges from zero to twice the average velocity. In all cases the acquisition matrix was 64 $\times$ 64 and zero filled to 128 $\times$ 128. A resolution of 0.250 mm pixel^{-1} in the slice direction and 0.250 mm pixel^{-1} in the phase direction was achieved. The slice thickness was 8 mm and Te = 6.8 ms.

The laminar flow of a Newtonian fluid in pipe flow is defined by a Reynolds number of $Re < 2000$. Figure 4.9 (a) displays a velocity profile of flow within the superficial direction V_z (Figure 4.8 (a)). The classic Poiseuille velocity profile for Newtonian fluids within a cylindrical channel with a $Re < 2000$ may be described by,

$$V_r = V_{max}\left(1 - \frac{r^2}{a^2}\right), \tag{4.19}$$

where V_{max} is the maximum centreline velocity in the channel, r is the position coordinate across the channel and a is the characteristic length of the channel. The small asymmetry in the experimentally determined flow profile is expected to be due to the finite entry-length of the pipe. Figure 4.9 (b) displays a radial profile taken from the direction of the superficial flow. This data further indicates the good agreement between the experimentally collected data and the theoretically predicted parabolic profile. While in the laminar flow regime, velocities should be contained to the V_z direction however in 4.8 (b) and (c) a transverse component is measured. The explanation for this may lie in the region of measurement, as the flow of hp gas is expanding rapidly from the 6.35 mm inlet to the 13 mm i.d. of the sample container proper before returning to a 6.35 mm outlet at the top of the cell. A secondary explanation may lie in the slight deviation from the profile seen in 4.9 (a) and (b) which indicates the possibility of interaction between the superficial flow and the walls of the sample container. Although, it must be noted that the most likely interpretation of the gradients across the V_x and V_y images in 4.9 (b) and (c) respectively, may be due to eddy currents arising from the application of the magnetic field gradients. Such an effect may be possibly rectified in future work via the collection of a zero flow images to allow for more

solid conclusions to be drawn from 3D velocimetry data.

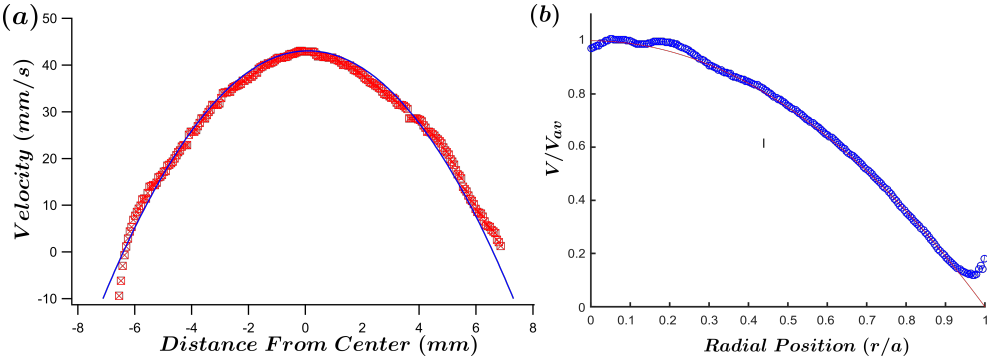


Figure 4.9: Velocity profile of the superficial or V_z flow in an empty cell at Re=56: (a) Velocity as a function of distance from the channel center. The theoretically predicted parabolic profile for laminar flow of a Newtonian fluid is shown by the solid line. (b) Radially averaged line profile of the z-velocity in the empty cell from Figure 4.8.

Figure 4.10 displays the magnitude of the reconstructed 3D vector, from the V_z, V_y and V_x velocities calculated with,

$$|V| \;=\; \sqrt{V_x^2 + V_y^2 + V_z^2}. \tag{4.20}$$

The overall contributions of the X and Y shown in Figure 4.8 (b) and (c) components appears minimal to the overall axial flow at this point. The angular offset from the Z directional flow is calculated by.

$$\theta \;=\; \arccos\left(\frac{V_z}{|V|}\right). \tag{4.21}$$

By examining the angular offset displayed in Figure 4.10 (b), it can be seen that flow is predominantly confined to the superficial direction (V_z) direction. There is however, a slight deviation at the walls of the sample container suggesting a degree of interaction with the container walls.

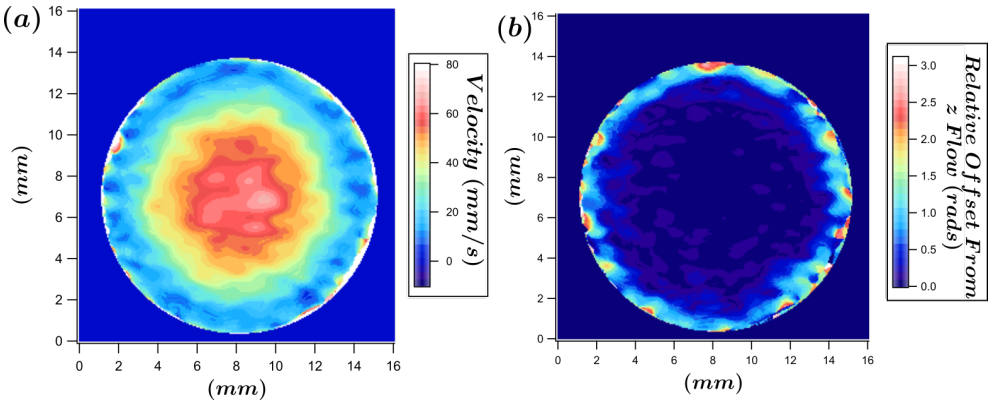


Figure 4.10: (a) The magnitude of V_x, V_y and V_z vectors displayed. Velocities in the x and y directions were acquired with the same parameters as the method described above apart from the *flow gradient strength* utilised being a factor of four higher as to capture the slower moving spins; (b) the relative size of in plane vector offset from flow in the superficial direction.

Experiments performed within the cylindrical container have shown that hp gas may be produced with a sufficient stability to allow for visualisation of parabolic laminar flow. The use of the described imaging protocol has provided robust results within the cylindrical channel and displays relatively little secondary flow near the centre of the container.

4.3.4 Flow in Steam Reformer pellets

Post initial calibration and characterisation of the technique the combined continuous flow SEOP-velocimetry technique was applied to the 4-channel, steam reformer pellets as described in Section 4.2.1. Gas was delivered to the system as described in the Figure 4.4.

Initial ^{129}Xe spectroscopy of the degassed sample indicated no materials phase peak. This suggests that while the hp ^{129}Xe may enter the pellet pore structure, the pore network is too large to induce a chemical shift of the gas phase ^{129}Xe. These results are consistent with the macro-porosity found via mercury porosimerty in Figure 4.5 and X-Ray CT in Figure 4.7.

Figure 4.11 displays a set of hp ^{129}Xe velocity maps, collected at six gas feed rates and thus, Reynolds numbers. The colour scale displays the magnitude of the flow in the superficial direction V_z. As the hyperpolariser used in this study has been designed specifically to produce hp gas at low pressures [44, 45] all measurements presented within the individual channels of the pellets are well within the laminar flow regime of $Re < 2000$ as defined by Equation 4.18.

To acquire these velocity maps, an 8 mm slice was selected within the pellet stack, so as to examine a location with a fully developed flow. These images were acquired with a 64 x 32 acquisition matrix with 16 flow encoding steps. The repetition time for each of these images is primarily determined by the rate at which the hp gases flow through the sample. As such Tr is set in each instance by empirically observing which delay provides the maximum signal intensity. Thus the amount of *fresh* hp gas container is maximised. This is due to each of the r.f. pulses in the imaging sequence fully destroying magnetisation of the hp gas. As such the acquisition time of the images in Figure 4.11 ranges from 3 mins and 16 seconds (a) to 13 mins and 04 seconds with $G_{max} = 0.231$ Tm^{-1} and Te = 6.8 ms.

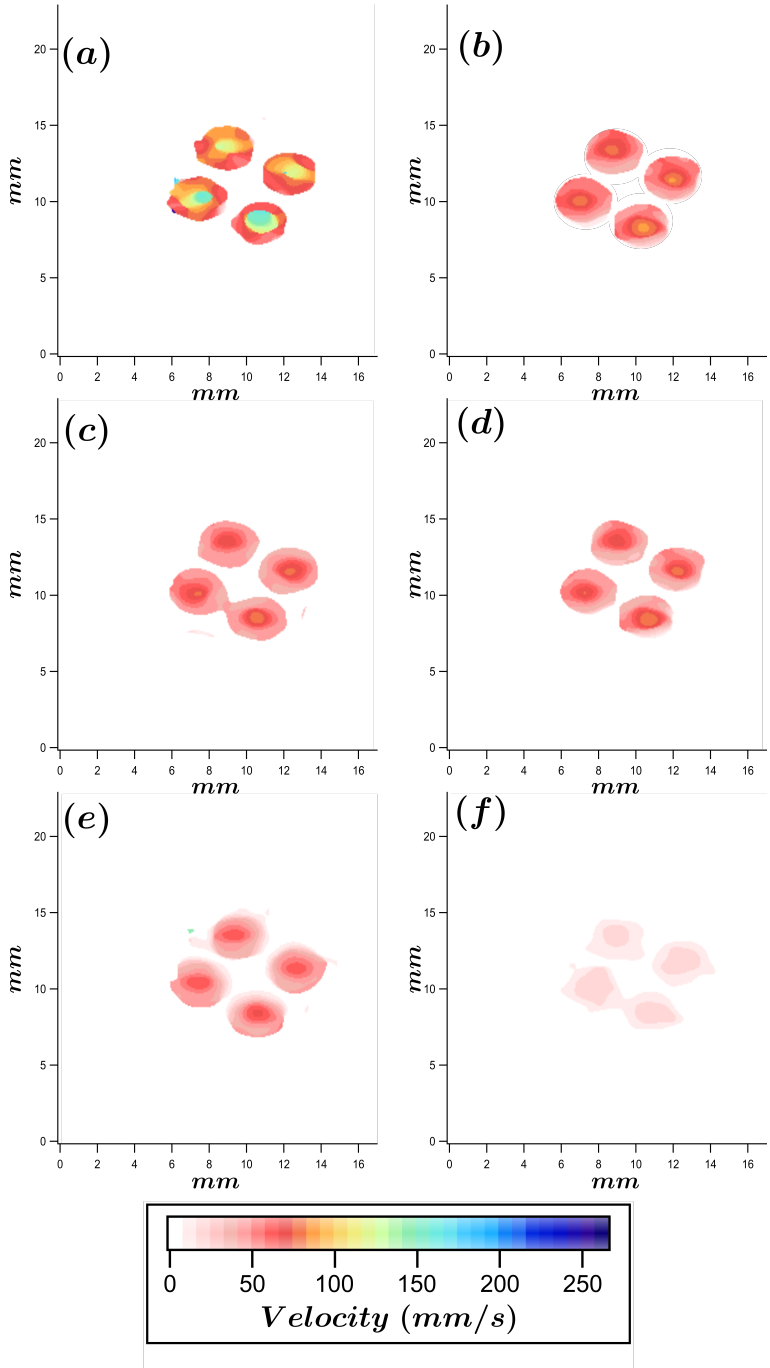


Figure 4.11: Displays six steady state velocity images collected in the X-Y plane with the velocities measured in the direction of the superficially flow, in the case the Z direction collected in the steam reforming pellets described in Figure 4.3. In all cases the acquisition matrix was 64 $\times$ 32 and zero filled to 128 $\times$ 128. A resolution of 0.3590 mm pixel^{-1} in the slice direction and 0.5332 mm pixel^{-1} in the phase direction was achieved. The slice thickness was 68 mm. Six feed rates were used in this data set. The pressure and temperature through the course of the experiment were 115 +/- 2 kPa and 21 +/- 1 ^{o}C respectively. The gas density ρ and viscosity μ under these conditions were 5.761 kg/m^3, and $2.28 \cdot 10^{-5}$ Pa s respectively. MR images; the average in channel velocity's and Re at these flow conditions are (a) 121 mm/s and 102, (b) 57 mm/s and 76, (c) 66 mm/s and 56, (d) 65 mm/s and 56, (e) 58 mm/s and 54, (f) 17 mm/s and 18. These values are based on the average axial flow from all channels and based on the parameters stated for both the ^{129}Xe and the pellets in section 4.3.3 this suggests all flow conditions are within the laminar flow regime.

Figure 4.12 displays the azimuthally averaged radial profiles of the superficial flow velocities (V_z) over the averaged four channels of each flow condition. Velocity profiles provide a clear outline of the spatial variance within the channels of the pellets. Line profiles are then collected across a given channel in each of the images. The solid lines within the images profiles are the calculated classical Poiseuille solution for the flow conditions. The dashed lines displayed are intended as a guide for the eye only.

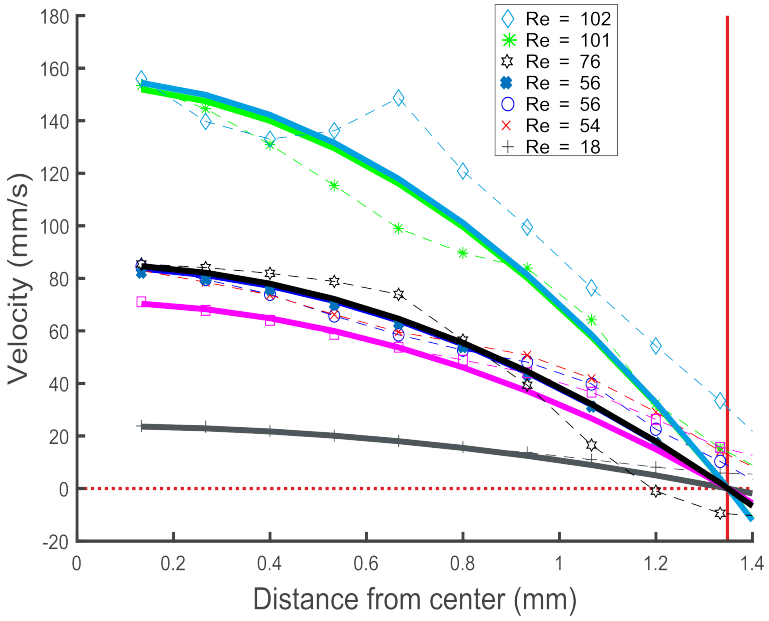


Figure 4.12: Radial velocity profile of the Z component velocity in the four channel pellets of the Re range of 18-102. Each profile is the averaged result from each of the four individual channels of the pellets. The solid lines display the theoretically predicted laminar flow profile as determined by the maximum centreline velocity in the channel. Dashed lines are intended only a guide for the reader's eye. The red *dashed* and *solid* lines are intended as a guide for the reader's eye and indicate the zero velocity and the boundary of the channel respectively.

A key feature observed in Figure 4.12 is the clear deviation these line profiles display from the no-flux boundary condition expected of laminar flow, clearly at such low Reynolds numbers the shear rate should not be sufficient with velocities at the porous walls of the channels clearly being above zero in all cases, suggesting a transverse flow into the porous

network of the pellets.

4.4 Conclusions

Improved optical pumping techniques, most notably the use of narrowed line width laser systems at close to atmospheric pressure has provided sufficient sensitivity for continuous flow SEOP velocimetry methodology to be used to study fluid dynamics inside a steam reformer pellets. Three orthogonal component velocity vectors were collected from flow of hp ^{129}Xe gas in a cylindrical pipe in the laminar regime in the X-Y plane. In this model system, good agreement is noted between the measured flow profiles and the theoretically predicted laminar flow profiles. Thus indicating the technique is suitable to utilised for measurements within more complex porous materials.

Within the steam reformer pellets, flow through and around the channel geometries can be interrogated in a quantitative fashion and radially averaged flow profiles were computed. Key results are that the deviations from Poiseuille flow in the radially averaged line profiles shown in Figure 4.12, suggesting interaction with the porous walls of the channels. This argument is lent extra weight via both X-Ray CT and mercury porosimetry measurements, which indicate the presence of large macro pores within the channels. As such it may be concluded there is significant interaction between the superficial gas flow and this pore structure.

This chapter demonstrates a methodology for rapid, accurate determination of fluid dynamics in systems relevant to chemical engineering applications and further developing hyperpolarised ^{129}Xe as a probe of porous

media. This technique provides a unique way to study non-invasively flow of gases at low pressures and temperatures allowing for gas diffusion to be probed in the transitional regime to be probed. Further this demonstration suggests promise for probing diffusion in Knudsen regime within samples with smaller pore structures, such as that of the combined SCR catalyst which will be disscussed in Chapter 5.

The methodology utilised within this chapter has been used to lay the groundwork for the investigations presented within Chapter 5 to investigate flow conditions in a more complex, hierarchical, porous media.

Bibliography

[1] P. T. Callaghan, "Rheo-NMR: nuclear magnetic resonance and the rheology of complex fluids," *Reports on Progress in Physics*, 1999.

[2] P. T. Callaghan, "Rheo-NMR and velocity imaging," *Current Opinion in Colloid and Interface Science*, vol. 11, no. 1, pp. 13–18, 2006.

[3] E. O. Fridjonsson, J. D. Seymour, G. R. Cokelet, and S. L. Codd, "Dynamic NMR microscopy measurement of the dynamics and flow partitioning of colloidal particles in a bifurcation," *Experiments in Fluids*, vol. 50, no. 5, pp. 1335–1347, 2011.

[4] M. D. Mantle, A. J. Sederman, and L. F. Gladden, "Single-and two-phase flow in fixed-bed reactors: MRI flow visualisation and lattice-Boltzmann simulations," *Chemical Engineering Science*, vol. 56, no. 2, pp. 523–529, 2001.

[5] L. F. Gladden and P. Alexander, "Applications of nuclear magnetic resonance imaging in process engineering," *Measurement Science and Technology*, vol. 7, pp. 423–435, 1999.

[6] I. V. Koptyug, R. Z. Sagdeev, L. Y. Khitrina, and V. N. Parmon, "A nuclear magnetic resonance microscopy study of mass transport in porous materials," *Appl. Magn. Reson.*, vol. 18, pp. 13–28, 2000.

[7] I. Koptyug, S. Altobelli, E. Fukushima, A. Matveev, and R. Sagdeev, "Thermally Polarized ^{1}H NMR Microimaging Studies of Liquid and Gas Flow in Monolithic Catalysts," *Journal of Magnetic Resonance*, vol. 147, pp. 36–42, 2000.

[8] I. V. Koptyug, S. A. Altobelli, E. Fukushima, A. V. Matveev, and R. Z. Sagdeev, "Thermally Polarized ^{1}H NMR Microimaging Studies of Liquid and Gas Flow in Monolithic Catalysts," *Journal of Magnetic Resonance*, vol. 147, pp. 36–42, nov 2000.

[9] I. V. Koptyug, "MRI of mass transport in porous media: Drying and sorption processes," *Progress in Nuclear Magnetic Resonance Spectroscopy*, vol. 65, pp. 1–65, 2012.

[10] L. F. Gladden and A. J. Sederman, "Recent advances in Flow MRI," *Journal of Magnetic Resonance*, vol. 229, pp. 2–11, 2013.

[11] Y.-Q. Song, "Novel NMR techniques for porous media research," *Cement and Concrete Research*, vol. 37, no. 3, pp. 325–328, 2007.

[12] R. W. Mair, G. P. Wong, D. Hoffmann, M. D. Hurlimann, S. Patz, L. M. Schwartz, and R. L. Walsworth, "Probing porous media with gas diffusion NMR.," *Physical review letters*, vol. 83, no. 16, pp. 3324–7, 1999.

[13] P. T. Callaghan, *Translational Dynamics and Magnetic Resonance: Principles of Pulsed Gradient Spin Echo NMR*. OUP Oxford, 2011.

[14] B. S. P. Capozzi F, Laghi l, *Magnetic Resonance in Food Science*. Special Publications, Cambridge: Royal Society of Chemistry, 2015.

[15] A. Gaunt, R. Morris, and M. Newton, "Magnetic Resonance Imaging: A Tool for Pork Pie Development," *Foods*, vol. 2, no. 3, pp. 393–400, 2013.

[16] S. J. Schmidt, X. Sun, J. B. Litchfield, and T. M. Eads, "Applications of magnetic resonance imaging in food science," *Critical Reviews in Food Science and Nutrition*, vol. 36, pp. 357–385, apr 1996.

[17] W. G. Schreiber, B. Eberle, S. Laukemper-Ostendorf, K. Markstaller, N. Weiler, A. Scholz, K. Bürger, C. P. Heussel, M. Thelen, and H.-u. Kauczor, "Dynamic ^{19}F-MRI of pulmonary ventilation using sulfur hexafluoride (SF_6) gas," *Magnetic Resonance in Medicine*, vol. 45, pp. 605–613, apr 2001.

[18] N. P. Ramskill, A. P. York, A. J. Sederman, and L. F. Gladden, "Magnetic resonance velocity imaging of gas flow in a diesel particulate filter," *Chemical Engineering Science*, vol. 158, pp. 490–499, feb 2017.

[19] D. A. Barskiy, A. M. Coffey, P. Nikolaou, D. M. Mikhaylov, B. M. Goodson, R. T. Branca, G. J. Lu, M. G. Shapiro, V. V. Telkki, V. V. Zhivonitko, I. V. Koptyug, O. G. Salnikov, K. V. Kovtunov, V. I. Bukhtiyarov, M. S. Rosen, M. J. Barlow, S. Safavi, I. P. Hall, L. Schröder, and E. Y. Chekmenev, "NMR Hyperpolarization Techniques of Gases," *Chemistry - A European Journal*, vol. 23, no. 4, pp. 725–751, 2017.

[20] M. Haake, A. Pines, J. A. Reimer, and R. Seydoux, "Surface-enhanced NMR using continuous-flow laser-polarized xenon," *Journal of the American Chemical Society*, vol. 119, no. 48, pp. 11711–11712, 1997.

[21] R. Seydoux, A. Pines, M. Haake, and J. A. Reimer, "NMR with a Continuously Circulating Flow of Laser-Polarized ^{129}Xe," *The Journal of Physical Chemistry B*, vol. 103, no. 22, pp. 4629–4637, 1999.

[22] E. Brunner, M. Haake, L. Kaiser, A. Pines, and J. Reimer, "Gas Flow MRI Using Circulating Laser-Polarized ^{129}Xe," *Journal of Magnetic Resonance*, vol. 138, no. 1, pp. 155–159, 1999.

[23] E. Brunner, "Applications of laser-polarized Xe-129 under continuous flow," *Magnetic Resonance in Chemistry*, vol. 37, no. Special:Issue SI, pp. Issue–S22, 1999.

[24] M. D. Mantle, A. J. Sederman, L. F. Gladden, S. Raymahasay, J. M. Winterbottom, and E. H. Stitt, "Dynamic MRI visualization of two-phase flow in a ceramic monolith," *AIChE Journal*, vol. 48, no. 4, pp. 909–912, 2002.

[25] L. F. Gladden, M. H. Lim, M. D. Mantle, A. J. Sederman, and E. H. Stitt, "MRI visualisation of two-phase flow in structured supports and trickle-bed reactors," *Catalysis Today*, vol. 79-80, pp. 203–210, 2003.

[26] L. F. Gladden and A. J. Sederman, "Magnetic Resonance Imaging and Velocity Mapping in Chemical Engineering Applications," *Annual Review of Chemical and Biomolecular Engineering*, vol. 8, no. 1, pp. 227–247, 2017.

[27] C. D. Melia, A. R. Rajabi-siahboomi, and R. W. Bowtell, "Magnetic resonance imaging of controlled release pharmaceutical dosage forms in three orthogonal directions are applied using," *Pharmaceutical Science & Technology Today*, vol. 1, no. 1, pp. 32–39, 1998.

[28] J. C. Richardson, R. W. Bowtell, K. Mäder, and C. D. Melia, "Pharmaceutical applications of magnetic resonance imaging (MRI)," *Advanced Drug Delivery Reviews*, vol. 57, no. 8, pp. 1191–1209, 2005.

[29] C. Kremser, K. Albrecht, M. Greindl, C. Wolf, P. Debbage, and A. Bernkop-Schnürch, "In vivo determination of the time and location of mucoadhesive drug delivery systems disintegration in the gastrointestinal tract," *Magnetic Resonance Imaging*, vol. 26, no. 5, pp. 638–643, 2008.

[30] P. F. De, A. E. Marble, B. J. Balcom, J. C. García, I. V. Masthikin, M. D. Thomas, and T. W. Bremner, "Embedded NMR sensors to monitor evaporable water loss caused by hydration and drying in Portland cement mortar," *Cement and Concrete Research*, vol. 39, no. 4, pp. 324–328, 2009.

[31] T. Hughes-Riley, M. I. Newton, J. W. Beau, J. Puigagut, E. Uggetti, J. Garcia, and R. H. Morris, "Advances in Clog State Monitoring for Use in Automated Reed Bed Installations," *Lakes, Reservoirs and Ponds*, vol. 8, no. 1, pp. 52–65, 2014.

[32] T. Hughes-Riley, E. R. Dye, D. Ortega Anderez, F. Hill-Casey, M. I. Newton, and R. H. Morris, "Temperature dependence of magnetic resonance probes for use as embedded sensors in constructed wetlands," *Sensors and Actuators, A: Physical*, vol. 241, pp. 19–26, 2016.

[33] F. Hill-Casey, T. Hughes-Riley, C. R. Bradley, M. I. Newton, and R. H. Morris, "Determining the clog state of constructed wetlands

using an embeddable Earth's Field Nuclear Magnetic Resonance probe," *diffusion fundamentals*, vol. 22, no. September 2014, pp. 1–7, 2014.

[34] A. J. Simpson, M. J. Simpson, and R. Soong, "Nuclear magnetic resonance spectroscopy and its key role in environmental research," *Environmental Science and Technology*, vol. 46, no. 21, pp. 11488–11496, 2012.

[35] N. P. Ramskill, L. F. Gladden, A. P. E. York, A. J. Sederman, J. Mitchell, and K. A. Hardstone, "Understanding the operation and preparation of diesel particulate filters using a multi-faceted nuclear magnetic resonance approach," *Catalysis Today*, vol. 216, pp. 104–110, 2013.

[36] S. Lowell and J. E. Shields, "Theory of mercury porosimetry hysteresis," *Powder Technology*, vol. 38, no. 2, pp. 121–124, 1984.

[37] S. P. Rigby and K. J. Edler, "The Influence of Mercury Contact Angle, Surface Tension, and Retraction Mechanism on the Interpretation of Mercury Porosimetry Data," *Journal of Colloid and Interface Science*, vol. 250, no. 1, pp. 175–190, 2002.

[38] E. W. Washburn, "The dynamics of capillary flow," *Physical Review*, vol. 17, no. 3, pp. 273–283, 1921.

[39] S. P. Rigby, R. S. Fletcher, and S. N. Riley, "Characterisation of porous solids using integrated nitrogen sorption and mercury porosimetry," *Chemical Engineering Science*, vol. 59, no. 1, pp. 41–51, 2004.

[40] I. Hitchcock, *Pore structure characterisation : The challenge to understand heterogeneous catalysts and fuel cells*. PhD thesis, University of Bath, 2011.

[41] I. Hitchcock, M. Lunel, S. Bakalis, R. S. Fletcher, E. M. Holt, and S. P. Rigby, "Improving sensitivity and accuracy of pore structural characterisation using scanning curves in integrated gas sorption and mercury porosimetry experiments," *Journal of Colloid and Interface Science*, vol. 417, pp. 88–99, 2014.

[42] A. A. Liabastre and C. Orr, "An evaluation of pore structure by mercury penetration," *Journal of Colloid And Interface Science*, vol. 64, no. 1, pp. 1–18, 1978.

[43] J. Kloubek, "Hysteresis in porosimetry," *Powder Technology*, vol. 29, no. 1, pp. 63–73, 1981.

[44] J. S. Six, T. Hughes-Riley, K. F. Stupic, G. E. Pavlovskaya, and T. Meersmann, "Pathway to Cryogen Free Production of Hyperpolarized Krypton-83 and Xenon-129," *PLoS ONE*, vol. 7, no. 11, 2012.

[45] T. Hughes-Riley, J. S. Six, D. M. L. Lilburn, K. F. Stupic, A. C. Dorkes, D. E. Shaw, G. E. Pavlovskaya, and T. Meersmann, "Cryogenics free production of hyperpolarized ^{129}Xe and ^{83}Kr for biomedical MRI applications," *Journal of Magnetic Resonance*, vol. 237, pp. 23–33, 2013.

Chapter 5

Hyperpolarised Xenon MRI Studies of Structure - Transport Relationships in Hierarchical Porous Media

The work presented within this chapter is currently being prepared for publication in a high impact chemical engineering journal with the title: *Hyperpolarised Xenon MRI Studies of Structure-Transport Relationships in Hierarchical Porous Media* with Mr Fraser Hill-Casey, Prof. Thomas Meersmann and Prof. Sean Rigby writing the paper. Further, iterations of this work has been presented in the poster sessions of the Johnson Matthey Academic Conference (JMAC) 2017, 2016 and 2015 by Mr Hill-Casey.

Mr Hill-Casey designed the NMR and MRI experimental protocols, collected the Relaxation data, the images, the drying curve data and analysed the data. Mr Hill-Casey and Mr Alan Dorkes designed and fabricated the sample containers and gas delivery systems. Dr Martin Corfield performed the X-ray CT imaging to Mr Hill-Casey's specifications. Dr Iain Hitchcock performed the Mercury Porosimetry experiments and analysis with Professor Rigby. Mr Hill-Casey and Dr Galina Pavloskaya

performed the pulse programming for the sequences used in this study. Dr Pavloskaya, Prof. Meersmann and Prof. Rigby provided assistance in interpretation of results and guidance in experimental design. Dr Hitchcock, Dr Thomas Hotchkiss and Dr Katherine Hardstone from Johnson Matthey PLC provided the Combined Selective Catalytic Reduction-Filtration Monolith sample.

5.1 Motivation

Catalysed diesel particulate filter (DPF) monoliths are a class of hierarchical porous solid that possess both ordered and disordered levels in the hierarchy. The structural characterisation of disordered porous solids and establishing the structure-transport relationship for such materials is an on-going challenge. Hyperpolarised (hp) gas magnetic resonance imaging (MRI) is a novel experimental technique that can elucidate the structure-transport relationship for such materials even in the low density Knudsen regime not accessible with other methods. In this study the structures of the levels in the hierarchy in catalysed DPFs based on monoliths have been characterised by MRI, and complementary methods including mercury porosimetry and computerised X-ray tomography (CXT). The contribution from each level, to mass transport, has been selectively established using hp gas-phase imaging of gas dispersion within DPF monoliths at variable water saturation, since it has been shown, using the MR methods, that these levels dry out in a progressive fashion. It has been seen that low pressure gas phase mass transport is dominated by the wall intersection regions of the monolith that have high macroporosity. The monolith wall regions themselves make a relatively small contribution to mass transport even when open due to the higher resis-

tance from the micro- and meso-porous washcoat layer predominantly localised to those zones. Complementary hp gas phase MRI velocimetry has also shown that the monolith wall intersections dominate mass transport. This work has shown that, unlike with past techniques, the gas phase mass transport can be directly imaged and the relative contributions from different levels in the structural hierarchy to the overall flux can be established with hp gas-phase MRI.

5.2 Introductions

Recently, hierarchical porous solids have become of particular interest for various applications, such as supercapacitors, PEM fuel cells, tissue engineering scaffolds, drug delivery devices, and heterogeneous catalysts [1–6]. One particular class of hierarchical porous solid is the catalysed diesel particulate filter (DPF) which reduces gas pollutant emissions from vehicle exhausts by selective catalytic reduction (SCR) and also filters out particulates. Catalysed DPFs typically consist of a catalytically-active washcoat applied to an inert monolithic support. The monolith comprises macroscopic-scale channels with macroporous ($>$ 50 nm) walls. The washcoat typically comprises microporous ($<$ 2 nm) zeolite crystallites and a mesoporous (2 $<$ 50 nm) alumina binder. Hence, the catalysed DPF is a hierarchical system with void spaces on four different levels.

Different hierarchical materials, and different levels in the porosity hierarchy within the same material, can possess differing levels of order, depending upon the synthesis method(s) of the materials. With catalysed DPFs the catalyst is applied as a washcoat, and then the system

is dried. Both the application and drying process may result in a heterogeneous distribution of washcoat within the amorphous macroporous wall structure of the monolith. Further, the amorphous nature of the washcoat binder means disorder at the mesoporous length-scale. Hence, the catalysed DPF system consists of a mixture of ordered (macroscopic channels and zeolite micropores) and disordered (washcoat distribution and binder mesopore network) structures.

The underlying structure of a hierarchical material affects its performance in application, often through the impact that structure has on mass transfer rates in the material. In operation of a catalysed DPF exhaust gas from the engine enters the inlet channels. Due to the impermeable plugs at the opposite end of these channels, the gas flow is forced to pass through the macroporous (and therefore permeable) walls, separating the macroscopic channels, where the meso-/micro-porous washcoat is located. The porous wall acts like a filter such that the particulates in the exhaust gas are deposited within the inlet channel, and potential gaseous pollutants are reacted away as the gas stream passes over the catalyst within the washcoat, allowing for clean gas to emerge from the outlet channels. However, for the catalytic clean-up of the exhaust gases to happen the gas stream must be routed through the pores containing the catalyst. The heterogeneity and disorder present in the washcoat spatial distribution and mesopore network architecture provide opportunities for both bypassing of the catalyst and creating resistance to flow, which would reduce overall performance in reducing emissions. Hence, it is critical to know how the individual levels in the hierarchical structure of the catalysed DPF affect mass transport. Previous work [7] has used mercury entrapped, following intrusion to different pressures, to progressively block off different ranges of pore sizes within a macro/meso-porous

catalyst pellet, and then their relative importance to mass transport was assessed via comparisons of the uptake of nitrogen gas before and after their loss. However, in order to prevent contamination with mercury vapour it must be frozen in place (mpt -38.8 ^{o}C), and thus the method is unsuitable for studying structure-transport relationships at other conditions. Further only the spatial distribution of the blocked pores was obtained (by computerised X-ray tomography (CXT) of the mercury) and not the spatial variation in mass transport rates.

Mass transport processes within catalysed DPFs, in particular, have been studied both by computer simulation and empirical means. The issue with the simulation is that it is necessary to understand the key aspects of the structure of the catalysed DPF that need to be incorporated into the computer model before the model delivers information on the flow, but that information on the flow will be inaccurate if the representation of the structure is too in error or incomplete. The empirical methods that can deliver the most detailed information on (structure and) mass transport are the imaging methods. Magnetic resonance imaging (MRI) methods have been used to study mass transport in monoliths and catalysed DPFs. A number of published works have obtained velocity-weighted images of flows in alumina monoliths with different channel geometries and have looked at the flow of thermally-polarised hydrocarbon gases (ethyne, butane and propane) [8–11]. Previous workers [12] studied drying processes in monoliths and liquid flow velocity in monolith channels using MRI. However, catalysed DPFs operate with the fluid flow largely in gas phase, and thus previous work [13] studied the flow of gaseous SF_6 within monolith channels, and considered the uniformity of permeation of the gas into the walls along the channel. However, in order to obtain sufficient NMR signal to image the gaseous SF_6 the system had

to be operated at high pressure so the gas density was high and thus meant the pore diffusion mechanism was molecular. In contrast, an *in operando* system requires gas pressures and density's at approximately atmospheric levels, as such diffusion can occur by the different Knudsen mechanism, which has much greater sensitivity to pore structure [14]. Further, the transport of the gas through the walls was only studied in an indirect way.

The high NMR signal intensity associated with hyperpolarized (hp) noble gases [15, 16] enables MRI of the gas phase at conditions of the Knudsen regime [17]. Beyond spatial encoding, pulsed field gradients (PFGs) can be used to extract temporally-resolved low pressure gas transport data on the transport of gases in porous materials using hp noble gas NMR spectroscopy [18–20] and MRI [17, 21–23]. Alternatively, remote-detection or time-of-flight MRI methods can be employed to explore gas flow within porous media such as silica aerogel [24] or for the characterisation of micro-fluidic reactors [25]. The latter study used para-hydrogen induced polarization instead of hp noble gases that allows monitoring of reactions. Hp ^{129}Xe time of flight dispersion can be used to MR image spatial heterogeneity [24]. In particular, the methodology provides insights into reactors that cannot be detected directly, such as if it takes place within the confinement of a conducting container material that does not allow for radiofrequency signals to penetrate.

However, the remote detection methodology does not allow for a directly detected dimension (i.e. frequency encoding of one of the spatial dimensions) and therefore may lead to prolonged experimental times, although this effect may be offset by more efficient detection methods using small radiofrequency coils [26]. In this work, the mass transport properties of

each region of the sample will be measured directly to avoid such complications.

It is the purpose of this work to utilise hp ^{129}Xe techniques to directly study gas phase mass transport at low pressure more akin to actual working conditions of catalysed DPF operation, which involve Knudsen regime pore diffusion. The other key aim is to assess the relative importance of different levels of the pore size hierarchy, and of structural heterogeneity, to mass transport. The relationship between structure and mass transport will be studied by progressively opening-up different levels in the pore size hierarchy for mass transport by progressive drying of an initially fully-saturated sample. NMR methods will be used to demonstrate that the drying process in the DPF occurs in a hierarchical fashion, with progressively smaller pores drying out with decreasing liquid saturation. MRI methods will also be used to obtain information on the spatial distribution of locally-averaged porosity and pore size. The findings from the NMR methods will be validated using mercury porosimetry and computerised X-ray tomography (CXT).

5.3 Experimental

5.3.1 Computerised X-ray Tomography

X-ray tomography images were obtained of a section of the Combined SCR filtration monolith. Using a coring tool, an approximately 2 cm diameter, 7 cm length core was taken from the monolith. The cutting procedure generated dust so an air gun was used to remove any excess powdered sample from the monolith channels after cutting. The sample was placed in an XRADIA Versa XRM - 500 X-Ray CT apparatus and

images were acquired with a resolution of 2.99 μm/pixel.

5.3.2 Mercury Porosimetry

Since mercury does not wet most substances, it will not spontaneously penetrate pores by capillary action. Therefore, an external pressure is needed to force the mercury to enter the pore structure, with the equilibrium pressure required being inversely proportional to the size of the pores. The radius of the pores (r) may be determined from the following semi-empirical equation:

$$r = \frac{-A + \sqrt{A^2 - 2B\,P_{hg}}}{P_{hg}} \tag{5.1}$$

where P_{hg} is the applied pressure and A and B are constants determined by the material. Equation 5.1 is empirical in origin and thus of limited scope and hence, is only applicable in a limited range of applications. Further the the size obyained from Equation 5.1 contains experimental error of approximately 4-5 %. For further discussion on mercury porosimetry the reader is directed to previous work by Rigby [27], Kloubek [28] and the discussion of the technique presented in Chapter 4.

5.3.3 Relaxometry

In order to probe, non-destructively the pore structure of the SCR monolith, the spin-lattice (T_1) and spin-spin (T_2) relaxation of the NMR signal were utilised to probe adsorbed ganglia sizes. The value of T_2 or T_1 may be converted to a surface area to volume ratio (S/V) by the adoption of a relaxation model. For a liquid imbibed within a confined space,

the relaxation rate decreases with decreasing S/V due to interactions, and reduced motion, within a thin surface-affected layer. Diffusional exchange between this interfacial layer and the remainder of the liquid (i.e. in the core of the pore) leads to an increased relaxation rate observed for the bulk liquid. For the systems studied in the this work, the liquid ganglia are several orders of magnitude smaller than the rms displacement of the probe water molecules during the course of the experiment, such that the 'two-fraction fast exchange model' [29, 30] can be used to calculate the relaxation rate. The observed relaxation rate $1/\mathrm{T}_{1,obs}$ is a weighted average of both contributions from the bulk liquid and pore surface:

$$\frac{1}{\mathrm{T}_{1,obs}} = \frac{1-P_s}{\mathrm{T}_{1,B}} + \frac{P_s}{\mathrm{T}_{1,S}}, \tag{5.2}$$

where $\mathrm{T}_{1,S}$ and $\mathrm{T}_{1,B}$ refer to the relaxation in the surface layer and bulk fluid, respectively. $\mathrm{T}_{1,obs}$ is the observed spin-lattice relaxation. P_s represents the proportion of spins absorbed in the surface layer and is described by:

$$P_s = \lambda \frac{S}{V}, \tag{5.3}$$

where λ is the thickness of the surface-affected layer, and S/V is the surface area to volume ratio. Substitution of Equation 5.3 into Equation 5.2 gives:

$$\frac{1}{\mathrm{T}_{1,obs}} = \left(1 - \lambda \frac{S}{V}\right) \frac{1}{\mathrm{T}_{1,B}} + \left(1 - \lambda \frac{S}{V}\right) \frac{1}{\mathrm{T}_{1,S}}. \tag{5.4}$$

In general $\mathrm{T}_{1,B} >> \mathrm{T}_{1,S}$ and thus S/V is given, approximately, by:

$$\frac{S}{V} = \frac{\mathrm{T}_{1,S}}{\lambda}\frac{1}{\mathrm{T}_1}. \tag{5.5}$$

Equivalent expressions to Equation 5.4 and 5.5 can be obtained for spin-spin relaxation. Further, for a completely saturated cylindrical pore, S/V would be equal to $2/r$, where r is the radius. Therefore, relaxation time is then proportional to the characteristic pore size.

It must be noted that typically when performing pore sizing by relaxometry, T_2 is preferred to T_1 due to the given volume the molecule explores during the characteristic time-scale of the relaxometry experiment. This is due to the spin-spin relaxation experiments typically allowing for less motional averaging effects. However, spin-lattice relaxation is particularly useful due its independence of any present internal magnetic field gradients which may occur at boundaries such as solid-liquid interfaces under the influence of a magnetic field[31]. Additional, for hp ^{129}Xe experiments it must be noted that T_1 is an obvious choice being as the probe is hyperpolarised and diffusive effects cause complications to the measurements of T_2 gas phase. Within this work both approaches have been utilised to provide a comprehensive interrogation of the pore structures present in the monolith.

5.3.4 NMR and MRI studies of drying.

Determination of T_1 at variable sample saturation for the two nuclei used in the studies was performed by initially drying the SCR monolith in a vacuum oven for 12 hours at 110 ^{o}C. The monolith segment was then saturated with either distilled water for ^{129}Xe (BOC gas, UK) and ^{1}H experiments, or deuterium oxide (sigma Aldrich, United Kingdom), for

Table 5.1: Relevant properties of the combined SCR filtration monolith channels used within this work.

Combined SCR-Filtration Monolith Properties	
Inlet Channel Diameter (mm)	0.8
Outlet Channel Length (mm)	1.2
Wall Thickness (mm)	0.2

15 minutes so as to saturate the pore structure.

The monolith segment (diameter 14.4 mm, length 25 mm) with generic channel dimensions as stated in Table 5.1 was placed inside a custom made acrylic container (i.d. 14.5 mm, length 25 mm) which was designed to minimise the empty volume (see Figure 5.1). This consideration was specifically important to the ^{129}Xe studies, since any volume not filled by the monolith segment would lead to a pool of xenon with an extremely long relaxation time. This would allow for exchange between xenon in contact with the sample and the pool of free slow-relaxing xenon.

Variable saturation of the SCR monolith was achieved by applying a vacuum to the sample between relaxation experiments to remove the moisture from the sample. In order to determine the free pore volume, the sample was removed from the NMR magnet and weighed to determine the change in moisture content between relaxation experiments.

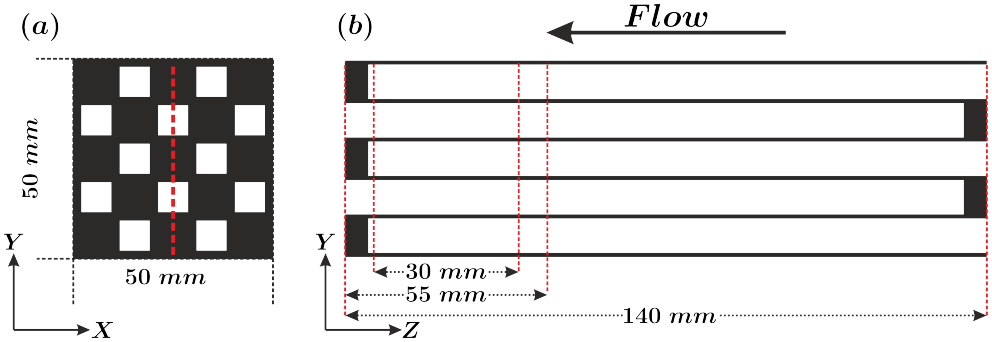


Figure 5.1: Schematic of the combined selective catalytic reduction monolith used in this work, illustrating a top-down view (a) and a longitudinal cross section (b); the location of the 55 mm indicates the length of the core used in this work with the position of the 30 mm (length) RF coil indicated showing where data was acquired, and the spatial dimensions of the monolith sample are also shown.

Measurements of Proton and Deuteron T_1 Relaxation

The changes in the T_1 of the ^1H or ^2H nuclei within a monolith segment, saturated either in ordinary or heavy water, were monitored over the drying of the monolith segment by use of a standard T_1 inversion recovery sequence [32]. Data were acquired using 16 inversion pulses, and then the recovery data was fitted to a bi-exponential model for low free pore volumes:

$$\frac{I}{I_0} = 1 - 2\left(A\, exp\left(-\frac{\tau}{T_{1A}}\right) + B\, exp\left(-\frac{\tau}{T_{1B}}\right)\right), \tag{5.6}$$

where A and B represent the given signal intensity that is proportional to the amount of the nuclei in the given local environment. Each fitted component indicated a separate population of nuclei relating to a given pore size.

T_{1A} and T_{1B} represent the relaxation time constants for the two pools of relaxation. It is noted that, during the drying process for both types of nuclei, the two pools of relaxation rate behaviour described will deplete at different rates, such that eventually this will result in a single remaining pool. In which case, the relaxation data was fitted to the expression:

$$\frac{I}{I_0} = 1 - 2 \cdot \exp\left(-\frac{\tau}{T_1}\right). \tag{5.7}$$

Deuterium spin-density imaging of SCR monolith

Deuteron spin density images were acquired at a range of free pore volumes with a standard gradient echo sequence, and the data analysed

using an *in-house* MATLAB toolbox. Raw 128 × 128 image acquisition matrices were apodized using a sine bell squared filter and zero filled to 256 × 256 before image reconstruction using a two dimensional Fourier transform. The in-plane resolution for these images was 0.12 mm × 0.12 mm in the read and phase directions.

Measurements of deuteron spin-spin relaxation in a fully saturated monolith

The spatial distribution of T_2 relaxation for deuterons within a fully saturated monolith was obtained using a spin-echo imaging sequence. Eight separate images were acquired with a variable echo time. Images were processed using an in-house MATLAB toolbox. Raw 128 × 128 image acquisition matrices were apodized using a sine bell squared filter and zero filled to 256 × 256 before image reconstruction using a two-dimensional Fourier transform. The in-plane resolution for these images were 0.12 mm × 0.12 mm in the read and phase directions. Subsequently each voxel was fitted to an exponential decay as given in Equation 5.7 in order to obtain the resulting T_2 map within the monolith segment. Histogram analysis was performed with IgorPro 7.0.5 (Wavemetrics, USA) using build-in Multi- Peak fitting 1.4 packages.

Measurements of xenon-129 T_1 relaxation

Longitudinal relaxation measurements of gas phase ^{129}Xe in the presence of the combined SCR monolith were determined by using a pulse sequence consisting of 64 small flip angle pulses (constant 12^o) spaced evenly with a time delay τ to collect a spectra at each time interval of the sequence. The sequence was initialised before delivery of gas to the NMR probe

containing the SCR monolith as to account for discrepancies in delivery time. So as to account for the aforementioned discrepancy only spectra after the maximum integrated intensity were processed. To extract T_1 values spectra were fit to the following equation;

$$\ln \frac{I_n}{I_{n=0}} = \left(\ln(\cos(\theta)) - \frac{\tau}{T_1} \right) \cdot n, \tag{5.8}$$

where $S_{(n)}$the signal is collected at spectra number n, $s_{(n=0)}$ is the spectra with the maximum intensity, n is the spectra number and $\cos(\theta)$ is the term accounting for the polarisation destruction from the applied RF pulse. This fitting was only applied to the linear region of the decay in each experiments [33–35]. Further spectral information was acquired at each drying instance by the application of a 90 degree pulse after gas delivery.

5.3.5 Hyperpolarised ^{129}Xe gas production and delivery.

Hyperpolarised ^{129}Xe was produced though Spin Exchange Optical Pumping (SEOP) (Figure 5.2) by a custom-built instrument described in detail elsewhere [15, 16]. Two methods are used for hp ^{129}Xe production within this work;

First, for relaxation experiments a 5 % Xe (natural abundance): 95 % N_2 SEOP fuel mixture was polarised in *batch mode*. The SEOP cell pressure was $\sim$ 158 kPa and spin polarisation was allowed to build up over 6 mins before delivering the now hp gas to the evacuated sample by pressure equalisation resulting in a detection cell pressure of 115 kPa. The nuclear spin polarisation for the batch mode was approximately 48 %

spin polarisation.However, since the hp ^{129}Xe was diluted with buffer gas from the SEOP process, a better measure of the expected signal intensity is the apparent polarization $P_{app} = P_x\,([\mathrm{Xe}]/[\mathrm{N_2}])$ that takes the dilution into account [15, 16]. For the mixture of 5 % Xe in 95 % N_2 that was used the $P_{app} = 2.4$ %.

Second, for the mass transport imaging measurements, hp ^{129}Xe was produced in continuous flow mode. The major difference with the first method is that the outlet of the SEOP cell is opened, and the inlet also remains open, thus providing a constant flow of gas which is polarised *in stream* [36]. The flow of gas in this mode was controlled using two needle valves, located before and after the sample. The spin polarisation in this mode was highly dependent on the time of flight that the ^{129}Xe remains in the SEOP apparatus. In the continuous flow mode a 25 % Xe (natural abundance) 75 % N_2 was used to provide a spin polarisation of $\sim$ 3.2 % and an apparent polarisation of $\sim$ 0.8 % from a cell residency time of $\sim$ 5 seconds and a steady state flow is allowed to form before imaging experiments are begun.

5.3.6 NMR and MRI experiments

A 9.4 T Burker Avance III Microimaging system (Bruker, Germany) was used for all experiments. ^{129}Xe experiments utilise a home build 15 mm saddle coil tuned to ^{129}Xe resonance frequency of 110.69 MHz were used for excitation and detection for all Xenon experiments For ^{1}H and ^{2}H experiments a two separate single channel 25 mm commercial probes (Bruker, Germany) tuned to 400.18 MHz and 61.43 MHz respectively were used for excitation and detection.

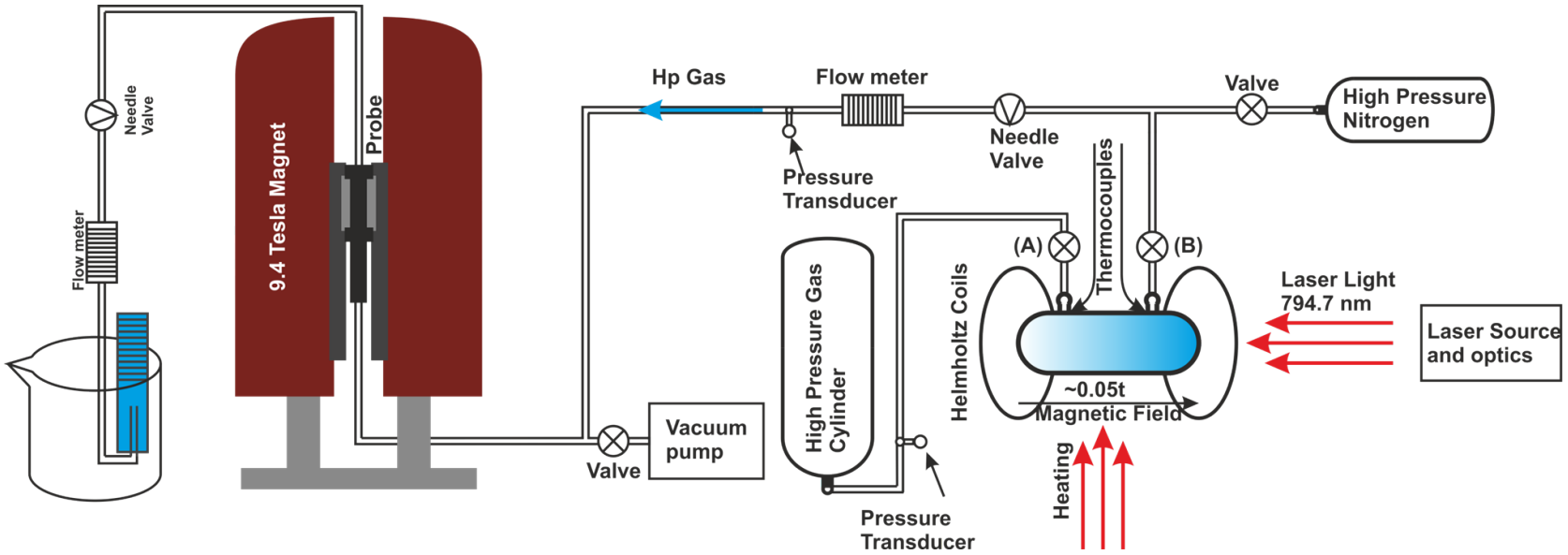


Figure 5.2: The experimental apparatus used for both **Batch Mode** and **Continuous Flow** Spin Exchange Optical pumping; The delivery path of the hp gas to the high field magnet and major components of the experimental apparatus are outlined. **Batch Mode** gas is delivered to the SEOP cell valves (A) and (B) are closed, the gas mix is then allowed to polarize for 6 minutes before being vacuum shuttled to the sample container. By contrast **Continuous flow** SEOP the gas mixture is delivered to the cell and both valves (A) and (B) remain open, allowing the gas to flow from the high pressure cylinder though the SEOP cell and to the sample. The pressure of the SEOP cell is controlled by use of a pressure regulator at the high pressure gas cylinder, the needle valves allow for fine adjustment of the flow rate through the sample container. High pressure Nitrogen and a Vacuum pump are used to control the drying of the sample.

5.3.7 MRI: Principles of MR velocimetry

Beyond simple spin density measurements, MRI may also be made sensitive to motional effects in samples and may be used to probe such characteristics as dispersion, diffusion, and velocity. Within this work MRI velocimetry was performed via the phase shift method [37–40] as described by the pulse sequence diagram given in Figure 5.3. A full treatment of the concepts of phase-shift MRI velocimetry is given in Chapter 4.

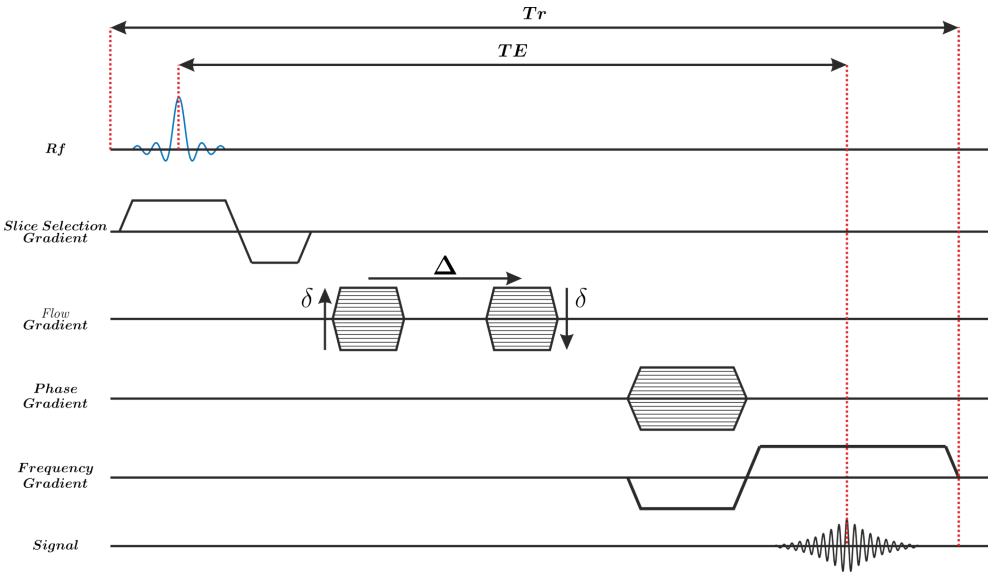


Figure 5.3: Timing diagram for a slice selective, gradient echo imaging sequence with the addition of a velocity encoding module; The first flow encoding gradient pulse of duration δ serves to encode the initial position of the spins. Molecular displacement during the delay Δ serves to both attenuate the amplitude of the collected signal (via stochastic motion) and imparts a net phase shift on the spins (via coherent motion). A second, equal and opposite flow encoding gradient is applied to refocus the magnetization. Since the magnetization is stored in the direction of flow during time Δ the primary dephasing effect is due to longitudinal relaxation. With the T_1 of hp ^{129}Xe being sufficiently long within the system of interest, the measurement of velocities is only limited by spins flowing out of the detection region.

5.3.8 MRI studies of mass transport

Sample preparation

A segment of SCR monolith (diameter 14.2 mm, length 65 mm) with generic channel dimensions as stated in Table 5.1 was dried for 12 hours in a vacuum oven at 110 ^{o}C, and then saturated in distilled water for 15 minutes. After saturation the sides and bottom of the monolith segment were wrapped in parafilm to ensure gas flow must leave only through the open channels. Gas was delivered to the central, dead-end channel by use of a 1/16' PFA tubing (Swagelok, Ohio U.S.A) modified to fit snugly within the channel. The modified PFA tube penetrated 6 mm into the monolith; as such the sample assembly was positioned within the aforementioned 15 mm homebuilt ^{129}Xe coil so to ensure that the inlet tube would not interfere with measurement. The drying of the SCR monolith, in this series of experiments, was performed, so as to conserve xenon between the experiments, by switching the gas flow to molecular nitrogen (N_2 5.0 grade) flowing at the same rate as that of the hp fuel mixture.

Spatial dispersion experiments

Two-dimensional, slice-selective, axial spin density images of steady state flow of dry hp ^{129}Xe were acquired by use of a simple gradient echo sequence [37]. The hp gas flowed through a single, closed end channel (see Figure 5.1) as described above at a rate of 250 mm^3/s at 21 ^{o}C.

Since the MR active gas in question is hyperpolarised in nature, each $\pi/2$ pulse of the imaging sequence will fully destroy the magnetisation of the gas within the rf coil. Therefore, the dominant effect on signal

replenishment is the rate at which the freshly polarised gas enters the detection region rather than the size of T_1. Thus, by altering the inter-pulse or recycle delay of the imaging sequence, we may investigate the process of dispersive mass transport across the monolith segment, as a longer inter-pulse delay would allow the gas to spread further throughout the structure before destruction of the magnetisation than a shorter one. Further, as the monolith dried, and, thus, the free pore volume fraction increased, the hp gas may transverse new pathways within the pore structure, and also potentially interacted with the paramagnetic components within the wash coat in the pore structure.

MR Velocimetry experiments

Gas velocity profiles were localised and a single non-slice selective image with a FOV = 17 cm × 23 cm, an imaging matrix of 64 × 32 (pixel resolution of 359 μm × 533 μm), Tr = 2000 ms and TE = 10 ms. It should be noted that the repetition time of the experiment was optimised so as to allow for a fresh gas load to be delivered to the sample after the magnetization had been destroyed by the preceding step and was not dependent upon the T_1 relaxation of the hp ^{129}Xe. Spatial resolution was achieved using shielded gradient coils providing a maximum gradient strength of 154 G cm^{-1}. Velocities were acquired in the z-direction and encoding parameters were as follows: $\Delta = 5$ ms, $\delta = 0.5$ ms and $G = 0.14$ Tm^{-1}. The image was acquired with 16 flow encoding increments and 4 scans were used to obtain a sufficient signal-to-noise ratio. The experiment time was 17 minutes and 02 seconds. x- and y- components of velocity were acquired in separate experiments by altering the spatial direction in which the flow encoding was applied. The Reynolds number of these given conditions are calculated as defined by Equation 5.9;

$$Re = \frac{\rho V_{av} D}{\mu}, \tag{5.9}$$

where ρ is the fluid density, V_{av} is the velocity in the direction of the superficial flow, μ is the fluid dynamic viscosity and D is the characteristic length scale of the channel.

5.4 Results

5.4.1 Computerised X-ray Tomography

Figure 5.4 shows a reconstructed cross-section image of the plane perpendicular to the axis of the square channels for a typical section of the SCR monolith used in this study. The images were obtained using an XRADIA Versa XRM-500 x-ray CT (Zeiss, Germany) with an in-plane resolution of 2.99 μm/pixel. Within the image, the bright white pixels correspond to the monolith walls, while the mid-grey pixels contained within the white regions are washcoat located within the monolith pores, and the dark-grey/black regions are empty pores and channels. The image of this purpose-made sample for this study shows that the washcoat material was more concentrated in the channel walls, and the wall intersections/corners are generally more porous, and were relatively devoid of washcoat material.

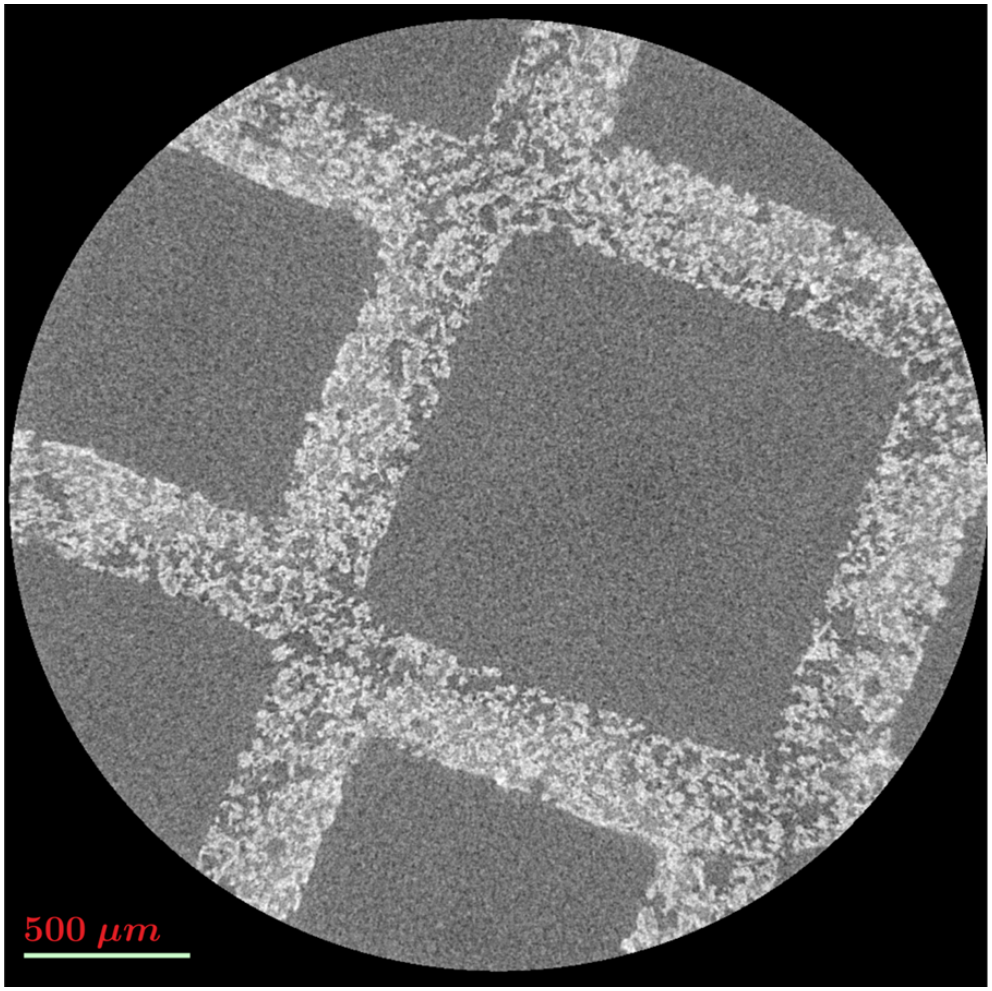


Figure 5.4: Reconstructed cross-section perpendicular to channels of washcoated monolith obtained from CXT. The bright white pixels are the monolith walls, the mid-grey pixels contained within the white regions are washcoat within the monolith pores, and the dark-grey/black regions are pores and channels. The scale bar corresponds to 500 mm. Resolution is 2.99 $\mu m/pixel$ with a 1015 x 1015 acquisition matrix.

5.4.2 Mercury porosimetry

Figure 5.5 shows the mercury intrusion curve for the washcoated monolith following analysis of the raw data using the Kloubek correlations [28]. The initial slope of the porosimetry curve may be intrusion into large-scale surface roughness on the surface of the monolith. The main intrusion curve proper suggests three key pore size modes occurring at sizes $\sim 10^4$ nm (=10 μm), ~ 500 nm, and ~ 5 nm. These data probably

correlate with three levels of porosity in the hierarchical structure of the sample, namely, (1) empty macroporous monolith pores and monolith pores partially filled with washcoat; (2) macroporosity between zeolite crystallites in washcoat, and, third, mesopores within the binder of the washcoat material.

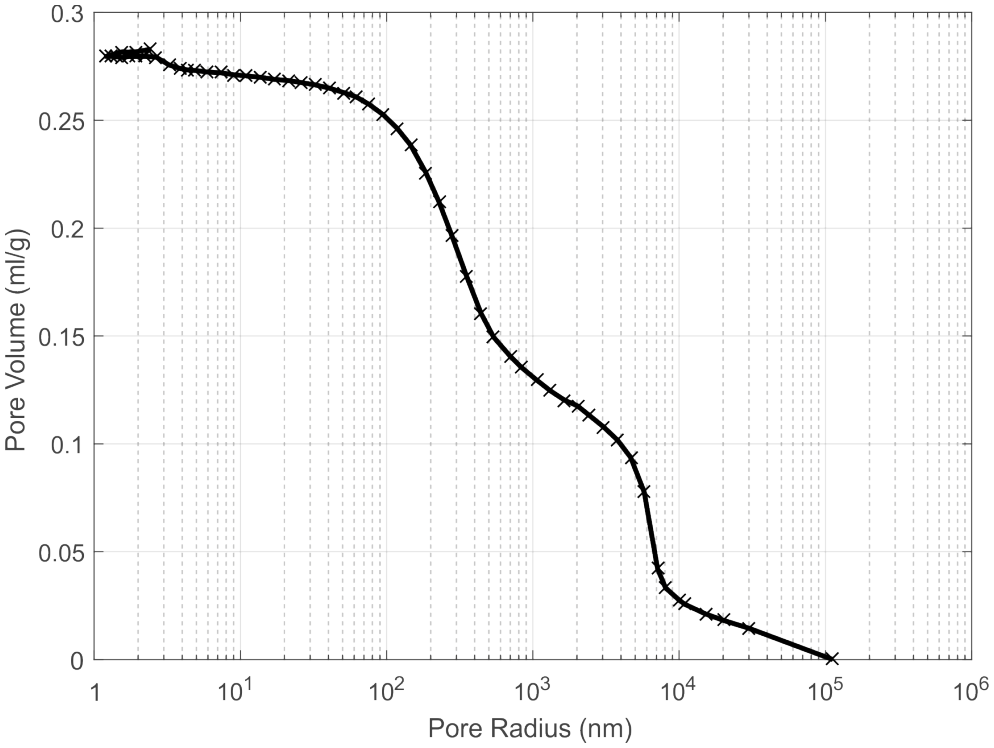


Figure 5.5: Mercury intrusion curve for Cu-free washcoated monolith analysed using Kloubek (1981) correlations [28] displaying three key intrusion modes.

5.4.3 NMR relaxometry studies of drying

Figures 5.6 (a) and (b) show the fitted spin-lattice relaxation time components for ^1H in H_2O, and ^2H in D_2O, respectively, as a function of the free pore volume for variable saturation states of a monolith during a drying experiment (i.e. T_1 relaxation as a function of water contents in the monolith walls). For both ^1H in H_2O, and ^2H in D_2O, at low and intermediate free pore volumes, there were both a slow and a fast component in the observed relaxation characterized by the long (T_1^{slow})

and a short (T_1^{fast}) relaxation time, respectively. At high free pore volume (low saturation) there is a single component (i.e. mono-exponential decay with a single time constant T_1 at a free pore volume $>$ 55 %). Such behaviour is indicated in elucidated in Figure 5.7 (a) and (b) which show raw inversion recovery data for ^1H in H_2O, and ^2H in D_2O at a low free pore volume and at high free pore volume. The measured ^1H T_1 at high free pore volume data is similar to the short T_1^{fast} component at lower free pore volume, indicating that both originate from regions with similar pore sizes. This suggests that, at high saturation, there are initially two regions of water with vastly different pore dimensions and with no substantial exchange between these regions through diffusion within the timescale of the measurement. It is also apparent from Figure 5.6 (a) that regions associated with the long T_1^{slow} component dry out first. According to the Brownstein-Tarr model (Equation 5.4), T_1^{slow} is expected for regions with larger pore sizes, while T_1^{fast} will originate from areas with more confined space in the porous hierarchy. Furthermore, at free pore fractions less than 25 % the times T_1^{slow} appear to substantially increase, leading to a steep slope in the T_1^{slow} curve. Since, from the Brownstein-Tarr relation, a long T_1 would be associated with larger pores, this suggests that the largest pores dry out first, followed by intermediate and smaller pores. In addition, the slope of the T_1 curve, at a free pore volume fractions of 90 %, appears to drop again significantly, indicating that even smaller pore structures are present.

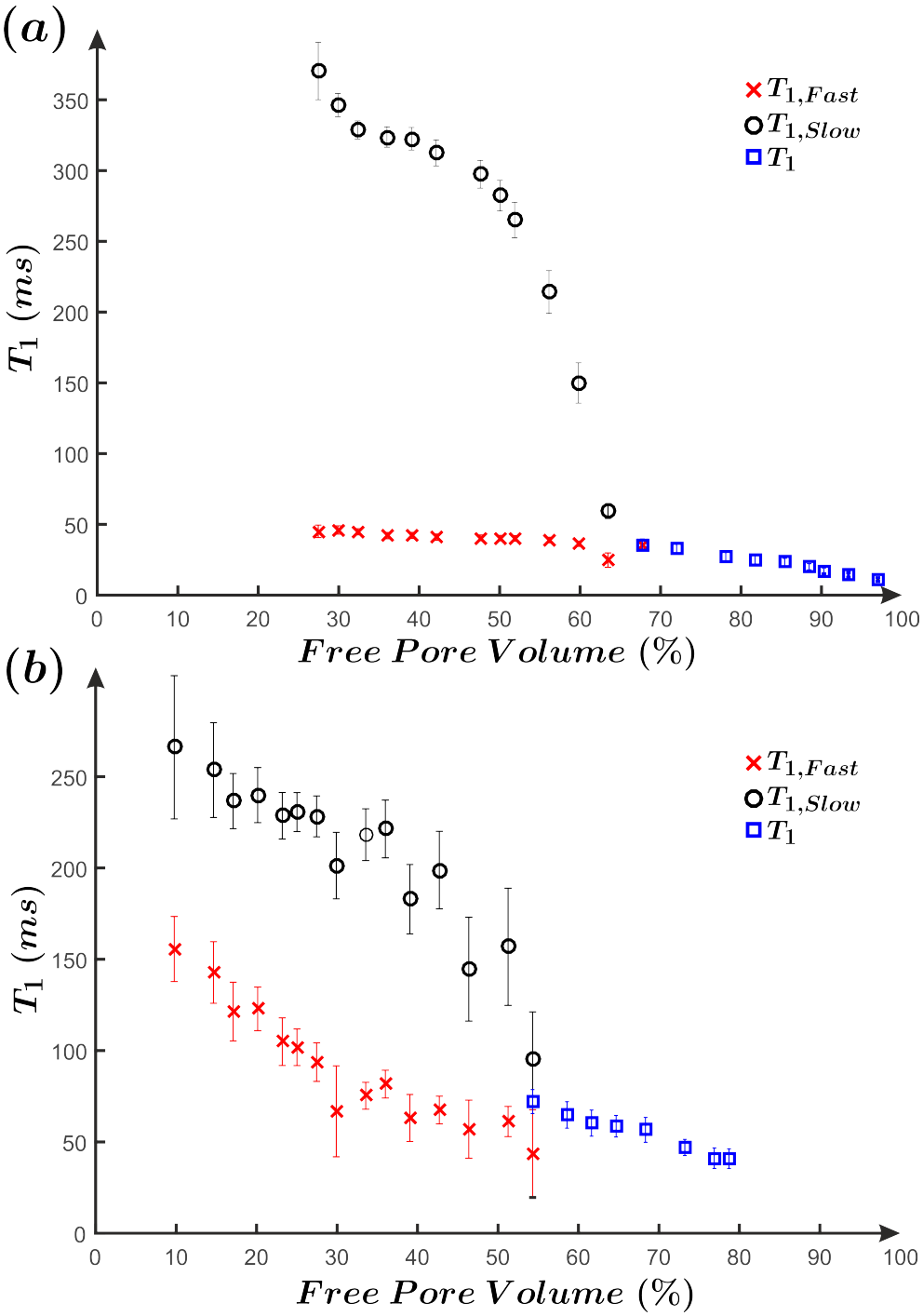


Figure 5.6: Spin-lattice relaxation time components for ^1H in H_2O (a), and ^2H in D_2O (b), as a function of the free pore volume for variable saturation states of a monolith during a drying experiment. Data was collected by use of a standard inversion recovery sequence with 16 recovery increments. The recovery times were tuned to each experiment as to provide suitable data for fittings. Each data point represents four averaged datasets and error bars are the standard deviation.

The ^2H_2O data in Figure 5.6 (b) also shows two steps in the curve for

the ^{2}H T_1^{slow} component occurring at similar free pore volumes to the corresponding curve for the ^{1}H T_1^{slow} component in the H_2O data. This is despite the fact that the two types of nuclei have completely different relaxation mechanisms, namely dipolar relaxation for ^{1}H, and quadrupolar relaxation for ^{2}H. This suggest that the observed effect is determined by the pore sizes, and not from potential paramagnetic sites. This is because paramagnetic sites would affect ^{2}H nuclei much less than ^{1}H due to the $\sim$ 6.5 times lower gyromagnetic ratio γ of the former (and given there is a γ^2 dependence for paramagnetic relaxation). Therefore, a consideration of the combined relaxation data for both nuclei in Figure 5.6 suggests that the three main step changes, during the drying process, occurring at free pore volume fractions of $\sim$ 25, $\sim$ 55, and $\sim$ 90 %, are indicative of the porous hierarchy of the monolith.

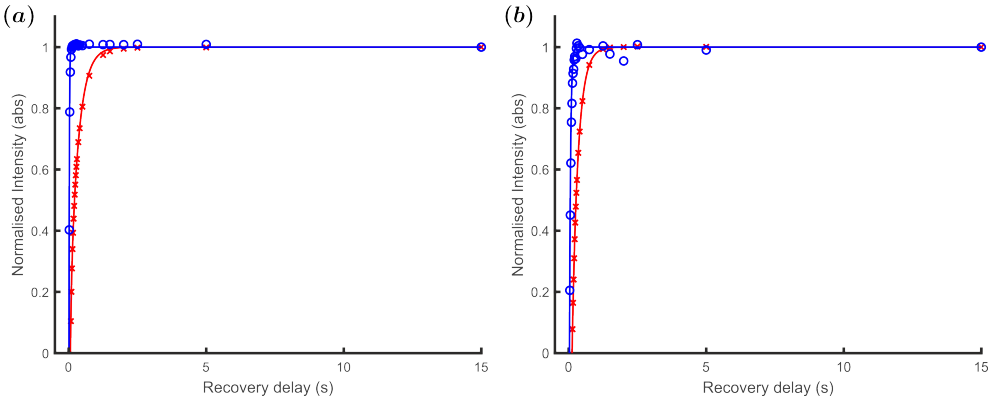


Figure 5.7: Raw inversion recovery data for ^{1}H in H_2O (a), and ^{2}H in D_2O (b), in a *dry* monolith (Blue circles) fitted to a mono-exponential model (Equation 5.7) and in a monolith at 25 % free pore volume (Red crosses) fitted to a bi-exponential model (Equation 5.6). Data was collected by use of a standard inversion recovery sequence with 16 recovery increments.

5.4.4 ^{2}H MRI studies of drying of monolith

Figure 5.8 shows spin density images for radial cross-sections of the monolith at different ^2H_2O saturations during a drying experiment. ^{2}H was used for this experiment due to the shorter T_1 relaxation times allowing

for more rapid signal averaging, as compared to that of the ^{1}H, thus reducing the total experiment times. Further, as mentioned above, $^{2}H_2O$ is relatively insensitive to the chemical heterogeneity in the form of paramagnetics present within the monolith. From a comparison of the images for spin density, which is directly proportional to $^{2}H_2O$ content, it can be seen that at 100 % saturation the highest concentration of (heavy) water is present within the highly porous intersections, with relatively less in the walls. At intermediate saturations (33 % water filled) the intersections have mostly dried out first, leaving the majority of the remaining liquid within the walls of the monolith. Further, at free pore volumes of 89 %, the then highest concentration of $^{2}H_2O$ remains in the walls, with relatively little visible in intersections. Thus suggests that the intersections dry out before the walls.

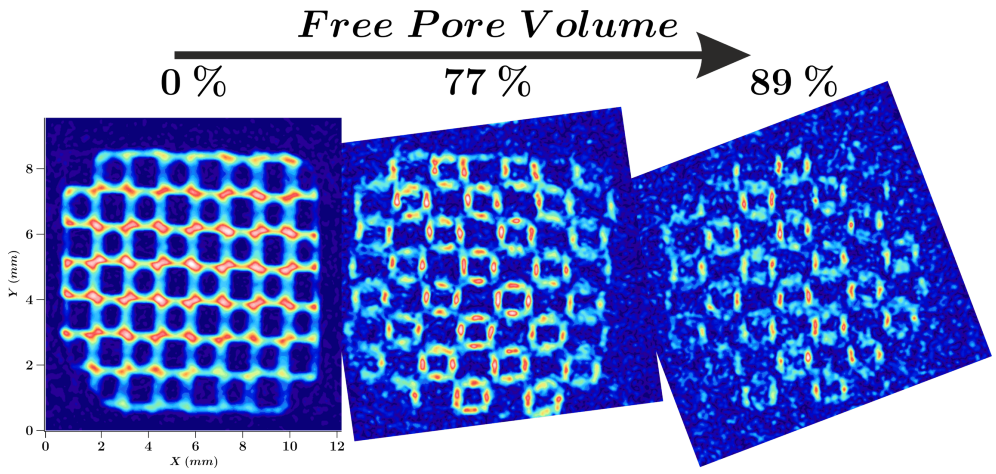


Figure 5.8: Non-normalised spin density images for radial cross-sections of monolith at two different $^{2}H_2O$ saturations during a drying experiment. White and red colours indicate higher spin density, while green and blue indicate low spin density. The images have been re-orientated such that the wall axes are aligned. The acquisition matrix was 128 $\times$ 128 and zero filled to 256 $\times$ 256 an in plane resolution of 0.109 mm pixel^{-1}. The slice thickness was 13 mm.

Figure 5.9 depicts a spin-spin (T_2) relaxation map of a SCR monolith fully saturated in $^{2}H_2O$, along with its associated histogram of T_2 values. From Figure 5.9, it can be seen that the longest T_2 values are located

within the intersections of the walls, having a value of $\sim$ 22 ms while a shorter component of $\sim$ 16 ms is located within the walls. This finding is further confirmed from examining the bimodal distribution of relaxation times (Multipeak fit 1.4, Igor Pro, Wave metrics, USA) given in the histogram displayed in Figure 5.9 (b). Since the Brownstein-Tarr relationship (Equation 5.4) suggests that, when fluids are relaxing within porous media longer relaxation times are associated with larger pores, then the largest pores are located in the intersections. Hence, these MRI data are consistent with the data reported above from CXT displayed in Figure 5.4.

5.4.5 ^{129}Xe NMR relaxometry studies of drying of monolith

Figure 5.10 (a) shows a schematic of the sample used for this series of experiments. The hp xenon gas was vacuum shuttled into the sample container holding the monolith segment. As the findings above demonstrate, during the drying procedure the moisture progressively left successive levels in the hierarchy of the pore structure. At the very lowest moisture contents (high free pore volumes) the smallest level of the pore structure was opened, thus allowing hp xenon gas to enter the smallest pores and experience a chemical shift of $\sim$ 89 ppm as shown in the spectrum in Figure 5.10 (b).

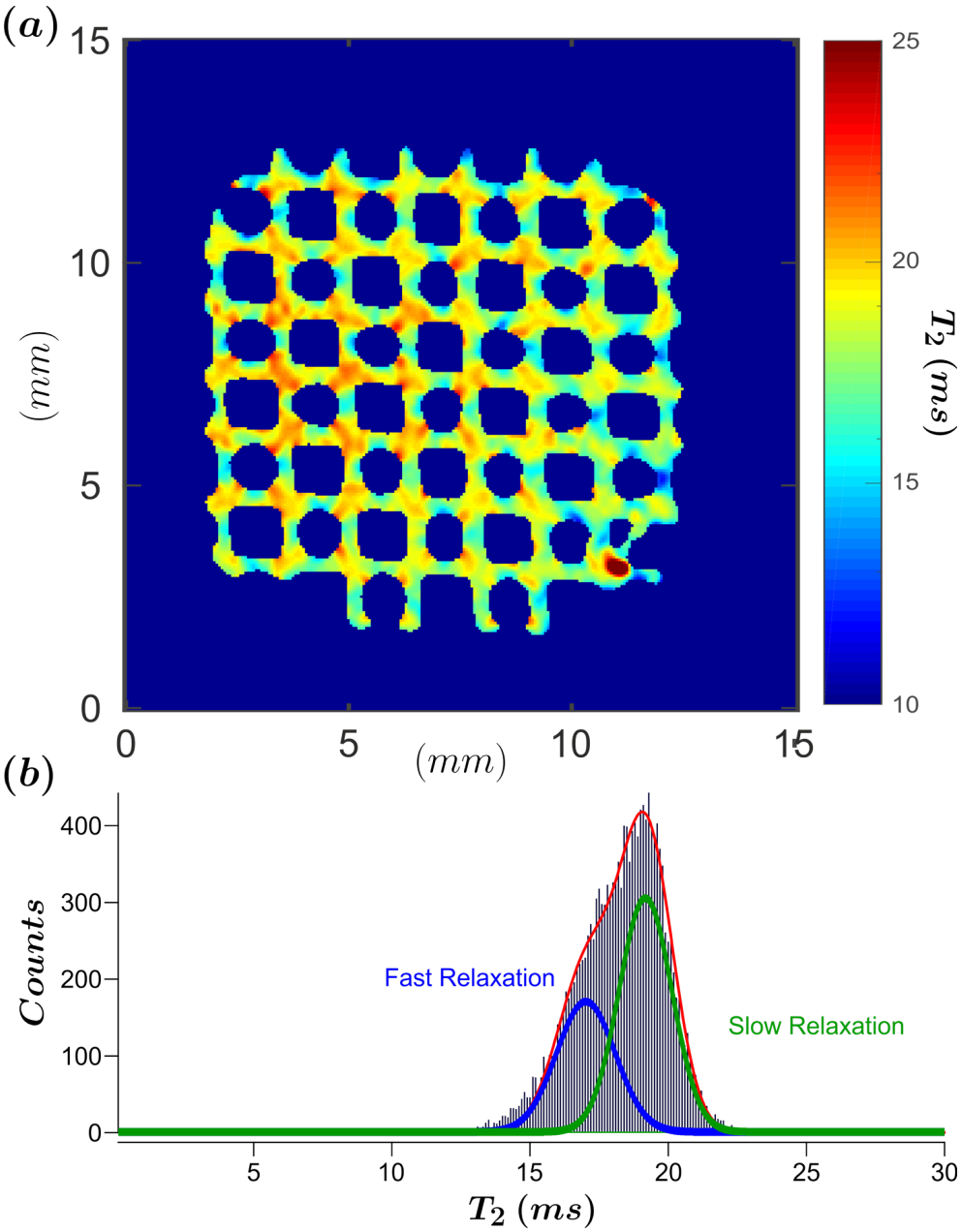


Figure 5.9: (a) Spin-Spin (T_2) relaxation map of a radial cross-section of monolith fully saturated in deuterium oxide. The image was calculated from 8 T_2 weighted images with an echo time ranging from 2.7 ms to 42 ms. The acquisition matrix was 128 $\times$ 128 and zero filled to 256 $\times$ 256 an in plane resolution of 0.109 mm pixel^{-1}. The slice thickness was 13 mm. It should be noted that some smaller channels appear to be circular, this is due to the ^2H_2O forming a meniscus at the intersections within the small channels. (b) histogram of the values of T_2 from the map displayed in (a) showing a bimodal distribution of the relaxation times.

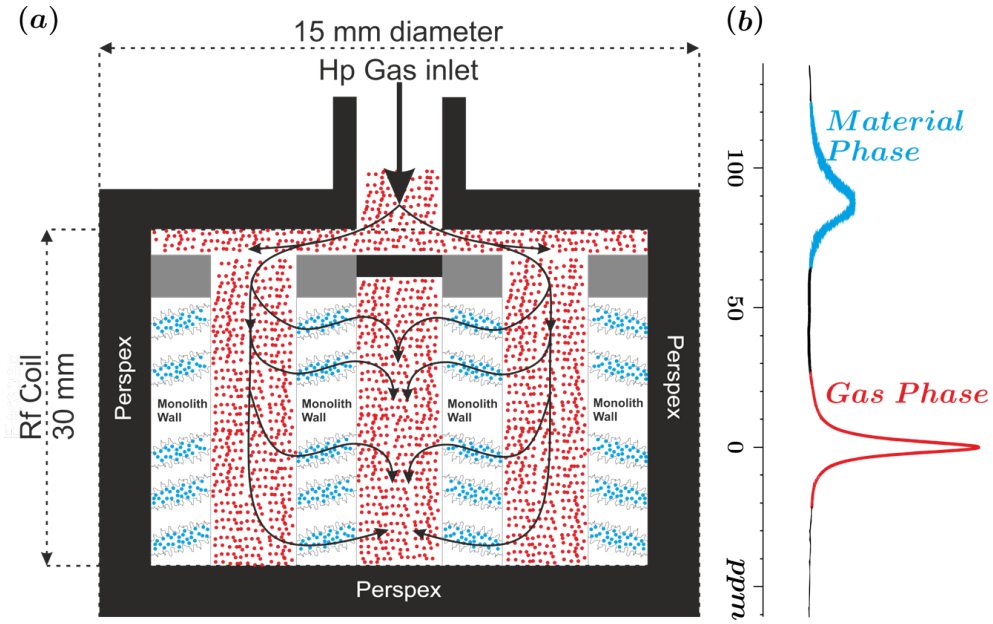


Figure 5.10: (a) Schematic of the Sample used in the Relaxation experiments. As the hp ^{129}Xe gas enters the monolith it is unbound in the gas phase (*red circles*) where as it moves through the porous monolith walls the hp ^{129}Xe experiences a large chemical shift in this state (*blue circles*) as indicated in the spectra in (b). (b) hp ^{129}Xe 1-D spectrum of gas in the monolith structure. The chemical shift separation between gas phase (*red*) and the imbibed phase (*blue*) is 89 ppm. The spectra is comprised of a single acquisition with the RF carrier frequency set between the two peaks to ensure even excitation.

Figure 5.11 shows the spin-lattice relaxation times for hyperpolarised ^{129}Xe in the gas phase located in the progressively increasing free pore volume of partially saturated samples during the drying experiments. It can be seen that these data show three main step changes in T_1 at free pore volume fractions of $\sim$ 20, $\sim$ 60 and $\sim$ 90 %, which are similar to the corresponding positions of the three main steps in the water data in Figure 5.6. Hence, relaxation time data from all three different nuclei all indicate that the drying of the monolith pore structure proceeds in a hierarchical fashion, with the largest pores drying out first, followed by intermediate, and then smaller pores. At the final free pore volume fraction step ($\sim$ 90 %) the pore structure is sufficiently open for the hp ^{129}Xe gas to enter the smallest level of pores.

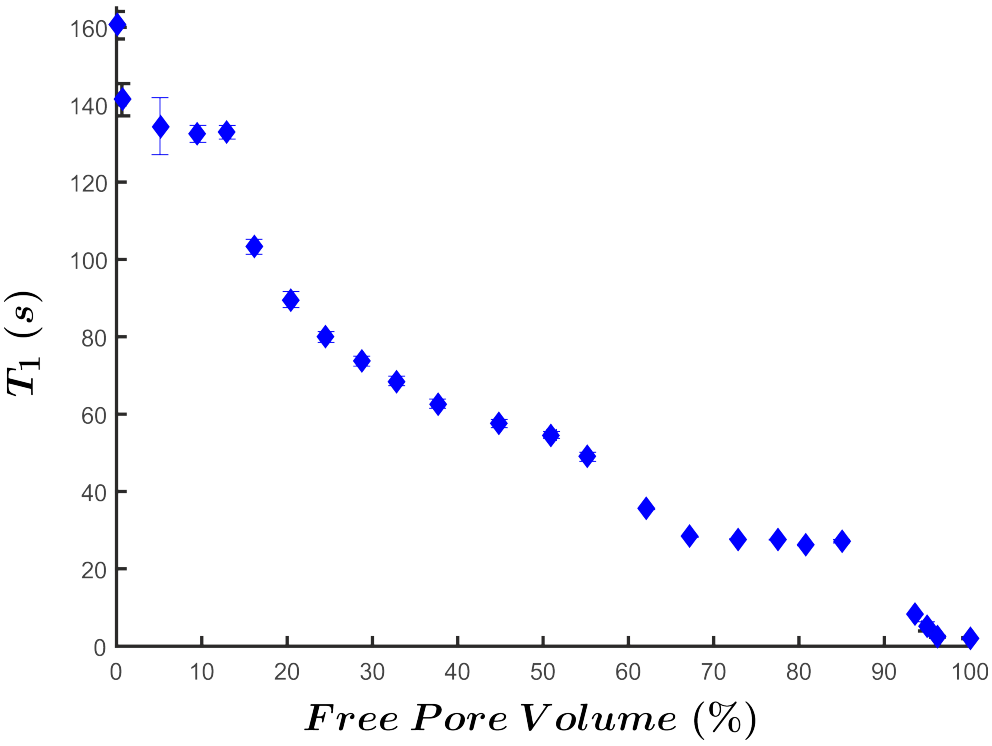


Figure 5.11: Variation in spin-lattice relaxation times for hyperpolarised ^{129}Xe with changing free pore volume of partially saturated samples during drying experiments. The data were acquired by a train of low flip angle pulses, as described in the main text. Each data point represents four averaged data points with the error bars indicating the standard error of the datasets for the T_1 relaxation time and the calculated free pore volume of each individually collected dataset.

MRI studies of xenon diffusional permeation at variable saturation levels

Figure 5.12 shows a schematic diagram depicting the pattern of gas flow within the SCR monolith segment used in this series of experiments. The hp ^{129}Xe gas flowed into a single channel with a blocked far end. Therefore, in order to exit the monolith segment, the hp gas was forced to cross through the monolith porous wall or intersection structures.

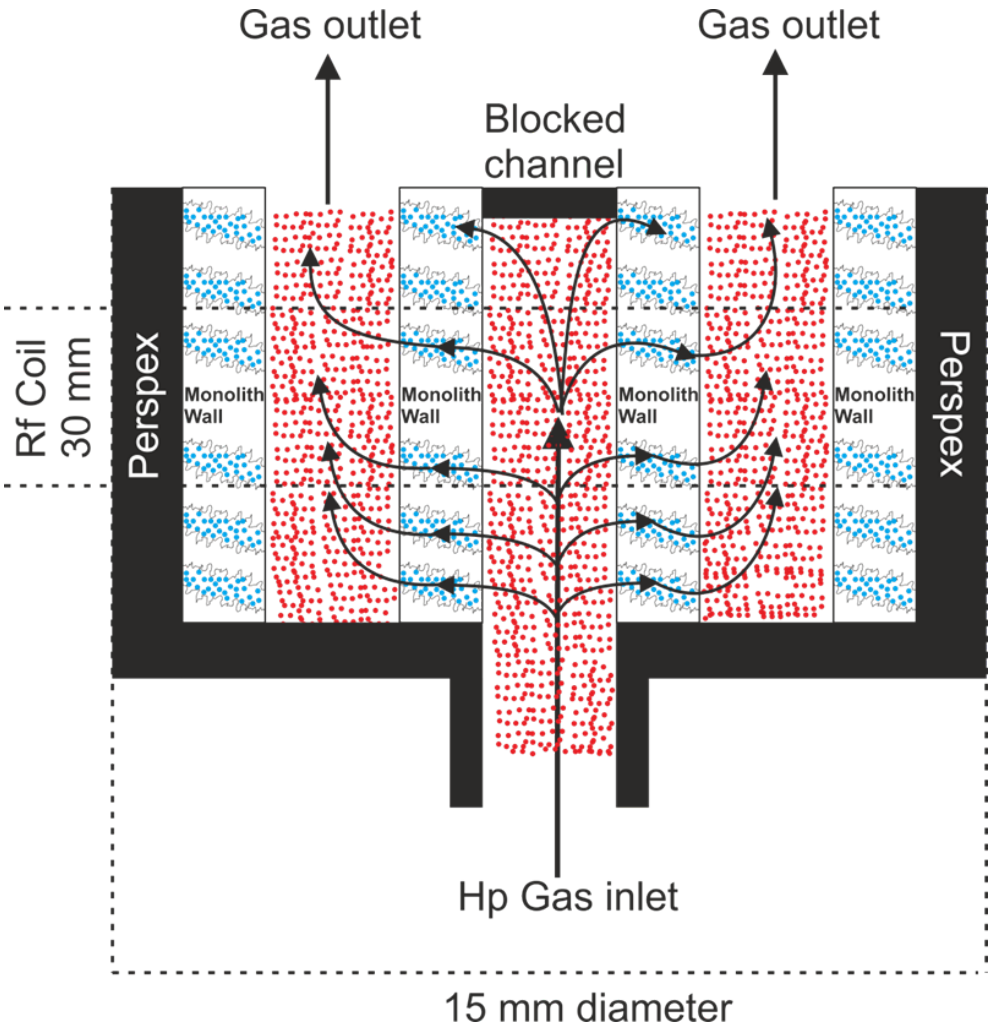


Figure 5.12: Schematic depiction of the flow pattern within a monolith segment with gas delivered to a single channel of the SCR filtration monolith. The hp ^{129}Xe enters the central, blocked far-end channel, and, thence, is forced to move through the substrate walls so as to escape the monolith. The outer walls and the bottom of the monolith was wrapped with Parafilm such that the only exit for the gas was that of the open channels at the top of the monolith.

Figure 5.13 shows images of the spatial dispersion of xenon, away from the central channel location of gas injection, with increasing transport time, for a monolith sample at different water saturation levels. Initially images suggest a film of water present within the corners of the monolith causing the channels to appear cylindrical. Such an effect is also observed in the $^{2}H_2O$ images in Figure 5.9 (a) and Figure 5.8 at low free pore volumes. This effect was magnified by the fact the hp ^{129}Xe gas was under flow within the experiment. Figure 5.13 (i) displays a spin density image

at 5 % free pore volume and 1.0 s hp gas replenishment delay with Figure 5.13 (ii) showing a line profile taken across the central *inlet* channel from (i) indicating a parabolic distribution of magnitudes. At all saturation levels, the dispersion pattern of the gas with increasing time lacks overall symmetry, thereby suggesting the distribution of porosity (and thence the distribution of washcoat within the monolith) through which it flows is heterogeneous. At low free pore volumes, permeation appears biased towards the highly porous corners of the channels. Further, at intermediate saturation levels, there is evidence of overall flow in directions perpendicular to the channel walls, probably indicating that flow though the walls begins to occur. It is noted that the aforementioned relaxation time data, from the drying experiments, suggests that the intermediate sized porosity is emptied of water in the drying step at free pore volumes of $\sim$ 55 %. However, the then availability of the intermediate-sized porosity for mass transport does not appear to lead to a corresponding increase in the spreading rate of the hp ^{129}Xe permeation front through the pore structure. At very high free pore volumes, where the drying curves suggested the smallest pore size were opened up, the intensity of the hp ^{129}Xe signal then drops substantially, thereby indicating that the paramagnetic sites within the small pores of the monolith structure were being exposed to cause rapid relaxation. Since the paramagnetic centres are associated with the catalytically active phase, this suggests that the catalyst is only largely accessed once molecules penetrate the smallest level in the pore size hierarchy in the drying curves.

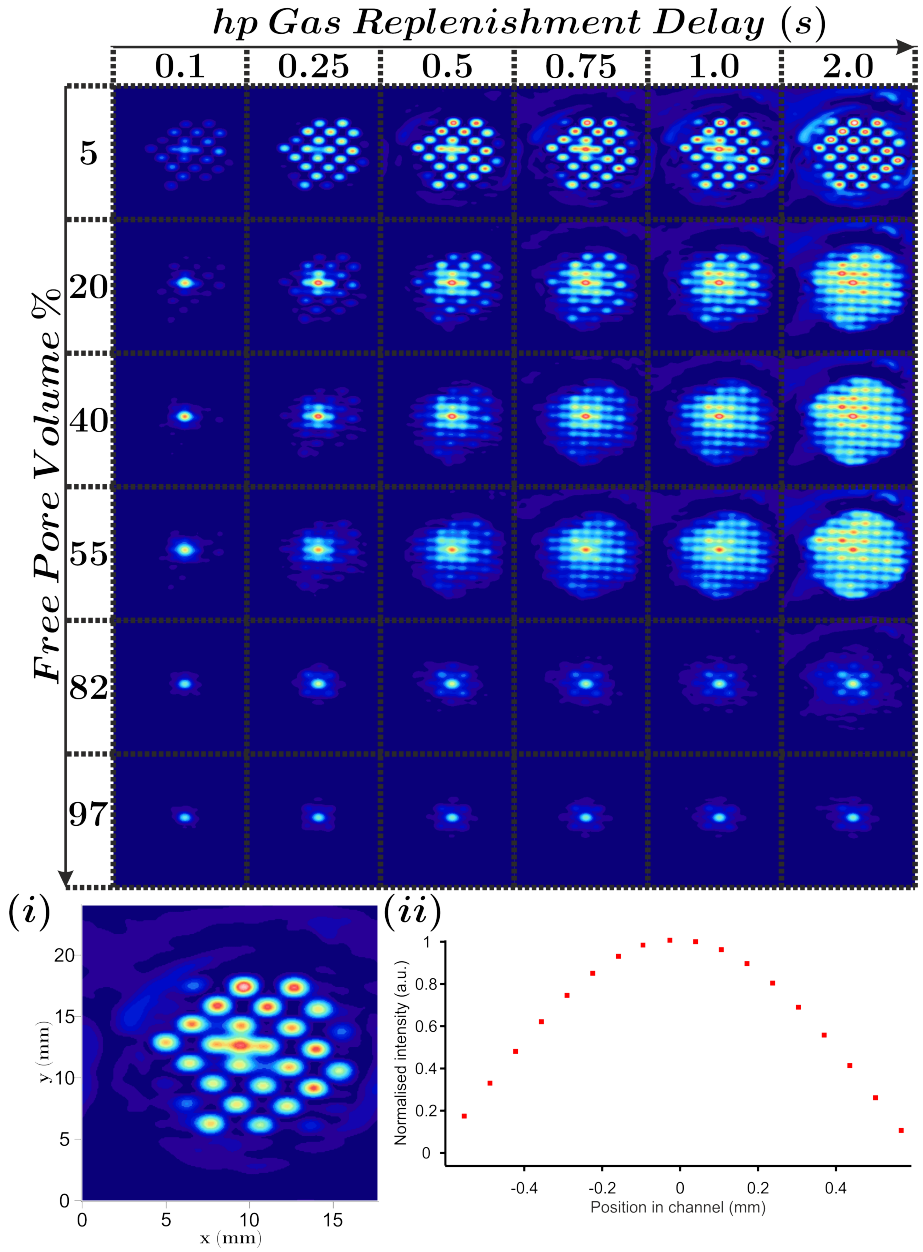


Figure 5.13: Two-dimensional spin density images of the the spatial dispersion of hp ^{129}Xe, within a radial cross-section of a combined SCR filtration monolith, with increasing transport time. High gas density is indicated by red colours, and lower densities are indicated by yellow to blue colours. Gas flowed at a constant rate through a single channel of the SCR monolith after it has been saturated in distilled water. The images were acquired by a standard gradient echo sequence. The hp gas replenishment delay was varied so as to provide an insight into the dispersive mass transfer from the delivery channel to the outlying channels. The acquisition matrix was 64×32, zero filled to 128×128, FOV read: 22.1 mm, FOV phase: 16.99 mm, FOV slice: 15.7 mm. The water in this series of experiments was used to occlude pathways within the SCR monolith's pore structure so as to reduce the effects of paramagnetic relaxation, and illustrate the flow pathways within the monolith pore structure. The drying was provided by the flow of the hp gas during the imaging experiment and molecular nitrogen when not imaging. (i) displays a spin density image at 5 % free pore volume and 1.0 s hp gas replenishment delay from above, (ii) shows a line profile of normalised magnitudes taken from the central *inlet* channel of (i)

5.4.6 MRI velocity imaging studies of flow in monoliths

Two dimensional velocimetry images in the radial (xy) plane of the SCR monolith were acquired at a free pore volume of $\sim$ 55 % and are shown in Figure 5.14. Each pixel is a local measurement of the axial component of the velocity vector (V_z). Examples of propagators are given in Appendix A. The higher velocities present in the image are represented by the red colour and lower velocities by dark blue. The same flow conditions as those used for the spin density mapping experiments were also used for this set. In Figure 5.14 (a) it can be seen that the maximum positive axial velocity occurs in the channel into which the hp ^{129}Xe has been injected, as might be expected. In the channels immediately adjacent to the injection channel, and separated by the walls from the injection channel, the flow is also positive as these channels have exits at the end opposite to that of injection. The area for flow available in these channels is larger than in the injection channel so the velocity is lower. In those channels neighbouring the injection channel along the diagonals of the channel grid, and thus separated from it by wall intersections, negative flow velocities can be observed. This negative velocity arises from a re-circulation of the flow entering these diagonal channels back from their closed ends (see Figure 5.1).

Figure 5.14 (b) displays the same data as Figure 5.14 (a) but the scale has been changes so as to make clearer the differences between flows with rates substantially lower than that in the injection channel. Figures 5.14 (c) and (d) show line profiles of velocity variation taken across arbitrary channels in the monolith (as identified in Figure 5.14 (b)). These profiles have been fitted to the theoretical prediction of the axial velocity profile

for laminar flow ($Re < 2000$) within a rectangular channel, as derived by Shah and London [41]:

$$\frac{u}{u_m} = \left(\frac{m+1}{m}\right)\left(\frac{n+1}{n}\right)\left[1-\left(\frac{y}{b}\right)^n\right]\left[1-\left(\frac{z}{a}\right)^m\right] \tag{5.10}$$

The profile displayed in Figure 5.14 (c) was taken orthogonal to the chosen channel wall, and demonstrates a good agreement to the theoretically derived laminar flow velocity profile. This agreement between observation and theory suggests the no-flux boundary condition used in the derivation was appropriate. This would suggest that little transverse flow was occurring across the wall of the channel. In contrast, the velocity profile shown in Figure 5.14 (d) was taken diagonally across, between the opposite corners of, the chosen channel, such that the two ends of the profile corresponded to opposite wall intersections. In this instance, poor agreement, between the theoretically predicted flow profile and experimental measurements, was obtained at the boundaries of the channel, thereby indicating significant transverse velocities through the wall intersections at the corners of the channels. This difference in shape, depending upon the orientation of the velocity profile across the channel, is explained by the particular distribution of remaining moisture content within the partially-saturated monolith. The remaining liquid was located primarily in the smallest size level of the pore hierarchy, which was located within the walls leaving the intersections empty, thus allowing for a substantive mass transport through the channel corners but not the walls. This substantial deviation from the no-flux boundary condition results in a poor fit to the theoretical profiles making that particular assumption. Additional line profiles from other channels and theoretical fittings are displayed in Appendix B.

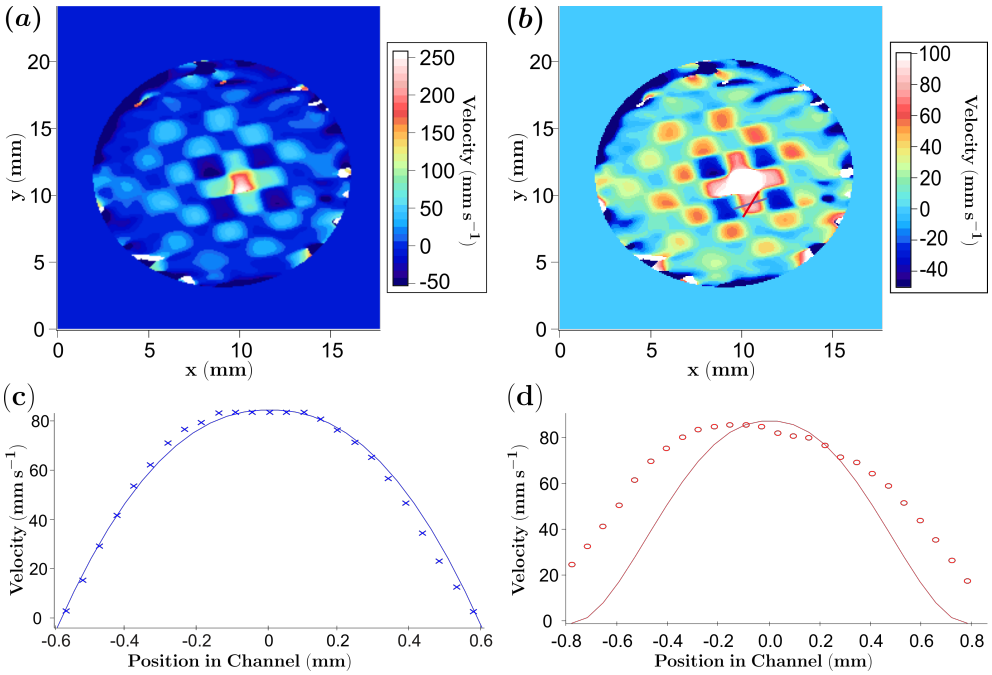


Figure 5.14: Axial velocity maps of radial cross-section of monolith segment. The acquisition matrix was 64 × 32, zero filled to 128 × 128, FOV read: 22.1 mm, FOV phase: 16.99 mm, FOV slice: 15.7 mm; (a) Axial velocity map of ^{129}Xe flowing in a channel with a reynolds number of 52 in the central channel. 12 pairs of flow encoding gradients of duration $\delta = 0.5$ ms separated by a delay $\Delta = 5$ ms were used to characterise the flow. 4 averages were used to gain sufficient SNR. A recycle delay of 2 s was utilised and led to a total experiment time of 4 mins. The image is scaled to the peak velocity measured in the central channel of 261 mm/s. The purple line represents the path of the line profile in (c), and the red arrow represents the line profile in (d); The second image (b) displays the same data as (a) but with velocity re-scaled, so as to better show up the slower gas velocities present in the system; (c) a diagonal line profile taken from an arbitrary channel in (a); (d) a line profile parallel to the wall of the monolith taken from an arbitrary channel in (a). The solid lines in (c) and (d) are fits of the experimental data (symbols) to the solution to laminar flow in a rectangular cross-section channel in Equation 5.10. Additional line profiles and the indicated theoretical profiles are presented in Appendix B.

The spatial variation in the distribution of transverse (i.e. radial direction) velocities were also studied by the alteration of the direction of the applied gradient. Three orthogonal velocity maps were acquired via altering the direction of the applied gradient, G_{flow}. The flow in the transverse directions was substantially lower than that measured for the axial component. Figure 5.15 shows the calculated angular offset of the resultant of the V_x and V_y components from the (axial) z-direction of the predominant flow within the central channel. The angular offset was

calculated from the expression:

$$\theta = \arccos\left(\frac{V_z}{\sqrt{V_x^2 + V_y^2 + V_z^2}}\right), \tag{5.11}$$

where θ is the direction of the resultant vector of the in-plane velocities, and the size of which is proportional to the size of the in-plane velocities relative to the axial velocity. The highest in-plane velocity flows were found for the four channels arrayed diagonally relative to the main injection channel. However, it is also particularly noted that, elsewhere in the image, the regions with the largest lateral flows occur in diagonal directions across the wall intersections.

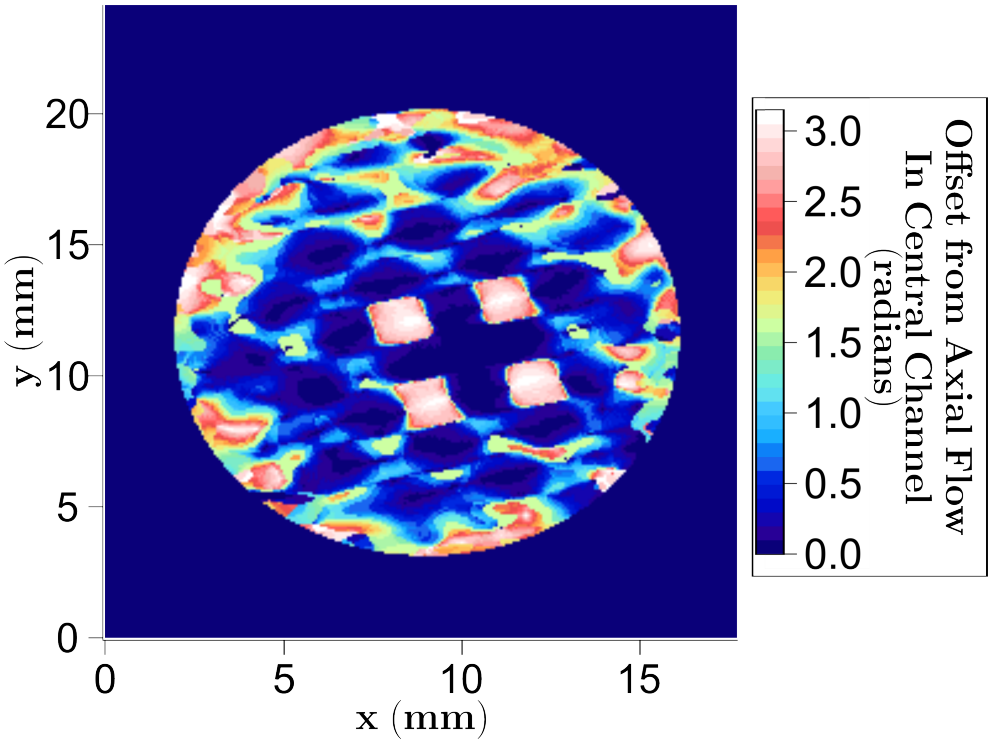


Figure 5.15: Radial cross-section map of the size of the angular offset between the resultant vector of the two in-plane velocity components and the axial velocity component from the central channel. The size of this offset is proportional to the size of the in-plane velocity components relative to the axial component within the Z direction in the central, injection channel.

5.5 Discussion

Mercury porosimetry data has demonstrated that the washcoated monolith has a hierarchical pore structure with three clear pore size modes. The sizes of these modes suggest that they belong to the large empty macropores in the monolith substrate, the macropores in the washcoat formed by the spaces left around the zeolite crystallites, and the mesopores in the binder in the washcoat. The CXT data suggests that the empty macropores in the monolith, and thence the regions of highest porosity, are predominantly located in the wall intersections, rather than the walls proper themselves. This claim is supported by the T_2 map of the fully saturated sample, suggesting the largest pores are found within the wall intersections.

The conditions of temperature and pressure of the detailed hp ^{129}Xe relaxometry and mass transport experiments are such that the mean free path as calculated from kinetic theory (as discussed in Chapter 4) is $\sim$ 55 nm. Considering this in the context of the mercury porosimetry it is clear that within the micropores (< 2 nm) of the zeolite crystallites and the mesopores ($2 < 50$ nm) of alumina binder, that diffusion within the Knudsen regime is being probed. Within the macropores of the monolith substrate itself however diffusion is within the molecular regime.

The NMR relaxometry studies of drying, both those using the liquid still imbibed in the pores, and that using hp ^{129}Xe gas imbibed into the empty voids, all suggest that the largest pores in the washcoated monolith dry out first, followed by the intermediate sized pores, and finally the smallest pores. Hence, the water saturation level can, thence, be used to selectively block particular levels in the pore network hierarchy, namely; all pores; intermediate and small pores; or only small pores. As proposed

above, this has allowed the particular contributions, of pores in different levels of the size hierarchy to mass transport, to be determined. Further, hp ^{129}Xe may be used to probe the smallest level of the pore hierarchy when the moisture content of $^{1}H_2O$ or $^{2}H_2O$ proves insufficient for signal detection.

The mass transport studies, of diffusional permeation and flow under a pressure gradient, both suggest that the higher porosity and larger pore sizes in the regions at the wall intersections make the greatest contribution to overall mass transport. These studies also indicated that even when the intermediate and smaller pores, located predominantly in the walls proper, are open; they make a relatively lesser contribution to mass transport. Hence, even though the monolith macropores only represent about a third of the overall pore volume in the mercury porosimetry data, they dominate the overall pattern of mass transport. This means that the distribution of the mass transport flux within the overall pore network is likely to lead to substantial bypassing of the regions of that network that contain catalyst.

5.6 Conclusions

It has been found that the washcoat of a SCR monolith catalyst is predominantly located in the channel walls, rather than the intersections. The macro-/meso-pore network structure is hierarchical and possesses three distinct levels of pore sizes. The largest sizes in the hierarchy are exclusively located in the channel wall intersections, with the intermediate and smallest sizes located in the walls. It has been seen that even when the intermediate level in the pore network hierarchy has been

opened, the mass transport is still dominated by the fluxes through the largest pores in the channel wall intersections. It is only when the gas can access the smallest level in the pore size hierarchy that substantial access to the catalytically-active phase is obtained. The pattern of mass transport behaviour thus suggests the potential for substantial bypassing of the catalyst.

Bibliography

[1] X. Wen, D. Zhang, L. Shi, T. Yan, H. Wang, and J. Zhang, "Three-dimensional hierarchical porous carbon with a bimodal pore arrangement for capacitive deionization," *Journal of Materials Chemistry*, vol. 22, no. 45, p. 23835, 2012.

[2] X. Wen, D. Zhang, T. Yan, J. Zhang, and L. Shi, "Three-dimensional graphene-based hierarchically porous carbon composites prepared by a dual-template strategy for capacitive deionization," *Journal of Materials Chemistry A*, vol. 1, no. 39, p. 12334, 2013.

[3] C. Fang, L. Shi, H. Li, L. Huang, J. Zhang, and D. Zhang, "Creating hierarchically macro-/mesoporous Sn/CeO_2 for the selective catalytic reduction of NO with NH_3," *RSC Adv.*, vol. 6, no. 82, pp. 78727–78736, 2016.

[4] W. F. Lai, A. S. Susha, and A. L. Rogach, "Multicompartment Microgel Beads for Co-Delivery of Multiple Drugs at Individual Release Rates," *ACS Applied Materials and Interfaces*, vol. 8, no. 1, pp. 871–880, 2016.

[5] A. Śrebowata, K. Tarach, V. Girman, and K. Góra-Marek, "Catalytic removal of trichloroethylene from water over palladium loaded microporous and hierarchical zeolites," *Applied Catalysis B: Environmental*, vol. 181, pp. 550–560, 2016.

[6] P. Yu, X. Zhao, Y. Li, and Q. Zhang, "Controllable growth of polyaniline nanowire arrays on hierarchical macro/mesoporous graphene foams for high-performance flexible supercapacitors," *Applied Surface Science*, vol. 393, pp. 37–45, 2017.

[7] A. Nepryahin, E. M. Holt, R. S. Fletcher, and S. P. Rigby, "Structure-transport relationships in disordered solids using integrated rate of gas sorption and mercury porosimetry," *Chemical Engineering Science*, vol. 152, pp. 663–673, 2016.

[8] I. V. Koptyug, S. A. Altobelli, E. Fukushima, A. V. Matveev, and R. Z. Sagdeev, "Thermally Polarized ^{1}H NMR Microimaging Studies of Liquid and Gas Flow in Monolithic Catalysts," *Journal of Magnetic Resonance*, vol. 147, pp. 36–42, nov 2000.

[9] I. V. Koptyung, A. V. Matveev, and S. A. Altobelli, "NMR studies of hydrocarbon gas flow and dispersion," *Applied Magnetic Resonance*, vol. 22, pp. 187–200, jun 2002.

[10] M. D. Mantle, A. J. Sederman, L. F. Gladden, S. Raymahasay, J. M. Winterbottom, and E. H. Stitt, "Dynamic MRI visualization of two-phase flow in a ceramic monolith," *AIChE Journal*, vol. 48, pp. 909–912, apr 2002.

[11] I. V. Koptyug, R. Z. Sagdeev, L. Y. Khitrina, and V. N. Parmon, "A nuclear magnetic resonance microscopy study of mass transport in porous materials," *Appl. Magn. Reson.*, vol. 18, pp. 13–28, 2000.

[12] N. P. Ramskill, L. F. Gladden, A. P. E. York, A. J. Sederman, J. Mitchell, and K. A. Hardstone, "Understanding the operation and preparation of diesel particulate filters using a multi-faceted nuclear magnetic resonance approach," *Catalysis Today*, vol. 216, pp. 104–110, 2013.

[13] N. P. Ramskill, A. P. York, A. J. Sederman, and L. F. Gladden, "Magnetic resonance velocity imaging of gas flow in a diesel particulate filter," *Chemical Engineering Science*, vol. 158, pp. 490–499, feb 2017.

[14] S. P. Rigby, M. Hasan, I. Hitchcock, and R. S. Fletcher, "Detection of the delayed condensation effect and determination of its impact on the accuracy of gas adsorption pore size distributions," *Colloids and Surfaces A: Physicochemical and Engineering Aspects*, vol. 517, pp. 33–44, 2017.

[15] J. S. Six, T. Hughes-Riley, K. F. Stupic, G. E. Pavlovskaya, and T. Meersmann, "Pathway to Cryogen Free Production of Hyperpolarized Krypton-83 and Xenon-129," *PLoS ONE*, vol. 7, no. 11, 2012.

[16] T. Hughes-Riley, J. S. Six, D. M. Lilburn, K. F. Stupic, A. C. Dorkes, D. E. Shaw, G. E. Pavlovskaya, and T. Meersmann, "Cryogenics free production of hyperpolarized ^{129}Xe and ^{83}Kr for biomedical MRI applications," *Journal of Magnetic Resonance*, vol. 237, pp. 23–33, dec 2013.

[17] G. Pavlovskaya, J. Six, T. Meersman, N. Gopinathan, and S. P. Rigby, "NMR imaging of low pressure, gas-phase transport in packed beds using hyperpolarized xenon-129," *AIChE Journal*, vol. 61, no. 11, pp. 4013–4019, 2015.

[18] R. W. Mair, G. P. Wong, D. Hoffmann, M. D. Hurlimann, S. Patz, L. M. Schwartz, and R. L. Walsworth, "Probing porous media with gas diffusion NMR.," *Physical review letters*, vol. 83, no. 16, pp. 3324–7, 1999.

[19] R. Mair, P. Sen, M. Hürlimann, S. Patz, D. Cory, and R. Walsworth, "The Narrow Pulse Approximation and Long Length Scale Determination in Xenon Gas Diffusion NMR Studies of Model Porous Media," *Journal of Magnetic Resonance*, vol. 156, no. 2, pp. 202–212, 2002.

[20] R. W. Mair, R. Wang, M. S. Rosen, D. Candela, D. G. Cory, and R. L. Walsworth, "Applications of controlled-flow laser-polarized xenon gas to porous and granular media study," *Magnetic Resonance Imaging*, vol. 21, no. 3-4, pp. 287–292, 2003.

[21] L. G. Kaiser, T. Meersmann, J. W. Logan, and a. Pines, "Visualization of gas flow and diffusion in porous media.," *Proceedings of the National Academy of Sciences of the United States of America*, vol. 97, no. 6, pp. 2414–2418, 2000.

[22] L. G. Kaiser, J. W. Logan, T. Meersmann, and A. Pines, "Dynamic NMR microscopy of gas phase Poiseuille flow," *J. Magn. Reson.*, vol. 149, no. 1, pp. 144–148, 2001.

[23] K. V. Kovtunov, V. V. Zhivonitko, I. V. Skovpin, D. A. Barskiy, and I. V. Koptyug, "Parahydrogen-Induced Polarization in Heterogeneous Catalytic Processes," in *TripleC*, vol. 11, pp. 123–180, 2012.

[24] E. Harel, J. Granwehr, J. A. Seeley, and A. Pines, "Multiphase imaging of gas flow in a nanoporous material using remote-detection NMR," *Nature Materials*, vol. 5, pp. 321–327, apr 2006.

[25] V. V. Zhivonitko, V. V. Telkki, and I. V. Koptyug, "Characterization of microfluidic gas reactors using remote-detection MRI and parahydrogen-induced polarization," *Angewandte Chemie - International Edition*, vol. 51, no. 32, pp. 8054–8058, 2012.

[26] J. Granwehr, E. Harel, S. Han, S. Garcia, A. Pines, P. N. Sen, and Y.-Q. Song, "Time-of-Flight Flow Imaging Using NMR Remote Detection," *Physical Review Letters*, vol. 95, p. 075503, aug 2005.

[27] S. P. Rigby and K. J. Edler, "The Influence of Mercury Contact Angle, Surface Tension, and Retraction Mechanism on the Interpretation of Mercury Porosimetry Data," *Journal of Colloid and Interface Science*, vol. 250, no. 1, pp. 175–190, 2002.

[28] J. Kloubek, "Hysteresis in porosimetry," *Powder Technology*, vol. 29, no. 1, pp. 63–73, 1981.

[29] K. R. Brownstein and C. E. Tarr, "Spin-lattice relaxation in a system governed by diffusion," *Journal of Magnetic Resonance (1969)*, vol. 26, no. 1, pp. 17–24, 1977.

[30] K. R. Brownstein and C. E. Tarr, "Importance of classical diffusion in NMR studies of water in biological cells," *Physical Review A*, vol. 19, no. 6, pp. 2446–2453, 1979.

[31] K. Washburn, C. Eccles, and P. Callaghan, "The dependence on magnetic field strength of correlated internal gradient relaxation time distributions in heterogeneous materials," *Journal of Magnetic Resonance*, vol. 194, pp. 33–40, sep 2008.

[32] P. T. Callaghan, *Translational Dynamics and Magnetic Resonance: Principles of Pulsed Gradient Spin Echo NMR*. OUP Oxford, 2011.

[33] J. H. Gao, L. Lemen, J. Xiong, B. Patyal, and P. T. Fox, "Magnetization and diffusion effects in NMR imaging of hyperpolarized substances," *Magnetic Resonance in Medicine*, vol. 37, no. 1, pp. 153–158, 1997.

[34] Z. I. Cleveland and T. Meersmann, "Density-independent contributions to longitudinal relaxation in 83Kr," *ChemPhysChem*, vol. 9, no. 10, pp. 1375–1379, 2008.

[35] K. F. Stupic, N. D. Elkins, G. E. Pavlovskaya, J. E. Repine, and T. Meersmann, "Effects of pulmonary inhalation on hyperpolarized krypton-83 magnetic resonance T_1 relaxation," *Physics in Medicine and Biology*, vol. 56, pp. 3731–3748, jul 2011.

[36] E. Brunner, "Applications of laser-polarized Xe-129 under continuous flow," *Magnetic Resonance in Chemistry*, vol. 37, no. Special:Issue SI, pp. Issue–S22, 1999.

[37] P. T. Callaghan, *Principles of Nuclear Magnetic Resonance Microscopy*. Oxford science publications, Clarendon Press, 1993.

[38] L. F. Gladden, M. H. Lim, M. D. Mantle, A. J. Sederman, and E. H. Stitt, "MRI visualisation of two-phase flow in structured supports and trickle-bed reactors," *Catalysis Today*, vol. 79-80, pp. 203–210, 2003.

[39] L. F. Gladden and A. J. Sederman, "Recent advances in Flow MRI," *Journal of Magnetic Resonance*, vol. 229, pp. 2–11, 2013.

[40] L. F. Gladden and A. J. Sederman, "Magnetic Resonance Imaging and Velocity Mapping in Chemical Engineering Applications," *Annual Review of Chemical and Biomolecular Engineering*, vol. 8, no. 1, pp. 227–247, 2017.

[41] R. Shah and A. London, "Laminar Flow Forced Convection in Ducts," 1978.

Chapter 6

Explosive production of Hyperpolarised ^{129}Xe and ^{83}Kr MRI contrast agents

The method of Hp gas production detailed in previous chapters as described, provides highly spin polarised gasses for *NMR* and *MRI* applications however the gas produced suffers from the effect of being dilute within it's buffer gas. This chapter details the novel method of separation of the hyperpolarisation species from its buffer gas. This work resulted in the peer-reviewed publication in the Journal: *The Proceedings of the National Academy of Science* entitled; *Molecular hydrogen and catalytic combustion in the production of hyperpolarised* ^{83}Kr *and* ^{129}Xe *MRI contrast agents* [1] and presented in the hyperpolarisation session at the international conference EUROMAR 2016.

This work was completed by Dr Nicola J. Rogers, Mr Fraser Hill-Casey, Dr Karl F. Stupic, Dr Joseph S. Six, Dr Clémentine Lesbats, Professor Sean P. Rigby, Professor Jacques Fraissard, Dr Galina E. Pavlovskaya, and Professor Thomas Meersmann.

Professor Meersmann conceived the general concept of the reactive buffer gas removal, Dr Stupic, Dr Pavlovskaya, and Professor Rigby assisted in

experimental design. Dr Rogers and Dr Lesbats performed the combustion research. Dr Six and Mr Hill-Casey performed the SEOP experiments and the infra-red data presented in the paper. Mr Hill-Casey presented the work in the hyperpolarisation session at Euromar 2016.

6.1 Introduction

The development of hyperpolarised (hp) noble gas MRI has resulted in a number of excellent protocols to probe different structural and functional aspects of lungs in health and disease [2–7]. Technological improvements [7–16] have enabled pulmonary hp ^{129}Xe MRI at high spatial resolution, thereby reducing the need for use of the scarcely available ^{3}He isotope. Furthermore, tissue solubility, large chemical shift range, and interaction with specific sensor molecules allow for a variety of hp ^{129}Xe applications in biomedical sciences and beyond [2–7, 17, 18]. Despite its nuclear electric quadrupole moment that causes rapid relaxation, the isotope ^{83}Kr (nuclear spin I = 9/2) can be hyperpolarisation through Rb Spin-Exchange Optical Pumping (SEOP) as first demonstrated by Grover [19] and explored in detail by Happer and coworkers [20]. Volk *et al.* first observed ^{83}Kr quadrupolar coupling in the gas phase that originated from the surface of the SEOP cell [21], and Mehring and coworkers described T_2 relaxation as a probe for the cell surfaces [22]. The intriguing properties of ^{83}Kr can be more generally used after the removal of the reactive Rb vapor to generate surface-sensitive MRI contrast [23].

Most recently, T_1 surface quadrupolar relaxation MRI contrast [24] with hp ^{83}Kr in excised lungs was demonstrated to be indicative of surface-to-volume changes in an animal model of emphysema [3]. Although hp ^{129}Xe

can be obtained through dynamic nuclear polarization [25] with high spin polarization levels of up to $P = 30\,\%$ [26], at present only SEOP can produce hp ^{129}Xe with $P \geq 90\,\%$. Furthermore, SEOP is currently the only method to provide hp ^{83}Kr for biomedical MRI applications [3].

During SEOP of ^{83}Kr or ^{129}Xe , the noble gas is diluted with a buffer gas, usually either a ^{4}He–N_2 mixture or pure N_2 gas. The buffer gas serves a dual purpose as it prevents destructive radiation trapping, originating from radiative electronic relaxation of rubidium [27, 28], but also causes pressure broadening of the Rb D_1 linewidth. Rubidium line broadening maximizes adsorption of laser light emitted by high-power solid devices, even if those are line narrowed.

6.1.1 Apparent polarisation

Since hyperpolarised gasses are produced diluted within a buffer gas, without separation, the calculated polarisation is somewhat disingenuous. Therefore to be able to compare the obtained polarisation with experiments that have separated the hyperpolarisation species from its buffer gas, it is useful to define the concept of *apparent polarisation* P_{app}.

$$P_{app} = P\frac{[NG]}{\sum_i [M_i]} \approx P\frac{p_{NG}}{p_{tot}} \tag{6.1}$$

This concept takes into account the scaling of the spin polarisation P, is taken into account via the noble gas number density $[NG]$, divided by the overall number density of all components M_i in the mixture [29, 30]. P_{app} provides a useful measure of the 'usable' polarisation in the

MR experiments accounting for when the hyperpolarisation gas is not separated from its buffer gas after SEOP.

Figure 6.1 displays data reprocessed from Six, 2012 [29] as to account for the apparent polarisation. The data shown here clearly indicates the both the dependence of total attainable polarisation on gas composition and, the importance of removing the hp gas from its SEOP buffer gas as to fully take advantage of the high spin polarisation state.

6.1.2 Cryogenic separation of hp gas

As to achieve the highest possible gas polarisations SEOP must be performed with low concentrations of the noble gas to be polarised. This is primarily due to the detrimental effect that high noble gas density, and thus, low buffer gas concentration has on the SEOP process.

Following SEOP, hp ^{129}Xe is cryogenically separated from the gas mixture. As to account for this dilution factor, under carefully chosen conditions to prevent polarization loss [31].

The outline of such technique tends to involve using a very slow flow of hp Gas, dilute within its buffer, to a a specially designed spiral of Pyrex glass, this *"freeze out cell"* is submerged within a dewar of liquid nitrogen. The assembly is kept within a homogeneous magnetic field typically within the $\sim 100's$ mT regime as to preserve the spin polarisation of the hp gas. Whereupon the hp gas will begin to solidify, after a given time the flow from the SEOP cell will be halted and a vacuum applied to the Pryex *"freeze out cell"* as to remove any remaining buffer gas. The *pure* hp gas may then be warmed back to room temperature as to return the hyperpolarised solid to the gas phase.

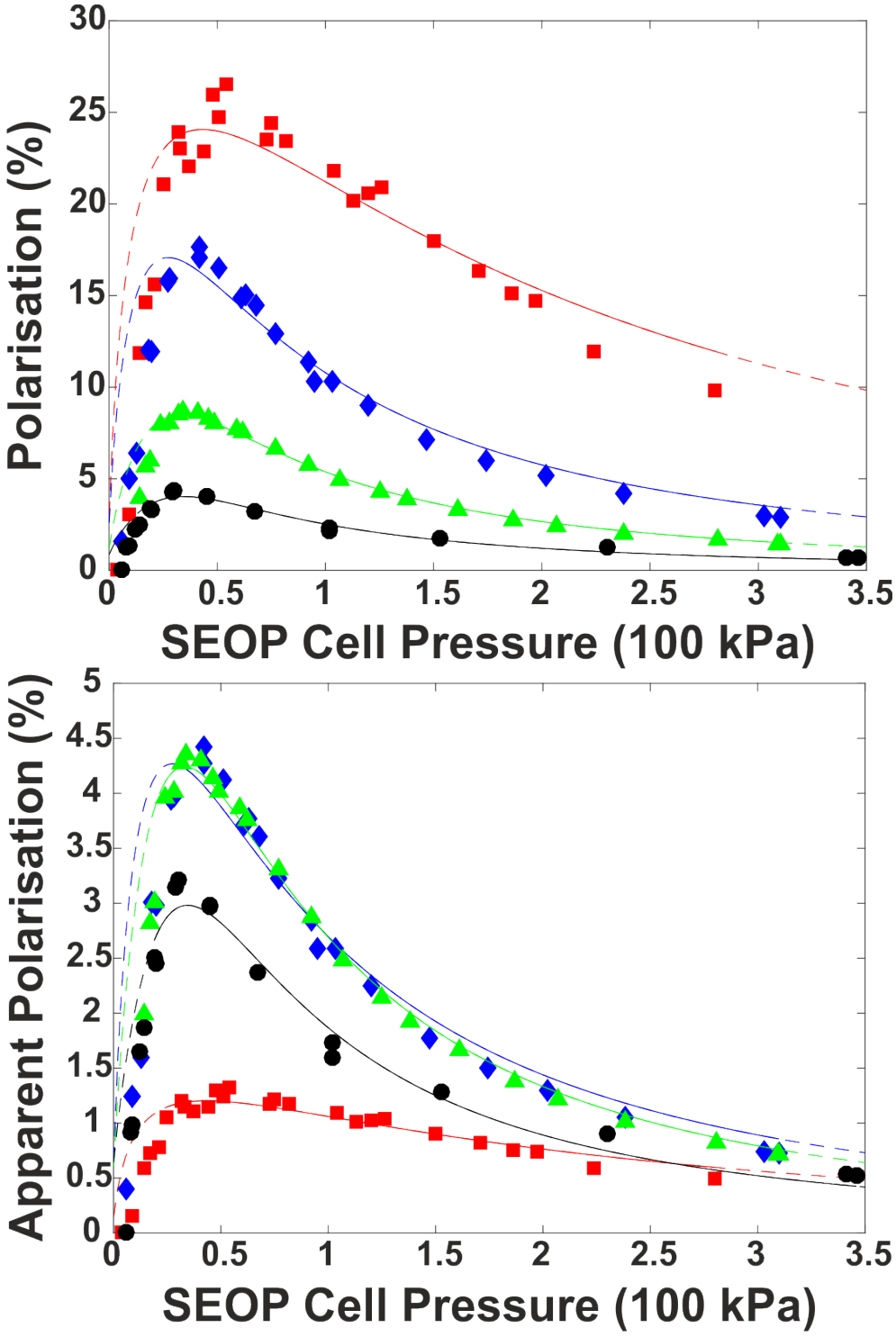


Figure 6.1: Apparent and Full Spin Polarisation as a function of SEOP cell pressures and ^{83}Kr N_2 gas compositions. Red squares: 5 % Kr, 95 % N_2; Blue diamonds: 25 % Kr, 75 % N_2; Green triangle: 49.5 % Kr, 50.5 % N_2; Black circles: 74.1 % Kr, 25.9 % N_2. Data is taken from reference [29, 30] and reprocessed to display (a) the calculated spin polarisation (not accounting for dilution) and (b) The Apparent Polarisation of the the data displayed in (a) with symbols retaining their meanings. Data analysis were performed as previously detailed in [29].

It is however only possible to utilise such a technique with gases such as ^{129}Xe which retain their hp state within the solid phase. To continue the example of ^{129}Xe when kept within a homogeneous magnetic field has been reported as T_1 of $\sim$ 87 min for a system used to produce medical grade hp ^{129}Xe [14].

Cryogenic separation thus adds a layer of complication to operational procedures for production of hp ^{129}Xe MRI. Further, a number of applications require multiple noble gas deliveries with, high polarization and high concentration is needed [7, 32–37]. Additionally, an extremely stable level of spin polarization is required for molecular imaging with hp ^{129}Xe biosensors using the hyperpolarised xenon chemical exchange saturation transfer (HyperCEST) methodology [18, 38–40]. Yet while cryogenic separation enables increased polarization in pure xenon gas it is inherently a *batch mode* production process and is unsuitable for translation to the continuous flow SEOP application such as the aforementioned HyperCEST methodologies.

In contrast ^{83}Kr with its large quadrupole moment leads to a rapid T_1 during the phase transition to a solid, on order of 4 s (see Figure 6.2, [41]). Whereas cryogenic separation may complicate and limit some hp ^{129}Xe applications, it is not an option at all for the hp ^{83}Kr production due to the fast quadrupolar relaxation.

To avoid cryogenic separation, SEOP at a high noble gas mole fraction has been explored in the past [7, 11, 15, 29, 30, 42]. Nevertheless, gas dilution is still required to ensure high spin polarization at the high production volumes required for MRI and the dilution therefore reduces MRI signal intensity per unit volume of inhaled gas. An innovative method developed by Kimura, Imai, Fujiwara, and coworkers [7, 11, 35], produces

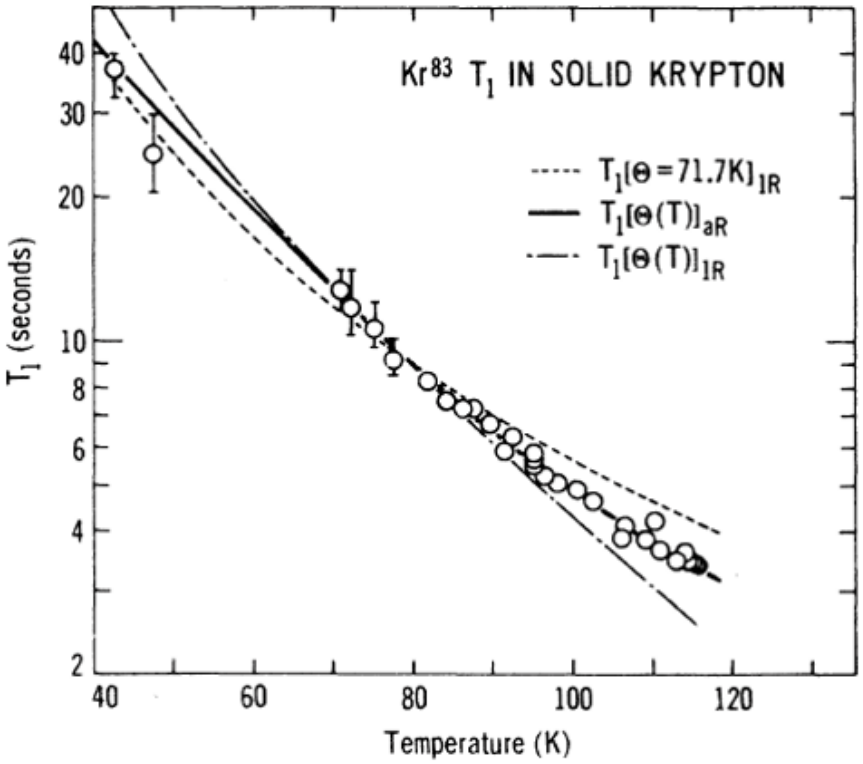


Figure 6.2: Longitudinal relaxation T_1 of solid ^{83}Kr reproduced from Cowgill *et al* 1973 [41] indicating the rapid relaxation of ^{83}Kr when solidifying.

a constant stream of 70 % concentrated hp ^{129}Xe but the polarization is typically in the $P = 10\,\%$ regime. In this work, ^{129}Xe and ^{83}Kr SEOP is attempted with mixtures containing molecular hydrogen as buffer gas and radiation quenching agent [43–47] that can subsequently be removed through catalytic combustion.

6.2 Spin Exchange Optical Pumping of ^{83}Kr and ^{129}Xe

6.2.1 Stopped Flow Spin Exchange Optical Pumping

The experimental apparatus used for batch mode SEOP to measure the polarisation of ^{129}Xe and N_2 is displayed in Figure 6.3 mixtures containing various concentrations of ^{129}Xe and ^{83}Kr were hyperpolarised in a borosilicate glass SEOP cell (length 120 mm, inner diameter = 28 mm) containing $\sim$ 1 gram of rubidium (99.75 % ; Alfa Aesar,Heysham,United Kingdom). The SEOP cell was seated within an aluminium oven with quartz windows and temperature controlled by use of a hot air gun. A set of double Helmholtz coils were used to provide a field of $\sim$ 5 mT across the SEOP cell. The cell is irradiated with laser light tuned to the D_1 transition of Rb using a Comet module (Spectra Physics) Laser with a 0.25 nm linewidth producing 23 W incident power at the SEOP cell entrance window. To monitor the D_2 florescence of Rb during SEOP process a HR2000+ Laser spectrometer (Ocean Optics, Fl, USA) was used.

For all experiments gas mixture's of 5 % Xe (or 5 % Kr), within the buffer gas (either N_2, CH_4 or H_2) were used. Noble gasses used in this work were naturally abundant (26.4 % for ^{129}Xe and 11.5 % for ^{83}Kr). Spin polarisation was determined as described by Six et al 2014 [24] and Meersmann et al 2015 [7].)

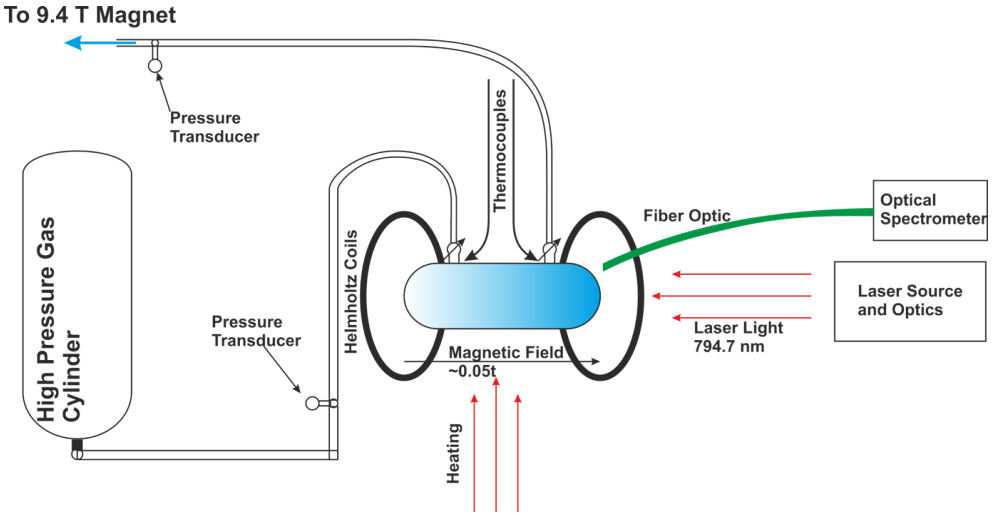


Figure 6.3: Experimental apparatus for batch mode SEOP experiments. A pair of Helmholtz coils are used to provide a magnetic field of $\sim$ 10 mt parallel to the SEOP cell and circularly polarized laser beam. The indicated optical spectrometer measures the D_2 florescence line ($\sim$ 780 nm) at the front of the SEOP cell via a fibre optic cable.

6.2.2 On Resonance Rubidium Hydride Formation.

The high spin-polarization values for ^{83}Kr with the H_2 in Figure 6.4 were achieved repeatedly over the course of 30 h SEOP over a time span of about 1 week and for ^{129}Xe over a duration of at least 6 h of continuous SEOP despite the formation of rubidium hydrides (RbH) during on-resonance D_1 laser irradiation [48].

Over time, a white RbH deposition was observed on all SEOP cell surfaces but to a lesser extent at the laser entry window. Furthermore, SEOP cell recycling, causing substantial removal of the RbH, was possible by increasing the temperature to 480 K for about 30 min with on-going laser irradiation while the cell was connected, via a Rb trap, to a vacuum pump.

Although excessive RbH build-up on the cell entry window will reduce laser irradiation, deposition on other cell surfaces may not necessarily adversely affect the achievable noble gas spin polarization. Previous work

demonstrated that the ^{129}Xe T_1 relaxation time increases for this spin $I = 3/2$ isotope because of RbH buildup [21, 49, 50]. RbH surface coating may therefore also reduce the ^{83}Kr, T_1 relaxation rates and improve SEOP. A detailed study by Cates and co-workers explored the effect of RbH surface deposition on the T_1 relaxation of ^{129}Xe as a function of field strength ($\geq$ 0.08 T) and temperature ($\leq$ 340 K) in a spherical 25 mm diameter cell [51]. Based on the results one may interpolate ^{129}Xe T_1 times in excess of 400 s at the conditions used in the current work, causing little interference during rapid SEOP.

6.2.3 Molecular hydrogen as a radiation quenching agent

High polarization values obtained with H_2 in Figure 6.4 i.e., in the absence of any N_2, are remarkable. Depending on SEOP temperature, the gas mixtures usually contain at least a partial pressure of 5 kPa of molecular nitrogen for radiation quenching to prevent radiation trapping of arbitrarily polarized fluorescence photons that severely reduce Rb polarization [27, 28].

Previous work investigating the efficacy of H_2 to quench Rb radiation found that the effective cross-sections for quenching of the D_1 and D_2 transitions are about 1 order of magnitude smaller for H_2 than for N_2 [43].

An empirical model of radiation quenching with H_2 is reported by Rosenberry but is limited to buffer gas pressures below 7 kPa [52]. Generally, H_2 has found little consideration as quenching agent at high gas density and temperature conditions typically used for SEOP production of hp

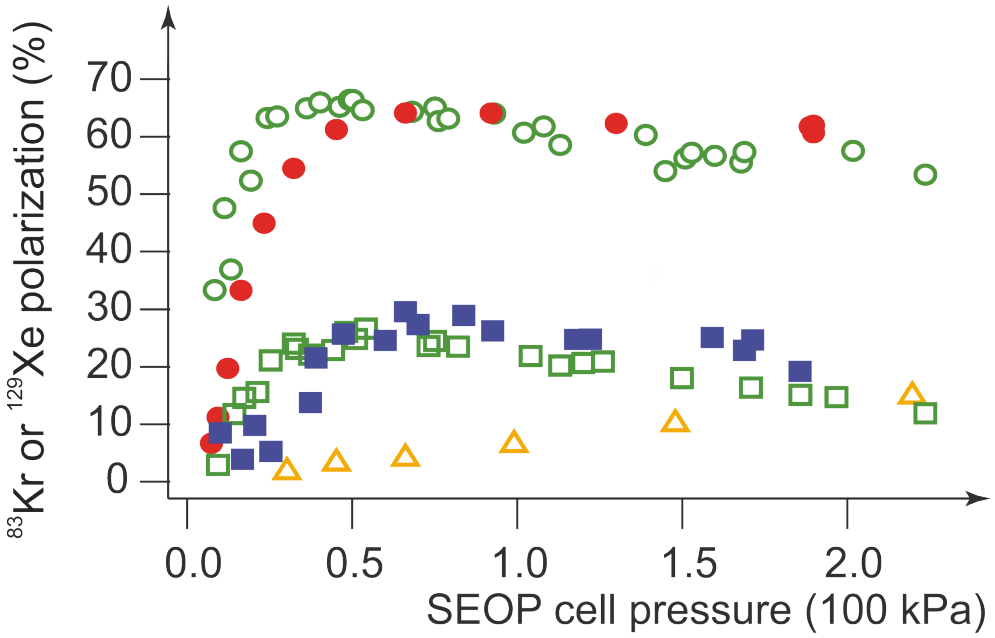


Figure 6.4: ^{83}Kr and ^{129}Xe polarisation as a function of SEOP-generated ^{129}Xe and ^{83}Kr spin polarization in mixtures containing 5 % noble gas and 95 % buffer gas as a function of total SEOP gas pressure. Specifically gas mixes are indicated by, Blue squares: 5 % Kr, 95 % H_2; Green squares: 5 % Kr, 95 % N_2; Red circles: 5 % Xe, 95 % H_2; Green circles: 5 % Xe, 95 % N_2; Yellow triangles: 5 % Xe, 95 % CH_4. Using H_2 as buffer gas, the ^{129}Xe spin polarization (obtained at 378 K) is shown in red filled circles and the ^{83}Kr polarization (obtained at 440 K) is displayed as blue filled squares. For comparison, previous data from ref. 39 with N_2 as buffer gas is shown for ^{129}Xe SEOP at 378 K (green open circles) and for ^{83}Kr SEOP at 433 K (green open squares). In contrast, CH_4 is an inefficient buffer gas that led to low spin polarization (orange open triangles)

^{129}Xe or hp ^{83}Kr for MRI applications.

The measurement of D_1 fluorescence at 795 nm, obscured by high-power laser radiation, is experimentally very demanding. Instead, the Rb D_2 fluorescence during SEOP was straightforwardly monitored in this work. The mixing cross-sections between the electronic states Rb* $5^2P_{1/2}$ and Rb* $5^2P_{3/2}$ are comparable for H_2 and N_2 [43] and the D_2 fluorescence should therefore provide at least qualitative insights into D_1 radiation quenching efficiency of the molecular hydrogen.

Figure 6.5 demonstrates that H_2 serves as a remarkably efficient radiation quenching agent at partial pressures above $\sim$ 40–60 kPa, where little fluorescence was detected during SEOP even at the very high tempera-

ture of 433 K. Therefore, H_2 can be used as radiation quenching agent during SEOP but the required partial pressure is about 10 times higher than that for N_2, in agreement with previous measurements of quenching cross-section reported by Hrycyshyn [43].

Below this critical partial pressure, radiation quenching is largely incomplete and a substantial difference in the D_2 fluorescence is observed between SEOP of ^{129}Xe and ^{83}Kr. Figure 6.5 depicts a higher fluorescence count at the elevated temperature used for ^{83}Kr SEOP (in the $433 - 440$ K range) where the Rb density is almost 20-fold increased compared with that for ^{129}Xe SEOP at 378 K.

At low buffer gas pressure, where radiation quenching is incomplete, the high Rb density for ^{83}Kr SEOP produces significantly more radiation trapping. The consequences of the increased radiation trapping can be observed in Figure 6.4 where, at buffer gas pressures below $\sim$ 50 KPa, the noble gas polarization obtained through SEOP with H_2 falls short compared with that with N_2.

The effect of Rb density on radiation trapping was previously studied at extremely low H_2 partial pressure (< 0.1 Pa) for the purpose of SEOP of dissociated atomic hydrogen [44–47]. Under these conditions, radiation quenching is effectively non existent and radiation trapping can be limited only by keeping the Rb densities very low through SEOP temperatures around or below 318 K.

In the current work, no adverse effect of H_2 as buffer gas at SEOP pressures above 40–50 kPa (with the exception of reversible RbH formation, discussed above in Section 6.2.2) was found compared with SEOP with N_2 under otherwise identical conditions, regardless of the temperature.

Note, that the high IR quenching cross section of H_2 is a rare exception

among small molecules without chemical double or triple bonds and Figure 6.4 and Figure 6.5 includes data obtained with CH_4 as buffer gas for comparison. The inefficient small quenching cross section of CH_4 [53] leads to an increased IR count of the D_2 transition line (Figure 6.5) and a correspondingly low ^{129}Xe spin polarization below that of hp ^{83}Kr Figure 6.4, a problem that was previously solved using a ternary mixture of 5 % Xe, 85 % CH_4, and 10 % N_2 [54].

However this solution was an imperfect one as, even with the catalytic separation technique, the hp gas will still be dilute by a factor of a two thirds due to the nitrogen. Further issues arise when considering molecular methane as a buffer gas for this process, namely that the reaction pathway leads produces H_2O and CO_2. While the H_2O may be removed by condensation away the CO_2 provides a greater challenge to rapidly remove while retaining polarisation of the hp gas in question. Further, incomplete combustion in the aforementioned reaction of CH_4 may lead to the production of carbon monoxide, a significant hazard if attempting to integrate this process into a clinical, or pre-clinical setting.

6.3 Catalytic separation of H_2 hyperpolarisation mixes

Efficient SEOP of noble gases in H_2 mixtures opens a path for oxidative buffer gas elimination that produces H_2O as the only reaction product. Most of the generated water vapor can straightforwardly be removed through condensation at ambient temperature. The resulting gas phase is composed of the purified hp noble gas in addition to a small remaining quantity of the water vapor.

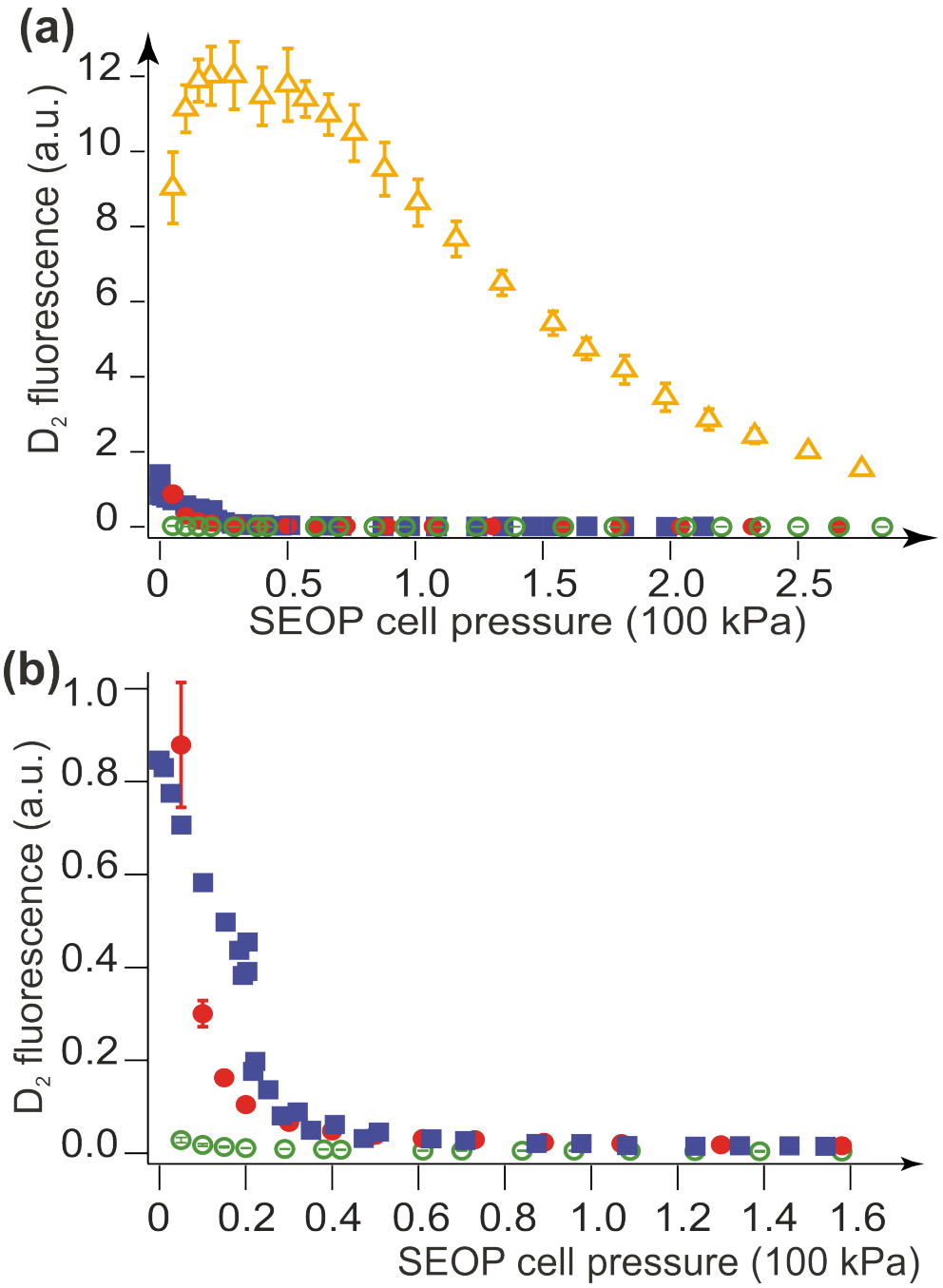


Figure 6.5: The D_2 fluorescence at 780 nm (in arbitrary units, a.u.) measured at the front of the cell during SEOP as indicated in Figure 6.3 for a range of gas mixes as indicated by, Blue squares: 5 % Kr, 95 % H_2; Green squares: 5 % Kr, 95 % N_2; Red circles: 5 % Xe, 95 % H_2; Green circles: 5 % Xe, 95 % N_2; Yellow triangles: 5 % Xe, 95 % CH_4. (a) indicated that sufficient radiation quenching with H_2 at 378 K (red circles) and at 433 K (blue squares) requires pressures above 50 kPa. Using N_2 (green open circles), the D_2 radiation is efficiently quenched at pressures above 5 kPa. (b) shows the high D_2 fluorescence measured for ^{129}Xe SEOP at 378 K with methane that is a very ineffective quenching gas.

Catalytic combustion experiments were performed within a 1.5 mm glassed walled vessel bespoke reaction vessel described in Figure 6.6, that contained 25 mg Pt/Al_2O_3 catalyst powder (1.5 wt % dry loading Pt on alumina).

Previous work demonstrated qualitatively the feasibility of hp ^{129}Xe MRI [54] of a methane combustion zone. To quantify the effect of catalytic hydrogen combustion on the noble gas spin polarization, the reaction vessel in Figure 6.6 was placed inside a home built probe tuned to either the resonance frequency of ^{83}Kr or ^{129}Xe at 9.4 T. As an additional safety measure catalytic reactions were performed at pressures below 30 kPa, with the reactor pressure being metered independently.

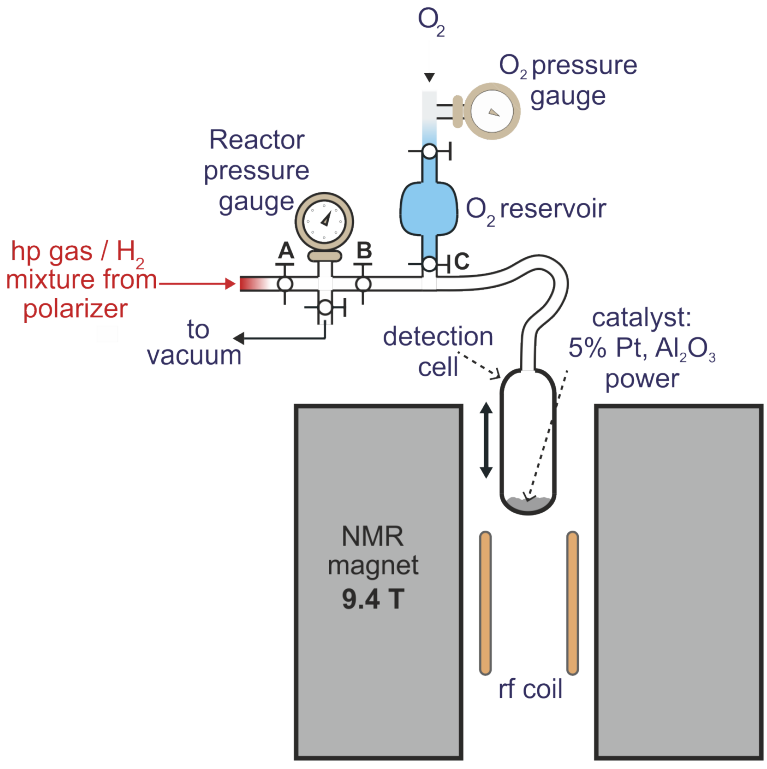


Figure 6.6: experimental apparatus used for combustion experiments. Using pressure equalization, the hp gas - H_2 mixture was shuttled to the reactor/detection cell containing the Pt catalyst. Oxygen was then injected from the O_2 reservoir to trigger the reaction.

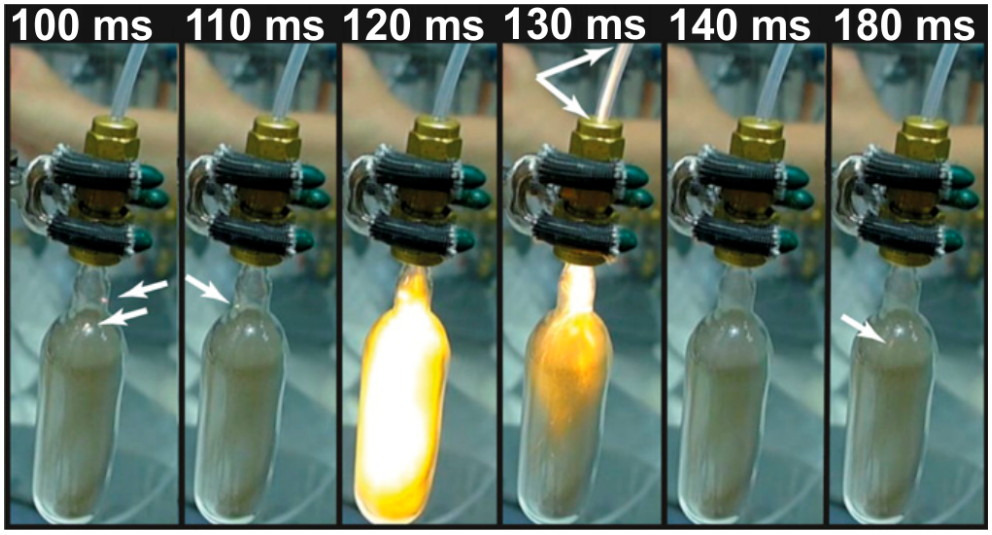


Figure 6.7: Exported Photos from 100 frame per second video of the reactor upon O_2 delivery. Approximately 100 *ms* after opening of valve C, minor combustion zones became visible (see white arrows), indicating that the catalytic oxidation of the H_2 gas had commenced. The major combustion event took place 20–30 ms thereafter and the combustion appeared to be largely completed within 80 ms. The reactor outside temperature increase was limited to approximately 5 K.

hp noble gas–H_2 mixture was shuttled into the reactor chamber that contained a small quantity of Pt. Monitoring of the signal decay was performed by use of a train of small flip angle rf pulsed applied at fixed time delays.

Over time through NMR spectroscopy provided the baseline data, shown as open circles in Figure 6.8, for hp ^{129}Xe and in Figure 6.9 for hp ^{83}Kr. For oxidative H_2 removal, O_2 was added, which led to hydrogen combustion within < 100 ms due to the presence of the Pt catalyst, as depicted in Figure 6.7.

The reactor pressure during this process was monitored (Figure 6.8 and Figure 6.9) but potential short pressure increases during the reaction were not detected at the time resolution of the pressure gauge. Upon adding O_2, slightly above the stoichiometric ratio, the pressure decreased within 15 s as the sole reaction product, H_2O, had condensed rapidly upon cooling. The temperature increase measured outside the reactor

was limited to 5 K and the final reactor pressure of 4.7 $\pm$ 0.5 kPa was close to that expected from the combined water vapour pressure at ambient temperature (3.2 kPa at 298 K) and the noble gas partial pressure (1.2 $-$ 1.3 kPa).

Monitoring the hp ^{129}Xe signal intensity (Figure 6.8), an initial signal increase was observed upon O_2 delivery, caused by hp ^{129}Xe influx from the connecting PFA tubing with 1.6 mm inner diameter that was pushed into the reaction chamber by the oxygen gas. Within 20 s, gas convection and diffusion returned the signal intensity approximately to the baseline value, indicating that the nuclear spin state had experienced no significant depolarization.

However, after the reaction, the ^{129}Xe relaxation was accelerated due to a small excess of paramagnetic O_2 (approximately 0.7 kPa partial pressure). Increasing the O_2 excess to 7.5 $\pm$ 0.5 kPa led to further accelerated ^{129}Xe signal decay.

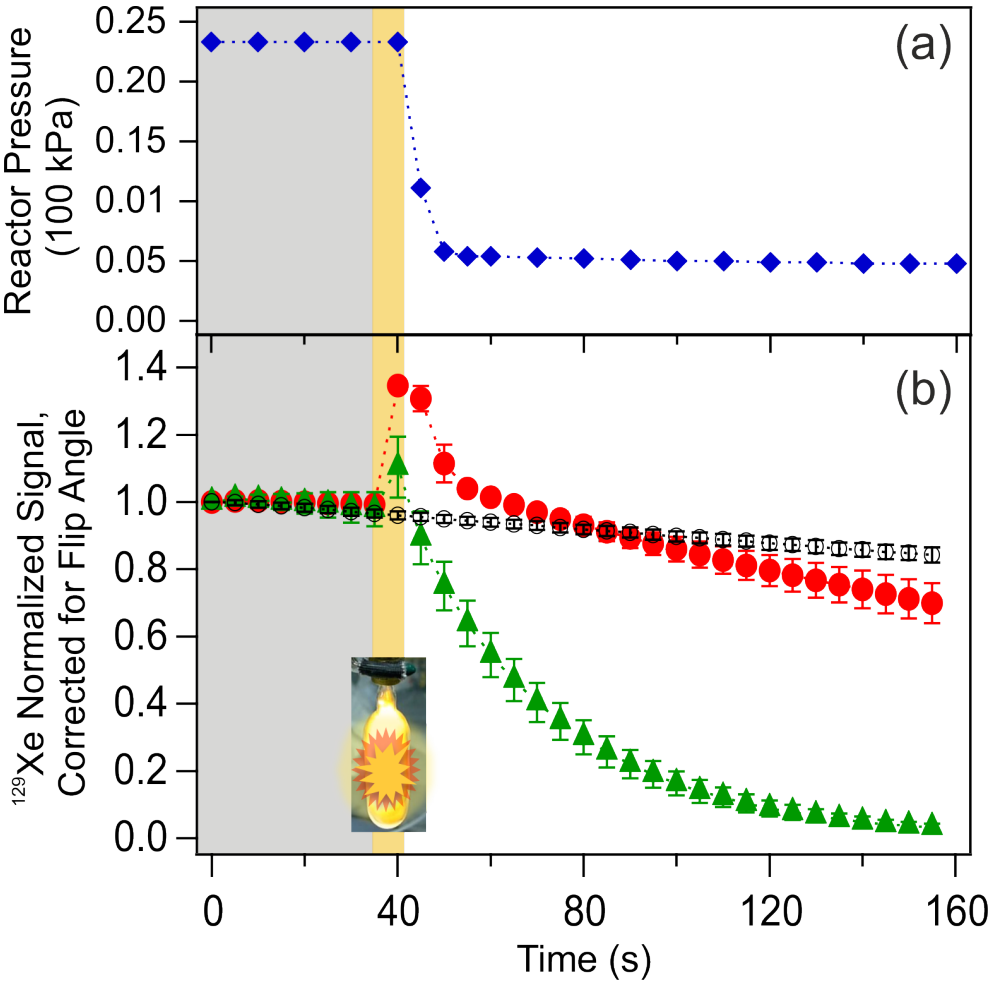


Figure 6.8: (a) In situ reactor pressure measurements (blue diamonds) during the combustion reaction of a 5 % ^{129}Xe 95 % H_2 gas mixture, with oxygen reservoir tap (tap C, Figure 6.6) opened at $t = 40$ s adding 11.2 $\pm$ 0.4 kPa partial pressure of O_2. Average initial partial pressure of $H_2 = 22.0 \pm 1$ kPa and the oxygen addition caused the pressure drop due to the combustion reaction (a short term pressure increase, if present, was not observed at the time resolution of the gauge). (b) NMR measurements performed in separate experiments without pressure gauge (i.e., tap B, Figure 6.6 was kept shut to reduce the dead volume of the experiment). Normalized integrated hp ^{129}Xe NMR signals following a 9° pulse during the catalytic oxidation with 13.4 $\pm$ 0.4 kPa oxygen (red circles) or 20.5 $\pm$ 0.5 kPa (green triangles) added at $t = 40$ s. Average initial partial pressure of $H_2 = 25.5 \pm 1$ kPa. Control signals with no oxygen/combustion (tap C, Figure 6.6, remained closed) shown as black open circles. Signal intensity data were corrected for flip-angle attenuation and are the average from three repeat measurements.

The hp ^{83}Kr data in Figure 6.9 demonstrate that combustion caused no signal loss and, in contrast to ^{129}Xe, the ^{83}Kr gas-phase relaxation was slowed after the reaction. The decrease of the ^{83}Kr T_1 relaxation was likely a consequence of competitive co-adsorption of water molecules on

the reactor surface that have been found previously to reduce krypton surface interactions [55].

The very low gyromagnetic ratio makes ^{83}Kr insensitive to paramagnetic relaxation even at higher (7.5 ± 0.5 kPa) oxygen partial pressure (Figure 6.9) [30]. An initial short-term signal increase upon O_2 gas delivery, present in the ^{129}Xe data, was not observed because hp ^{83}Kr located in the connecting PFA tubing depolarized due to fast quadrupolar T_1 relaxation in the presence of the fluorocarbon surface [56].

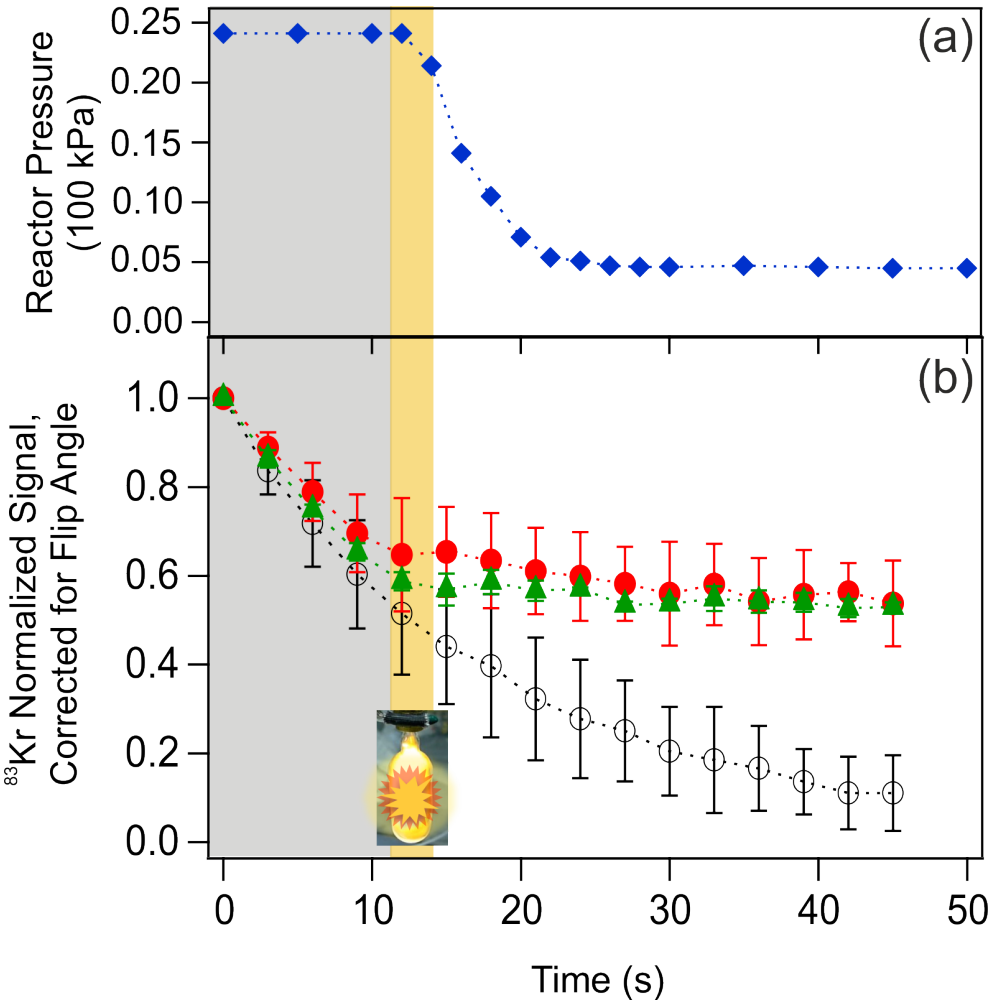


Figure 6.9: (a) Pressure curve of combustion reaction of a 5 % ^{83}Kr 95 % H_2 gas mixture with 11.2 ± 4 kPa O_2 added after 12 s causing the reaction and observed pressure drop. Average initial partial pressure of H_2 = 23.5 ± 1 kPa. (b) Normalized integrated hyperpolarised ^{83}Kr NMR signals following a 12° pulse during the combustion reaction adding 13.4 ± 0.4 kPa (red circles) and 20.5 ± 0.5 kPa (green triangles) partial pressure of oxygen. Average initial partial pressure of H_2 = 27.5 ± 2.5 kPa. Black open circles show control signals for a 5 % Kr 95 % H_2 gas mixture with no combustion. Signal intensity data were corrected for flip-angle attenuation and are the average from three repeat measurements.

6.4 Conclusions

To conclude, the data presented within this chapter presents for the first time to our knowledge a near instantaneous method of removing a SEOP buffer gas while retaining the hyperpolarisation spin state of ^{83}Kr. Furthermore, this method is of significant interest to the construction of a

fully automated production method for hyperpolarisation ^{129}Xe without the need for expensive, and technically complex cryogenic separation techniques.

However, challenges do arise, namely that the produced hp gas is at a low pressure after catalytic buffer gas removal it must be returned to atmospheric pressure for a range of application such as biomedical or flow measurements. Recompression has previously been demonstrated with little polarization loss for hp ^{129}Xe [11, 30] and acceptable 1/4 polarization loss for hp ^{83}Kr [30]. Based on the result in this work, this would suggest that purified hp ^{83}Kr with 21 % spin polarisation is now feasible, a sevenfold improvement over recent hp ^{83}Kr work with 3 % apparent polarization that already allowed for MRI with 0.795×0.635 mm^2 resolution in *ex vivo* lungs [3].

Note that the experimental setting was for the sole purpose of proof of concept demonstration and can be substituted by combustion under continuous flow within a catalytic converter such as those discussed in Chapters 5. Furthermore, direct contact between H_2 and O_2 may be avoidable through the use of recyclable metal oxides similar to those used in chemical looping combustion [57]. Reactive H_2 removal may take place in a small flow-through catalytic converter placed downstream from the SEOP cell that would facilitate gas transport through the generated pressure gradient. Kimura, Imai, Fujiwara, and coworkers used a peristaltic pump for continuous hp ^{129}Xe recompression after continuous flow SEOP at low pressures [7, 11, 35], a concept that could be further extended by flow-through catalytic buffer gas removal before recompression. Enabling on-demand production of an uninterrupted, continuous flow of hp ^{129}Xe at high spin polarization and purity, this concept should be of high value

for a variety of applications ranging from material science to biomedical MRI. If required, hp ^{129}Xe could also be stored before recompression (and even before H_2 removal), using the extraordinary slow T_1 relaxation of ^{129}Xe described in the past for gas phase xenon under certain conditions [58–61].

Finally, the presented concept does not involve any toxic reagents or reaction products and the complete absence of nitrogen and carbon prevents any accidental generation of nitrogen oxides (NOx) and carbon monoxide (CO) during combustion. Any H_2 passing through the buffer gas removal step, however unlikely, can straightforwardly be detected through reliable hydrogen microsensors.

Bibliography

[1] N. J. Rogers, F. Hill-Casey, K. F. Stupic, J. S. Six, C. Lesbats, S. P. Rigby, J. Fraissard, G. E. Pavlovskaya, and T. Meersmann, "Molecular hydrogen and catalytic combustion in the production of hyperpolarized ^{83}Kr and ^{129}Xe MRI contrast agents," *Proceedings of the National Academy of Sciences*, vol. 113, pp. 3164–3168, mar 2016.

[2] J. P. Mugler and T. A. Altes, "Hyperpolarized ^{129}Xe MRI of the human lung," *Journal of Magnetic Resonance Imaging*, vol. 37, pp. 313–331, feb 2013.

[3] D. M. L. Lilburn, C. Lesbats, J. S. Six, E. Dubuis, L. Yew-Booth, D. E. Shaw, M. G. Belvisi, M. A. Birrell, G. E. Pavlovskaya, and T. Meersmann, "Hyperpolarized ^{83}Kr magnetic resonance imaging of alveolar degradation in a rat model of emphysema," *Journal of The Royal Society Interface*, vol. 12, pp. 20150192–20150192, may 2015.

[4] Z. Liu, T. Araki, Y. Okajima, M. Albert, and H. Hatabu, "Pulmonary hyperpolarized noble gas MRI: Recent advances and perspectives in clinical application," *European Journal of Radiology*, vol. 83, pp. 1282–1291, jul 2014.

[5] L. L. Walkup and J. C. Woods, "Translational applications of hyperpolarized ^{3}He and ^{129}Xe," *NMR in Biomedicine*, vol. 27, pp. 1429–1438, dec 2014.

[6] K. Ruppert, "Biomedical imaging with hyperpolarized noble gases," *Reports on Progress in Physics*, vol. 77, p. 116701, nov 2014.

[7] T. Meersmann and E. Brunner, eds., *Hyperpolarized Xenon-129 Magnetic Resonance*. New Developments in NMR, Cambridge: Royal Society of Chemistry, 2015.

[8] B. Driehuys, G. D. Cates, E. Miron, K. Sauer, D. K. Walter, and W. Happer, "High-volume production of laser-polarized ^{129}Xe," *Applied Physics Letters*, vol. 69, pp. 1668–1670, sep 1996.

[9] I. C. Ruset, S. Ketel, and F. W. Hersman, "Optical Pumping System Design for Large Production of Hyperpolarized ^{129}Xe," *Physical Review Letters*, vol. 96, p. 053002, feb 2006.

[10] F. W. Hersman, I. C. Ruset, S. Ketel, I. Muradian, S. D. Covrig, J. Distelbrink, W. Porter, D. Watt, J. Ketel, J. Brackett, A. Hope, and S. Patz, "Large Production System for Hyperpolarized ^{129}Xe for Human Lung Imaging Studies," *Academic Radiology*, vol. 15, pp. 683–692, jun 2008.

[11] H. Imai, J. Fukutomi, A. Kimura, and H. Fujiwara, "Effect of reduced pressure on the polarization of ^{129}Xe in the production of hyperpolarized ^{129}Xe gas: Development of a simple continuous flow mode hyperpolarizing system working at pressures as low as 0.15 atm," *Concepts in Magnetic Resonance Part B: Magnetic Resonance Engineering*, vol. 33B, pp. 192–200, aug 2008.

[12] G. Schrank, Z. Ma, A. Schoeck, and B. Saam, "Characterization of a low-pressure high-capacity ^{129}Xe flow-through polarizer," *Physical Review A*, vol. 80, p. 063424, dec 2009.

[13] J. P. Mugler, T. A. Altes, I. C. Ruset, I. M. Dregely, J. F. Mata, G. W. Miller, S. Ketel, J. Ketel, F. W. Hersman, and K. Ruppert, "Simultaneous magnetic resonance imaging of ventilation distribution and gas uptake in the human lung using hyperpolarized xenon-129," *Proceedings of the National Academy of Sciences*, vol. 107, pp. 21707–21712, dec 2010.

[14] G. Norquay, S. R. Parnell, X. Xu, J. Parra-Robles, and J. M. Wild, "Optimized production of hyperpolarized ^{129}Xe at 2 bars for in vivo lung magnetic resonance imaging," *Journal of Applied Physics*, vol. 113, p. 044908, jan 2013.

[15] P. Nikolaou, A. M. Coffey, L. L. Walkup, B. M. Gust, N. Whiting, H. Newton, S. Barcus, I. Muradyan, M. Dabaghyan, G. D. Moroz, M. S. Rosen, S. Patz, M. J. Barlow, E. Y. Chekmenev, and B. M. Goodson, "Near-unity nuclear polarization with an open-source ^{129}Xe hyperpolarizer for NMR and MRI," *Proceedings of the National Academy of Sciences*, vol. 110, pp. 14150–14155, aug 2013.

[16] M. S. Freeman, K. Emami, and B. Driehuys, "Characterizing and modeling the efficiency limits in large-scale production of hyperpolarized ^{129}Xe," *Physical Review A*, vol. 90, p. 023406, aug 2014.

[17] M. M. Spence, S. M. Rubin, I. E. Dimitrov, E. J. Ruiz, D. E. Wemmer, A. Pines, S. Q. Yao, F. Tian, and P. G. Schultz, "Functionalized xenon as a biosensor," *Proceedings of the National Academy of Sciences*, vol. 98, pp. 10654–10657, sep 2001.

[18] L. Schroder, T. J. Lowery, C. Hilty, D. E. Wemmer, and A. Pines, "Molecular Imaging Using a Targeted Magnetic Resonance Hyperpolarized Biosensor," *Science*, vol. 314, pp. 446–449, oct 2006.

[19] B. C. Grover, "Noble-Gas NMR Detection through Noble-Gas-Rubidium Hyperfine Contact Interaction," *Physical Review Letters*, vol. 40, pp. 391–392, feb 1978.

[20] S. R. Schaefer, G. D. Cates, and W. Happer, "Determination of spin-exchange parameters between optically pumped rubidium and Kr," *Physical Review A*, vol. 41, pp. 6063–6070, jun 1990.

[21] C. H. Volk, T. M. Kwon, J. G. Mark, Y. B. Kim, and J. C. Woo, "Measurement of the Rb-^{131}Xe Spin-Exchange Cross Section in ^{131}Xe Relaxation Studies," *Physical Review Letters*, vol. 44, pp. 136–139, jan 1980.

[22] R. Butscher, G. Wäckerle, and M. Mehring, "Nuclear quadrupole surface interaction of gas phase ^{83}Kr: comparison with ^{131}Xe," *Chemical Physics Letters*, vol. 249, pp. 444–450, feb 1996.

[23] G. E. Pavlovskaya, Z. I. Cleveland, K. F. Stupic, R. J. Basaraba, and T. Meersmann, "Hyperpolarized krypton-83 as a contrast agent for magnetic resonance imaging," *Proceedings of the National Academy of Sciences*, vol. 102, pp. 18275–18279, dec 2005.

[24] J. S. Six, T. Hughes-Riley, D. M. Lilburn, A. C. Dorkes, K. F. Stupic, D. E. Shaw, P. G. Morris, I. P. Hall, G. E. Pavlovskaya, and T. Meersmann, "Pulmonary MRI contrast using Surface Quadrupolar Relaxation (SQUARE) of hyperpolarized ^{83}Kr," *Magnetic Resonance Imaging*, vol. 32, pp. 48–53, jan 2014.

[25] A. Comment, S. Jannin, J.-N. Hyacinthe, P. Miéville, R. Sarkar, P. Ahuja, P. R. Vasos, X. Montet, F. Lazeyras, J.-P. Vallée, P. Hautle, J. A. Konter, B. van den Brandt, J.-P. Ansermet, R. Gruetter, and G. Bodenhausen, "Hyperpolarizing Gases via Dynamic Nuclear Polarization and Sublimation," *Physical Review Letters*, vol. 105, p. 018104, jul 2010.

[26] A. Capozzi, C. Roussel, A. Comment, and J.-N. Hyacinthe, "Optimal Glass-Forming Solvent Brings Sublimation Dynamic Nuclear Polarization to ^{129}Xe Hyperpolarization Biomedical Imaging Standards," *The Journal of Physical Chemistry C*, vol. 119, pp. 5020–5025, mar 2015.

[27] W. Happer, "Optical Pumping," *Reviews of Modern Physics*, vol. 44, pp. 169–249, apr 1972.

[28] M. E. Wagshul and T. E. Chupp, "Optical pumping of high-density Rb with a broadband dye laser and GaAlAs diode laser arrays: Application to ^{3}He polarization," *Physical Review A*, vol. 40, pp. 4447–4454, oct 1989.

[29] J. S. Six, T. Hughes-Riley, K. F. Stupic, G. E. Pavlovskaya, and T. Meersmann, "Pathway to Cryogen Free Production of Hyperpolarized Krypton-83 and Xenon-129," *PLoS ONE*, vol. 7, no. 11, 2012.

[30] T. Hughes-Riley, J. S. Six, D. M. Lilburn, K. F. Stupic, A. C. Dorkes, D. E. Shaw, G. E. Pavlovskaya, and T. Meersmann, "Cryogenics free production of hyperpolarized ^{129}Xe and ^{83}Kr for biomedical MRI

applications," *Journal of Magnetic Resonance*, vol. 237, pp. 23–33, dec 2013.

[31] N. N. Kuzma, B. Patton, K. Raman, and W. Happer, "Fast Nuclear Spin Relaxation in Hyperpolarized Solid ^{129}Xe," *Physical Review Letters*, vol. 88, p. 147602, mar 2002.

[32] D. Baumer, E. Brunner, P. Blümler, P. P. Zänker, and H. W. Spiess, "NMR Spectroscopy of Laser-Polarized ^{129}Xe Under Continuous Flow: A Method To Study Aqueous Solutions of Biomolecules," *Angewandte Chemie International Edition*, vol. 45, pp. 7282–7284, nov 2006.

[33] Z. I. Cleveland, H. E. Moller, L. W. Hedlund, and B. Driehuys, "Continuously Infusing Hyperpolarized ^{129}Xe into Flowing Aqueous Solutions Using Hydrophobic Gas Exchange Membranes," *The Journal of Physical Chemistry B*, vol. 113, pp. 12489–12499, sep 2009.

[34] M. Duewel, N. Vogel, C. K. Weiss, K. Landfester, H.-W. Spiess, and K. Münnemann, "Online Monitoring of Styrene Polymerization in Miniemulsion by Hyperpolarized 129-Xenon NMR Spectroscopy," *Macromolecules*, vol. 45, pp. 1839–1846, feb 2012.

[35] H. Imai, H. Matsumoto, E. Miyakoshi, S. Okumura, H. Fujiwara, and A. Kimura, "Regional fractional ventilation mapping in spontaneously breathing mice using hyperpolarized ^{129}Xe MRI," *NMR in Biomedicine*, vol. 28, pp. n/a–n/a, oct 2014.

[36] G. Norquay, G. Leung, N. J. Stewart, G. M. Tozer, J. Wolber, and J. M. Wild, "Relaxation and exchange dynamics of hyperpolarized ^{129}Xe in human blood," *Magnetic Resonance in Medicine*, vol. 74, pp. 303–311, aug 2015.

[37] A. Causier, G. Carret, C. Boutin, T. Berthelot, and P. Berthault, "3D-printed system optimizing dissolution of hyperpolarized gaseous species for micro-sized NMR," *Lab Chip*, vol. 15, no. 9, pp. 2049–2054, 2015.

[38] C. Witte, V. Martos, H. M. Rose, S. Reinke, S. Klippel, L. Schröder, and C. P. R. Hackenberger, "Live-cell MRI with Xenon Hyper-CEST Biosensors Targeted to Metabolically Labeled Cell-Surface Glycans," *Angewandte Chemie International Edition*, vol. 54, pp. 2806–2810, feb 2015.

[39] Y. Wang and I. J. Dmochowski, "Cucurbit[6]uril is an ultrasensitive ^{129}Xe NMR contrast agent," *Chem. Commun.*, vol. 51, no. 43, pp. 8982–8985, 2015.

[40] N. Tassali, N. Kotera, C. Boutin, E. Léonce, Y. Boulard, B. Rousseau, E. Dubost, F. Taran, T. Brotin, J.-P. Dutasta, and P. Berthault, "Smart Detection of Toxic Metal Ions, Pb 2+ and Cd 2+ , Using a ^{129}Xe NMR-Based Sensor," *Analytical Chemistry*, vol. 86, pp. 1783–1788, feb 2014.

[41] D. F. Cowgill and R. E. Norberg, "Spin-lattice Relaxation and Chemical Shift of ^{83}Kr in Solid and Lifiuid Krypton," *Physical Review B*, vol. 8, pp. 4966–4974, dec 1973.

[42] P. Nikolaou, A. M. Coffey, L. L. Walkup, B. M. Gust, C. D. LaPierre, E. Koehnemann, M. J. Barlow, M. S. Rosen, B. M. Goodson, and E. Y. Chekmenev, "A 3D-Printed High Power Nuclear Spin Polarizer," *Journal of the American Chemical Society*, vol. 136, pp. 1636–1642, jan 2014.

[43] E. S. Hrycyshyn and L. Krause, "Inelastic collisions between excited alkali atoms and molecules. VII. Sensitized fluorescence and quenching in mixtures of rubidium with H_2 , HD, D_2 , N_2 , CH_4 , CD_4 , C $_2H_4$, and C_2H_6," *Canadian Journal of Physics*, vol. 48, pp. 2761–2768, nov 1970.

[44] L. Young, R. Holt, M. Green, and R. Kowalczyk, "Laser-driven polarized sources of hydrogen and deuterium," *Nuclear Physics A*, vol. 497, pp. 529–533, jun 1989.

[45] S. G. Redsun, R. J. Knize, G. D. Cates, and W. Happer, "Production of highly spin-polarized atomic hydrogen and deuterium by spin-exchange optical pumping," *Physical Review A*, vol. 42, pp. 1293–1301, aug 1990.

[46] L. Anderson and T. Walker, "The effect of radiation trapping on a high field spin exchange optically pumped target," *Nuclear Instruments and Methods in Physics Research Section A: Accelerators, Spectrometers, Detectors and Associated Equipment*, vol. 316, pp. 123–127, jun 1992.

[47] L. Anderson and T. Walker, "Spin exchange optical pumping of hydrogen and deuterium nuclei," *Nuclear Instruments and Methods in Physics Research Section A: Accelerators, Spectrometers, Detectors and Associated Equipment*, vol. 357, pp. 220–224, apr 1995.

[48] A. Tam, G. Moe, and W. Happer, "Particle Formation by Resonant Laser Light in Alkali-Metal Vapor," *Physical Review Letters*, vol. 35, pp. 1630–1633, dec 1975.

[49] T. M. Kwon, J. G. Mark, and C. H. Volk, "Quadrupole nuclear spin relaxation of ^{131}Xe in the presence of rubidium vapor," *Physical Review A*, vol. 24, pp. 1894–1903, oct 1981.

[50] Z. Wu, W. Happer, M. Kitano, and J. Daniels, "Experimental studies of wall interactions of adsorbed spin-polarized ^{131}Xe nuclei," *Physical Review A*, vol. 42, pp. 2774–2784, sep 1990.

[51] S. Rohrbaugh, H. T. J. Wang, J. Singh, W. A. Tobias, and G. D. Cates, "Magnetic decoupling of ^{129}Xe nuclear spin relaxation due to wall collisions with RbH and RbD coatings," *Physical Review A*, vol. 86, p. 043413, oct 2012.

[52] M. A. Rosenberry, J. P. Reyes, D. Tupa, and T. J. Gay, "Radiation trapping in rubidium optical pumping at low buffer-gas pressures," *Physical Review A*, vol. 75, p. 023401, feb 2007.

[53] N. D. Zameroski, W. Rudolph, G. D. Hager, and D. A. Hostutler, "A study of collisional quenching and radiation-trapping kinetics for Rb(5p) in the presence of methane and ethane using time-resolved fluorescence," *Journal of Physics B: Atomic, Molecular and Optical Physics*, vol. 42, p. 245401, dec 2009.

[54] K. F. Stupic, J. S. Six, M. D. Olsen, G. E. Pavlovskaya, and T. Meersmann, "Combustion resistance of the ^{129}Xe hyperpolarized nuclear spin state," *Phys. Chem. Chem. Phys.*, vol. 15, no. 1, pp. 94–97, 2013.

[55] Z. I. Cleveland, K. F. Stupic, G. E. Pavlovskaya, J. E. Repine, J. B. Wooten, and T. Meersmann, "Hyperpolarized ^{83}Kr and ^{129}Xe NMR Relaxation Measurements of Hydrated Surfaces: Implications for Materials Science and Pulmonary Diagnostics," *Journal of the American Chemical Society*, vol. 129, pp. 1784–1792, feb 2007.

[56] K. F. Stupic, Z. I. Cleveland, G. E. Pavlovskaya, and T. Meersmann, "Quadrupolar relaxation of hyperpolarized krypton-83 as a probe for surfaces," *Solid State Nuclear Magnetic Resonance*, vol. 29, pp. 79–84, feb 2006.

[57] L. Chen, X. Yang, X. Li, G. Li, and C. Snape, "Prediction of formation of gas-phase bubbles correlated by vortices in the fuel reactor of chemical looping combustion," *Fuel Processing Technology*, vol. 130, pp. 235–244, feb 2015.

[58] B. C. Anger, G. Schrank, A. Schoeck, K. A. Butler, M. S. Solum, R. J. Pugmire, and B. Saam, "Gas-phase spin relaxation of ^{129}Xe," *Physical Review A*, vol. 78, p. 043406, oct 2008.

[59] B. N. Berry-Pusey, B. C. Anger, G. Laicher, and B. Saam, "Nuclear spin relaxation of ^{129}Xe due to persistent xenon dimers," *Physical Review A - Atomic, Molecular, and Optical Physics*, vol. 74, no. 6, pp. 1–9, 2006.

[60] M. Repetto, E. Babcock, P. Blümler, W. Heil, S. Karpuk, and K. Tullney, "Systematic T_1 improvement for hyperpolarized 129-xenon," *Journal of Magnetic Resonance*, vol. 252, pp. 163–169, mar 2015.

[61] K. F. Stupic, Z. I. Cleveland, G. E. Pavlovskaya, and T. Meersmann, "Hyperpolarized ^{131}Xe NMR spectroscopy," *Journal of Magnetic Resonance*, vol. 208, pp. 58–69, jan 2011.

Chapter 7

Neon-21 As A New Probe Of Porous Media

This chapter will describe the Spin Exchange Optical Pumping (SEOP) of Neon-21 in the current polariser system based at Nottingham. Mr Fraser Hill-Casey performed and devised all experiments described within the chapter. Professor Thomas Meersmann and Mr Hill-Casey designed the experiments.

7.1 Introduction

The past 20 years have seen a great development in production methodologies for hyperpolarisation of ^{3}He [1, 2] and ^{129}Xe [3–6], with extremely high nuclear spin polarisation being achievable for biomedical [7] and materials studies [8]. Beyond spin 1/2, ^{131}Xe ($I = 3/2$) has been explored as a probe for porous materials [9–11]. ^{83}Kr ($I = 9/2$) has begun to receive increasing attention as a probe of surfaces [12, 13] and, more recently the potential for biomedical applications [14] in pulmonary imaging of lung disease [15–17].

In contrast to the extensive literature above, the isotope ^{21}Ne has received

little attention since first the reported observation in 1956 by Hubbs and co-workers [18] using atomic beam resonance.

The only stable Nuclear Magnetic Resonance (NMR) active isotope of the noble gas neon, ^{21}Ne, has an extremely low natural abundance of only 0.27 %, and a resonance frequency of 31.59 MHz at 9.4 Tesla. Due to its spin of $I = 3/2$, ^{21}Ne thus posseses a nuclear electric quadrupole moment [19].

The electric quadrupole moment of the neon nucleus is susceptible to interactions with the electric field gradients (EFG) and, as such, is sensitive to distortions in the electron cloud [20, 21]. As such, much like ^{131}Xe and ^{83}Kr work by Grover [22] and Ghosh [23, 24] has indicated that ^{21}Ne T_1 relaxation will be dominated by the quadrupole interactions except in cases when extremely high concentrations of paramagnetic substances are present.

NMR investigations using ^{21}Ne have been limited primaily by its extremely low natural abundance of $\sim 0.27\,\%$, low gyromagnetic ratio and its low density within the gas phase. As such, only one high resolution study of ^{21}Ne in the literature, investigating the dependence of ^{21}Ne chemical shift within solvents [25]. However, despite this, NMR studies have been performed in the liquid and solid phase [26]. Further gas phase NMR studies have been possible but been confined to isotropically enriched ^{21}Ne samples.

Recent investigation of the ^{21}Ne isotope has been confined to its use in Potassium-Neon co-magnetometers [23, 24, 27, 28]. ^{21}Ne provides an attractive isotope for use in such applications due to its low gyromagnetic ratio (γ), as the sensitivity of such magnetometers is inversely proportional to γ. The use of ^{21}Ne in these systems has been shown to provide

a sensitivity enhancement of an order of magnitude [23] to the more common He-K system. The K-^{21}Ne co-magnetometer has found further use as a navigational gyroscope [23, 24], and as an ultra sensitive method for measurement of Charge, Parity and Time reversal symmetry (CPT) violations [27, 28]. Further work by Ghosh, described the longitudinal relaxation time of the magnetisation of the gas phase ^{21}Ne to be be 214 ± 10 amagat min where an amagat is defined as the density of an ideal gas at standard temperature and pressure (101.325 kPa and 274.15 K respectively). It must be stressed that these measurement by Gosh were made in the presence of the alkali metal used to perform the optical pumping which, will reduce the relaxation times via Ne-Alkali metal collisions.

Grover *et al* [22] has also performed Spin Exchange Optical Pumping of ^{21}Ne and measured its T_1 relaxation time, suggesting a relaxation time of 240 amagat min, consistent with the work performed by Ghosh. It must be noted that Grover utilised Rb as the alkali metal rather K used by Ghosh. However the relevant exchange cross sections do not vary significantly between these two alkali metal species.

Norberg and co-workers [26] found that the frozen isotopically enriched ^{21}Ne has a longitudinal relaxation time of $T_1 = 390$ s at ~ 16.6 K. When undergoing the phase transition from solid to liquid the neon longitudinal relaxation will rapidly decrease to $T_1 = 90$ s, within the liquid phase at 3.6 K, the $T_1 = 28$ s. Such measurements indicate similar behaviour for quadrupole noble gases such as ^{131}Xe, ^{83}Kr and ^{21}Ne, which leads to the conclusion that SEOP buffer gas separation procedures, such as cryogenic separation, will not be possible. However the possibility exists to incorporate the explosive separation techniques discussed in Chapter

6.

The ^{21}Ne chemical shift in various solvents has been subjected to investigation by, currently, only a single experimental study, as well as a number of theoretical studies. These indicate a chemical shift range approximately 16 times lower than that of ^{129}Xe [29]. However relaxation times in such systems has not been probed due to low sensitivity of the experiment.

Previously, Spin Exchange Optical Pumping with alkali metal vapour has been successfully applied to produce ^{21}Ne, however, experiments have been confined to highly isotropically enriched, low volume samples. Further, these presented values have significant variance in the reported attained polarisation. Grover (1983) reports a 0.2 % spin polarisation of a 200 Torr sample of ^{21}Ne and suggests higher polarisation values would be attainable with higher densities. Chupp (1985) reports a peak polarisation of $\sim$ 30 % measured in a 300-600 Torr samples [30]. More recently measurements made by Ghosh *et al* indicated a Neon spin polarization of $\sim$ 8 % measured at 180 ^{o}C without a SEOP quenching gas. Smiciklas *et al* (2011) reported a spin polarisation of $15 - 17$ % was attainable at higher Neon density [27]. However, all of these measurements have been limited to *in situ* detection within the optically pumped cells at low fields, in the presence of the alkali metal and without any SEOP buffer gas.

Separation from the paramagnetic and highly reactive alkali metal vapour used in the optical pumping is both well described and commonplace for $I = 1/2$ nuclei such as ^{129}Xe and ^{3}He and more recently for $I > 1/2$ nuclei such as ^{83}Kr and ^{131}Xe. All measurements with ^{21}Ne have been made in the presence of the alkali metal. The ability to separate the hp

gas from the alkali metal is imperative for application to medical systems and most material science applications.

Within this work we aim, for the first time, to polarise ^{21}Ne by using Spin Exchange Optical Pumping, with a buffer gas as a radiation quenching agent, to separate the hp ^{21}Ne from the alkali metal, and perform the measurement at high magnetic fields. Further, the potential for use as a surface sensitive contrast agent will be explored by characterising the longitudinal relaxation behaviour as a function of pore volume.

7.2 Materials and Methods

7.2.1 NMR parameters

All measurements within this proof of concept study were performed with a 9.4 T wide-bore (89 mm) superconducting magnet with an Avance III spectrometer (Bruker, Germany). Excitation and detection of the NMR signal is achieved with a homebuilt r.f coil (16.5 mm i.d.) tuned to the resonance frequency of ^{21}Ne (31.59 MHz). The bandwidth of the aforementioned probe is sufficient to also reach the resonance frequency of ^{131}Xe of (32.82 MHz). In these experiments a high pressure, thermally polarised ^{131}Xe sample was used to shim the magnetic field before ^{21}Ne NMR. This was possible due to the extremely short T_1 of ^{131}Xe in the gas phase.

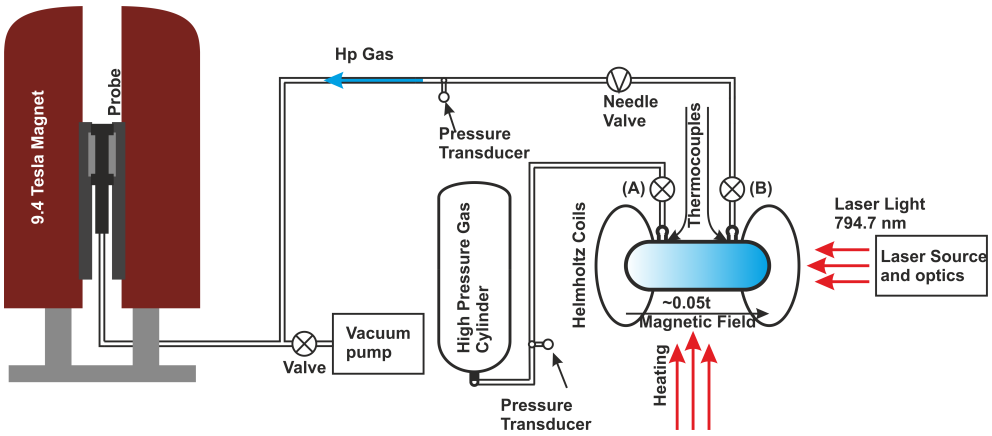


Figure 7.1: Apparatus for batch mode Spin Exchange Optical Pumping production for ^{21}Ne. Thermally polarised gas is delivered to the Pump cell containing alkali metal, both valves (A) and (B) are then closed to allow for spin polarisation to reach an equilibrium value before gas is transported to a evacuated sample container within the r.f. Coil.

7.2.2 Hyperpolarised ^{21}Ne Production by batch mode Spin Exchange Optical Pumping

Spin Exchange Optical Pumping of noble gases with alkali metals is a well explored phenomenon and has been described in detail in Chapter 3 and the experimental apparatus is much the same as that used for the hyperpolarisation of non-quadrupole nuclei such as ^{129}Xe ($I = 1/2$). The exipermental apparatus for the descirbed exiperments is displayed in Figure 7.1. The gas mixtures used for experiments reported in this work ranged from 5 % to 90 % Neon (naturally abundant) with molecular N_2 added to act as a radiation quenching agent. The pressure within the SEOP cell was varied between 54 kPa and 610 kPa. While optical pumping of both ^{129}Xe [3, 5, 6] and ^{83}Kr [5, 6] at both low and high gas densities have been thoroughly explored, ^{21}Ne has been somewhat neglected. The experiments that have been performed have determined that high noble gas densities were vital for obtaining the highest ^{21}Ne signal intensity. The primary reason for this is to account for the low natural abundance of ^{21}Ne (at only $\sim$ 0.27 %). The setup described herein has

been demonstrated previously as the first method for successful separation of the hp noble gas from the rubidium vapour. For the SEOP process the gas mixture was hyperpolarised in a borosilicate glass cell ($l = 120$ mm, $i.d. = 28$ mm) containing ~ 1 g of rubidium metal (99.75 %; Alfa Aesar, Heysham, England, UK). The SEOP cell was housed in an aluminium oven with quartz windows and the temperature controlled by use of heated air gun (Steinel, Peterborough, England, UK). A pair of double Helmholtz coils were used to produce a homogeneous magnetic field of $B_0 \sim 10$ mT across the SEOP cell. In all cases a line narrowed laser system (30 W incident power, 0.15 nm linewidth, Spectra Physics, Santa Clara, CA, USA) tuned to the D_1 transition of rubidium (794.7 nm) was used to irradiate the SEOP Cell with a collimated, circularly polarised light with a power of 23.3 W at the front of the SEOP Cell. Figure 7.1 shows the SEOP apparatus used in these experiments.

The delivery methodology used in these series of experiments was altered slightly from the standard batch mode delivery. In order to obtain sufficient signal intensity, for NMR measurements it was found that the entire SEOP pump cell must be utilised, as to account for the *dead volume* within the pump cell. The *dead volume* refers to the area within the SEOP cell which is not irradiated by laser light and as such, means no polarisation build up will occur. To account for this a concept referred to as *over pressure delivery* is utilised where in Figure 7.1 valve B is opened and valve A remains open forcing the hp gas within the SEOP cell to equilibrate across the evacuated sample volume while also pushing thermally polarised gas though the cell.

Figure 7.2 (A) displays the initial determination of the resonance frequency of thermally polarised ^{21}Ne. To acquire this signal, a 750 kPa

sample of Neon (natural abundance) also containing a highly porous foam to act as a relaxation agent via increasing the T_1 relaxation via quadrupole interaction. This serves to allow for more rapid signal averaging to be performed, which is a necessity when considering the large number of scans required to see even a small SNR. In order to achieve the presented SNR of $\sim$ 15, 20480 scans were used with an inter pulse delay of 15 seconds giving a total experiment time of 59 hours. Figure 7.2 (B) shows a spectrum acquired after a single scan of a hp 90 % Neon (na) 10 % N_2 the data here indicates a polarisation of $\sim$ 3 % with a linewidth of 6 Hz.

7.2.3 Polarization build-up of hyperpolarised ^{21}Ne in batch mode

The SEOP dependence on temperature was probed in Figure 7.3 (A). It was found that operating at a temperature of $\sim$ 463 K produces an optimal rubidium vapour pressure for SEOP. The drop off occurring after $\sim$ 467 K indicates that Rb-Ne collisions are increasing, and are proving detrimental to the SEOP process.

The pumping time dependence of the hyperpolarised ^{21}Ne in batch-mode experiments is displayed in Figure 7.3 (B). In these experiments the pump cell was maintained at 463 K under constant laser irradiation. It was determined that $\sim$ 15 mins provided optimal spin polarisation of 4.4 %. It should be noted that this value is over twice that of the maximum reported value of ^{131}Xe polarisation measured in similar conditions.

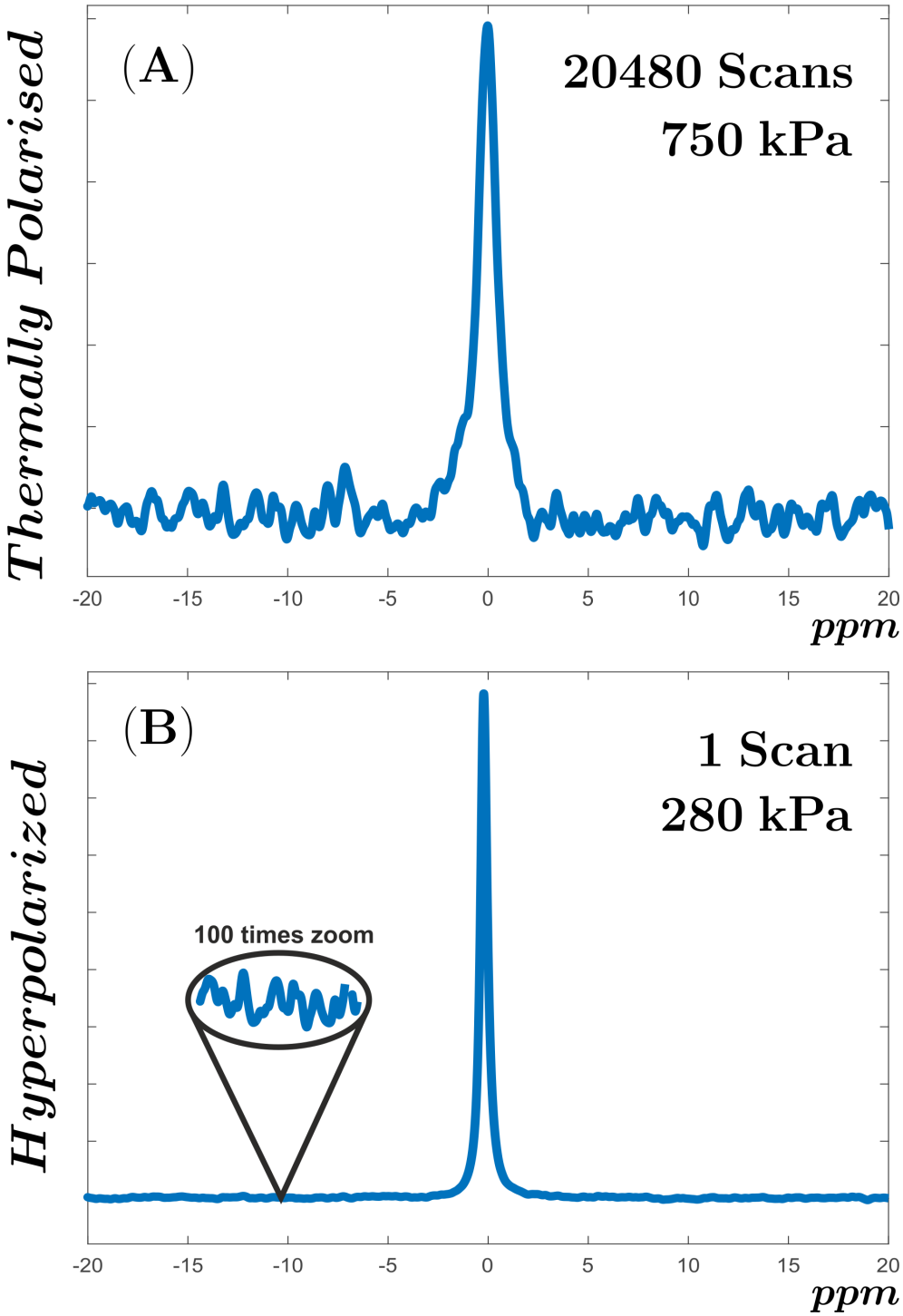
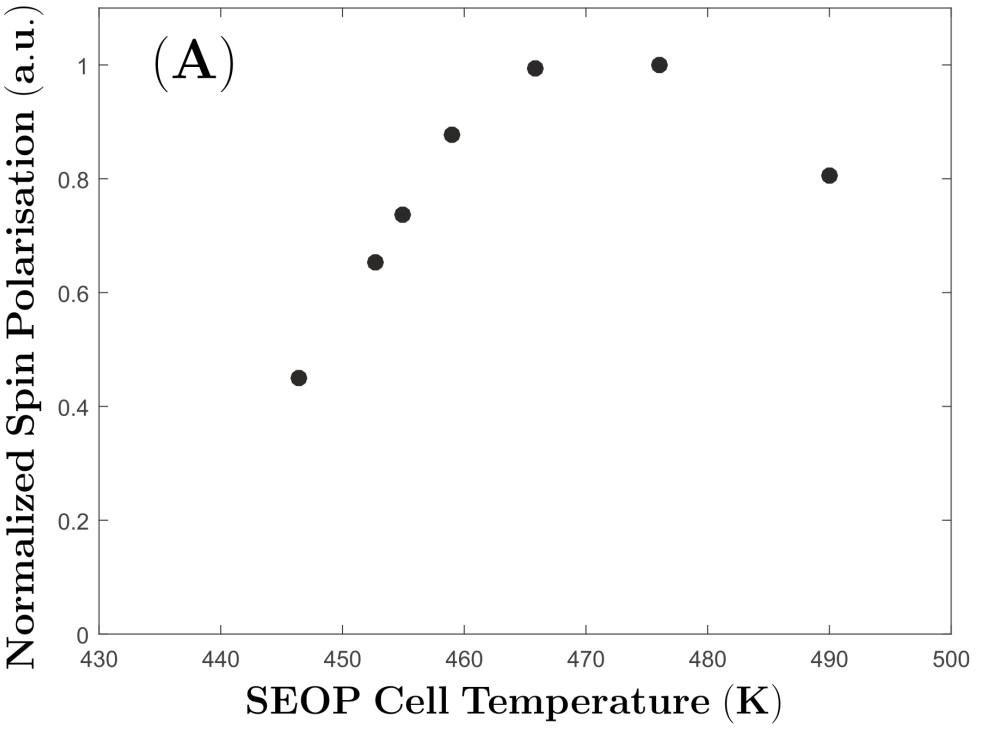


Figure 7.2: Thermally polarised sample compared to hyperpolarised sample of ^{21}Ne (A) A thermally polarised ^{21}Ne signal at ($\sim$ 295 K) at 750 kPa, to achieve the displayed SNR ($\sim$ 15), 20480 scans were accumulated with a total experiment time of 59 hours (B) Spectra from a hyperpolarisation ^{21}Ne from a sample containing 280 kPa of neon with an SNR of ($\sim$ 100), Note that the SNR in (B) is significantly greater than that of (A) despite the difference in total ^{21}Ne concentration. Finally note that the resonance frequency is dependent upon the gas pressure, in both (A) and (B) the radio frequency pulse was set to the resonance frequency in each case.



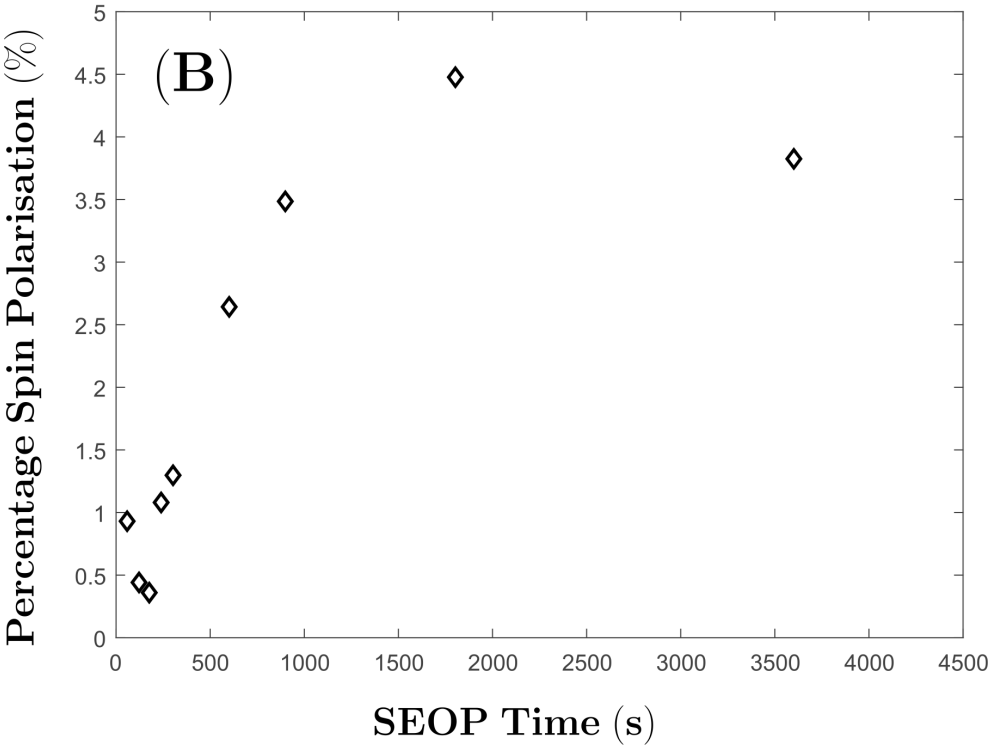


Figure 7.3: ^{21}Ne Spin Polarisation resulting from a set of differing Spin Exchange Optical Pumping parameters (A) Spin polarisation as a function of SEOP cell temperature for a gas mix of 90 % Neon (na) and 10 % N_2 collected after 1000 seconds SEOP time. (B) Spin polarisation of ^{21}Ne as a function of of polarization time collected at 463 K. Fresh gas was introduced to the SEOP cell and polarisation was allowed to build up over a given time before transfer to a detection cell.

7.2.4 Measurements of D_2 Fluorescence

To investigate the effects of the high Neon concentrations in the gas mixes used within this work, a USB 2000 optical spectrometer (Ocean Optics, FL, USA) was positioned so as to interrogate the radiative emission from the alkali metal. This D_2 fluorescence provides a useful measure of the efficiency of the Spin Exchange Optical Pumping process. The dependence of D_2 fluorescence upon the SEOP pressure was interrogated via filling the SEOP cell to a high pressure with the indicated gas mixture while under optical pumping conditions. The gas is the slowly released from the SEOP cell. At sub-atmospheric pressures the pressure of the SEOP pressure is controlled by application of a vacuum, thus allowing for a full range of pressure measurements to be made.

Figure 7.4 shows the aforementioned emission of the D_2 transition. Spectra were acquired at 480 K with four ^{21}Ne concentrations. Each data point represents four averaged data sets, with error bars indicating the calculated standard deviation. Key results are that the high Rb density within the cell means at all N_2-^{21}Ne, mixes the quenching of the D_2 is insufficient. As such it will be beneficial to move toward using higher concentrations of N_2 so as to fully quench the D_2 florescence and achieve optimum spin polarisation. However due to the nature of the study performed herein, we have noted that the main barrier to creating sufficient SNR in NMR experiments is, in fact, the density of Neon.

The information gained from the D_2 florescence line will be useful for guiding experiments utilising isotopically enriched gas mixes, which will allow experiments to be performed at lower partial pressures of Neon. This is, however, beyond the scope of this work.

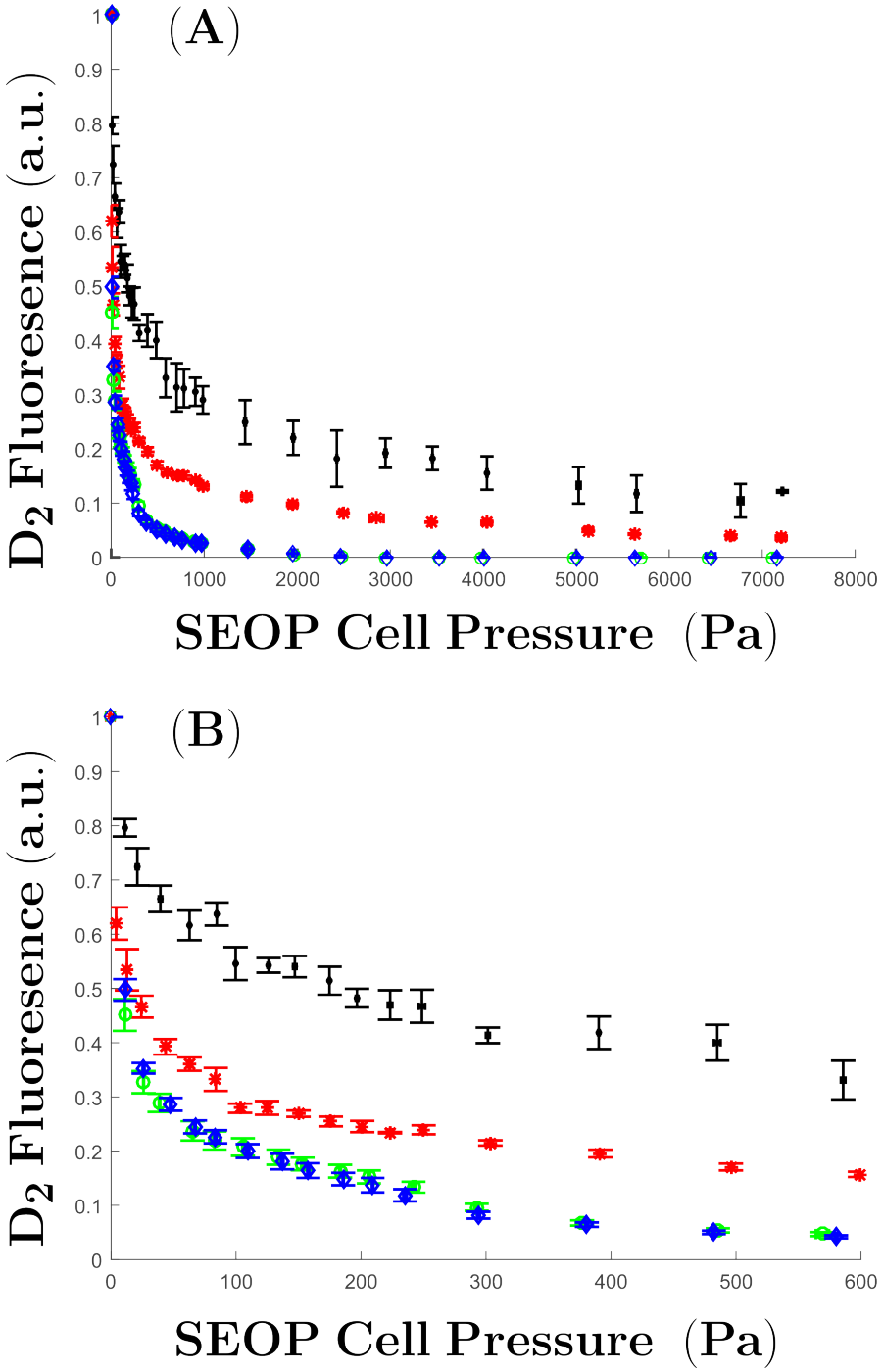


Figure 7.4: The D_2 fluorescence at 780 nm (in arbitrary units, a.u.) measured at the front of the cell during SEOP as indicated in Figure 7.1. Black Circles: 90 % Ne, 10 % N_2; Red Asterixs: 50 % Ne, 50 % N_2; Green Open Circles: 25.47 % Ne, 74.53 % N_2; Blue Diamond: 5.2 % Ne, 94.8 % N_2. (A) displays the D_2 fluorescence of the aforementioned gas mixes between 0 and 730 kPa. Key results indicate insufficient radiation quenching with low concentrations of N_2 at 463 K (Black circles) is evident at low pressures and high ^{21}Ne concentrations. Effective quenching for the 5.2 % and 25.47 % ^{21}Ne concentrations occurs only after 7.5−8.0 kPa SEOP pressure, a deviation from data presented in Chapter 6 this is expected due to the higher temperature and rubidium vapour density used for ^{21}Ne SEOP. The high Neon concentration mixes (90 % and 50 %) are clearly insufficiently quenched at all SEOP cell pressures. (B) Shows the D_2 fluorescence at low SEOP pressures measured for ^{21}Ne SEOP at 463 K further elucidating the quenching profiles.

7.2.5 Longitudinal Relaxation measurements in hyperpolarised systems

T_1 measurements were obtained with the home built, r.f. probe described in Section 7.2.1. A pulse sequence consisting of 32 constant, small flip angle pulses spaced evenly with a time interval τ . An FID is acquired after the application of each pulse. In each instance the pulse sequence was run after the pressure in the sample chamber had equilibrated with the the pump cell pressure. Figure 7.5 indicates a typical detection scheme for a T_1 measurement within this system. The T_1 value for a given data set is extracted by fitting to the following form;

$$\ln\left(\frac{I}{I_0}\right) = \left(\ln\left(\cos\left(\theta\right)\right) - \frac{\tau}{T_1}\right) \cdot n, \tag{7.1}$$

where I is the signal for a given experiment, I_0 is the signal at the maximum intensity, τ is the inter-pulse delay. The $\cos(\theta)$ term in Equation (7.1) takes the polarisation destruction into account from the 12^o flip angle RF pulse. To ensure that even the short relaxation times are probed the sequence is stated before delivery and thus, the fitting is only applied to the linear region (where the pressure will have equlibriated) [31–33].

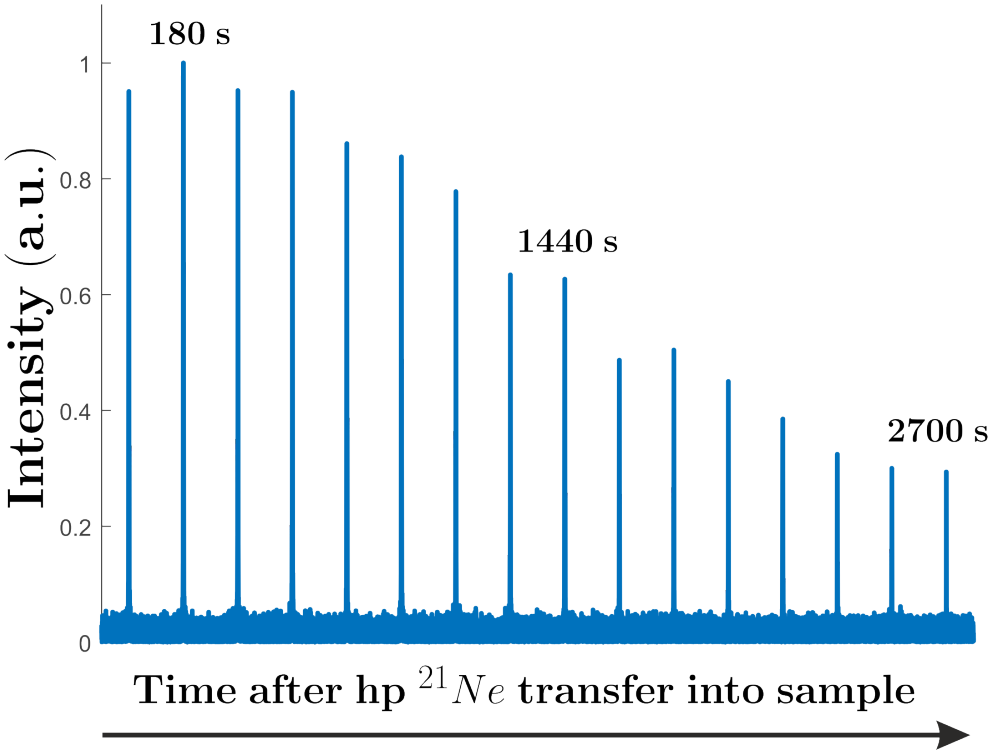


Figure 7.5: signal intensity decay resulting from the T_1 relaxation and the application of a series of small (12^o) flip angle pulses. Using batch mode SEOP hyperpolarisation ^{21}Ne is transferred into the NMR tube (Dehydrated, Borosilicate glass). Signal is acquired by application of of a series 12^o r.f. pulses spaced by a time τ, which is tuned to the relaxation in individual experiments.

7.2.6 Sample Preparation

To probe the dependence of ^{21}Ne longitudinal relaxation upon void spaces glass beads were used to provided a model surface. Glass beads of diameters, $0.5-2.5$ mm (Biospec Products, Inc, Bartlesville, OK) were used to provide the model void spaces for this series of experiments. These beads were assumed to be in an arrangement resembling the closest packing of spheres with a constant total pore volume of 26 % of the overall sample, the pores in this case are hexagonal and are assumed to to be an ideal pack for the smaller bead dimensions. However, when utilising the larger dimensions, specifically that of the 2.5 mm beads, the packing deviates from the *ideal* due to the finite sample container dimensions.

In this series of relaxation experiments different pore sizes have been explored along with two different surfaces. Firstly, beads used as received from the supplier were degassed under vacuum conditions overnight, and henceforth referred to as untreated beads. Secondly Siloxane treated beads, which are untreated beads cleaned by washing in 1 : 1 : 5 solution of 30 % v/v NH_4OH, 30 % v/v H_2O_2 and distilled water while stirring vigorously. Following the initial treatment the beads were then washed for 15 min with a 1 : 1 : 5 solution of 30 % v/v HCl, 30 % v/v H_2O_2 and distilled water at 358 K while stirring. The beads were then dried in a vacuum oven for 1 h at 523 K. Finally the beads were siliconized with a 1 : 10 solution of SurfaSil^{TM} (Pierce Biotechnology Inc, Rockford, IL) in acetone and washed with distilled water then dried in accordance with manufacturer's instructions.

7.3 Results and Discussion

Glass beads of four different sizes (0.1 mm, 0.5 mm, 1.0 mm and 2.5 mm) were placed within four separate NMR tubes (13.8 mm i.d) which is connected to the SEOP cell by the method described Figure 7.1. Results from the T_1 relaxation measurements with ^{21}Ne are displayed in Table 7.1 and compared to ^{83}Kr and ^{131}Xe relaxation data, reprocessed from literature [11, 13].

The ^{21}Ne relaxation rate was found to be inversely proportional to pore size with larger pores producing longer relaxation times, while smaller pores produced shorter relaxation times. This is consistant with the expectation that longitudinal relaxation of quadrupole species is dependent on surface collisions, as observed before in literature with ^{131}Xe [10, 34–

36] and most notably ^{83}Kr [13, 15, 16, 32]. It must be noted that due to the extremely rapid surface adsorption and desorption events (typically on the order of nanoseconds) that the hp ^{21}Ne spin-density signal is actually that of the gas phase but the main contributing factor to the T_1 relaxation will be the effects of the surface. As such this relaxation signal may be interpreted via the Brownstein and Tarr two fraction [37] fast exchange model. Thus further allowing the linking of the gas phase relaxation time with the pore size.

If quadrupole interactions on the surface are the only contribution to the observed relaxation, a linear dependence between relaxation rate and pore size would be expected. However in the data presented in Figure 7.6 there is clear deviation from the linear behaviour for both the literature ^{83}Kr values and the ^{21}Ne values from this work. This deviation is most notable at large bead diameters which would be accounted for by non ideal packing of the beads within the sample container due to the finite dimensions of the NMR tube and an increased interaction with the wall itself.

In this study the longest T_1 relaxation value observed for ^{21}Ne was that of the gas phase in the NMR tube in the absence of beads, such that $T_1 = 2825$ s as with the reported literature value for ^{83}Kr and ^{131}Xe at $T_1 = 150$ s and $T_1 = 19.4$ s.

Within this work we have been unable to investigate the relaxation in bead packs of diameters < 0.5 mm due to the limited signal obtained after the application of the small flip angle pulse. It should however be possible to perform such measurements in future with greater optimisation of the Spin Exchange Optical Pumping process and with even limited isotopic enrichment of the gas mix.

Table 7.1: ^{21}Ne relaxation times in void spaces of glass beads. longitudinal relaxation times of ^{21}Ne were measured using hyperpolarisation ^{21}Ne at 310 kPa and 9.4 T and 293 K. The ^{83}Kr values are reproduced from literature for comparison and were measured at 100 kPa and 9.4 T at 293 k.

Bead Dia. (mm)	^{21}Ne Untreated Beads T_1 (s)	^{83}Kr Untreated Beads T_1 (s)	^{21}Ne Siloxane Treated Beads T_1 (s)	^{83}Kr Siloxane Treated Beads T_1 (s)
Empty Cell (13.8 mm I.d.)	2825	- - -	- - -	- - -
2.5	602.95	35.2	- - -	- - -
1.0	254.63	20.5	908.4	9.0
0.5	187.44	17.9	- - -	- - -
0.1	- - -	6.5	- - -	- - -

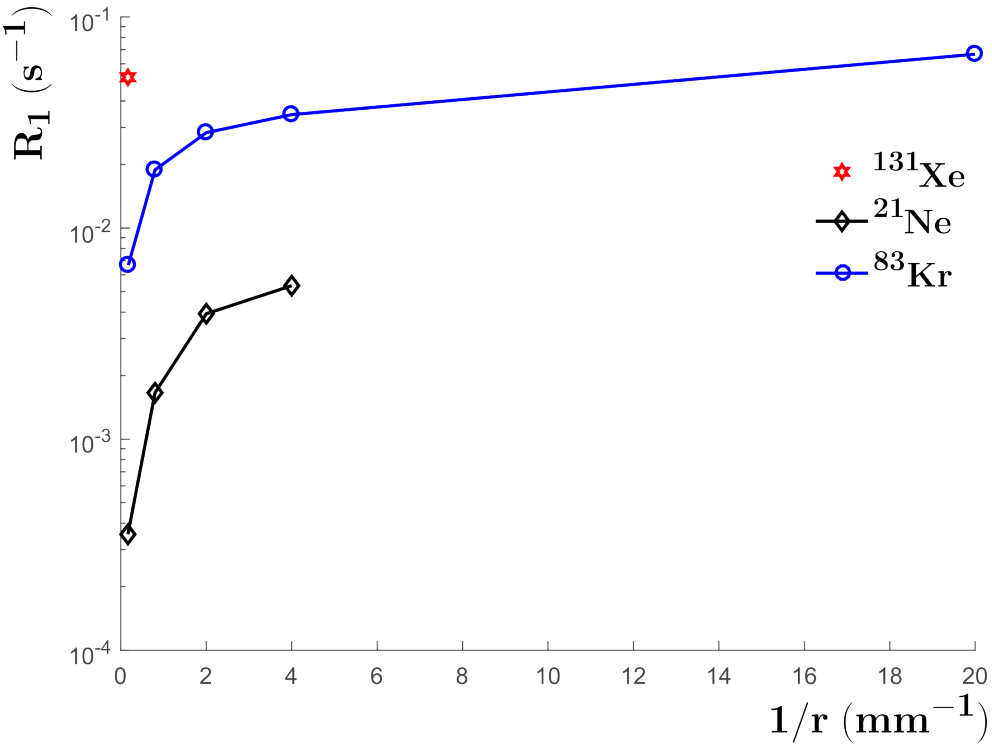


Figure 7.6: Relaxation Rate (R_1) verse the inverse bead radii from the experimental results shown in 7.1. The inverse radius is directly proportional to the surface to volume ratio in the porous samples. Relaxation rates for ^{21}Ne, ^{83}Kr and ^{131}Xe in untreated glass beads are displayed on a semilogarithmic plot. The lines within the figures are intended as only a guide for the eye. The ^{83}Kr data is reproduced from literature [13]

.

The longitudinal relaxation of hyperpolarised ^{21}Ne was further probed as a function of pressure within the 13.8 mm i.d. NMR tube filled with 2.5 mm untreated beads as to allow for the T_1 to be reduced to a suitable time scales to perform measurements.

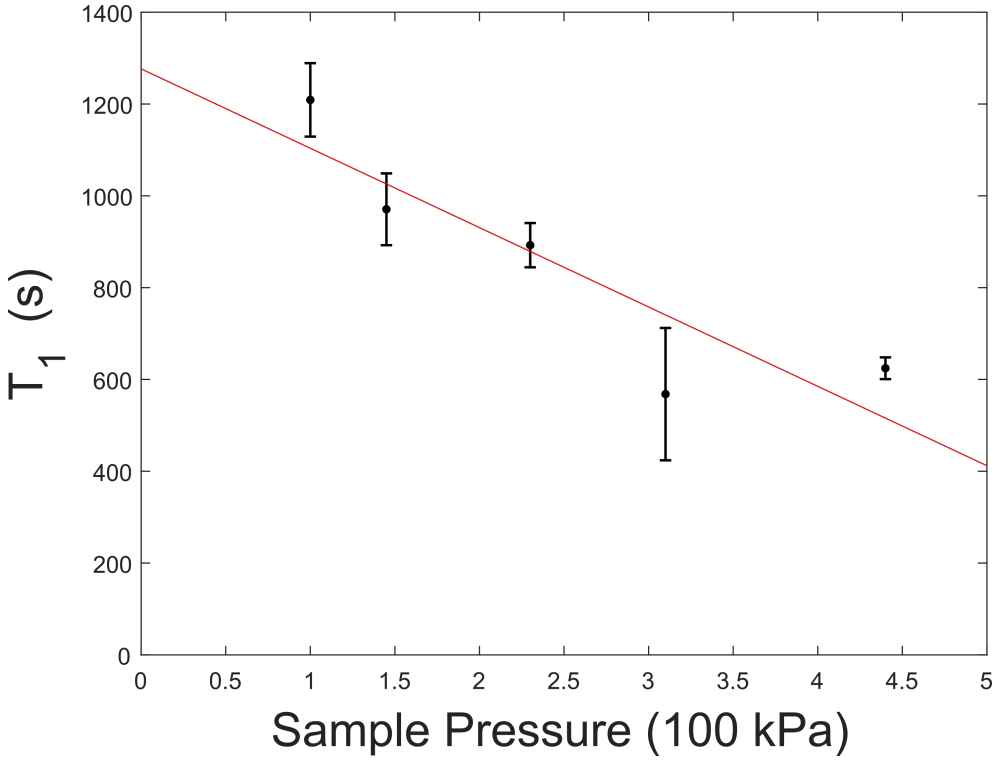


Figure 7.7: Longitudinal relaxation of hyperpolarisation ^{21}Ne as a function of pressure within the sample volume. A 15 mm NMR tube was filled with 2.5 mm diameter beads, gas was delivered via the top of the magnet to the detection cell. Error bars on the data points are the result are the uncertainty from three experiments. The T_1 is inversely proportional to the cell filling density indicating the dominant relaxation mechanism is that of the quadrupole relaxation, consistent with expectations

Further, due to the large nuclear quadrupole moment it is expected that the dominant source of relaxation to be the interaction with the walls of the NMR tube, with only a negligible contribution from Dipole-Dipole interactions. It is expected that the T_1 of neon to be inversely proportional to the detection chamber pressure. In Figure 7.7 it can be observed that T_1 behaves as expected, and implies a relationship between longitudinal relaxation and neon gas density of,

$$\rho \cdot T_1 = 213.4 \pm 35\, amagat\, min. \tag{7.2}$$

The pressure dependence of T_1 in the absence of walls has previously been explored in the literature by Grover [22], Ghosh [23, 24] and Li [28]. However, all previous measurement have been made *insitu* of the SEOP pumping cell at high temperatures ($\sim$ 453 K) as such it would be expected that the Rb-^{21}Ne interactions would increase the T_1 relaxation. In this work as detailed measurements are made *ex-situ* from the pump cell. To keep experiment time manageable it was necessary to utilise the 2.5 mm glass beads as a relaxation agent.

7.4 Conclusions

Hyperpolarised ^{21}Ne free from paramagnetic and highly reactive rubidium vapour has been produced for the first time. Signal enhancements of over 900 times that of thermally polarized ^{21}Ne were obtained using high density ^{21}Ne Spin Exchange Optical Pumping which lead to SNR more than sufficient for NMR and possible MRI applications.

The sensitivity of hp ^{21}Ne to the surface to volume ratio of porous material has been demonstrated and compared to measurements previously presented within the literature for ^{83}Kr and ^{131}Xe. While sensitivity is a current challenge for ^{21}Ne NMR the concept of using isotopically enriched gas mixtures would be able to provide massive enhancement to the currently detected signal. Further, when operating with isotopically enriched gas mixes we expect that SEOP processes will be performed at low Neon gas density and large buffer gas density's, much like with current ^{83}Kr and ^{129}Xe SEOP production methods. As such separation

techniques may be utilised to assist in the production of *purified* hp Neon. Due to the ^{21}Ne experiencing a limited T_1 relaxation time within the solid phase much like ^{83}Kr traditional cryogenic separation is expected to not be possible, however, the method of SEOP with H_2 and subsequent catalytic separation [38] presented within Chapter 6 should be possible.

The results presented indicate that it is entirely reasonable to imagine that hp ^{21}Ne may be able to follow a research pathway similar to that of ^{83}Kr. However the notable difference in the approximate order of magnitude difference in relaxation times which opens the door for experiments such as the remote detection [39–42] of metal surfaces (due to long T_1 times), remote detection relaxometry in human lungs and indeed imaging applications if isotropically enriched gas can be acquired in sufficient quantity. The long T_1 of ^{21}Ne in even small pores further allows for transportation between production facility's and experimental locations to be technically simple as with other medically used gasses such as ^{129}Xe and ^{3}He.

The measurement's detailed within this chapter present a complementary method to the currently well established techniques concerning ^{129}Xe and ^{83}Kr. Further investigation is warranted into the behaviour of this gas in Spin Exchange Optical Pumping conditions due to the deviations of our measurements from that of those mentioned by Ghosh. Further work into its behaviour on surfaces is also warranted as to further categorise the behaviour of ^{21}Ne quadrupole relaxation with different surface chemistry. Results presented within this chapter are encouraging for further increasing the spin polarisation of ^{21}Ne with a more concerted study. A potential future application of remotely detected hp ^{21}Ne is the use of

remotely detected relaxometry [43] at low fields for biomedical studies of tissues. Of particular interest would be investigations of surfaces of electrically conducting materials not typically able to be studied with conventional NMR.

Bibliography

[1] M. J. Couch, B. Blasiak, B. Tomanek, A. V. Ouriadov, M. S. Fox, K. M. Dowhos, and M. S. Albert, "Hyperpolarized and Inert Gas MRI: The Future," *Molecular Imaging and Biology*, vol. 17, no. 2, pp. 149–162, 2015.

[2] M. S. Albert and F. T. Hane, *Hyperpolarized and Inert Gas MRI: From Technology to Application in Research and Medicine*. Science Direct e-books, Elsevier Science & Technology, 2016.

[3] D. A. Barskiy, A. M. Coffey, P. Nikolaou, D. M. Mikhaylov, B. M. Goodson, R. T. Branca, G. J. Lu, M. G. Shapiro, V.-v. Telkki, V. V. Zhivonitko, I. V. Koptyug, O. G. Salnikov, K. V. Kovtunov, V. I. Bukhtiyarov, M. S. Rosen, M. J. Barlow, S. Safavi, I. P. Hall, L. Schröder, and E. Y. Chekmenev, "NMR Hyperpolarization Techniques of Gases," *Chemistry - A European Journal*, vol. 23, pp. 725–751, jan 2017.

[4] P. Nikolaou, A. M. Coffey, L. L. Walkup, B. M. Gust, N. Whiting, H. Newton, S. Barcus, I. Muradyan, M. Dabaghyan, G. D. Moroz, M. S. Rosen, S. Patz, M. J. Barlow, E. Y. Chekmenev, and B. M. Goodson, "Near-unity nuclear polarization with an open-source ^{129}Xe hyperpolarizer for NMR and MRI," *Proceedings of the National Academy of Sciences*, vol. 110, no. 35, pp. 14150–14155, 2013.

[5] J. S. Six, T. Hughes-Riley, K. F. Stupic, G. E. Pavlovskaya, and T. Meersmann, "Pathway to Cryogen Free Production of Hyperpolarized Krypton-83 and Xenon-129," *PLoS ONE*, vol. 7, no. 11, 2012.

[6] T. Hughes-Riley, J. S. Six, D. M. L. Lilburn, K. F. Stupic, A. C. Dorkes, D. E. Shaw, G. E. Pavlovskaya, and T. Meersmann, "Cryogenics free production of hyperpolarized ^{129}Xe and ^{83}Kr for biomedical MRI applications," *Journal of Magnetic Resonance*, vol. 237, pp. 23–33, 2013.

[7] D. M. Lilburn, G. E. Pavlovskaya, and T. Meersmann, "Perspectives of hyperpolarized noble gas MRI beyond ^{3}He," *Journal of Magnetic Resonance*, vol. 229, pp. 173–186, 2013.

[8] G. Pavlovskaya, J. Six, T. Meersman, N. Gopinathan, and S. P. Rigby, "NMR imaging of low pressure, gas-phase transport in packed beds using hyperpolarized xenon-129," *AIChE Journal*, vol. 61, no. 11, pp. 4013–4019, 2015.

[9] I. L. Moudrakovski, C. I. Ratcliffe, and J. A. Ripmeester, "^{131}Xe, a New NMR Probe of Void Space in Solids," *Journal of the American Chemical Society*, vol. 123, pp. 2066–2067, mar 2001.

[10] T. Meersmann, M. Deschamps, and G. Bodenhausen, "Probing Aerogels by Multiple Quantum Filtered ^{131}Xe NMR Spectroscopy," *Journal of the American Chemical Society*, vol. 123, pp. 941–945, feb 2001.

[11] K. F. Stupic, Z. I. Cleveland, G. E. Pavlovskaya, and T. Meersmann, "Hyperpolarized ^{131}Xe NMR spectroscopy," *Journal of Magnetic Resonance*, vol. 208, no. 1, pp. 58–69, 2011.

[12] G. E. Pavlovskaya, Z. I. Cleveland, K. F. Stupic, R. J. Basaraba, and T. Meersmann, "Hyperpolarized krypton-83 as a contrast agent for magnetic resonance imaging," *Proceedings of the National Academy of Sciences*, vol. 102, pp. 18275–18279, dec 2005.

[13] K. F. Stupic, Z. I. Cleveland, G. E. Pavlovskaya, and T. Meersmann, "Quadrupolar relaxation of hyperpolarized krypton-83 as a probe for surfaces," *Solid State Nuclear Magnetic Resonance*, vol. 29, pp. 79–84, feb 2006.

[14] J. S. Six, T. Hughes-Riley, D. M. Lilburn, A. C. Dorkes, K. F. Stupic, D. E. Shaw, P. G. Morris, I. P. Hall, G. E. Pavlovskaya, and T. Meersmann, "Pulmonary MRI contrast using Surface Quadrupolar Relaxation (SQUARE) of hyperpolarized ^{83}Kr," *Magnetic Resonance Imaging*, vol. 32, no. 1, pp. 48–53, 2014.

[15] Z. I. Cleveland, G. E. Pavlovskaya, N. D. Elkins, K. F. Stupic, J. E. Repine, and T. Meersmann, "Hyperpolarized ^{83}Kr MRI of lungs," *Journal of Magnetic Resonance*, vol. 195, pp. 232–237, dec 2008.

[16] Z. I. Cleveland, G. E. Pavlovskaya, K. F. Stupic, J. B. Wooten, J. E. Repine, and T. Meersmann, "Detection of tobacco smoke deposition by hyperpolarized krypton-83 MRI," *Magnetic Resonance Imaging*, vol. 26, pp. 270–278, feb 2008.

[17] D. M. L. Lilburn, C. Lesbats, J. S. Six, E. Dubuis, L. Yew-Booth, D. E. Shaw, M. G. Belvisi, M. A. Birrell, G. E. Pavlovskaya, and T. Meersmann, "Hyperpolarized ^{83}Kr magnetic resonance imaging of alveolar degradation in a rat model of emphysema.," *Journal of the Royal Society, Interface / the Royal Society*, vol. 12, no. 107, pp. 20150192–, 2015.

[18] J. C. Hubbs and G. M. Grosof, "Spin of Neon-21," *Physical Review*, vol. 104, pp. 715–717, nov 1956.

[19] G. M. Grosof, P. Buck, W. Lichten, and I. I. Rabi, "Quadrupole moment of Ne^{21}," *Physical Review Letters*, vol. 1, pp. 214–215, sep 1958.

[20] L. G. Werbelow, "NMR dynamic frequency shifts and the quadrupolar interaction," *The Journal of Chemical Physics*, vol. 70, pp. 5381–5383, jun 1979.

[21] R. Eggenberger, S. Gerber, H. Huber, and M. Welker, "Spin-lattice relaxation time and quadrupole coupling constant of ^{21}Ne in liquid neon," *Chemical Physics*, vol. 177, pp. 91–98, nov 1993.

[22] B. C. Grover, "Production of a nuclear-spin-polarized ^{21}Ne sample," *Physical Review A*, vol. 28, pp. 2521–2522, oct 1983.

[23] R. K. Ghosh, *Spin Exchange Optical Pumping of Neon and Its Applications*. PhD thesis, Princeton, 2009.

[24] R. K. Ghosh and M. V. Romalis, "Measurement of spin-exchange and relaxation parameters for polarizing Ne21 with K and Rb," *Physical Review A - Atomic, Molecular, and Optical Physics*, vol. 81, no. 4, pp. 1–10, 2010.

[25] P. Diehl, O. Muenster, and J. Jokisaari, "Magnetic resonance of ^{21}Ne in liquid solvents," *Chemical Physics Letters*, vol. 178, pp. 147–149, mar 1991.

[26] R. Henry and R. E. Norberg, "Pulsed Nuclear Magnetic Resonance of Ne21 in Solid and Liquid Neon," *Physical Review B*, vol. 6, pp. 1645–1653, sep 1972.

[27] M. Smiciklas, J. M. Brown, L. W. Cheuk, S. J. Smullin, and M. V. Romalis, "New Test of Local Lorentz Invariance Using a ^{21}Ne - K Comagnetometer," *Physical Review Letters*, vol. 107, p. 171604, oct 2011.

[28] R. Li, W. Fan, L. Jiang, L. Duan, W. Quan, and J. Fang, "Rotation sensing using a K-Rb- ^{21}Ne comagnetometer," *Physical Review A*, vol. 94, no. 3, pp. 1–7, 2016.

[29] E. Y. Lau and J. T. Gerig, "Solvent effects on nuclear shielding of neon," *The Journal of Chemical Physics*, vol. 103, pp. 3341–3349, sep 1995.

[30] T. E. Chupp and K. P. Coulter, "Polarization of ^{21}Ne by Spin Exchange with Optically Pumped Rb Vapor," *Physical Review Letters*, vol. 55, pp. 1074–1077, sep 1985.

[31] J. H. Gao, L. Lemen, J. Xiong, B. Patyal, and P. T. Fox, "Magnetization and diffusion effects in NMR imaging of hyperpolarized substances," *Magnetic Resonance in Medicine*, vol. 37, no. 1, pp. 153–158, 1997.

[32] Z. I. Cleveland and T. Meersmann, "Binary-collision-induced longitudinal relaxation in gas-phase ^{83}Kr.," *The Journal of chemical physics*, vol. 129, p. 244304, dec 2008.

[33] K. F. Stupic, N. D. Elkins, G. E. Pavlovskaya, J. E. Repine, and T. Meersmann, "Effects of pulmonary inhalation on hyperpolarized krypton-83 magnetic resonance T 1 relaxation," *Physics in Medicine and Biology*, vol. 56, pp. 3731–3748, jul 2011.

[34] R. Butscher, G. Wäckerle, and M. Mehring, "Nuclear quadrupole interaction of highly polarized gas phase ^{131}Xe with a glass surface," *The Journal of Chemical Physics*, vol. 100, pp. 6923–6933, may 1994.

[35] G. Pavlovskaya, A. K. Blue, S. J. Gibbs, M. Haake, F. Cros, L. Malier, and T. Meersmann, "Xenon-131 Surface Sensitive Imaging of Aerogels in Liquid Xenon near the Critical Point," *Journal of Magnetic Resonance*, vol. 137, pp. 258–264, mar 1999.

[36] Y. Millot, P. Man, M.-A. Springuel-Huet, and J. Fraissard, "14-P-27-Quantification of electric-field gradients in the supercage of Y zeolites by comparing the chemical shifts of ^{131}Xe (I=3/2) and ^{129}Xe (I=1/2)," p. 354, 2001.

[37] K. R. Brownstein and C. E. Tarr, "Spin-lattice relaxation in a system governed by diffusion," *Journal of Magnetic Resonance (1969)*, vol. 26, no. 1, pp. 17–24, 1977.

[38] N. J. Rogers, F. Hill-Casey, K. F. Stupic, J. S. Six, C. Lesbats, S. P. Rigby, J. Fraissard, G. E. Pavlovskaya, and T. Meersmann, "Molecular hydrogen and catalytic combustion in the production of hyperpolarized ^{83}Kr and ^{129}Xe MRI contrast agents.," *Proceedings of the National Academy of Sciences of the United States of America*, vol. 113, pp. 3164–8, mar 2016.

[39] C. Hilty, E. E. McDonnell, J. Granwehr, K. L. Pierce, S.-I. Han, and A. Pines, "Microfluidic gas-flow profiling using remote-detection NMR," *Proceedings of the National Academy of Sciences*, vol. 102, pp. 14960–14963, oct 2005.

[40] E. Harel, J. Granwehr, J. A. Seeley, and A. Pines, "Multiphase imaging of gas flow in a nanoporous material using remote-detection NMR," *Nature Materials*, vol. 5, pp. 321–327, apr 2006.

[41] A. J. Moule, M. M. Spence, S.-I. Han, J. a. Seeley, K. L. Pierce, S. Saxena, and A. Pines, "Amplification of xenon NMR and MRI by remote detection," *Proceedings of the National Academy of Sciences*, vol. 100, pp. 9122–9127, aug 2003.

[42] J. Granwehr, E. Harel, S. Han, S. Garcia, A. Pines, P. N. Sen, and Y.-Q. Song, "Time-of-Flight Flow Imaging Using NMR Remote Detection," *Physical Review Letters*, vol. 95, p. 075503, aug 2005.

[43] Z. I. Cleveland, G. E. Pavlovskaya, K. F. Stupic, C. F. Lenoir, and T. Meersmann, "Exploring hyperpolarized ^{83}Kr by remotely detected NMR relaxometry," *Journal of Chemical Physics*, vol. 124, no. 4, 2006.

Chapter 8

Conclusions and Outlook

The major goal of this thesis has been two-fold. Firstly to investigate the application of ^{129}Xe to porous media structures and secondly to develop new, advanced Spin Exchange Optical Pumping (SEOP) production methodologies.

The first third of this thesis introduces the reader to the concepts of Nuclear Magnetic Resonance (NMR) and Magnetic Resonance Imaging (MRI). An outline of the general techniques for hyperpolarisation (hp) is given with an emphasis on the physical and experimental considerations of SEOP. The second third of this work details the application of hp gas imaging to that of porous media. The final third of this work details the development of Spin Exchange Optical Pumping techniques.

Chapter 4 details the further development of the improved optical pumping techniques devloped by Six [1] and Hughes-riley [2] for application to the continuous flow SEOP production methodology [3]. This enhanced production methodology has been used to study fluid dynamics within a cylindrical pipe via use of phase shift velocity measurements [4, 5]. Good agreement is noted between the theoretically predicted Poiseuille flow for flow conditions used in the experiments and the measured results.

Within steam reformer pellets, flow patterns through and around the channel geometries were interrogated in a quantitative fashion, radially averaged and flow profiles were acquired. Results indicated a deviation from the *no-slip* condition at the walls of the channels indicating a significant interaction between the superficial flow and the pore structure. Further, X-Ray CT and mercury porosimetry were used to characterise the porosity of the sample, with results lending credence to the suggestion that there is significant interaction between the superficial flow of hp gas and the pore structure. The key outcome of this work has been the development and characterisation of the phase-shift MRI velocimetry technique and its combination with hp ^{129}Xe via continuous flow SEOP at ambient pressures and temperatures. As such this technique allowed for the probing of diffusion in the Knudsen regime. This technique was utilised heavily within Chapter 5.

Work presented in **Chapter 5** details a multi-modal, multi-nuclear investigation of the hierarchically organised pore structure of a combined selective catalytic reduction monolith. X-Ray Computed Tomography was used to spatially locate the catalytic washcoat within the highly porous substrate. It was noted that there was a clear bias of the catalytic wash-coat to be located within the walls of the monolith substrate rather than the highly porous corners. This assertion was supported by T_2 maps of the fully saturated sample.

Mercury Porosimetry was utilised to elucidate the pore sizes within the monolith. The mercury intrusion curve suggested a hierarchically organised structure with three main intrusion modes corresponding to, the large and partially filled pores; the macroporosity between zeolite crystallites within the washcoat and finally the mesopores within the washcoat

binder material.

NMR relaxometry of ^{1}H, ^{2}H and hp ^{129}Xe was used to probe the drying of the monolith segment. As expected, all three studies indicated that the largest pores dry out first, followed by the intermediate and then finally the smallest pores. As such it was possible to selectively block levels of the pore structure and, so examine the contributions of each level of this pore hierarchy to the overall mass transport. A key feature of the ^{129}Xe gas phase relaxometry was the ability to probe the smallest level of the pore hierarchy after the $^{1}H_2O$, $^{2}H_2O$ moisture content proved insufficient for signal detection.

Mass transport studies of ^{129}Xe of diffusional permeation and flow under a pressure gradient both clearly indicate that the higher (relative to the walls) and larger pore sizes within the wall intersections make the greatest contribution to the overall mass transport. This means even though the macroporosity of the monolith pore structure only accounts for a $\sim$ third of the overall pore volume it contributes disproportionally to the overall mass transport. Therefore, it was concluded from the mass transport behaviour that there is significant potential for substantial bypassing of the catalyst within the walls and washcoat.

In **Chapter 6** the novel production methodology of utilising molecular hydrogen as a SEOP buffer gas and its subsequent separation [6] is described.

Molecular hydrogen is shown to be an efficient radiation quenching agent for the process of hyperpolarisation of ^{129}Xe and crucially ^{83}Kr. The polarised state of ^{129}Xe and ^{83}Kr was measured by high field NMR which determined that H_2 acted suitably as an SEOP buffer gas to provide a polarisation of approximately, that which may be obtained via use of

N_2.

Measurement of the D_2 florescence line of rubidium under SEOP conditions via use of an optical spectrometer was used to probe the efficacy of the radiation quenching of a number of gas mixes. H_2 was found to suitably quench the radiative emissions, destructive to the SEOP process at high gas densities ($>$ 35 kPa).

Combustive separation of the noble gas - buffer gas mix was achieved by the addition of known quantities of O_2 catalytically triggered via use of a platinum on alumina oxide catalyst. This process, performed within a bespoke reaction chamber was performed *ex-situ* from the SEOP pump cell. A high speed video of the process was used to investigate the combustion event and, suggests the separation process is complete within 150 ms of the delivery of O_2.

Furthermore, the NMR signal intensity of both ^{129}Xe and ^{83}Kr were measured during the combustion process. Key ^{129}Xe results indicate that the T_1 relaxation was increased due to the interaction with the paramagnetic O_2. However, despite this, the ^{129}Xe still has a sufficient signal intensity for biomedical applications. The evolution of the NMR signal of ^{83}Kr was also monitored and, in contrast to the ^{129}Xe data, it was seen that ^{83}Kr T_1 relaxation in fact decreases after the combustions event; a likely consequence of the competitive co-adsorption of water molecules on the reactor surface [7]. The presented concept does not involve any toxic reagents and produces no harmful bi-products. The crucial conclusion of this chapter was that the combustion event does not affect the polarisation state of the hp gas, be it ^{129}Xe or ^{83}Kr. Furthermore, this detailed scheme allowed for the first time the separation of hp ^{83}Kr from its buffer gas. Based on results garnered within this work it would suggests that

purified hp ^{83}Kr with 21 % spin polarisation would be attainable, a seven fold enhancement over recent hp ^{83}Kr results [1, 2].

The work within **Chapter 7** presented the first measurements of hyperpoalrised ^{21}Ne *ex-situ* from the SEOP pump cell. Optimisation of the SEOP process, temperature and polarisation build-up time allowed for a signal enhancement of over 900 times that of thermally polarised ^{21}Ne to be obtained. Via utilisation of relaxation experiments, the sensitivity of hp ^{21}Ne to the surface to volume ratio of porous material has been demonstrated and comparison to measurements previously presented within the literature for ^{83}Kr [8] and ^{131}Xe [9] were made. The notable difference between ^{21}Ne and other previously investigated species is the the approximate order of magnitude difference in relaxation times, which opens the door for experiments such as the remote detection of metal surfaces (due to long T_1 times), remote detection relaxometry in human lungs and indeed imaging applications.

Future work is warranted as to categorise further the behaviour of ^{21}Ne quadrupole relaxation and the relaxation behaviour with samples of differing surface chemistry. Additionally, a more concerted study into the SEOP dynamics is shown to be required as the ability to increase SNR without resorting to isotopically enriched gasses would greatly increase the viability of this technology.

A potential future application of hp ^{21}Ne is the use of remotely detected relaxometry at low magnetic fields for biomedical studies of tissues. Of particular interest would be investigations of surfaces of electrically conducting materials not typically able to be studied with conventional NMR.

Finally, the extremely long T_1 times measured, even in the model small

pores, indicate that a further use for this technique would be the investigation of the smallest level pores present within the combined SCR-filtration monolith used in Chapter 5. An interesting research stream would be the exploration of the viability of utilising isotropically enriched ^{21}Ne for imaging studies within porous materials

Overall the work presented within this document has shown major contributions to both the field of porous media magnetic resonance studies, and the understanding of SEOP fundamentals. Finally the explosive production methodology represents a major step forward for the utilisation and validation of ^{83}Kr as a MRI contrast agent for *in vivo* pulmonary studies. Techniques, such as Surface Quadrupolar Relaxation (SQUARE) [10] will be *scaled up* from the pre-clinical environment to human studies. Moreover, such techniques previously shown to act as unique probes of pulmonary diseases in anminal models of emphysema [11] and Asthma [12] study of animal models of lung diseases will be evaluated for the study of lung diseases in humans.

The initial steps towards these experiments have begun with the design and construction of a new multi-modal SEOP polariser which will be installed at the Philips 7 Tesla clinical scanner at the Sir Peter Mansfield Imaging Center at the University of Nottingham. This hyperpolariser was designed and built by Mr Fraser Hill-Casey, University of Nottingham Machinists Mr Alan Dorkes (Sir Peter Mansfield Imaging Center) and Mr Andrew Merrick (Medical Engineering unit) have fabricated many of the components for the hyperpolariser.

Bibliography

[1] J. S. Six, T. Hughes-Riley, K. F. Stupic, G. E. Pavlovskaya, and T. Meersmann, "Pathway to Cryogen Free Production of Hyperpolarized Krypton-83 and Xenon-129," *PLoS ONE*, vol. 7, no. 11, 2012.

[2] T. Hughes-Riley, J. S. Six, D. M. L. Lilburn, K. F. Stupic, A. C. Dorkes, D. E. Shaw, G. E. Pavlovskaya, and T. Meersmann, "Cryogenics free production of hyperpolarized ^{129}Xe and ^{83}Kr for biomedical MRI applications," *Journal of Magnetic Resonance*, vol. 237, pp. 23–33, 2013.

[3] E. Brunner, "Applications of laser-polarized ^{129}Xe under continuous flow," *Magnetic Resonance in Chemistry*, vol. 37, pp. S14–S22, dec 1999.

[4] P. T. Callaghan, "Rheo-NMR and velocity imaging," *Current Opinion in Colloid and Interface Science*, vol. 11, no. 1, pp. 13–18, 2006.

[5] P. T. Callaghan, *Translational Dynamics and Magnetic Resonance: Principles of Pulsed Gradient Spin Echo NMR*. OUP Oxford, 2011.

[6] N. J. Rogers, F. Hill-Casey, K. F. Stupic, J. S. Six, C. Lesbats, S. P. Rigby, J. Fraissard, G. E. Pavlovskaya, and T. Meersmann, "Molecular hydrogen and catalytic combustion in the production of hyperpolarized ^{83}Kr and ^{129}Xe MRI contrast agents," *Proceedings of the National Academy of Sciences*, vol. 113, pp. 3164–3168, mar 2016.

[7] Z. I. Cleveland, K. F. Stupic, G. E. Pavlovskaya, J. E. Repine, J. B. Wooten, and T. Meersmann, "Hyperpolarized ^{83}Kr and ^{129}Xe NMR Relaxation Measurements of Hydrated Surfaces: Implications for Materials Science and Pulmonary Diagnostics," *Journal of the American Chemical Society*, vol. 129, pp. 1784–1792, feb 2007.

[8] K. F. Stupic, Z. I. Cleveland, G. E. Pavlovskaya, and T. Meersmann, "Quadrupolar relaxation of hyperpolarized krypton-83 as a probe for surfaces," *Solid State Nuclear Magnetic Resonance*, vol. 29, pp. 79–84, feb 2006.

[9] K. F. Stupic, Z. I. Cleveland, G. E. Pavlovskaya, and T. Meersmann, "Hyperpolarized ^{131}Xe NMR spectroscopy," *Journal of Magnetic Resonance*, vol. 208, no. 1, pp. 58–69, 2011.

[10] J. S. Six, T. Hughes-Riley, D. M. Lilburn, A. C. Dorkes, K. F. Stupic, D. E. Shaw, P. G. Morris, I. P. Hall, G. E. Pavlovskaya, and T. Meersmann, "Pulmonary MRI contrast using Surface Quadrupolar Relaxation (SQUARE) of hyperpolarized ^{83}Kr," *Magnetic Resonance Imaging*, vol. 32, no. 1, pp. 48–53, 2014.

[11] D. M. L. Lilburn, C. Lesbats, J. S. Six, E. Dubuis, L. Yew-Booth, D. E. Shaw, M. G. Belvisi, M. A. Birrell, G. E. Pavlovskaya, and T. Meersmann, "Hyperpolarized ^{83}Kr magnetic resonance imaging of alveolar degradation in a rat model of emphysema.," *Journal of the Royal Society, Interface / the Royal Society*, vol. 12, no. 107, pp. 20150192–, 2015.

[12] D. M. Lilburn, A. L. Tatler, J. S. Six, C. Lesbats, A. Habgood, J. Porte, T. Hughes-Riley, D. E. Shaw, G. Jenkins, and T. Meersmann, "Investigating lung responses with functional hyperpolarized xenon-129 MRI in an ex vivo rat model of asthma," *Magnetic Resonance in Medicine*, vol. 76, no. 4, pp. 1224–1235, 2016.

Appendix A

Flow propagators

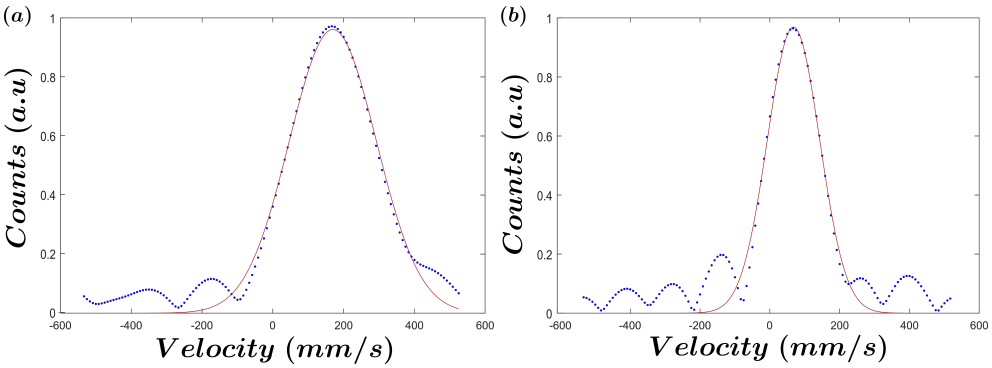


Figure A.1: Flow propagator from the channels within the central channel of the SCR monolith. (a) displays an example of a flow propagator taken from the center of a channel. (b) indicates a further propagator taken at the center of the channel directly below the center. In both cases the red trace indicates a Gaussian distribution of the flow propagator.

Appendix B

Monolith Channels Velocity Line Profiles

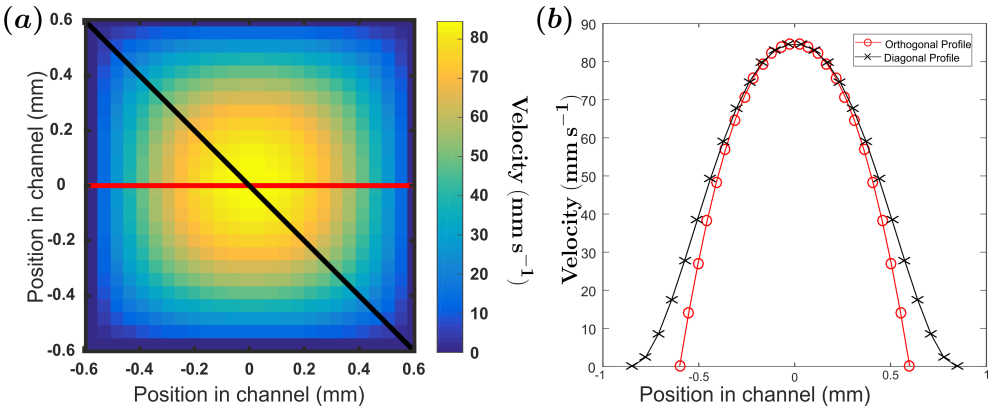


Figure B.1: Theoretical orthogonal and diagonal line profiles of Laminar flow in a rectangular channel plotted via use of Equation 5.10 in the main body of the text. (a) indicates an image of the modelled flow in a single channel of the combined selective catalytic reduction - filtration monolith used in this work. (b) displays an orthogonal (red line/circles) and a diagonal (black crosses/line) line profiles from (a). Each point in (b) indicates a sampled velocity of the theoretical model.

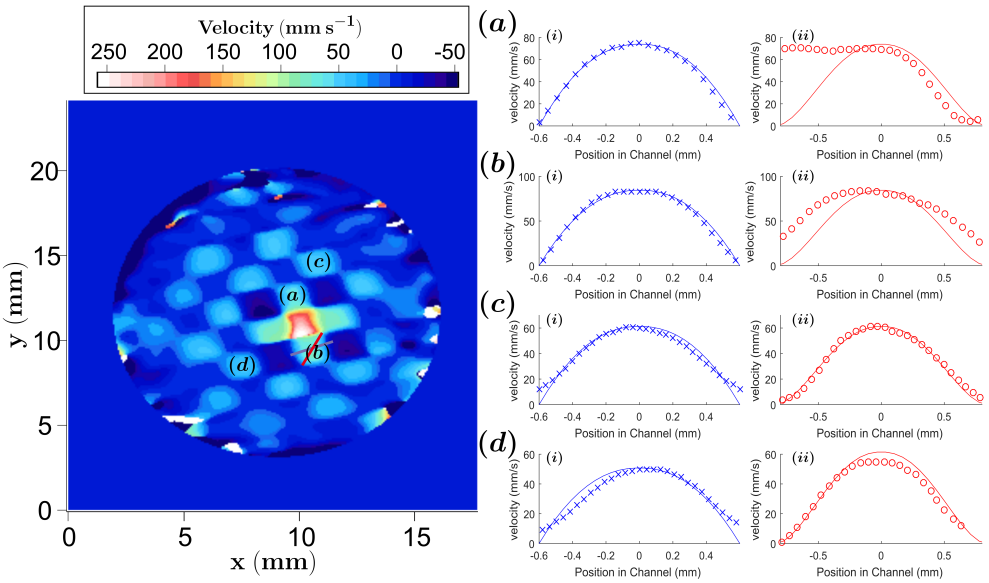


Figure B.2: Axial velocity maps of radial cross-section of monolith segment. The acquisition matrix was 64 × 32, zero filled to 128 × 128, FOV read: 22.1 mm, FOV phase: 16.99 mm, FOV slice: 15.7 mm. Axial velocity map of flow with Re = 52 in the central channel. 12 pairs of flow encoding gradients of duration $\delta = 0.5$ ms separated by a delay $\Delta = 5$ ms were used to characterise the flow. 4 averages were used to gain sufficient SNR. A recycle delay of 2 s was utilised and led to a total experiment time of 4 mins. The image is scaled to the peak velocity measured in the central channel of 261 mm/s. The purple line represents an orthogonal line profile, and the red arrow represents a diagonal line profile in; (a-d) indicate channels rom which line profiles were taken. In each sub figure (i) indicates line profile akin to that indicated by the purple line, orthogonal to the channel walls. Sub-figure (ii) displays line profiles taken from locations such as the Red line, diagonal across the channels. The solid lines in (a-d), sub-figures (i) and (ii) are fits of the experimental data (symbols) to the solution to laminar flow in a rectangular cross-section channel in Equation 5.10 within the main body of text.